UNIVERSITY OF ICELAND

Ph.D. Dissertation

In Chemistry

BDPA radicals for DNP-NMR and a new method for RNA spin-labeling

Iram Munir Ahmad

June 2026

FACULTY OF PHYSICAL SCIENCES

BDPA radicals for DNP-NMR and a new method for RNA spin-labeling

Iram Munir Ahmad

Dissertation submitted in partial fulfillment of a
Philosophiae Doctor degree in Chemistry

Advisor
Snorri Þór Sigurðsson

Ph.D. Committee
Guðmundur G. Haraldsson
Benjamín Ragnar Sveinbjörnsson
Elvar Örn Viktorsson

Opponents
Bela E. Bode
Már Másson

Faculty of Physical Science
School of Engineering and Natural Sciences
University of Iceland
Reykjavik, June 2026

BDPA radicals for DNP-NMR and a new method for RNA spin-labeling

Dissertation submitted in partial fulfillment of a *Ph.D.* degree in Chemistry

Faculty of Physical Sciences
School of Engineering and Natural Sciences
University of Iceland
Dunhagi 3
107 Reykjavik
Iceland

Telephone: 525 4000

Bibliographic information:
Iram Munir Ahmad, 2026, *BDPA radicals for DNP-NMR and a new method for RNA spin-labeling*, Ph.D. dissertation, Faculty of Physical Sciences, University of Iceland, 244 pp.

Author ORCID: 0000-0002-7163-6132
ISBN: 978-9935-585-03-5

Abstract

Dynamic nuclear polarization (DNP) is a powerful approach for overcoming the low sensitivity of nuclear magnetic resonance (NMR) spectroscopy and has extensive applications in the study of both materials and biological systems. Electron paramagnetic resonance (EPR) and fluorescence spectroscopy are highly important complementary techniques and are particularly valuable for studying nucleic acid structure and dynamics. The broader application of these methods, however, depends on the availability of suitable polarizing agents and site-specific spectroscopic probes, respectively. This thesis focuses on the development of 1,3 bisdiphenylene-2-phenylallyl (BDPA)-based polarizing agents for DNP-NMR and a facile spin labeling strategy for nucleic acids.

The first part describes the development of tailored BDPA derivatives for high-field DNP-NMR. The synthesis of the key precursor, tetrabromo BDPA, was first optimized. A tetraazide-BDPA building block was subsequently prepared, enabling conjugation to a variety of alkynes via copper-catalyzed azide-alkyne cycloaddition. Using this strategy, four BDPA derivatives with varied polarity, size, and steric shielding were prepared. Of these, a BDPA-dendrimer derivative exhibited enhanced persistence and superior DNP performance, achieving the highest liquid-state DNP enhancement reported to date in viscous solutions.

The second part describes a noncovalent RNA spin labeling strategy based on helical stacking of small RNA hairpins, containing the rigid spin label **Çm**, on RNA duplexes. Complementary overhangs promoted efficient hairpin-duplex stacking, monitored by EPR spectroscopy. In addition, collaborative projects involving incorporation of rigid and semi-rigid spin labels and fluorophores in nucleic acids to study their structure, dynamics and interactions with proteins using EPR and fluorescence spectroscopies, are recounted.

Útdráttur

Mögnun á kjarnskautun (e. dynamic nuclear polarization, DNP) er aðferð sem er notuð til að auka næmni kjarnsegulgreininga (e. nuclear magnetic resonance, NMR) og er afar mikilvæg fyrir rannsóknir á föstu efni og líffræðilegum sameindum. Litrófsgreiningar sem byggja á rafeindasegulgreiningu (e. electron paramagnetic resonance, EPR) og flúrljómun eru sömuleiðis mjög mikilvægar til að greina byggingu og hreyfingu kjarnsýra. Almenn notkun þessara aðferða er þó háð aðgengi að hentugum skautunarefnum (e. polarizing agent) fyrir DNP-NMR og sértækum spunamerkjum fyrir EPR. Þessi ritgerð lýsir hönnun og efnasmíði á 1,3-bistvífenýlen-2-fenýlallýl (BDPA)-afleiddum skautunarefnum fyrir DNP-NMR, auk nýrrar og einfaldrar aðferðar til spunamerkinga á kjarnsýrum.

Fyrri hlutinn lýsir þróun sérhannaðra BDPA-afleiða fyrir DNP-NMR í sterku segulsviði. Efnasmíði forverans, tetrabrómó-BDPA, var fyrst bestuð. Þar næst var tetraazíð-BDPA afleiða smíðuð, sem getur tengst ýmsum alkýnum með koparhvötuðum asíð-alkýn smellihvörfum. Þessi aðferð var notuð til efnasmíða á fjórum BDPA-afleiðum, með mismunandi skautun, stærð og rúmhindrun. Af þeim efnum sýndi greinótt BDPA-afleiða aukinn stöðugleika og betri DNP-eiginleika en áður þekktust. Þessi afleiða gaf hæstu DNP mögnun í seigfljótandi lausnum til þessa.

Síðari hlutinn lýsir aðferð til spunamerkingar kjarnsýra með ósamgildum tengjum. Aðferðin byggir á stöflun RNA hárnála (e. hairpin), sem innihalda stífa spunamerkið **Çm**, á RNA tvíliður. Samsvarandi (e. complementary) hangandi endar (e. overhangs) stuðluðu að skilvirkri RNA-RNA stöflun, sem var staðfest með EPR litrófsgreiningu. Auk þess er öðrum samstarfsverkefnum lýst, þar sem bygging og hreyfing kjarnsýra var rannsökuð, ásamt víxlverkunum við prótein, með notkun spuna- og flúrljómunarmerkja ásamt litrófsgreiningu.

Dedicated to my parents, Shabana and Munir for their love, and support,
and to my younger self, for always holding on and hanging in there

Table of Contents

List of Figures

List of Schemes

List of publications and my contribution

I. Ahmad IM, Roy P, Kuzhelev A and Sigurdsson ST, Tetra-substituted BDPA radicals via click-chemistry for liquid-state DNP, *Chem. Commun.* **2026**, 62, 10685-10689.

My contribution was major: Development of the synthetic strategy, including the design of the BDPA derivatives; synthesis, purification and characterization of all the compounds; collection and analysis of NMR, HPLC, UV-Vis, IR and CW-EPR data; writing of the first draft of the manuscript and contribution to its revision.

II. Ahmad IM, Endeward B, Prisner TF and Sigurdsson ST, Non-covalent spin-labeling of RNA with short hairpins containing the rigid spin label Çm, *Chem. Eur. J.* **2025**, 32, e03253.

My contribution was major: Design of the oligonucleotide sequences, planning and development of strategy; synthesis, purification and analysis of the unmodified and spin-labeled oligonucleotides; HPLC and CW-EPR data collection and analysis; preparation of the initial draft of manuscript and contribution to its subsequent revision.

III. Chadda R, Kaushik V, Ahmad IM, Deveryshetty J, Holehouse A, Sigurdsson ST, Biswas G, Levy Y, Bothner B, Cooley R, Mehl R, Dastvan R, Origanti S and Antony E, Partial wrapping of single-stranded DNA by Replication Protein A and modulation through phosphorylation, *Nucleic Acids Res*. **2024**, 52, 11626–40.

My contribution was minor: Synthesis and analysis of the spin-labeled oligonucleotides; participated in reviewing and editing the manuscript.

IV. Florian H, Halbritter A-LJ, Ahmad IM, Braun M, Sigurdsson ST and Wachtveitl J, Förster resonance energy transfer within the neomycin aptamer, *Phys. Chem. Chem. Phys.* **2024**, *26*, 7157-65.

My contribution was minor: Synthesis and analysis of the fluorescence-labeled oligonucleotides; involved in reviewing and editing the manuscript.

V. Mardini M, Palani RS, Ahmad IM, Mandal S, Jawla SK, Bryerton E, Temkin RJ, Sigurdsson ST and Griffin RG, Frequency-swept dynamic nuclear polarization, *J. Magnet. Reson.* **2023**, *353*, 107511.

My contribution was minor: Synthesis and characterization of the trimethylammonium BDPA radical; participated in reviewing and editing the manuscript.

VI. Kuzhelev A, Denysenkov D, Ahmad IM, Bagryanskaya E, Tormyshev V, Sigurdsson ST and Prisner T, Solid effect dynamic nuclear polarization in viscous liquids using narrow line polarizing agents at 9.4 T, *J. Am. Chem. Soc.* **2023**, *145*, 10268-74.

My contribution was minor: Synthesis and characterization of the trimethylammonium BDPA radical, one of the three radicals used in this study; involved in reviewing and editing the manuscript.

Abbreviations

A	Adenine
2′-NH_2U	2′-aminouridine
BDPA	1,3- bisdiphenylene-2- phenylallyl
bTbk	Bis-TEMPO-bis-ketal
BTnE	Bis-TEMPO-n-ethylene glycol
C	Cytosine
CE	Cross effect
CIDNP	Chemically induced dynamic nuclear polarization
CRC	Collaborative Research Centre
Cryo-EM	Cryogenic electron microscopy
CuAAC	Cu-catalyzed azide-alkyne cycloaddition
CW	Continuous wave
Ç	rigid spin-labeled nucleoside “C-spin” for DNA
Çm	rigid spin-labeled nucleoside “C-m-spin for RNA
Ċ	rigid spin-labeled nucleoside “C-dot for DNA
Ċm	rigid spin-labeled nucleoside “C-dot for RNA
DEER	Double electron-electron resonance
DMSO	Dimethyl sulfoxide
DMT	Dimethoxytrityl
DNA	Deoxyribonucleic acid
DNP	Dynamic nuclear polarization
ds	double-stranded
DPAGE	Denaturing polyacrylamide gel electrophoresis
DQ	Double quantum
DQC	Double quantum coherence
ENDOR	Electron-nuclear double resonance
EPR	Electron paramagnetic resonance
ESEEM	Electron spin echo envelope modulation
FRET	Förster resonance energy transfer

G	Guanine
HPLC	High-performance liquid chromatography
HYSCORE	Hyperfine sublevel correlation
MAS	Magic angle spinning
MG	Malachite green
μw	Microwave
nt	nucleotide
NMR	Nuclear magnetic resonance
OE	Overhauser effect
OP	Optical pumping
PA	Polarizing agent
PEG	Polyethylene glycol
PELDOR	Pulsed electron-electron double resonance
p-H_2	Parahydrogen
PHIP	Parahydrogen induced polarization
REDOR	Rotational echo double resonance
RIDME	Relaxation induced dipolar modulation enhancement
RNA	Ribonucleic acid
RPA	Replication protein A
SABRE	Signal amplification by reversible exchange
SE	Solid effect
SELEX	Systematic evolution of ligands by exponential enrichment
SDSL	Site-directed spin labeling
SIFTER	Single-frequency technique for refocusing dipolar couplings
ss	single-stranded
T_B	Build-up time
TMR	Tetramethylrhodamine
t-BuOK	Potassium tert-butoxide
TEDOR	Transferred echo double resonance
TEMPO	2,2,6,6-Tetramethylpiperidine-1-oxyl
TLC	Thin layer chromatography
TM	Thermal mixing
UV-Vis	Ultraviolet-visible

ZQ	Zero quantum

Acknowledgements

I would like to begin by expressing my deepest gratitude to my doctoral advisor, Prof. Snorri Þór Sigurðsson, for his guidance, encouragement, and unwavering support throughout my PhD studies. His approach to research and addressing problems, his attention to detail, and his focus on critical thinking have all had a lasting effect on me as a researcher. I am truly grateful for all that he has taught me, not only in research, but also in how to approach challenges with diligence, patience, and curiosity.

I am also sincerely thankful to the members of my PhD committee, Prof. Guðmundur G. Haraldsson, Assoc. Prof. Benjamín Ragnar Sveinbjörnsson, and Asst. Prof. Elvar Örn Viktorsson, for their time, support, and valuable input during my doctoral studies. Their comments, perspectives, and encouragement have been greatly appreciated. I would also like to thank my distinguished opponents, Prof. Bela E. Bode and Prof. Már Másson, for taking the time to review my work.

My thanks also go to the present and past members of our research group for their support, kindness, and the pleasant working environment they helped create. I am grateful for the conversations, help, and camaraderie along the way, as well as for the coffee breaks, laughter, and small everyday moments that made the long days in the lab more enjoyable. I would also like to thank Gunnar Reginsson and Sigríður Jónsdóttir for their assistance with analyses, and Oskar Kettler and Sverrir Guðmundsson for their help during teaching and for their support in managing laboratory equipment.

I would also like to acknowledge the Icelandic Centre of Research (Rannís), the University of Iceland Teaching Assistantship Grant, and the Aðalsteinn Kristjánsson Memorial Fund for their financial support. Their support made this work possible.

Finally, I would like to thank my family for all their love and support throughout this journey. I am especially grateful to my parents for their constant belief in me, for their sacrifices, and for always encouraging me to keep going. Their support has meant more than words can express. I am also deeply thankful to my little sister for always having my back. My heartfelt thanks go to my partner, whose love, patience, and support carried me through both the

difficult and the joyful moments of this PhD, and who has always been my biggest cheerleader throughout this journey.

Completing this journey would not have been possible without the support of all these people, and I will always remain deeply thankful.

Aims of the thesis

The aim of this thesis was two-fold. **Part A** aimed to develop BDPA derivatives for high-field DNP-NMR spectroscopy. The first objective was to improve the synthesis of an important BDPA intermediate, followed by establishing a versatile synthetic approach that would allow easy and efficient incorporation of structural modifications to BDPA. These modifications were intended to improve properties important for DNP applications, including radical persistence, solubility, and DNP performance. **Part B** entails labeling of nucleic acids for EPR and fluorescence studies. In particular, the first aim here was to establish a practical noncovalent RNA spin-labelling strategy based on helical stacking of **Çm**-labeled RNA hairpins onto RNA duplexes. This approach was intended to reduce the synthetic effort normally required for site-directed spin labeling, while providing a modular method for introducing rigid spin labels into RNA systems for EPR-based structural studies. In addition, this part aimed to use spin- and fluorescence-labeled nucleic acids in collaborative studies of nucleic acid structure, dynamics, and biomolecular interactions.

The two parts of the thesis are structured as follows:

A. **BDPA radicals for DNP-NMR**: This part focuses on the optimization of the synthesis of a key BDPA intermediate and the development of a divergent synthetic route to tunable BDPA derivatives for high-field DNP-NMR. It further examines a highly sterically shielded, high molecular weight BDPA derivative for persistence and liquid DNP performance.
   The work associated with this part is described in Chapter A2 and Paper I.

B. **Labeling of nucleic acids with spin labels and fluorophores**: This part focuses on the development of a noncovalent RNA spin-labeling approach based on helical stacking of RNA hairpins containing the rigid spin label **Çm** onto RNA duplexes. It also includes collaborative projects involving incorporation of rigid and semi-rigid spin labels and fluorescent probes into nucleic acids, aimed at investigating nucleic acid structure, dynamics, and biomolecular interactions.

The work associated with this part is described in Chapter B2, B3 and in Paper II, III and IV.

Part A BDPA radicals for DNP-NMR

A1 Introduction

The world is built upon the invisible architecture of molecules. From the synchronized chemistry that sustains life within a cell to the engineered lattices of a high-performance battery, the behaviour of complex systems depends not only on composition, but also on how molecules are arranged and their dynamics. These structure-function relationships control key outcomes across science and technology. Therefore, understanding the structure and dynamics of these complex systems is of fundamental importance for elucidating biological function and for the rational design and optimization of functional materials. Various techniques provide the means to directly probe structure and dynamics at the molecular level. The next section gives an overview of these major techniques, before focusing on NMR spectroscopy, which is central to part A of this thesis.

1.1 Techniques to study structure and dynamics

Among the various techniques developed for studying the structure and dynamics of molecules, X-ray crystallography is one of the most established methods which provides three-dimensional structures at near-atomic resolution.[1] While crystallography can deliver highly detailed structural information and has been applied to a broad range of proteins and macromolecular complexes, it has limitations. It requires high-quality crystals, which can be challenging and time-consuming to obtain.[2] Moreover, crystallization requires large amounts of material (milligrams), which can be difficult to produce, particularly for biomolecules such as proteins and nucleic acids.[3, 4] In addition, flexible regions of molecules with many conformational states, cannot be resolved using X-ray crystallography.[5] As an alternative that avoids crystallization, cryo-electron microscopy (cryo-EM) has become a powerful structural technique, especially for large assemblies.[6] In cryo-EM, samples are rapidly vitrified (flash-freezing in liquid ethane) and imaged using an electron beam under cryogenic conditions.[7] These images are then computationally reconstructed into 3D density maps from which structural models can be built.[8] Cryo-EM can reach near-atomic resolution

for many systems and is well suited to complexes that are difficult to crystallize. Usually, the achievable resolution using cryo-EM is about 2-4 Å,[9] but recent reports have obtained resolutions of about 1.2 Å, which is as good as the best crystallographic structures.[10, 11] Additionally, since the images depict static 'frozen' states, molecular dynamics must be determined from the diverse shapes observed (conformational heterogeneity) rather than measurement of real-time motion.[12]

Spectroscopic techniques such as Förster resonance energy transfer (FRET)[13-15] and electron paramagnetic resonance (EPR)[16-18] provide complementary information on structure and dynamics under near-native conditions. In FRET, two fluorophores, a donor and an acceptor are site-specifically attached to the molecule. Upon excitation of the donor, energy is transferred to the acceptor, allowing precise measurement of distances (~2-10 nm) and conformational changes. In EPR spectroscopy, paramagnetic centers such as nitroxide spin labels are incorporated into the system under study. Pulsed EPR techniques, like pulsed electron-electron double resonance (PELDOR), also known as double electron-electron resonance (DEER), measure dipolar interactions between two spins, providing long-range distance information (~1.5-10 nm). Both methods are highly sensitive and are particularly valuable for studying conformational changes, interactions, and distances in functional environments. However, they provide lower structural resolution and require incorporation of fluorescent dyes or paramagnetic labels.

Nuclear magnetic resonance (NMR) spectroscopy is one of the most important analytical techniques, offering several advantages over the other techniques.[19-21] Specifically, it is non-invasive, can be performed in native environments, and provides site-specific information on both structure and dynamics. A major strength of modern NMR is the use of multidimensional (2D and 3D) pulse techniques, that provide spectral information across additional frequency dimensions, reduce overlap, and enable detailed structural analysis at atomic resolution.[22, 23] NMR can also monitor molecular interactions and conformational dynamics across a wide range of timescales.[24] The following section introduces the basic principles of NMR spectroscopy, discusses key limitations, and outlines strategies by which these limitations can be addressed.

1.2 NMR spectroscopy

NMR spectroscopy derives structural and dynamic information by exploiting the magnetic properties of atomic nuclei in a magnetic field. NMR can only detect nuclei with non-zero spin ($I \neq 0$), because they have intrinsic angular momentum and an associated magnetic moment. Many commonly observed nuclei such as ^{1}H, ^{13}C, ^{15}N, and ^{31}P have a spin of ½ (I = 1/2), which usually produce sharp, high-resolution signals. Moreover, many quadrupolar nuclei ($I > 1/2$), like ^{2}H, ^{14}N, and ^{23}Na, are also NMR-active but show broader spectral lines due to interactions of their quadrupole moment with local electric field gradients. Under an external magnetic field B_0, nuclear spins align either parallel or antiparallel to the field, resulting in two energy states (**Figure 1**). When a radiofrequency pulse is applied, transition of spins from ground state (m = +1/2) to excited state (m = −1/2) occurs. The transition occurs at a characteristic resonance frequency, called the Larmor frequency $\omega_n = \gamma B_0$. Here, γ is the gyromagnetic ratio, which is unique to each nucleus and determines both the resonance frequency and intrinsic sensitivity. Each nucleus experiences a unique effective field due to the local electronic environment, called magnetic shielding. It produces chemical shifts that provide information on local bonding, functional groups, and overall molecular structure. NMR measurements can be performed in solution, solid and, less commonly, in the gas phase.

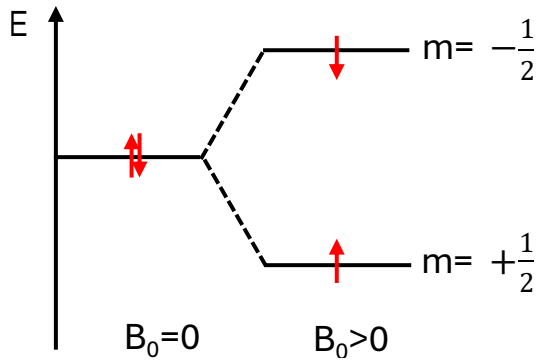

Figure 1 Energy level splitting of a spin 1/2 nucleus in an external magnetic field B_0 due to Zeeman effect.

Solution-state NMR is the most widely used form of NMR that provides high-resolution structural information. The rapid molecular tumbling in solution averages out anisotropic nuclear interactions, resulting in sharp spectral lines. However, when rotational motion slows down, for example in larger molecules, it causes spectral line broadening. Therefore,

many large biomolecular assemblies, aggregates, various functional materials (>30 kDa) cannot be studied at high resolution using solution-state NMR.[25]

For compounds that are difficult to analyze using solution-state NMR, solid-state NMR provides a powerful alternative.[26] Unlike solution-state NMR, solid-state NMR produces strong orientation-dependent (anisotropic) interactions like through-space dipolar coupling and chemical shift anisotropy. Dipolar couplings can be used to determine distances of ~1–6 Å by measuring the dipolar couplings between specific nuclei using various pulsed solid-state NMR techniques like rotational echo double resonance (REDOR)[27] and transferred echo double resonance (TEDOR).[28] Chemical anisotropy, however, causes broad spectral lines known as "powdered patterns", resulting in reduced spectral resolution.[29, 30] Anisotropy can be averaged out using magic-angle spinning (MAS). It involves spinning the sample at a 54.74° angle with respect to B_0 (**Figure 2A**).[30-32] **Figure 2B** shows an example of NMR spectrum of polycrystalline glycine under static conditions and with MAS at 7.0 kHz.[25] With MAS, a single sharp line for the carboxyl carbon of glycine is obtained along with the spinning sidebands that appear at integer multiples of the sample rotation frequency.[25] The MAS-NMR technique has been utilized to obtain high-resolution data on various solid samples, involving various biological systems, including amyloid fibrils,[33] membrane proteins,[34, 35] biomaterials[36] and heterogenous catalysts.[37] Nonetheless, similar to other NMR techniques, a major challenge for MAS-NMR, is its inherent lack of sensitivity, which limits its use.

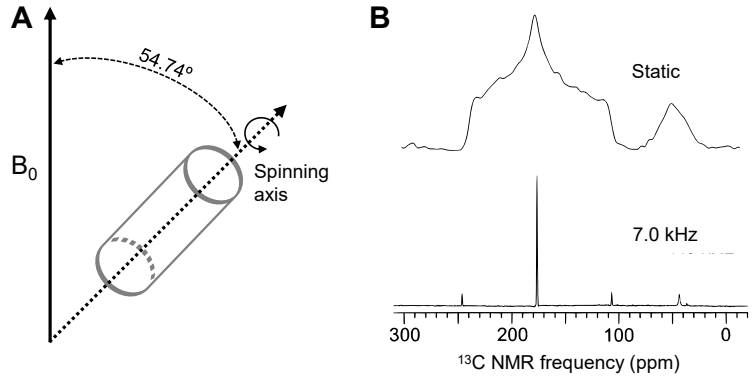

Figure 2 A. A schematic diagram of MAS of a sample at the magic angle. **B**. A ^{13}C-NMR spectrum of polycrystalline glycine in static field vs obtained with magic angle spinning at the frequency of 7.0 kHz. **Figure 2B** is printed with permission from *Annu. Rev. Chem*., **2001**, 52, 575-606.

1.2.1 Low sensitivity of NMR

Despite the widespread use of NMR spectroscopy, it faces a fundamental limitation due to its inherently low sensitivity. The sensitivity of NMR is directly proportional to the population difference between the two nuclear spin states in the presence of a magnetic field. At thermal equilibrium, this population difference is described by the Boltzmann spin polarization, defined as the ratio of the difference in number of spins and total number of spins in the two states:

$$\frac{N1-N2}{N1+N2} = \tanh\left(\frac{\gamma\hbar B_0}{2K_B T}\right) \qquad \text{(Eq. 1)}$$

Here, N1 and N2 represent populations of the lower and higher energy nuclear spin states, respectively, γ is the gyromagnetic ratio, $\hbar$ is the reduced Planck constant; B_0 is the external magnetic field strength, K_B is the Boltzmann constant, and T is temperature in Kelvin. Under typical NMR conditions (9.4 T and 300 K), the Boltzmann spin polarization is very low between nuclear spin states, leading to low sensitivity (**Figure 3A**). For example, the Boltzmann spin polarization for ^{1}H is about 0.003%, while for less abundant nuclei, such as ^{13}C and ^{15}N, polarization is even lower (approximately 0.0008% and 0.0003%, respectively).[38] Since the Boltzmann spin polarization of nuclei depends upon the B_0 and temperature (Eq. 1), higher B_0[39, 40] and lower temperatures[41, 42] have been widely used to increase polarization. However, even at very high magnetic fields like 18.8 T, and temperatures as low as 10 K, the polarization of ^{1}H nuclei reaches only about 0.2%.[43]

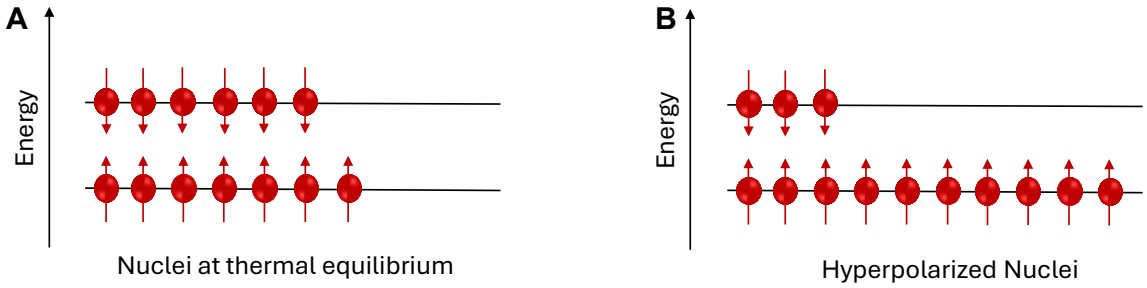

Figure 3 A. Small population difference between spin states at thermal equilibrium, resulting in very low polarization. **B**. Increase in population difference of nuclei after hyperpolarization.

Various hyperpolarization techniques have been developed over the past years to enhance the NMR sensitivity by several orders of magnitude.[44] Hyperpolarization creates a strongly non-equilibrium spin distribution, in which most spins occupy a single spin state (**Figure**

3B). Some important hyperpolarization methods, namely parahydrogen induced polarization (PHIP),[45] chemically induced dynamic nuclear polarization (CIDNP), optical pumping (OP), and dynamic nuclear polarization (DNP) are described below.

PHIP uses nuclear spin-singlet state of parahydrogen (p-H_2) where two hydrogen nuclei are antisymmetric. The hyperpolarization is generated by breaking the symmetry of the singlet, which is achieved by catalytic hydrogenation, where p-H_2 is added to an unsaturated substrate.[46, 47] Recently, a non-hydrogenative PHIP involving no chemical modification has been developed, called signal amplification by reversible exchange (SABRE).[48, 49] Here, p-H_2 and substrate bind reversibly to a metal complex, where polarization is transferred from p-H_2 to the substrate via exchange couplings. The substrate then dissociates in a hyperpolarized state without undergoing chemical transformation. NMR enhancements produced using PHIP are of the order 10^2–10^5.[50] PHIP does not need very specialized hardware like many other hyperpolarization techniques do and can produce very high levels of polarization. However, the method needs a substrate with good binding-affinity with the metal catalyst, limiting the types of molecules that can be studied. In addition, the polarization lifetime for PHIP is limited by T_1 of the polarized nucleus and ranges from seconds to minutes.[50]

The hyperpolarization technique CIDNP produces polarization through radical-pair reactions, which could either be heat- or light-driven (Photo-CIDNP).[51, 52] Photo-CIDNP is more commonly used and has been utilized in both liquid and solid systems. For example, photosensitizer dyes can be stimulated by light and interact with molecules in solution that donate electrons, creating a radical pair that causes the photo-CIDNP effect. CIDNP works especially well with heteroaromatic compounds and aromatic amino acids[53] like tryptophan[54] and tyrosine (Tyr)[55]. It has been extensively utilized to investigate protein folding and reaction mechanisms.[56, 57] The average NMR enhancement is between 1 and 10^2.[51] CIDNP is a great tool for studying protein structure and folding because it is very selective for molecular sites in specific amino acids. By selectively amplifying signals from these residues, it can elucidate reaction pathways and local environments within biomolecules. However, the polarization produced usually only lasts for a few milliseconds to a few seconds.[58] Additionally, since the effect relies on particular photochemical or thermally induced reactions, its applicability to materials and non-reactive systems is still limited.

Another technique that uses light is OP. Here, circularly polarized light transfers angular momentum of light to excite electrons, which transfers polarization to nuclear spins. OP has been mainly used to polarize noble gas nuclei, such as ^{129}Xe and ^{3}He.[59] One important application of this technique is high-contrast lung imaging.[60] Apart from imaging, OP has recently been used in atomic clocks, which provide the ultra-precise timing required for GPS technology.[61] Another application is optically pumped magnetometers, which use hyperpolarized alkali vapors to detect tiny biomagnetic fields from the brain.[62] Furthermore, OP has also been applied to semiconductors, such as gallium arsenide and silicon, to develop quantum computing materials.[63] In the gas phase, the polarization is sustained for very long, up to hours.[64] An advantage of OP is that it requires neither low temperatures nor any paramagnetic doping. However, its application is mainly limited to noble gases and certain semiconductors.

Among all the hyperpolarization techniques, DNP is the most popular and widely applicable. It involves polarization transfer from electron spins to nuclear spins using microwave irradiation. It is applicable to any system with an NMR-active nucleus. It has been successfully employed in various fields such as in materials,[65] heterogeneous catalysts,[66] polymers[67] and biological tissues[68]. The following section provides a detailed overview of the principle of DNP, various DNP polarization pathways and the typical instrumentation setup.

1.3 Dynamic Nuclear Polarization (DNP)

The concept of DNP was first proposed theoretically by Albert Overhauser in 1953.[69] The central idea revolved around the large difference between electron and nuclear spin polarization, with electron spins possessing a polarization that is several hundred folds higher than that of nuclear spins.[70] For instance, at 100 K and 14.1 T, the spin polarization of electrons is 9.1% while that of proton spins is 0.014% (**Figure 4**). In DNP this high polarization of electrons can be transferred to nuclear spins in the presence of microwave (μw) irradiation. To achieve this, the sample is doped with a source of unpaired electrons known as a polarizing agent (PA). Electron spins are excited in the presence of μw and polarization is transferred to nuclear spins, resulting in enhanced NMR signal. The theoretical enhancement in NMR signal (ε_{max}) that can be achieved by DNP is given by the ratio of electronic and nuclear polarizations. For ^{1}H, the theoretical signal enhancement is

~660, while for lower-γ nuclei such as ^{13}C and ^{15}N the enhancements are ~2600 and ~6600, respectively.[71] In practice, however, experimental enhancements, defined as the ratio of the NMR signal intensities with and without μw ($\varepsilon_{on/off}$), are lower than predicted by theory.[38] This definition assumes that the μw-off signal represents the thermal Boltzmann polarization.[38]

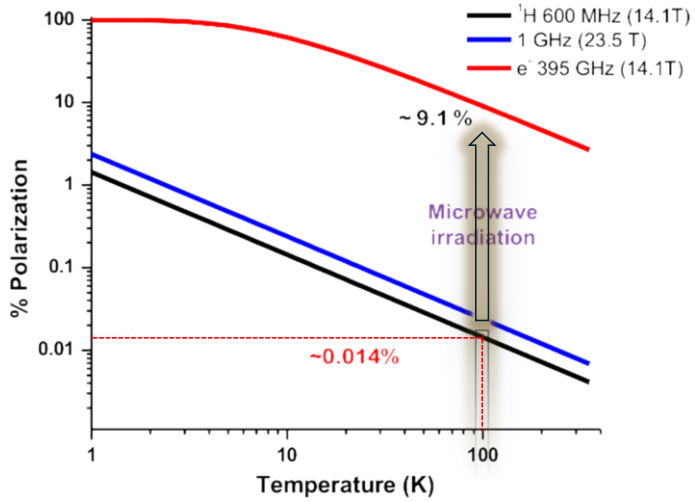

Figure 4 Electron and nuclear polarization as a function of temperature and magnetic field. The polarization of an electron (red solid line) and ^{1}H (black line) at 100 K and 14.1 T are highlighted (red dashed line). The ^{1}H polarization gain with moving to a higher magnetic field (blue line) is shown for comparison. **Figure 4** is reproduced with permission from *Biomolecules*, **2020**, 10(9), 1246.

However, $\varepsilon_{on/off}$ is not a true measure of enhancement. There are other factors that affect the observed NMR signal. One such factor is depolarization, which is the loss of polarization under MAS without μw.[72] Another important factor, known as paramagnetic bleaching (or quenching), causes the nuclei near the radical to relax too fast, which leads to loss of signal.[72, 73] To account for these factors, the term Absolute sensitivity Σ has been introduced (Eq. 2).[72]

$$\Sigma = \varepsilon_{on/off} \times \varepsilon_{Depo} \times \varepsilon_{quenching} \qquad \text{(Eq. 2)}$$

However, precise measurement of ε_{Depo} is time-consuming and technically challenging. Another important factor that severely affects the enhancement is build-up time (T_B). It determines how fast the polarization is established and, therefore, a shorter T_B causes faster signal averaging.[38] Thus, a more accessible metric for comparing the performance of new PAs has been introduced: Overall DNP sensitivity, which is defined as the signal to noise ratio (S/N) per square root unit time (Eq. 3).[74-76]

$$Sensitivity = \frac{S}{N} * \frac{1}{\sqrt{T_B}} \quad \text{(Eq. 3)}$$

This quantity reflects both the magnitude of enhancement and the speed at which polarization is generated, making it particularly useful when evaluating and optimizing new PAs for DNP applications.

1.3.1 Mechanisms of polarization transfer in DNP

In DNP, the transfer of polarization of unpaired electrons to nuclear spins occurs through various mechanisms, [38, 77] namely the Overhauser Effect (OE),[78] the Solid Effect (SE),[79-81] the Cross Effect (CE)[82, 83] and Thermal Mixing (TM)[84]. All the mechanisms do not occur simultaneously, rather the type of mechanism that is operational during the DNP experiments depends on the type and concentration of the radical used, the magnetic field, temperature and μw frequency. The active DNP mechanism can be identified by a DNP field profile, which is a plot of the NMR enhancement as a function of B_0 (**Figure 5**). Below is a description of the four important DNP mechanisms, along with their DNP field profiles.

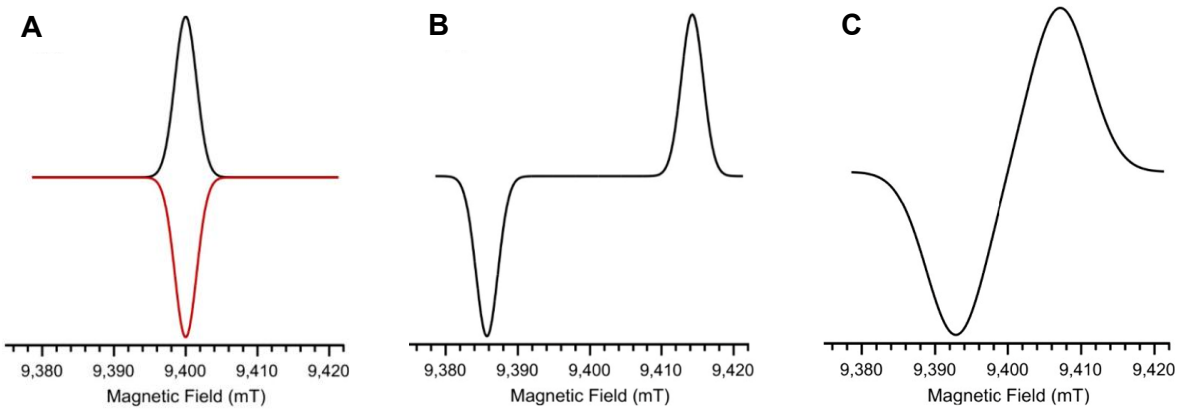

Figure 5. Simulated DNP field sweep profiles expected ^{1}H hyperpolarization in the case of (**A**) the Overhauser effect where the ZQ relaxation dominates (black) or the DQ relaxation dominates (red) (**B**) the SE, and (**C**) the CE/TM. **Figure 5** is printed with permission from *J. Phys. Chem. Lett.* **2025**, *16* (14), 3420-3432.

The Overhauser effect (OE)

The OE was the first DNP mechanism to be reported, originally observed in metals in 1953.[69] Later, it was also observed in liquids and insulating solids.[78, 83, 85] It is a two-spin process involving electron-nuclear cross-relaxation. For OE to be efficient, it requires fast molecular motion to modulate hyperfine interactions between the electron and a nucleus.[85] OE involves two important relaxation pathways, namely, zero- and double-quantum relaxation pathways.

In a zero-quantum transition, the spins of the electron and the nucleus flip in opposite directions at the same time, which keeps the total spin quantum number the same.[77] During a double-quantum transition, both spins flip in the same direction at the same time, which changes their spin states at the same time. These coupled spin-flip processes cause transfer of polarization from the electron to the nucleus. The efficiency of OE is however limited by correlation times and T_1 relaxation of the nucleus.[77] The typical DNP field profile of OE is broad and has a single extremum value of enhancement (**Figure 5A**). The enhancement sign could either be positive or negative and is determined by the dominant electron-nuclear relaxation pathway (**Figure 5A**). Electron-nuclear relaxation pathway through contact (scalar) coupling yields a positive enhancement, while dipolar coupling produces a negative enhancement.[77, 86]

Solid Effect (SE)

The SE is a two-spin process like OE. In contrast to the OE, however, polarization transfer in the SE occurs through μw-driven forbidden transitions.[87] These transitions involve simultaneous flipping of both the electron and nuclear spins. Polarization transfer occurs when μw frequency equals sum or the difference of the electron (ω_e) and the nuclear Larmor frequency (ω_n):

$$\omega_{\mu w} = \omega_e + \omega_n \quad \text{(Eq. 4)}$$

SE is efficient when the EPR linewidth (δ) of the PA is much smaller than the nuclear Larmor frequency (ω_n). Therefore, a PA with a narrow EPR line is desirable.[77, 88] The DNP field profile of SE is characterized by two symmetrical positive and negative maxima separated by a magnetic field difference corresponding to $2\omega_n$ (**Figure 5B**).[77]

The cross effect (CE)

The CE is a three-spin process that involves two electrons and a nuclear spin.[89] For CE to occur efficiently, two electrons must be dipolar coupled and their corresponding electron spin resonance frequencies must be separated by ω_n:

$$\omega_{e1} - \omega_{e2} = \omega_n \quad \text{(Eq. 5)}$$

PAs such as nitroxides, that have a broad EPR linewidth satisfy this condition.[38] The DNP profile for CE shows a broad positive or negative peak centered around the electron Larmor frequency (**Figure 5C**).[77]

Thermal mixing (TM)

TM is a multi-spin process that resembles CE, but involves a larger ensemble of interacting spins.[71] It occurs only when there is a strong electron-electron dipolar coupling and when the homogeneously broadened EPR spectrum is larger than the nuclear Larmor frequency ($\delta > \omega_n$). This condition usually occurs at high concentrations of PAs and at very low temperatures (10 K). The DNP-profile for TM resembles CE (**Figure 5C**).[38]

Propagation of polarization through spin-diffusion

Polarization transfer from electron spins of PA through a particular DNP mechanism listed above initially occurs with a few nuclei, close to the radical. However, propagation of polarization of nuclei to the bulk occurs via spin-diffusion. Spin-diffusion involves polarization exchange between homonuclear spins through dipole-dipole interactions between the homonuclear spins.[38]

1.3.2 Experimental setup for DNP

DNP experiments can be implemented in different experimental conditions depending on the sample state, temperature, magnetic field, and the operative DNP mechanism. In liquid-state DNP, typically exploiting the OE and more recently SE, the polarization is generated directly in solution without MAS, at or near ambient temperature through electron-nuclear cross-relaxation promoted by molecular motion.[90-92] In dissolution DNP, which combines cryogenic and ambient-temperature stages, the polarization is first built up in a frozen glassy sample at low temperature and high field, and the hyperpolarized material is then rapidly dissolved and transferred for liquid-state NMR or MRI detection.[93, 94] In solid-state MAS DNP, polarization is generated and detected directly in the solid-state under MAS, most commonly at cryogenic temperatures. Solid-state MAS DNP currently represents the most widely used DNP technique for structural characterization of materials and biomolecules by NMR,[38] and its instrumentation is described below.

The implementation of MAS DNP requires additional hardware beyond a conventional NMR spectrometer. A schematic representation of a MAS DNP-NMR instrument is shown

in **Figure 6**.[95] The central component is the high-frequency μw source. In modern DNP systems, it is usually a gyrotron which is a high-power microwave vacuum electronic oscillator. In the gyrotron the electron beam is accelerated through superconducting magnet. The electron beam passes through a radiofrequency resonant cavity, where it undergoes gyration (rotation) under the influence of magnetic field. Gyration leads to conversion of beam energy to μw radiation. Most advanced gyrotrons generate μw with a frequency of 593 GHz, enabling DNP experiments at magnetic fields up to 21.1 T.[96, 97]

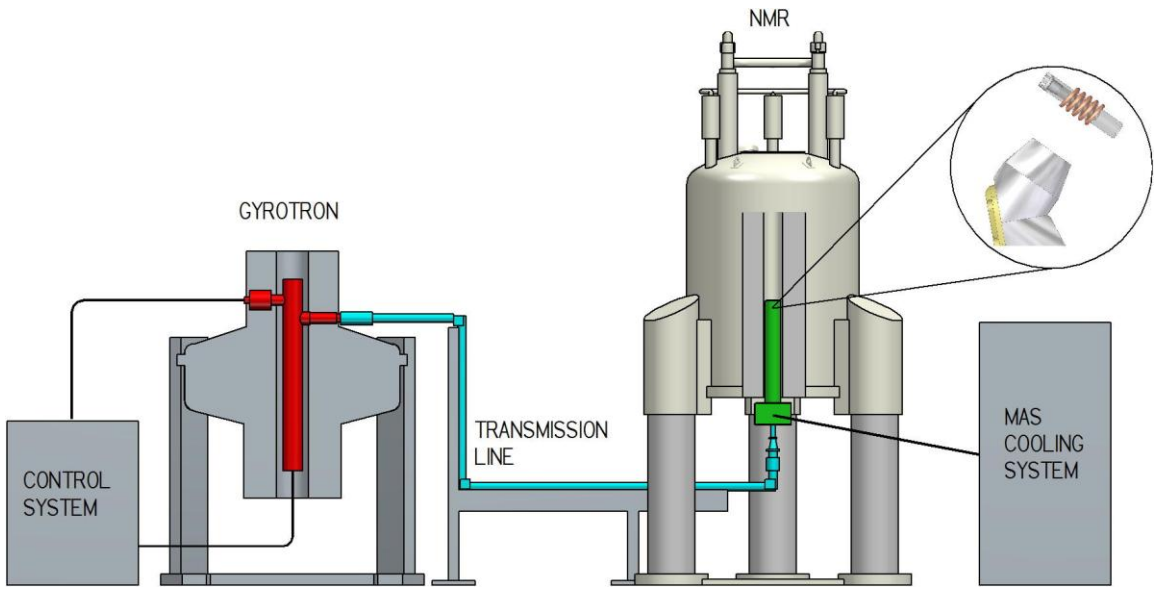

Figure 6 Schematic of a modern commercial DNP-NMR spectrometer. **Figure 6** is printed with permission from *J. Magn. Reson*. **2016**, *264*, 88–98.

The delivery of the μw radiation to the samples is achieved using waveguides (transmission lines), which allows μw delivery with minimal loss of power.[98] Most solid-state DNP-NMR experiments are performed at cryogenic temperatures.[77] Cooling at temperatures below 100 K is achieved using N_2 or He gases. In solid-state DNP, the sample is contained in a cylindrical rotor that can be made of sapphire, zirconia or diamond to withstand low temperatures and high spinning speeds. The rotor diameter determines the achievable spinning frequency. For example, a 3.2 mm rotor can typically reach spinning speeds of up to 15 kHz,[99] whereas smaller rotors, such as 0.7 mm rotors, can achieve spinning rates as high as 65 kHz.[100] More recently, spherical rotors have been introduced as an alternative to conventional cylindrical rotors.[101] These rotors can achieve very high and stable spinning frequencies; for example, spinning rates of up to 68 kHz have been reported for 2 mm diameter rotors.[102]

The instrumental requirements varies depending on the DNP experiment being performed. In liquid-state DNP, polarization is generated directly in solution, at or near ambient temperature, so cryogenic cooling is not required. Instead, the setup requires a double-resonance probe that combines μw irradiation of the liquid sample with NMR detection. At high magnetic fields, efficient microwave delivery is challenging because aqueous samples can suffer from strong dielectric losses and microwave-induced heating. To address this, liquid-state DNP probes use resonator designs such as a Fabry–Perot resonator for microwave excitation combined with a stripline resonator for NMR detection[92, 103] Dissolution DNP, by contrast, requires a dedicated polarizer operating at cryogenic temperature together with a rapid-dissolution and transfer system that delivers the hyperpolarized material to a separate NMR or MRI detector before relaxation occurs.[94]

1.4 Polarizing agents for DNP

As mentioned before, a PA is a compound containing unpaired electron spins that act as the source of electron spin polarization that is transferred to nuclear spins in DNP. The most commonly used PAs are stable organic radicals such as nitroxides, eg. TEMPO and carbon-centered radicals like Finland trityl and 1,3-bisdiphenylene-2-phenylallyl (BDPA) as well as most recently developed verdazyl radicals (**Figure 7**).[104] Apart from organic radicals, paramagnetic metal-ion complexes such as Gd-DOTA and Mn-DOTA are also used for DNP (**Figure 7**).[105]

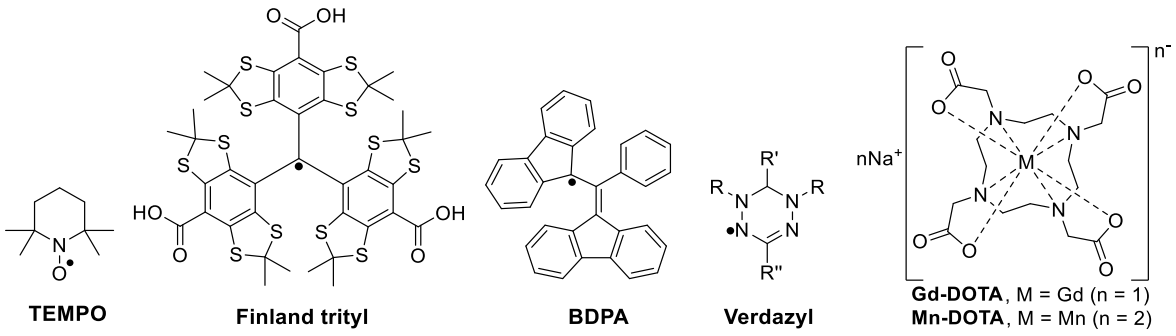

Figure 7 The PAs commonly used in DNP experiments, TEMPO, Finland trityl, BDPA, verdazyl, Gd- and Mn-DOTA.

The DNP performance of a PA is linked to its EPR linewidth, which is influenced by electron spin relaxation behavior. In particular, a faster transverse relaxation time (T_{2e}) leads to a broader EPR spectrum.[38, 106] A broad EPR spectrum causes reduced excitation of the electronic spins and, therefore, requires higher microwave power to achieve efficient

saturation. In contrast, a narrow EPR linewidth is easier to saturate, which is especially beneficial at high fields.[77]

These EPR characteristics are determined by the structure and electronic properties of the radical. Therefore, the design and optimization of PAs remain an active area of research for improving DNP performance. The following section provides a detailed discussion of the main classes of persistent organic radicals.

1.4.1 Nitroxides

Nitroxide radicals are the most widely used PAs for DNP due to their high persistence and fairly easy synthesis. Their broad EPR linewidth helps satisfy the CE condition.[38] As mentioned in **section 1.3.1**, CE requires two dipolar-coupled electrons. Therefore, biradicals, where two radicals are brought into close proximity for stronger electron-electron coupling, are required for efficient CE. Biradicals are efficient even at relatively low concentrations (~5-10 mM), which helps reduce paramagnetic bleaching effects and gives better NMR resolution.[107, 108]

Several nitroxides biradicals, also known as bisnitroxides, with improved DNP performance have been prepared over the years. The first approach to improve nitroxide biradicals for DNP began by optimizing the electron-electron dipolar coupling. Bis-TEMPO ethylene glycol (BT*n*E) biradicals (**Figure 8**), in which two TEMPO units were connected by flexible polyethylene glycol (PEG) linkers of varying lengths were synthesized.[109] Among these, BT*2*E (**Figure 8**), exhibited an optimal linker length and provided several-fold enhancement relative to the mononitroxide TEMPO.[109] Based on this design a water-soluble nitroxide biradical, TOTAPOL (**Figure 8**) was developed.[108] However, the flexibility of its linker resulted in multiple conformations, and limited optimal electron-electron coupling.

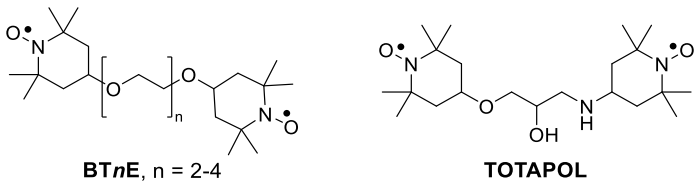

Figure 8 The initial design of nitroxide biradicals.

To overcome the limitations of a flexible linker, attention shifted to developing bisnitroxides with rigid linkers. The aim was also to achieve a favorable relative orientation of their *g*-

tensors of the two nitroxide units. The *g*-tensor reflects how unpaired electron interacts with the external magnetic field and can vary with molecular orientation.[106] Keeping this in mind, bTbk (**Figure 9**) was developed with a rigid spirocyclic linker, thereby locking the relative orientation of the TEMPO moieties.[110] Further structural modification resulted in bCTbk (**Figure 9**).[111] Here spirocyclohexyl groups were introduced to increase the T_{1e} relaxation.[112] Indeed, bCTbk showed slower electron relaxation and improved performance (ε ~100 at 9.4 T) than bTbk. Later, phenyl groups were added to cyclohexyl rings to give TEKPol (**Figure 9**).[106] The increased molecular weight lengthened the electron relaxation time due to reduced molecular motion in the glassy matrix,[113] thus resulting in higher DNP efficiency and overall sensitivity (ε ~200 at 9.4 T, S = 38 $s^{-1/2}$).[106] However, its limited aqueous solubility excluded its use in biological applications.

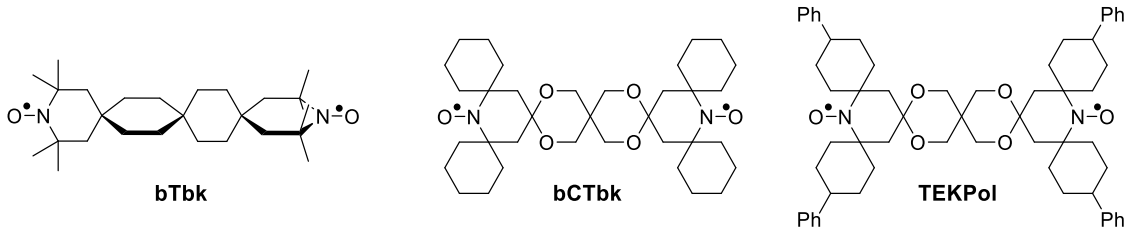

Figure 9. Nitroxide biradicals with rigid linkers

To address the solubility challenges for biological applications, Bis-TEMPO tethered by urea (bTurea) was developed in which two TEMPO moieties were linked with urea linkage. It was first described in 1965[114] and tested as DNP PA by Hu et al.[109] It was reported to be three times more efficient than TEMPO. This design based on the bTurea scaffold led to the development of AMUPol (**Figure 10**), a derivative of bTurea series with PEGylated chains.[115] It showed good aqueous solubility and excellent DNP performance (ε ~230 at 9.4 T) due to its semi-rigid structure and optimal electron-electron coupling.[115] Later, bcTol[116] and bcTol-M[117] (**Figure 10**), also with the bTurea scaffold but with hydrophilic functional groups on spirocyclohexyl, showed improved solubility and DNP performance (ε ~230 and 240 respectively at 9.4 T).

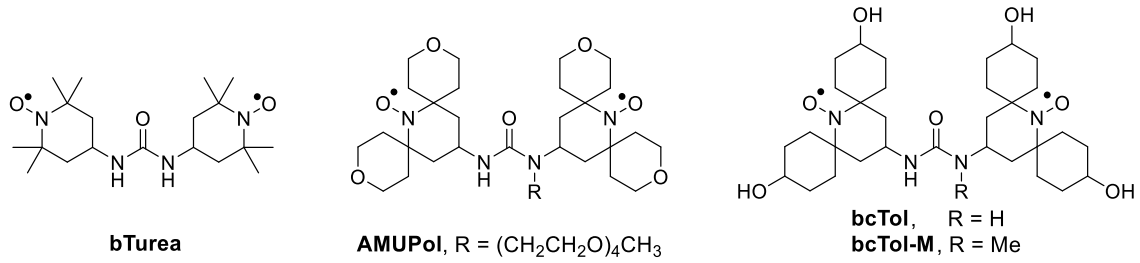

Figure 10 Water-soluble nitroxide biradicals.

Recently, it has been recognized that the local geometry around the unpaired electron significantly influences nitroxide DNP performance. In particular, the orientation of substituents near the radical center can affect how efficiently polarization is transferred. For example, o-HydrOPol ($\varepsilon \sim 330$ at 9.4 T) is markedly more efficient than c-HydrOPol ($\varepsilon \sim 30$ at 9.4 T) (**Figure 11**).[118] In o-HydrOPol, the spiro-tetrahydropyran rings at the α-position are oriented away from the radical center (open form), whereas in c-HydrOPol, they are directed towards it (closed form). It has been suggested that greater solvent accessibility to the electron spin in o-HydrOPol enhances polarization transfer. Under identical conditions, o-HydrOPol shows roughly two-fold higher efficiency than AMUPol, which can adopt both open and closed conformations. However, subsequent studies have suggested that improved performance cannot be attributed solely to solvent accessibility, but also on the relative orientation of the nitroxide moieties.[119]

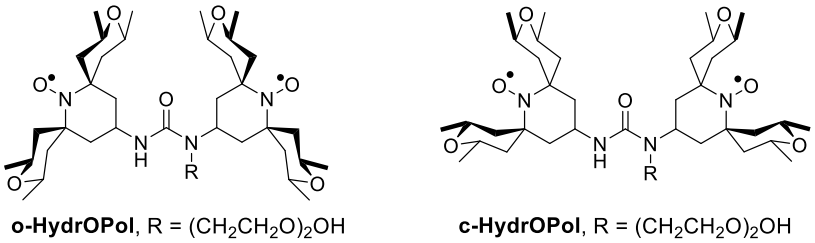

Figure 11 Open and closed nitroxide biradicals.

A simulation-guided design was used to prepare class of asymmetric biradicals called AsymPol, containing a TEMPO and a PROXYL radical that are connected by a short, rigid amide linker.[120] This design provided strong electron-electron coupling and negligible depolarization at 9.4 T. Among the AsymPols, AsymPol-POK (**Figure 12**) exhibited significantly shorter build-up times compared to AMUPol and TEKPol.[120] An improved derivative, cAsymPol-POK (**Figure 12**), with the spirocyclohexyl groups instead of methyl groups adjacent to the nitroxide group further reduced build-up times.[121] TinyPols are

another class of biradicals showing reduced depolarization at high fields.[122] They contain a short yet flexible linker, with M-TinyPol (**Figure 12**) being the best in series (ε ~90, 18.8 T).[122] Most recently, TJPol-1 (**Figure 12**), an acrylamide-linked nitroxide biradical was introduced.[123] It combined structural features of key biradicals, specifically, high solubility of AMUPol, the rigidity of TEKPol and strong coupling of AsymPol. TJPol-1 exhibited a much lower T_B and a much higher overall sensitivity than AMUPol.[123]

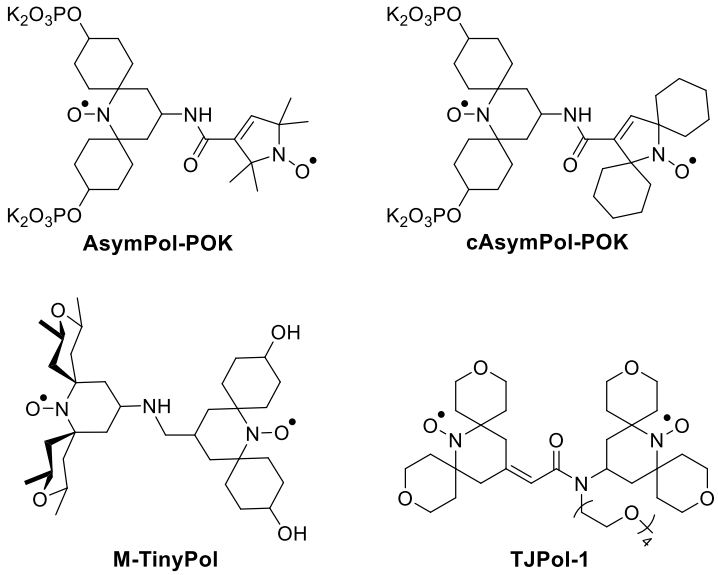

Figure 12 Nitroxide biradicals at high magnetic field (≥ 18.8 T).

1.4.2 Carbon-centered radicals

Carbon-centered radicals overcome the intrinsic limitations of nitroxide PAs that are particularly apparent at high-field. Unlike nitroxides, carbon-centered radicals do not possess strong heteronuclear hyperfine coupling and have reduced g-anisotropy. As a result, they exhibit narrower EPR linewidths. Narrow EPR linewidths lead to a longer T_{1e} and, therefore, efficient microwave saturation.[68, 124] Such characteristics make carbon-centered radicals particularly attractive for DNP at high-field (> 9.4 T), especially for DNP mechanisms involving monoradicals, such as the SE and OE. Below is a description of important carbon-centered radicals for DNP.

Verdazyl radical

Verdazyl radicals, first discovered in 1963,[125] are not the usual carbon-centered radicals. The electron spin is not strictly centered at the carbon, rather is delocalized over a tetrazinyl ring,

a conjugated system of four nitrogens and a central carbon. Unlike nitroxides, these radicals are stable even in the presence of reductants such as ascorbate.[126] Triphenylverdazyl (**Figure 13**) was the first verdazyl to be used for DNP in liquids at low field (1.4 T).[127] Later, a water-soluble verdazyl radical called verdazyl ribose (**Figure 13**) exhibited CE DNP performance close to 4-hydroxy-TEMPO.[126]

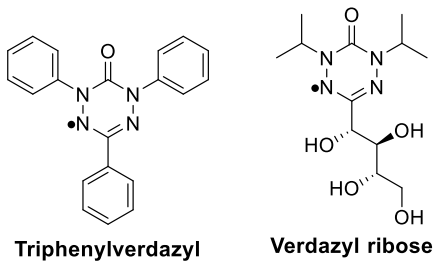

Figure 13 Reported verdazyl monoradicals for DNP.

Trityl radical

Trityl radicals constitute a triphenyl methyl core. The first trityl radical was discovered in 1900 by Gomberg and was named after him as Gomberg's trityl (**Figure 14**).[128] It was, however, an unstable radical. Further improvements increased stability through steric protection. Halogenated trityls[129] exhibited increased persistence but had poor aqueous solubility and limited functionalization. The development of the Finland trityl (**Figure 14**) marked significant improvement in persistence and water-solubility. However, it showed aggregation due to hydrophobic interactions, which causes inhomogeneous broadening of EPR. OX063 (**Figure 14**) with hydroxyethyl groups was then introduced and was found to be more hydrophilic than the Finland trityl.[130, 131] Trityl radicals are important narrow-line monoradicals for DNP and have been widely applied in OE and SE DNP, as well as in dissolution DNP.[93, 132, 133] However, trityl radicals still have drawbacks, including a relatively lengthy synthesis and limited synthetic tunability.

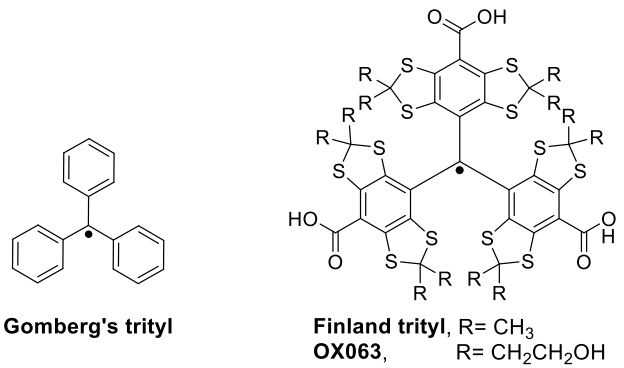

Figure 14 Examples of trityl monoradicals.

BDPA

BDPA[134] (**Figure 7**) is another important carbon-centered radical. Like trityl radicals, BDPA derivatives are relevant for DNP mechanisms that benefit from narrow EPR linewidths, particularly SE and OE DNP.[133, 135] An advantage of BDPA over trityl is its relative ease in synthesis[136, 137] and narrower EPR line.[138] However, the unsubstituted BDPA had limited persistence and poor aqueous solubility. To induce solubility, WS-BDPA (**Figure 15**) with ethyl carboxylic groups was synthesized. However, it showed limited solubility (1 mM PBS buffer at pH 8).[139] A sulfonated BDPA (SA-BDPA) (**Figure 15**) synthesized in 2012 exhibited excellent aqueous solubility (40 mM in glycerol/water), but yielded a mixture of radicals.[138] It was not suitable for further conjugation, and its persistence has not been reported. More recently, tetraalkylammonium BDPA radicals were reported, to address both water-solubility and persistence.[140] Among these radicals, the trimethylammonium BDPA (BDPA-NMe_3) (**Figure 15**) showed improved solubility (>150 mM in glycerol/water) and persistence.[140] Yet its stability in aqueous solutions remained limited, primarily due to radical dimerization.[141-143]

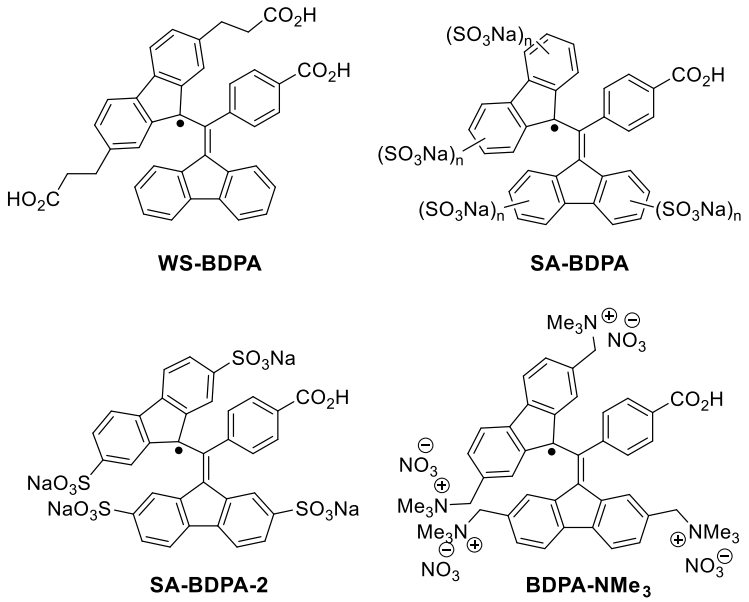

Figure 15 Examples of BDPA monoradicals.

1.4.3 Heterobiradicals

An ideal biradical PA for CE-DNP should possess two sharp EPR lines separated by the nuclear Larmor frequency. However, such a PA does not exist. To approximate this condition, heterobiradicals, also called hybrid radicals, have been developed, where a narrow

EPR-line radical, such as a carbon-centered radical is connected to a nitroxide. The separation in their EPR spectra of a carbon-centered radical and a nitroxide closely matches the ^{1}H Larmor frequency. The first demonstration of this concept was exhibited using an equimolar mixture of trityl and TEMPO, which showed improved CE DNP performance compared to monoradicals.[144] The first covalently linked nitroxide-trityl heterobiradical was TEMTriPol-1 (**Figure 16**).[145] It showed excellent DNP enhancement at 18.8 T.[74, 145] However, it suffered from aggregation. Later, solubility in water was increased by incorporating a carboxylic substituent on the nitroxide linker, to give NATriPols.[146] NATriPol-3 (**Figure 16**) was the best performing radical in the NATriPol series.[146] Further improvements in solubility led to development of SNAPols.[147] SNAPol-1 (**Figure 16**) exhibited the best DNP performance that has been reported for a water-soluble hybrid radical at 18.8 T thus far.[147] However, its applicability suffered from a challenging synthesis. A series of heterobiradicals called PyrroTriPols contain a rigid piperazine linker to restrict conformations and preserve optimal electron-electron interactions.[75] These radicals proved suitable for both aqueous (PyrroTriPol) and organic solvents (PyrroTriPol-OMe) (**Figure 16**) and exhibited higher overall sensitivity than TEMTriPols.[75] Building on the same core structure as PyrroTriPols, STAPols were introduced for cellular applications.[148] STAPol-1 (**Figure 16**), bearing ethyl substituents on the nitroxide moiety for enhanced reduction resistance, represents one of the best-performing biradicals at 14.1 and 21.1 T.[148]

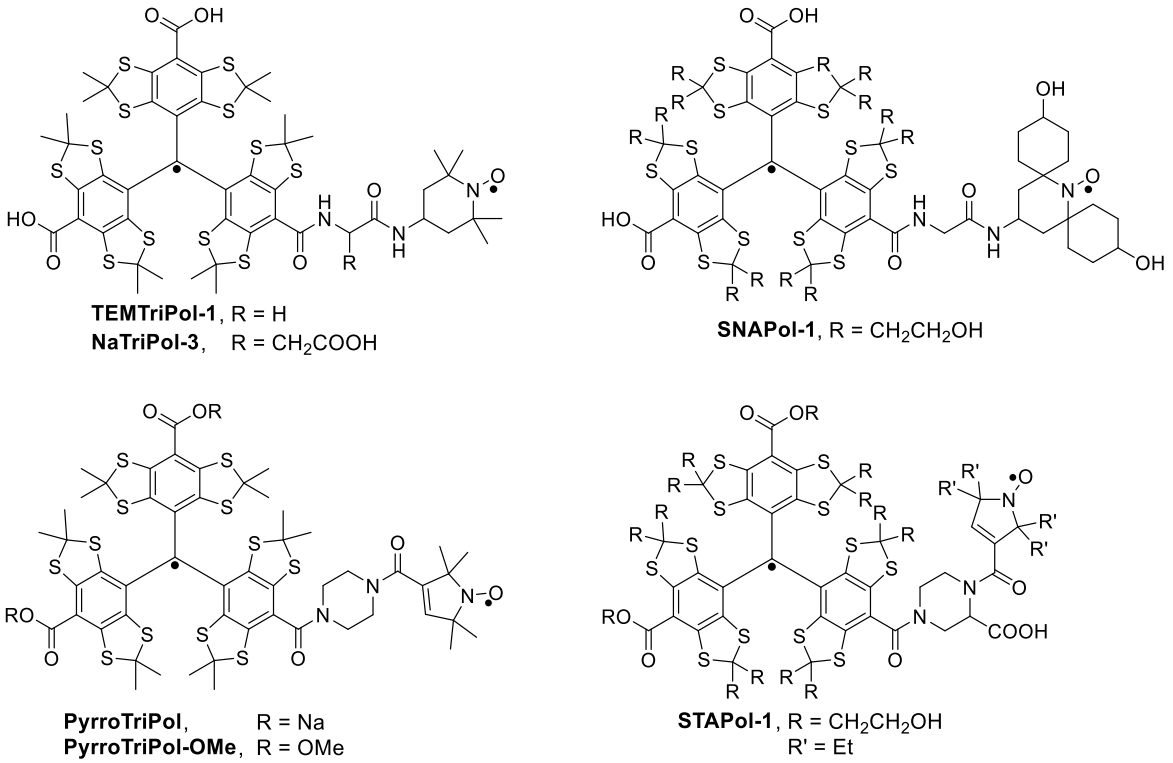

Figure 16 Trityl nitroxide radicals TEMTriPol-1, NaTriPol-3, SNAPol-1, PyrroTriPol, PyrroTriPol-OMe and STAPol-1.

While trityl-nitroxides with great DNP performance have been developed, BDPA-nitroxides are still underexplored. The first reported BDPA-nitroxide was BDPA conjugated to a TEMPO, known as BDPA-TEMPO (**Figure 17**).[137] However, there were no reports on its DNP evaluation. A subsequent BDPA-ester-TEMPO (**Figure 17**) with a modified linker exhibited strong exchange coupling and was applied in dissolution DNP at 3.35 T and 1.4 K.[149] However, the first successful BDPA-nitroxide for CE DNP was HyTEK2 (**Figure 17**) for organic solvents at very high field (21.1 T).[150] Its short methylene linker enabled optimal electron-electron coupling, while functionalization of the nitroxide with bulky 4-phenyl spirocyclohexyl groups lengthened the electron relaxation time. However, the limited BDPA persistence particularly due to dimerization can complicate handling. As for the water-soluble BDPA-nitroxides, the first example, was wsBDPA-TEMPO, where BDPA-NMe_3 was coupled with TEMPO (**Figure 17**).[140] However, its DNP performance was not reported.

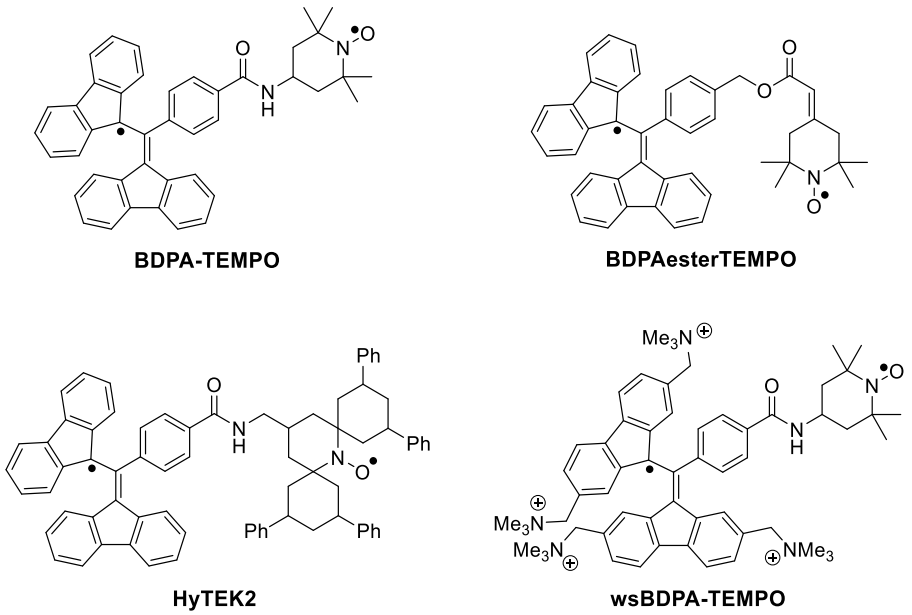

Figure 17 Examples of BDPA-nitroxide biradicals.

Apart from BDPA- and trityl-nitroxides, two verdazyl nitroxides, namely VerTEMPol (**Figure 18**) and VerTEKol (**Figure 18**) have recently been introduced for DNP in organic solvents.[151] VerTEKol achieved four-fold higher enhancement compared to TEKPol, although it did not surpass the performance of HyTEK2. In summary, HyTEK2 remains the benchmark heterobiradical for CE-DNP in organic solvents at high-field. Nevertheless, the limited persistence of BDPA, and the lack of highly efficient aqueous BDPA-nitroxide systems restricts broader application and highlights the need for further development of BDPA radicals.

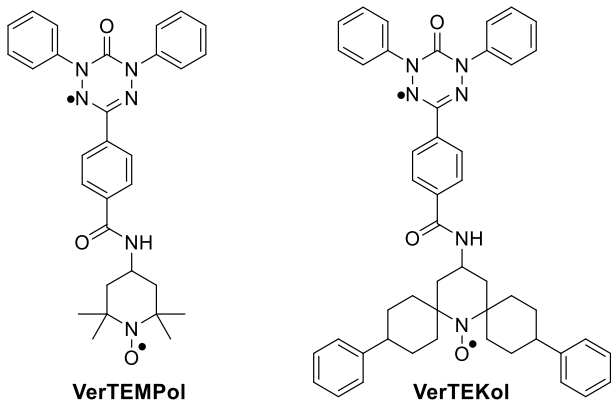

Figure 18 Examples of verdazyl-nitroxide biradicals for DNP.

1.5 Contribution of Part A of this dissertation

Despite possessing several interesting DNP properties, application of BDPA as a PA is limited due to its instability. **Part A** of this Ph.D. thesis addresses this challenge. The main strategy is synthesis of a tunable BDPA that enables incorporation of various bulky and hydrophilic substituents to BDPA to mitigate dimerization of the radical and thereby increase its persistence.

A2 Synthesis of BDPA radicals for DNP-NMR

The BDPA radical is a highly promising PA for DNP-NMR due to its narrow EPR linewidth,[138] which enables efficient microwave saturation and polarization transfer. It exhibits a mixed-valence character, where the radical constantly hops between two positions, creating the internal motion necessary to efficiently transfer polarization in insulating solids through OE.[152] Additionally, it has an advantage of easier synthesis relative to the trityl radical.[136, 137] However, the practical application of BDPA radicals remains a challenge due to their instability. As discussed in the previous chapter, although the water-soluble radical BDPA-NMe_3 was persistent in DMSO, it showed limited persistence in aqueous solutions.[140] The limited persistence was likely due to the tendency of tetraalkylammonium salts to aggregate in water,[141-143] leading to dimerization.

Steric hindrance has been shown to increase persistence in trityl radicals.[129, 153, 154] Therefore adding sterically hindered groups is desirable. Apart from this, different NMR applications require different solvent environments, like aqueous solvents for biological systems and organic solvents for materials science and synthetic chemistry, therefore, there is a need for BDPA with varied properties. Consequently, our focus was to develop a strategy that would allow us to prepare BDPA derivatives where the solubility could be varied by incorporation of organic and hydrophilic groups and stability could be improved by attaching sterically hindered groups. However, the reported synthesis of tetrabromo BDPA, the key intermediate of BDPA-NMe_3, was lengthy, low-yielding and tedious. This synthetic bottleneck makes the preparation of new BDPA derivatives impractical. Therefore, before the synthesis of new BDPA radicals we focused on the optimization of the tetrabromo BDPA derivative.

2.1 Optimized synthesis of the tetrabromo BDPA

The synthesis of the tetrabromo BDPA derivative involved 12 tedious steps.[140] The synthesis was optimized to 7 steps and the overall yield increased drastically from 0.04% to 13%. The most notable improvement in the procedure was the optimization of the synthesis of dibromomethyl fluorene **1** (**Scheme 1**). The old route involved 6 steps to go from fluorene

(**2**) to **1** (**Scheme 1**). The synthesis was optimized to a single step conversion, using bromomethylation of **2** to give **1**.

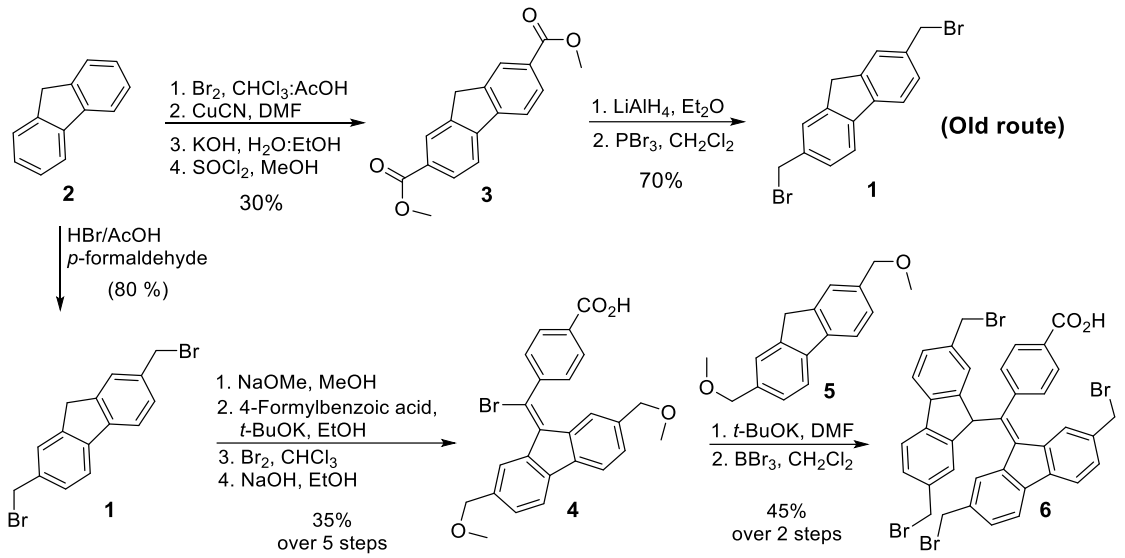

Scheme 1 Improved synthesis of dibromomethyl fluorene **1**, followed by synthesis of tetrabromo BDPA **6**.

Thus, the tetrabromo BDPA derivative was synthesized using optimized **1** (**Scheme 1**). The bromides in the dibromomethyl fluorene **1** were substituted with methoxy groups to give compound **5**. Subsequent condensation of **5** with 4-formylbenzoic acid, followed by bromination and elimination, afforded **4** in good yield over five steps. Compound **4** was coupled with **5** to give the tetrabromo BDPA **6** in moderate yield over two steps.

2.1.1 Synthesis and applications of BDPA-NMe_3

The optimized tetrabromo BDPA **6** was used to prepare the BDPA-NMe_3 radical by previously reported procedure.[140] The bromides of **6** were substituted with trimethylammonium groups to yield 7 in excellent yield, and subsequent radical generation to give BDPA-NMe_3 radical in good yields (**Scheme 2**).

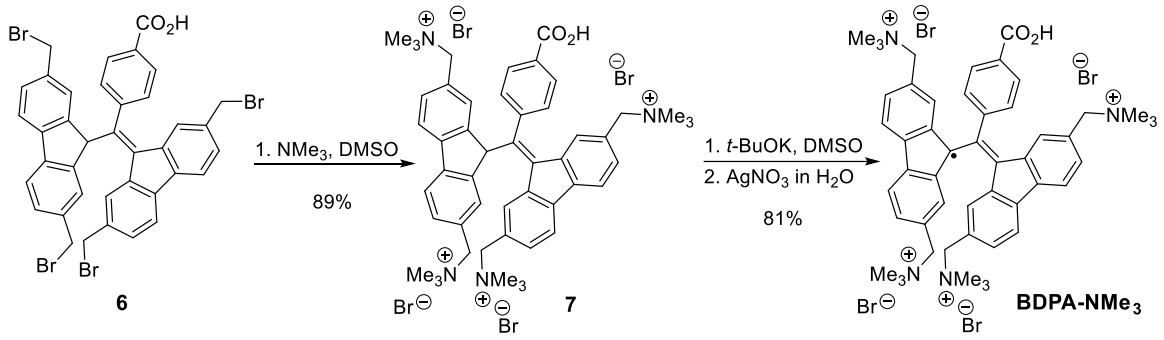

Scheme 2 Synthetic scheme of BDPA-NMe_3.

BDPA-NMe_3 was then evaluated for DNP performance using advanced microwave instrumentation in collaboration with Prof. Bob Griffin (MIT, USA). Here, BDPA-NMe_3 enabled Overhauser DNP enhancements of ~25 in aqueous glycerol mixtures at 9 T, highlighting its potential for applications in biological systems.[155]

DNP in viscous liquids has recently emerged as an important approach, since the reduced molecular tumbling in viscous solutions leads to efficient polarization transfer at high magnetic fields and temperature.[156, 157] Carbon-centered radicals such as BDPA have shown promising DNP performance in viscous liquids, exhibiting SE DNP at high field and 315 K.[158] Therefore, BDPA-NMe_3 was further investigated for DNP in viscous liquids in collaboration with Dr. Kuzhelev, Goethe University, Frankfurt.[133] The liquid DNP performance of BDPA-NMe_3 was compared with trityl-radicals OX063 and the Finland trityl. Among them, OX063 exhibited the highest DNP enhancement. It was hypothesized that the DNP performance correlated with the molecular weight of radicals, with larger radicals producing higher enhancement. Based on this hypothesis we decided to synthesize high molecular weight, water-soluble BDPA containing bulky substituents to increase its persistence and DNP performance.

2.2 Synthesis of tunable BDPA radicals

To access a wide variety of BDPA derivatives with tailored properties, there is a need for a flexible and divergent synthetic strategy. In particular, the introduction of sterically demanding and water-soluble groups was expected to improve radical persistence and enhance DNP performance. Thus, several synthetic approaches were explored to functionalize the tetrabromo BDPA **6**, which are discussed in the following sections.

2.2.1 Nucleophilic substitution

The first strategy involved the incorporation of bulky, water-soluble substituents to BDPA through nucleophilic substitution. Here, the bromide groups in the tetrabromo BDPA **6** were reacted with molecules bearing nucleophilic, bulky and hydrophilic groups (**Scheme 3**). However, due to the presence of an acidic allylic proton in BDPA, BDPA forms anion under basic conditions. Therefore, to evaluate if this strategy would work without a base, a model reaction was performed in the presence of a non-nucleophilic base proton sponge and in the absence of basic conditions. Benzyl bromide was reacted with molecules with nucleophilic atoms like sulfur in glutathione and phosphorous and in tris(2-carboxyethyl)phosphine (TCEP), respectively. Both these nucleophiles are hydrophilic and imparted steric environment due to their size. Moreover, reaction with TCEP was anticipated to yield a charged, water-soluble product. However, no substitution products were observed under base-free conditions, indicating that a base was required for the reaction to proceed.

Subsequently, reactions were attempted using tetrabromo BDPA **6** with glutathione and TCEP in the presence of proton sponge (**Scheme 3**). It resulted in the consumption of starting material **6**. Monitoring the reactions by thin-layer chromatography (TLC) proved challenging, as both the starting materials and expected products were highly water-soluble. Second, both glutathione and TCEP lacked UV absorbance above 240 nm, limiting their detection by HPLC. However, BDPA contains an acidic allylic proton and therefore forms BDPA anion under basic conditions. Furthermore, as expected, BDPA anion formed in the presence of base proton sponge leading to BDPA radical in the presence of air. Since the reactions were difficult to control and monitor, an alternative strategy was pursued.

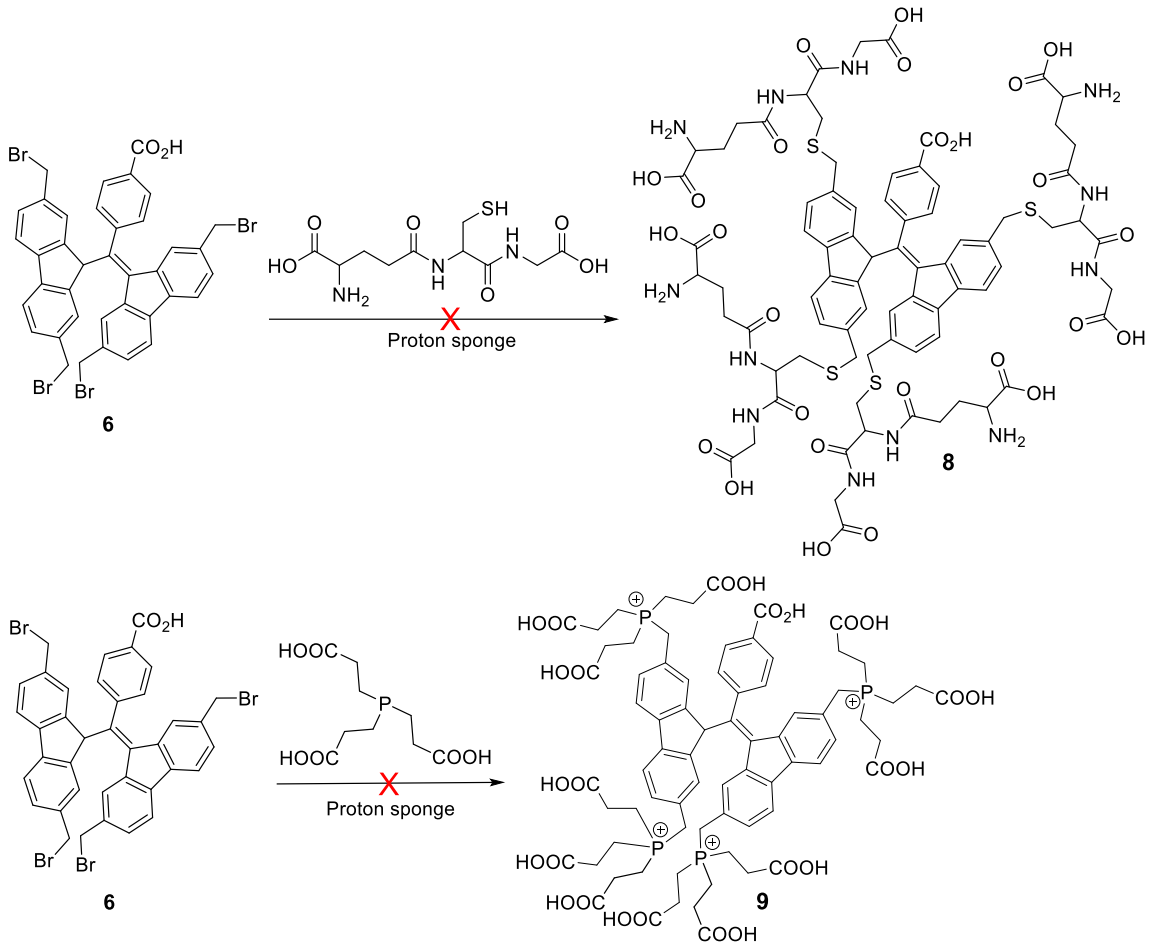

Scheme 3 Proposed synthesis of water-soluble BDPA derivatives **8** and **9** by nucleophilic substitution.

2.2.2 Tetraalkyne derivative of BDPA for click reaction

An alternative strategy for incorporation of different groups to BDPA, utilizing the copper-catalyzed azide-alkyne cycloaddition (CuAAC) approach was attempted. This required the synthesis of a tetraalkyne derivative of BDPA **10**, that could be conjugated with various azide-bearing groups (**Scheme 4**). The proposed synthesis involved a one-step conversion of tetrabromo BDPA **6** to **10**. Compound **6** was treated with propargyl alcohol in the presence of NaH. However, the strong basicity of NaH caused anion formation of BDPA. Moreover, **6** was not consumed even after keeping the reaction for a longer time, and led to degradation of **6**, producing multiple spots on the TLC. Since the direct introduction of propargyl groups to BDPA was not feasible, a modified approach was investigated.

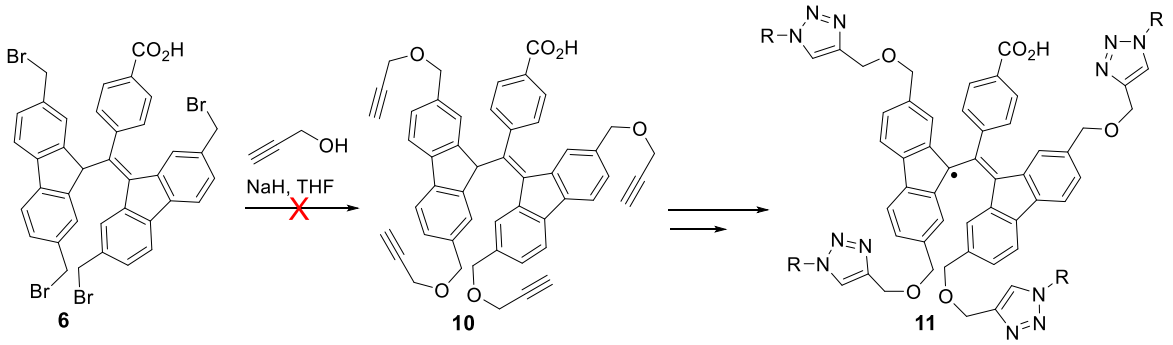

Scheme 4 Proposed synthesis of water-soluble BDPA radicals from tetraalkyne derivative of BDPA using CuAAC (R = hydrophilic group).

The modified route involved incorporation of propargyl groups to the dibromomethyl fluorene **1** (**Scheme 5**). Synthesis began with propargylation of **1**, which gave an alkyne derivative of fluorene **12** in good yield. This was followed by condensation of **12** with 4-formyl benzoic acid to give **13** in fair yields. Bromination and subsequent elimination gave **14** in low yield. However, condensation of **14** with **12** was unsuccessful, probably due to the presence of multiple alkyne groups in the presence of base, causing deprotonation of alkynes. Excess of base was also added, however that led to multiple side products on TLC. Consequently, we modified our approach to instead synthesize a tetraazide derivative of BDPA.

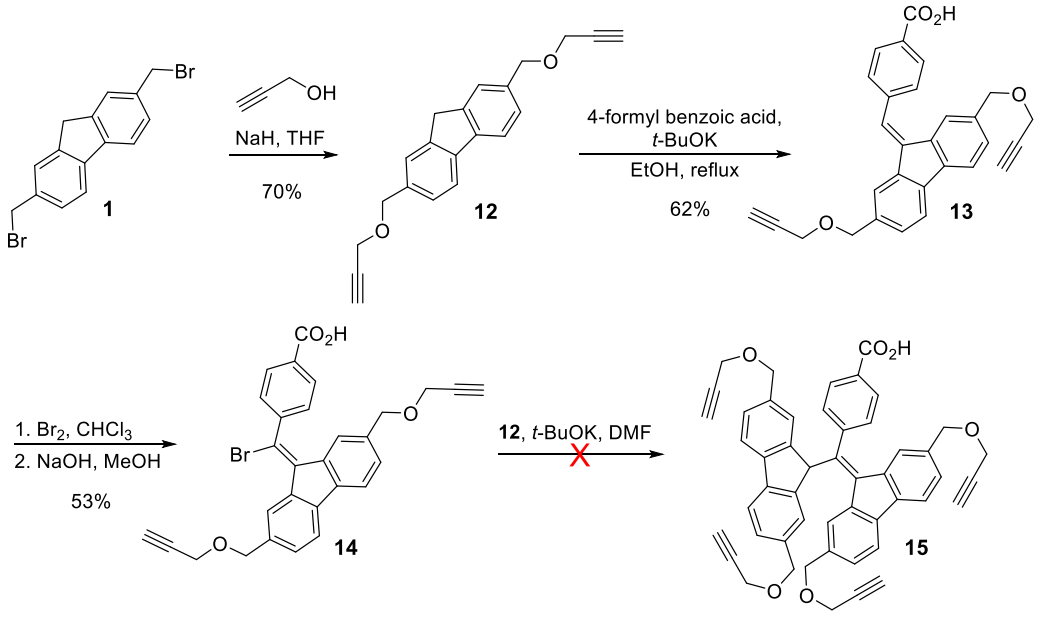

Scheme 5 Modified synthesis of BDPA tetraalkyne derivative.

2.2.3 BDPA tetraazide derivative for synthesis of BDPA radicals

To overcome the limitations of previous approaches, a tetraazide derivative of BDPA **16** was prepared where the azides could be readily conjugated to various alkyne-bearing groups using CuAAC (**Scheme 6**). Therefore, **16** served as a building block that could be used for the preparation of BDPA derivatives with tunable solubility for both organic and aqueous matrices, steric properties, and molecular weight. Synthesis began with the substitution of bromide groups in the tetrabromo BDPA **6** with azides to give **16** in excellent yield. To demonstrate the versatility of this strategy, four BDPA derivatives were prepared by CuAAC of **6** with various alkynes (**Scheme 6**). Alkynes **17a-d** were chosen for conjugation to building block **16**: **17a** was for organic solvents and further derivatization, **17b-d** were to introduce hydrophilicity and steric shielding, thus, yielding BDPA derivatives **18a-d**. Compounds **18a-c** were isolated by precipitation in good yields, while **18d** was purified by column chromatography.

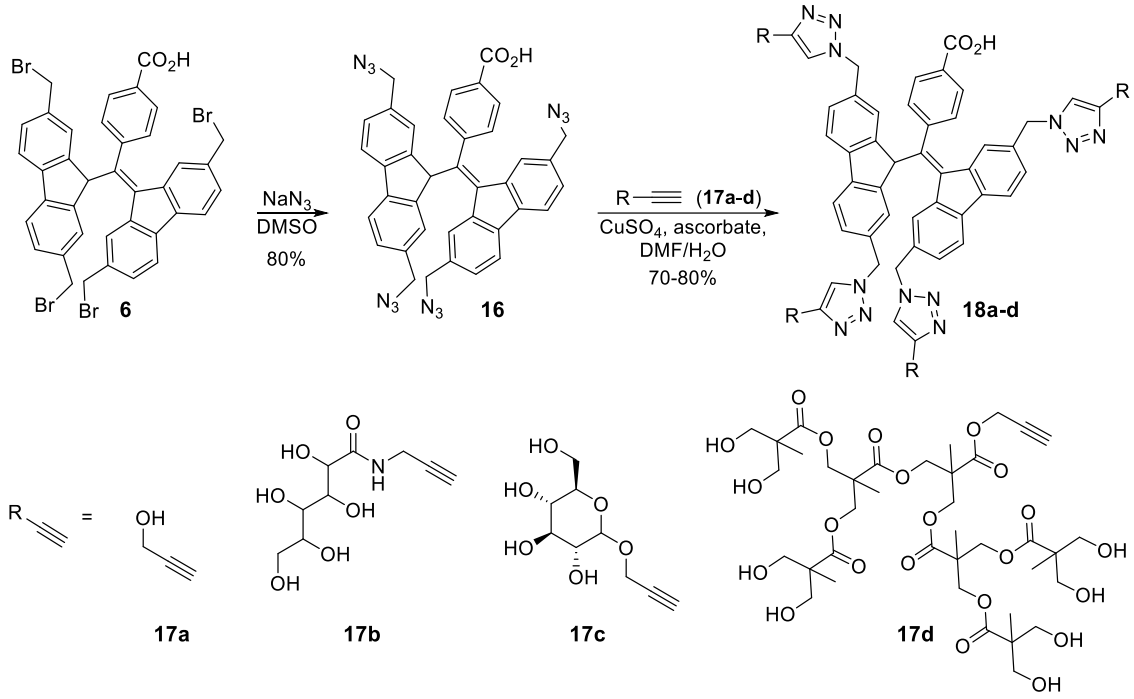

Scheme 6 Synthesis of BDPA derivatives using CuAAC and the corresponding alkyne substrates.

The solubility of the derivatives was evaluated in different solvents. All derivatives were soluble in DMSO. BDPA-sugar **18c** and BDPA dendrimer **18d** were water-soluble. However, BDPA-OH **18a** and BDPA-hydroxyamide **18b** were water-insoluble. Various strategies can be used to improve hydrophilicity, such as phosphitylation and sulfation. To demonstrate increased hydrophilicity, sulfation of **18a** was performed (**Scheme 7**), affording

water-soluble BDPA-sulfate **20** in excellent yield; **18a** was selected for this transformation to avoid complications arising from multiple hydroxyl groups in **18b**.

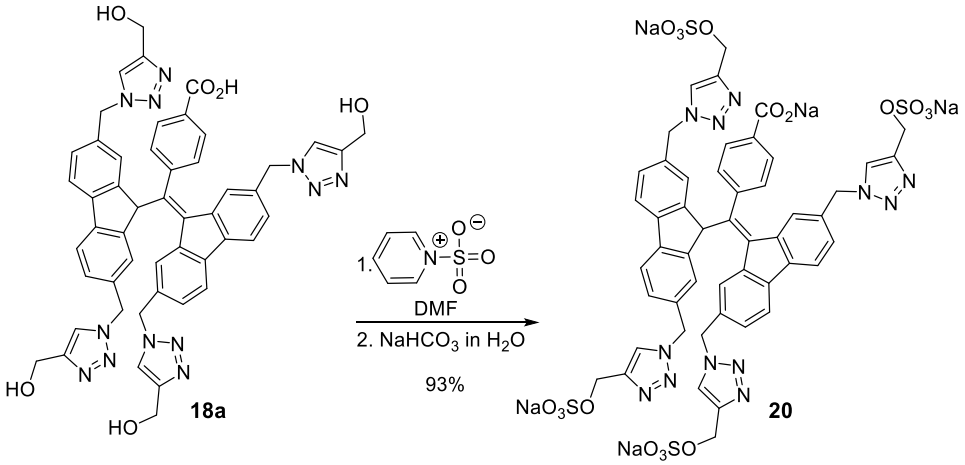

Scheme 7 Synthesis of BDPA-sulfate **20** from **18a**.

The corresponding radicals **19a-d** and **21** were generated by treatment of **18a-d** and **20** with *t*-BuOK to form the BDPA anion, followed by oxidation with $AgNO_3$ (**Scheme 8**). However, **18d** was prone to hydrolysis of its esters in the presence of a base and therefore required optimization of the anion formation step. The usual time period for anion generation was 30 min. However, for **18d**, the HRMS analysis showed multiple hydrolysis peaks and no product peak after 30 min. Therefore, the anion formation reaction was monitored by mass spectrometry as well as UV-Vis with time. No hydrolysis products were detected by mass analysis within the first 10 min of base treatment. Accordingly, the reaction time for anion formation for **18d** was reduced to 10 min, followed immediately by oxidation to generate the corresponding radical **19d**.

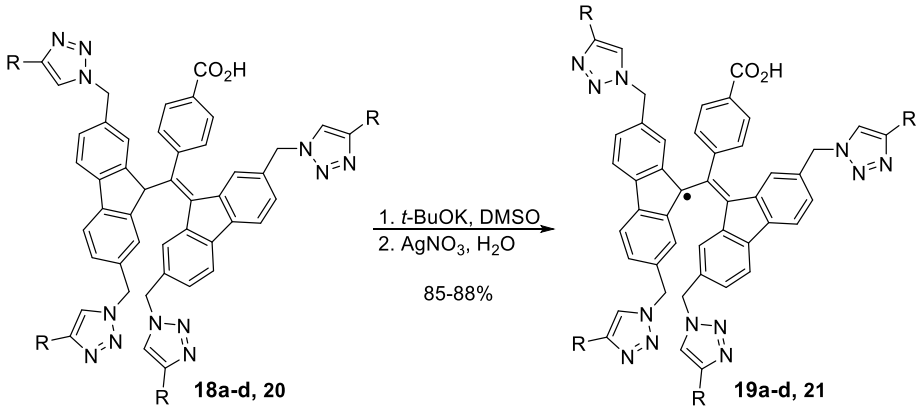

Scheme 8 Synthesis of water-soluble BDPA radicals **19a-d** and **21** from compounds **18a-d** and **20**.

To determine the extent of anion formation in **19d** and the corresponding radical after $AgNO_3$ oxidation, a UV-Vis study was performed (**Figure 19**). **18d** was treated with *t*-BuOK and aliquots were withdrawn at every 5 min intervals over a period of 30 min, and the UV-vis spectrum was recorded to monitor the formation of BDPA anion with time. This was followed by subjecting the aliquot to immediate oxidation with $AgNO_3$ and the corresponding UV-Vis spectrum were recorded again to monitor BDPA radical formation. The UV-Vis data showed that anion formation increased gradually with time (620 nm), indicating that complete conversion of **18d** to the BDPA anion was not achieved within 10 min. Upon oxidation with $AgNO_3$, the characteristic absorption band of the BDPA radical (500 nm) increases progressively with longer base treatment times. Therefore, only partial radical formation (~60%) was observed. This observation was also confirmed by spin-counting of radical **19d**, where an absolute radical concentration of ~5.6 mM was obtained from a 10 mM solution of **19d**.

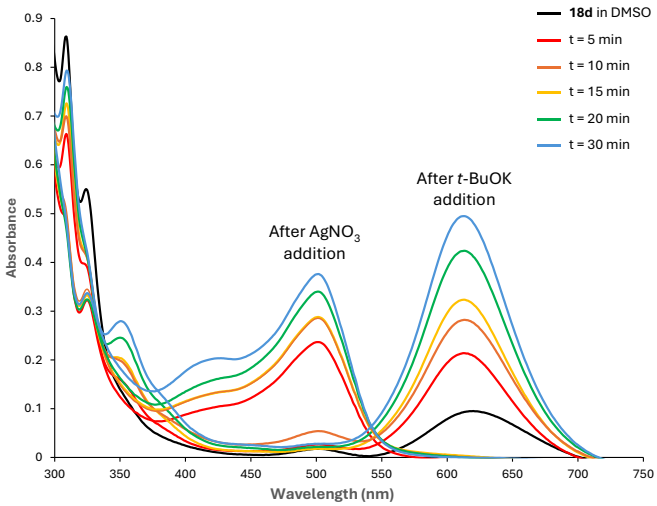

Figure 19 The UV-vis spectra of **18d** after addition of t-BuOK and radical generation with $AgNO_3$ with time.

To neutralize the residual base after radical generation, acid treatment was required. The effect of 0.1 M HCl on radical **19d** was monitored for 1 h by UV-Vis spectroscopy (**Figure 20**). It was seen that the radical degraded by more than 30% within 1 h (**Figure 20**, **right**). Based on these observations, acid was unsuitable, and water was used instead to quench residual *t*-BuOK.

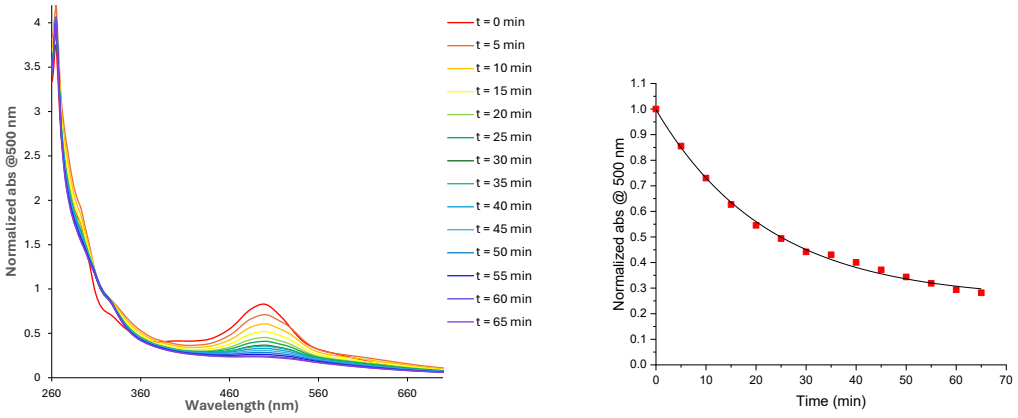

Figure 20 The UV-vis absorbance spectra of **19d** (left) and its corresponding normalized absorbance at 500 nm (right), plotted as a function of time in 0.02 M HCl.

To evaluate the effect of bulky dendrimer groups on the persistence of radical **19d**, we studied its persistence in various solvents using UV-Vis spectroscopy (**Figure 21**). In water, the half-life of **19d** was ~2 days, indicating higher persistence than BDPA-NMe_3 (Half-life <24h). In DMSO, **19d** showed an unusual increase in the radical concentration in the beginning and plateaued after 4 days. This unusual behavior was likely due to the presence of unreacted non-radical **18d**. It was observed that in DMSO, residual non-radical **18d** gradually converted to the BDPA anion, followed by slow oxidation to the radical **19d** in the presence of air. Once the plateau was reached, **19d** was persistent in DMSO for at least 25 days. In glycerol the half-life of **19d** was ~8 days.

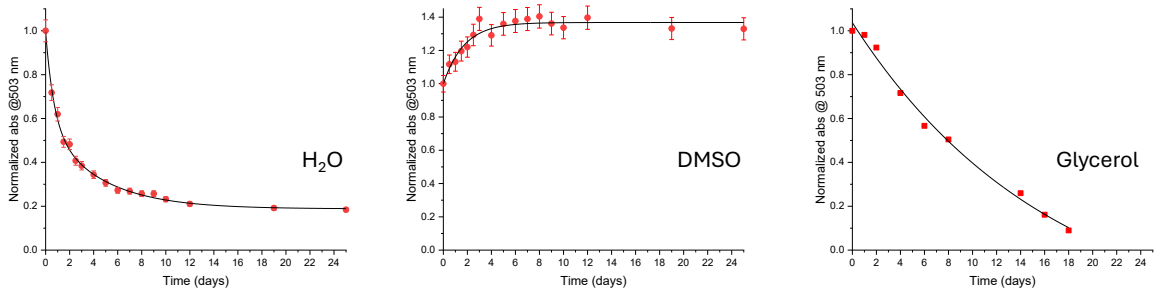

Figure 21 Persistence of the BDPA-dendrimer **18d** in H_2O, DMSO and glycerol at 23 °C, monitored by UV-Vis spectroscopy.[140]

Given its better persistence and higher molecular weight, the liquid DNP performance of BDPA-dendrimer **19d** was evaluated in collaboration with Dr. Andrei Kuzhelev (Goethe University, Frankfurt). The results showed **19d** to have the highest liquid DNP performance in viscous solutions till date.

2.3 Summary of Paper I

Paper I described a divergent strategy for the preparation of a tunable BDPA and has demonstrated its application to liquid DNP. This approach enabled preparation of BDPA with tailored properties such as solubility, persistence, size and steric shielding. This involved preparation of a tetraazide BDPA intermediate which served as building block for further functionalization through CuAAC chemistry. Four different alkynes were conjugated to the tetraazide precursor yielding four BDPA derivatives: BDPA-OH, BDPA-hydroxyamide, BDPA-glucose, and BDPA-dendrimer. These derivatives exhibited distinct solubility behavior, with BDPA-glucose and BDPA-dendrimer being inherently water-soluble.

Among these derivatives, BDPA-dendrimer was selected for further investigation due to its favorable combination of water solubility and high molecular weight. It showed higher persistence compared to BDPA-NMe_3 in both water and DMSO, highlighting the beneficial effect of increased steric-hindrance. The BDPA-dendrimer was subsequently evaluated for liquid DNP experiments in viscous glycerol at 9.4 T and 315 K. At a concentration of 20 mM, a DNP enhancement of $\varepsilon = 40 \pm 5$ was observed and which was nearly 2 times higher than that of the enhancements produced by OX063 under same conditions. Measurements at 10 mM and 40 mM yielded enhancements of $\varepsilon = 18 \pm 3$ and 57 ± 6, respectively, demonstrating an increase in enhancement with radical concentration. Overall, this work shows that increasing the molecular weight and steric environment of BDPA derivatives leads to improved persistence and enhanced DNP performance.

2.4 Conclusion

In summary, a strategy for the development of tunable BDPA derivatives for DNP-NMR was presented in this chapter. Before synthesizing new BDPA derivatives, the synthesis of the key BDPA intermediate tetrabromo BDPA (**6**) was optimized with an improvement from 12 to 7 synthetic steps. For increasing the persistence of the radical, two initial strategies, based on nucleophilic substitution and tetraalkyne-functionalized BDPA were attempted however they were unsuccessful. We introduced a readily accessible building block tetraazide BDPA (**16**) which enabled functionalization of BDPA based on polarity, size and persistence. A series of four BDPA radicals was synthesized using this strategy. The BDPA-

dendrimer derivative **19d** showed the most favorable combination of properties and was selected for detailed investigation of persistence and liquid DNP studies. Notably, **19d** demonstrated the highest liquid-state DNP enhancement reported to date in viscous solutions.

A3 Conclusions for Part A

The work presented in **Chapter A2** of this thesis centered on the development of BDPA-based polarizing agents for high-field DNP-NMR, with an emphasis on improving synthetic accessibility, persistence, and DNP performance. An important outcome of this work was the optimization of the synthesis of tetrabromo BDPA, the key intermediate for BDPA derivatives. By reducing the number of synthetic steps from 12 to 7 and substantially improving the overall yield from 0.04% to 13%, this work made the preparation of new BDPA derivatives more feasible. Using this improved route, BDPA-NMe_3 was prepared and evaluated in two collaborative DNP studies. With Prof. Bob Griffin (MIT, USA) OE DNP was performed using BDPA-NMe_3, giving enhancements of ~25 in aqueous glycerol mixtures at 9 T, demonstrating its potential for applications in biological systems. In collaboration with Dr. Andrei Kuzhelev (Goethe University, Frankfurt) BDPA-NMe_3 was evaluated for DNP in viscous liquids and compared with OX063 and Finland trityl. These studies suggested that the DNP performance is influenced by molecular weight of the polarizing agent, thereby motivating the design of larger and more sterically protected BDPA derivatives. Several strategies were explored to functionalize the BDPA to incorporate large sterically hindered water-soluble groups, leading to the preparation of a tetraazide BDPA derivative, which enabled efficient CuAAC-based conjugation to different alkynes and provided access to four BDPA derivatives with varied polarity, steric shielding, and molecular weight. Among the derivatives prepared, the so-called BDPA-dendrimer showed the most favorable combination of properties. It was water-soluble, more persistent than BDPA-NMe_3, and had the highest molecular weight. The BDPA-dendrimer gave liquid-state DNP enhancement of 57 at 40 mM in glycerol, the highest thus far (Paper I).

Overall, this work established a practical synthetic strategy for the preparation of tunable BDPA radicals. In addition, the synthetic platform described in this work should enable the preparation of more complex BDPA-based architectures, including mixed-radicals such as BDPA-nitroxide or BDPA-trityl conjugates for different DNP applications. Taken together, this work provides both a practical synthetic foundation and a clear direction for the continued development of BDPA-based polarizing agents for high-field DNP-NMR.

Part B Labeling of nucleic acids with spin labels and fluorophores

B1 Introduction

Nucleic acids are essential biomolecules that play a central role in sustaining life. They were discovered in 1869 by a Swiss scientist, Friedrich Miescher, who first isolated phosphate-rich molecules from cell nuclei, which he termed "nuclein".[159] These molecules were later identified as nucleic acids.[160] In 1938, William Astbury and Florence Bell recorded the first X-ray diffraction patterns of DNA, providing early structural insights, although natural form was not resolved.[161] In 1952, when Rosalind Franklin obtained high-resolution X-ray crystallographic images of DNA fibers, which was a big step towards understanding the structure of DNA.[162] The following year, the double helical structure of DNA was proposed by James Watson and Francis Crick, which was a breakthrough in molecular biology.[163]

Nucleic acids mainly occur as deoxyribonucleic acid (DNA) and ribonucleic acid (RNA). In their classical roles, DNA serves as the long-term storage medium for genetic information, which is transmitted from one generation to the next, while RNA mainly converts genetic information into proteins. However, apart from protein synthesis various other important functions of RNA have been discovered which will also be described in the next section.

1.1 Functions of RNA

Protein synthesis (translation) involves three different types of RNAs to convert the genetic code into polypeptides: messenger RNA (mRNA), which carries genetic information from DNA to ribosomes, ribosomal RNA (rRNA), a key structural and catalytic component of the ribosome, and transfer RNA (tRNA), which delivers amino acids to the ribosome and decodes the mRNA sequence.[164-166] As mentioned before, RNAs also have many roles beyond translation (**Figure 22**). A major part of this functional diversity stems from non-coding RNAs (**Figure 22**) that regulate gene expression and cellular pathways. For instance, small nuclear RNAs (snRNAs) function within the spliceosome, a ribonucleoprotein

complex composed of snRNAs and proteins.[167] snRNAs enable intron removal from pre-mRNA to form mature mRNA and thereby regulate gene output.[168] Some non-coding RNAs are also involved in suppressing gene expression by targeting mRNA. MicroRNAs (miRNAs), approximately 22 nucleotide (nt) long single-stranded (ss) non-coding RNAs, bind with mRNA to block expression or promote degradation of mRNA.[169] Similarly, small interfering RNAs (siRNAs), which are a 20-27 nt double-stranded (ds) RNAs bind to mRNA post-transcriptionally, trigger degradation and prevent translation.[170] Small nucleolar RNAs (snoRNAs) function in the nucleolus, where they guide the chemical modification and processing of rRNA,[171] while long non-coding RNAs (lncRNAs), which are RNAs longer than 200 nt, have diverse regulatory roles in chromatin organization, transcriptional control, RNA processing, and post-transcriptional gene regulation.[172] Ribozymes act as RNA catalysts and drive key biochemical reactions such as phosphodiester bond cleavage and ligation.[173] In translation, ribozymes have a major function of catalysis of peptide-bond formation in the ribosome.[174]

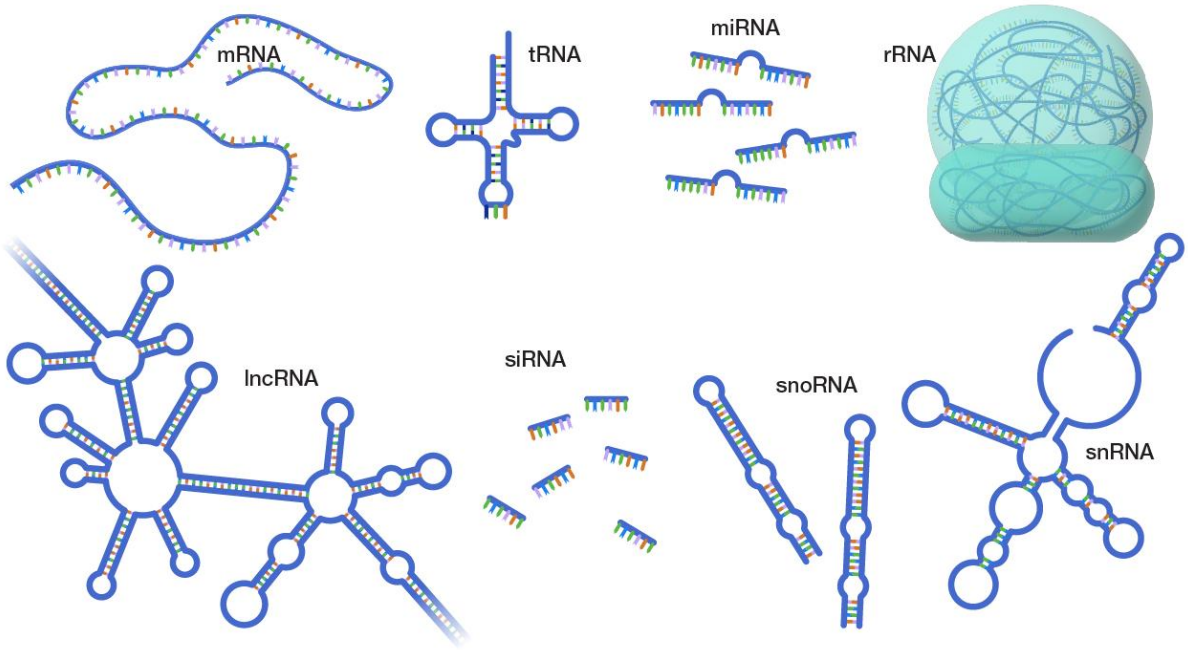

Figure 22. Various types of RNAs produced within a cell. Figure courtesy: National Human Genome Research Institute https://www.genome.gov/.

Another class of regulatory non-coding RNAs involved in control of gene expression are riboswitches.[175, 176] These are ssRNAs, usually 25-100 nt in length, found in the 5′-untranslated regions of mRNAs. Riboswitches contain an aptamer domain and an expression platform. The aptamer domain binds a wide range of targets, including amino acids, proteins,

drugs, and various small molecules, with remarkable affinity and specificity, which causes a conformational change in the expression platform of the riboswitch.[177] This conformational change causes alteration in the secondary structure of the riboswitch, leading to change in gene expression. For example, the xpt riboswitch binds guanine,[178] a nucleobase required for DNA and RNA synthesis. At high intracellular guanine levels, ligand binding to the aptamer domain induces a conformational change in the expression platform that represses translation of genes involved in guanine biosynthesis (**Figure 23B**). Conversely, when guanine levels are low, the riboswitch remains unbound, allowing expression of these genes and restoration of guanine levels (**Figure 23A**).[179] Therefore, aptamer domains serve as highly versatile molecular sensors and have attracted interest for applications in biotechnology and synthetic biology.

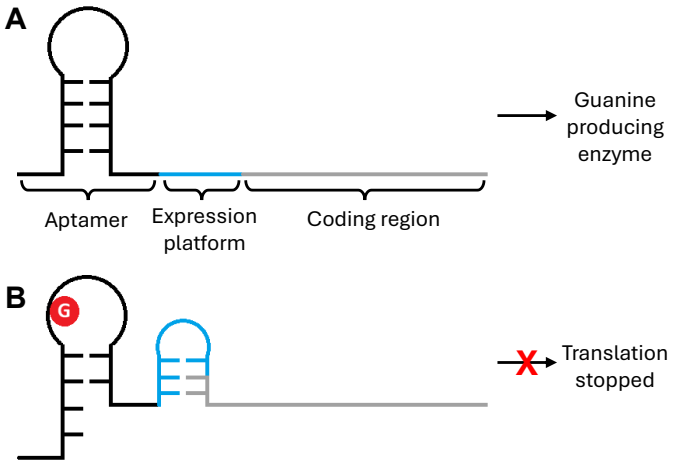

Figure 23. Schematic illustration of the guanine riboswitch xpt with low intracellular guanine levels, producing guanine producing enzyme (**A**) and with high intracellular guanine levels causing binding of guanine to the aptamer domain to stop translation (**B**).

However, most naturally occurring riboswitches recognize only their native ligands and function within the cell, which limits their practical applications. This has led to the development of engineered synthetic aptamers.[180, 181] Synthetic aptamers are commonly obtained by a standard *in vitro* method known as systematic evolution of ligands by exponential enrichment (SELEX) (**Figure 24**).[182, 183] It involves discovery of aptamers from large random nucleic-acid libraries. The library is incubated with a target molecule, allowing RNA sequences with affinity for the target to bind, while non-binding sequences remain free in solution. The non-binding candidates are discarded, while the target-bound aptamers are recovered, reverse transcribed and amplified. The enriched pool is subjected to a new SELEX cycle.[184]

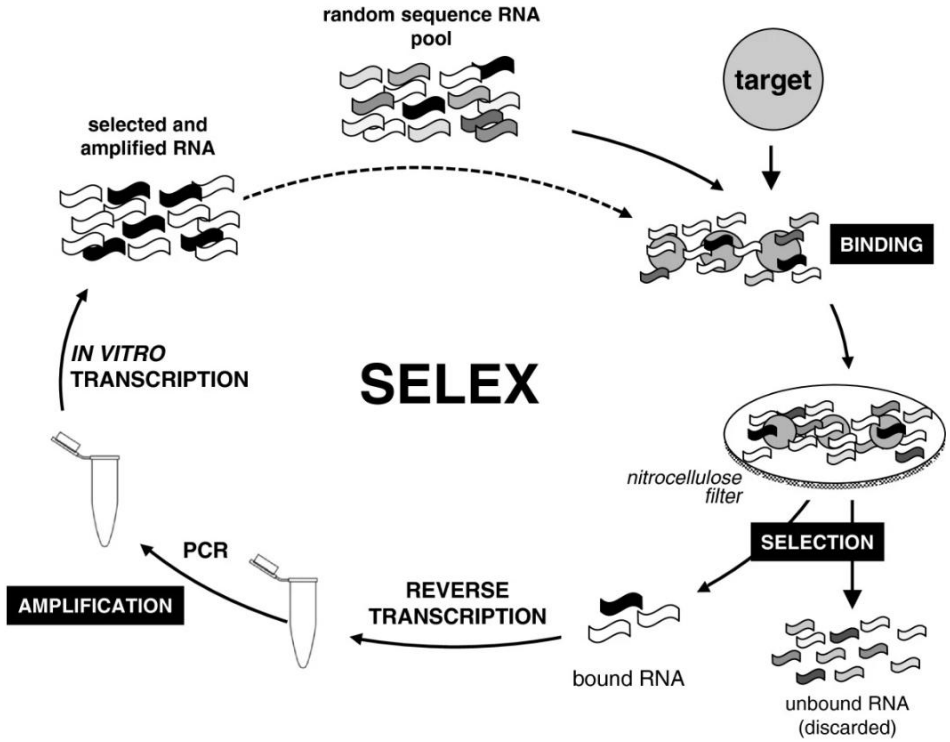

Figure 24. A schematic illustration of SELEX of RNA. This figure has been reproduced with permission from *Biol. Res.* **2014**, 47, 2.

In recent years, RNA-based therapeutics have become a major focus in modern medicine.[185] There are many types of RNA therapeutics, such as mRNA vaccines that deliver synthetically produced mRNAs that are translated by the cellular machinery to produce a therapeutic protein.[186] This approach gained widespread recognition with the rapid development of mRNA vaccines against COVID-19.[187] Antisense oligonucleotides are another class of RNA therapeutics that are short, single-stranded nucleic acids designed to bind complementary RNA sequences and modulate gene expression.[188] siRNAs have also been lately used in therapeutic applications, where chemically synthesized siRNA molecules are designed to be complementary to the mRNA of a disease-associated gene.[189] It binds to the mRNA and promotes its degradation and decreases expression of the target protein.

Investigating the structure and dynamics of nucleic acids is essential to fully understand these complex and varied biological functions of nucleic acids. Over the past several decades, a variety of biochemical and biophysical methods have been developed to probe their three-dimensional architecture, conformational flexibility, and molecular interactions. The main techniques used for these studies are briefly described in the next section.

1.2 Structure Determination of Nucleic Acids

Several techniques have been used to study the structure and function of biomolecules, including nucleic acids, and they have been briefly discussed in **Chapter A1** of this thesis. Among them, X-ray crystallography, Cryo-EM, and NMR spectroscopy, are high-resolution techniques that provide detailed structural information at near-atomic resolution. However, these techniques have their limitations, such as requiring good crystals for X-ray, size limitations in Cryo-EM and low sensitivity of NMR. In contrast, techniques like fluorescence and EPR spectroscopy, which although provide low-resolution, are highly sensitive techniques for studying biomolecular structure and dynamics under more native conditions. The next section describes fluorescence and EPR spectroscopy in detail.

1.2.1 Fluorescence spectroscopy

Fluorescence spectroscopy relies on fluorophores, which are molecules that produce fluorescence by absorbing light at a specific wavelength and re-emitting at a longer wavelength.[190] Many fluorescence experiments involve a single fluorophore attached to nucleic acid, where the fluorophore reports changes in microenvironment.[191] One such change is fluorescence emission quenching, which is decrease in the fluorescence signal intensity due to the interaction of fluorophore with nearby molecules.[192] Fluorescence signals can also change through spectral shifting where the emission maximum of a fluorophore shifts to shorter (blue shift) or longer wavelengths (red shift).[193] These shifts arise from changes in polarity, hydrogen bonding, or stacking interactions in the local environment of fluorophore. Fluorescence anisotropy[194] is another fluorescence method which uses polarized light to measure the changing orientation of a molecule in space while fluorescence lifetime measurements provide information about the average time a fluorophore remains in the excited state before emitting a photon.[195]

While single-fluorophore measurements probe local environmental changes, Förster resonance energy transfer (FRET), also known as fluorescence resonance energy transfer can also be used to obtain distance and dynamics information by nonradiative energy transfer between two fluorophores.[14, 196] **Figure 25A** shows a Jablonski diagram of the FRET process. The energy transfer takes place from the excited donor in the S_1 state to an acceptor in the ground-state (S_0 state), thereby exciting the acceptor to its S_1 state.[197] [198]The efficiency of this energy transfer, known as FRET efficiency (E) depends mainly on the donor-acceptor

distance (r), their relative orientation and the donor-acceptor distance at which 50% of excitation energy is transferred, known as the Förster distance (R_0).[14] FRET efficiency increases with decrease in distance between the donor and acceptor fluorophores and is given by:

$$E = \frac{R_0^6}{R_0^6 + r^6} \quad \text{(Eq. 6)}$$

FRET is classified as homo- or hetero-FRET depending on the fluorophore pair used.[199] Hetero-FRET uses different donor and acceptor molecules. For the fluorophores to form a hetero-FRET pair, donor emission must overlap acceptor absorption (**Figure 25B**). Hetero-FRET allows the measurement of distances in the range of ~10-100 Å.[200] It is widely used for studying the tertiary structure and for single-molecule studies (smFRET) of nucleic acids.[15, 201] Conversely, homo-FRET involves two identical fluorophores.[202] For Homo-FRET, fluorophores with a small stokes-shift should be used, as overlap between absorption and emission spectra allows energy transfer.[198] The fluorophores being identical, homo-FRET is monitored through fluorescence anisotropy measurements.[203] Another powerful and highly sensitive technique to study the structure and dynamics of nucleic acids is EPR spectroscopy and will be discussed in detail in the following section.

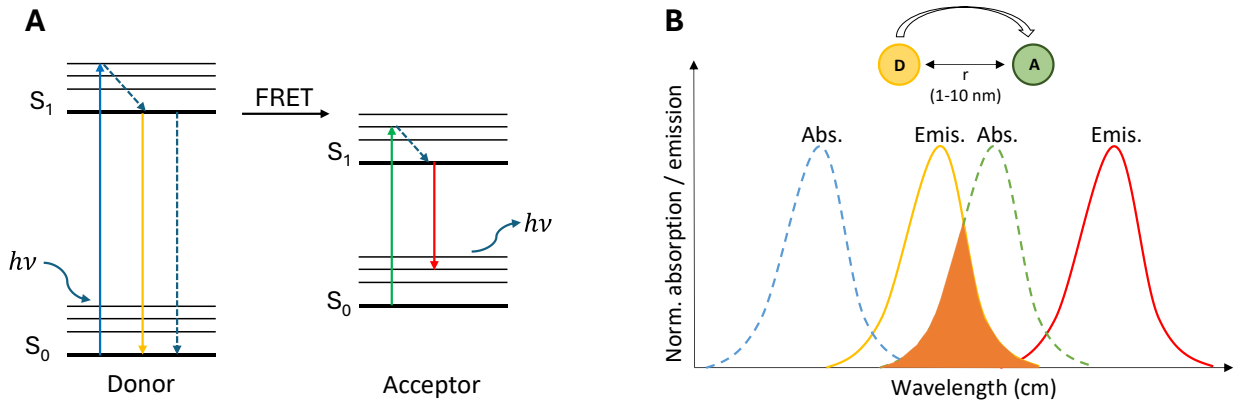

Figure 25. **A**. A Jablonski diagram demonstrating the FRET process. **B**. Absorption and emission spectra of donor- and acceptor molecules.

1.3 EPR spectroscopy

EPR spectroscopy, also known as Electron spin resonance (ESR) spectroscopy, is a magnetic resonance technique that detects μw-induced transitions of unpaired electron spins from a lower to a higher energy level.[204] EPR can be divided into two main types, namely continuous wave (CW) and pulsed EPR spectroscopy. In CW-EPR, the sample is irradiated

with a constant μw frequency while sweeping the magnetic field.[205] EPR line shapes are highly sensitive to rotational motion and local dynamics of the paramagnetic center. Therefore, it can reveal information on dynamics based on the spectral line shape analysis.[206] Moreover, line broadening due to dipolar-coupling reports inter-spin proximity and can be used for short-range distance measurements between two spin centers up to ~25 Å.[207]

Pulsed EPR on the other hand involves a constant magnetic field , and the sample is irradiated with high-power μw pulses.[208] Pulsed EPR techniques can be broadly classified according to the interactions they measure. For example, hyperfine spectroscopy methods, such as electron-nuclear double resonance (ENDOR),[209] electron spin echo envelope modulation (ESEEM)[210], and hyperfine sublevel correlation (HYSCORE)[211] spectroscopy, probe electron-nuclear interactions and provide information about the local chemical environment surrounding the paramagnetic center. To access longer electron-electron inter-spin distances, pulsed dipolar EPR spectroscopy is utilized. Various pulsed EPR techniques have been developed, such as pulsed electron-electron double resonance (PELDOR),[212] also known as double electron-electron resonance (DEER),[213] relaxation-induced dipolar modulation enhancement (RIDME),[214] single-frequency technique for refocusing dipolar couplings (SIFTER),[215] and double quantum coherence (DQC).[216] These techniques can be used to measure longer distances in the range of ~15–160 Å by evaluating the magnetic dipolar coupling between two electron spins.[17, 217]

The four-pulse PELDOR is one of the most widely used pulsed EPR methods.[218, 219] The basic principle of a PELDOR experiment is to measure distances between two paramagnetic centers by monitoring the dipolar interaction between two groups of spins.[220] It uses two microwave frequencies: observer frequency ($\nu_{observe}$) and pump frequency (ν_{pump}) (**Figure 26A**). $\nu_{observe}$ detects the first spin ensemble (observed spins) and generates a spin echo through a sequence of microwave pulses (**Figure 26B**).[221] ν_{pump} inverts the second spin ensemble that interacts with the observed spins and is placed near the strongest part of the EPR signal to excite as many spins as possible (**Figure 26B**). The refocused Hahn echo is generated with the three pulses of $\nu_{observe}$ which make up the detection sequence (**Figure 26A**). These pulses include a π/2 pulse, and two π pulses (**Figure 26A**). A single pump inversion π-pulse (red) is applied between the second and third detection pulses at time t (**Figure 26A**). The resulting time-trace is used to extract the interspin distance (**Figure 26C**).

It yields a time trace of the dipolar frequency which is converted to distance distribution using simulation or Tikhonov regularization (**Figure 26C**).[222]

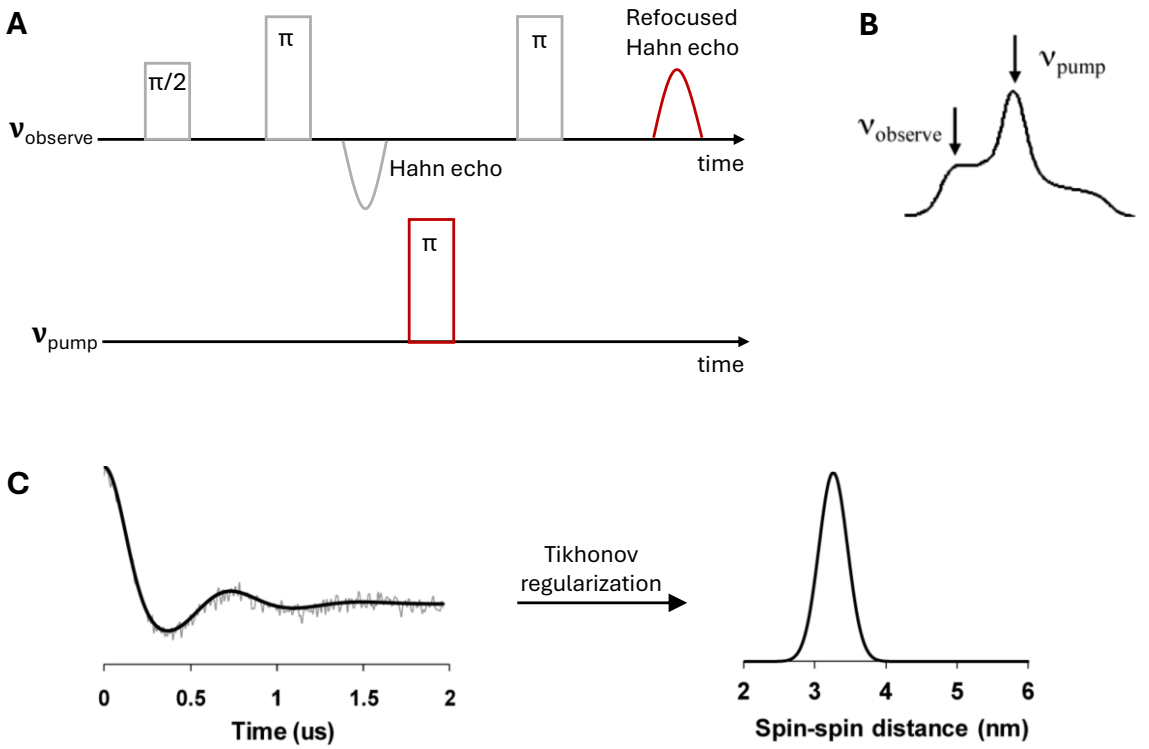

Figure 26. PELDOR distance measurements. **A**. A four-pulse PELDOR sequence showing the observer pulses at $\nu_{observe}$ and a pump π pulse at ν_{pump} applied at a variable time. **B**. EPR spectrum indicating the positions of the observer ($\nu_{observe}$) and pump ν_{pump} frequencies. **C**. A PELDOR time-trace (left) and the distance distribution (right) obtained by Tikhonov regularization. **Figure 26B** and **C** courtesy: National MagLab

EPR spectroscopy offers some advantages for studying nucleic acids compared to other methods. It is a very sensitive technique and requires very small amount of sample (nmoles) as compared to NMR and X-ray crystallography which generally requires micromole quantities of sample.[223, 224] Unlike solution-state NMR, EPR has no size limitation and can be used to study large molecular assemblies.[225] However, nucleic acids are inherently diamagnetic. Therefore, to be studied using EPR, they require incorporation of paramagnetic centers, also known as spin labels. This can be achieved by site-directed spin labeling (SDSL),[226] which will be described in the next section.

1.4 Site-directed spin labeling (SDSL)

Spin labels can be attached to nucleic acids at specific sites of interest through SDSL, either covalently or noncovalently (**Figure 27**).[227-230] In covalent labeling, spin labels are linked to

the nucleic acid via covalent bonds, either after synthesis, known as post-synthetic labeling (**Figure 27A**) or during synthesis using the phosphoramidite approach (**Figure 27B**).[228] Noncovalent labeling relies on noncovalent interactions between the spin label and the nucleic acid such as hydrogen bonding or π–π stacking (**Figure 27C**).[231-233] Each of these approaches will be discussed in more detail in the following sub-sections.

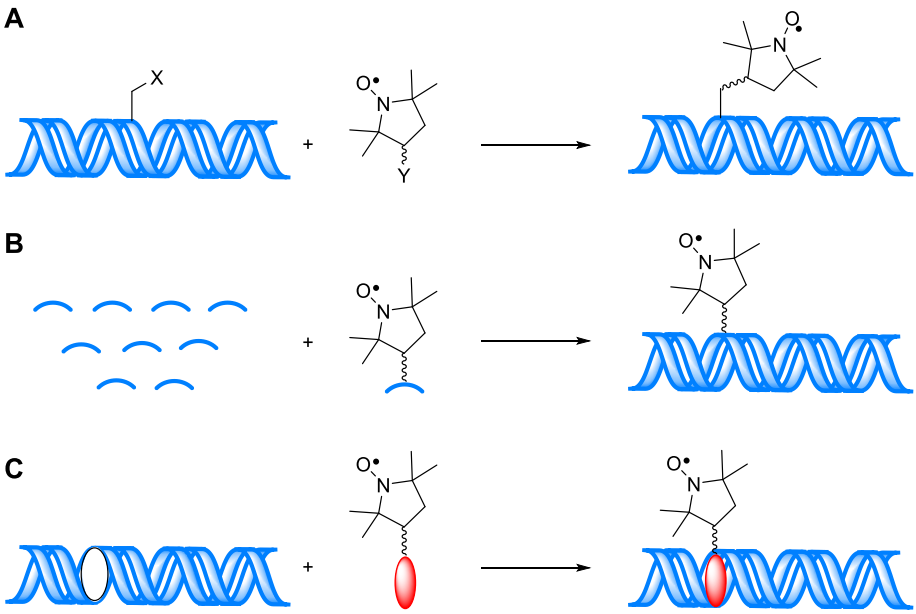

Figure 27. SDSL of nucleic acids. **A**. Post-synthetic spin labeling where X and Y represent functional groups that undergo a reaction to form a covalent bond between the spin label and the oligonucleotide. **B**. The phosphoramidite approach. **C**. Noncovalent spin labeling by usage of an abasic site.

1.4.1 Post-synthetic spin labeling

As mentioned before, post-synthetic spin labeling enables covalent attachment of spin labels to specific sites within the oligonucleotide after its synthesis (**Figure 27A**). This approach relies on the presence of uniquely reactive functional groups at defined positions within the oligonucleotide, which can react selectively with complementary functional groups on spin-labeled reagents.[228, 229] These reactive groups in the oligonucleotide can be introduced through either chemical or enzymatic synthesis. A major advantage of this method is that the spin label is not exposed to the potentially harsh conditions of solid-phase synthesis, such as detritylation under acidic conditions, which could partially reduce the spin label.[234, 235] Furthermore, the modified oligonucleotides and the reagents for SDSL are often commercially available, which avoids the tedious synthesis of a spin-labeled phosphoramidite for the phosphoramidite approach.[229] However, this approach is not

without limitations. Incomplete labeling and non-specific reactions can occur due to the presence of naturally nucleophilic sites in nucleic acids, such as exocyclic amino groups, the N7 position of purines, and non-bridging phosphate oxygens, which may react undesirably with the labeling reagent. [229]

1.4.2 The phosphoramidite approach

The first synthetic DNA was reported by Michelson and Todd in 1955, who synthesized a simple dinucleotide.[236] Over the following 25 years, continuous advancements in oligonucleotide chemistry led to a major breakthrough in 1981 with the development of the phosphoramidite approach by Caruthers.[237] This approach has since become the foundation of modern solid-phase DNA synthesis. The phosphoramidite approach enables SDSL using spin-labeled phosphoramidite monomers (**Figure 28**) that are used for incorporation of nucleotides by automated solid-phase oligonucleotide synthesis.[238] The phosphoramidites are made of 2′-deoxyribonucleosides for DNA and ribonucleosides for RNA. Key protecting/activating groups define phosphoramidite reactivity during synthesis.[239] The 5′-OH is protected with a 5′-dimethoxytrityl (DMT) group, while the 3′-OH is phosphitylated to give a phosphoramidite. The 2′-OH in RNA phosphoramidite is silyl-protected to prevent side reactions. Exocyclic amines on C, A, and G are protected as amides.

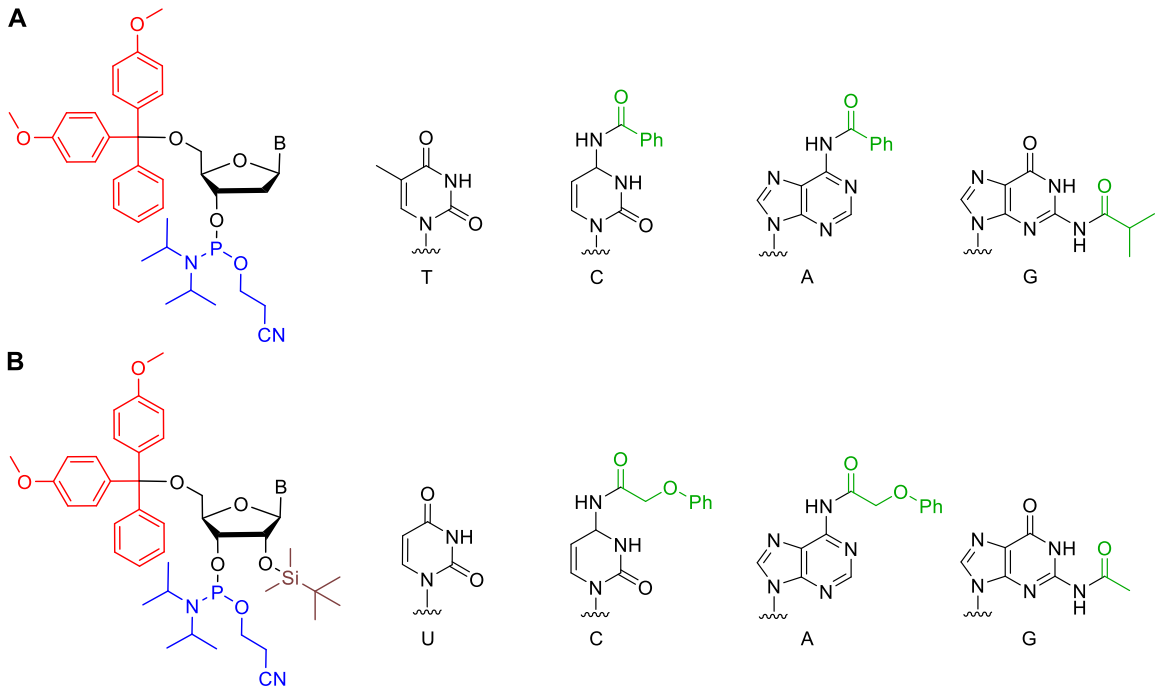

Figure 28. Structure of 2′-deoxyribonucleoside (**A**) and ribonucleoside (**B**) phosphoramidites and the corresponding bases with examples of some protecting groups. The 5′-hydroxyl is protected as a dimethoxytrityl ether (DMT) (red), the 3′-hydroxyl is phosphitylated (blue), the 2′-hydroxyl group of

ribonucleoside phosphoramidite is silyl protected (brown) and the exocyclic amino groups of C, A and G are protected as amides (green).

Unlike natural DNA synthesis, which proceeds from the 5′- to 3′- direction, solid phase synthesis is performed from the 3′- to the 5′- end. The synthesis involves a recurring five-step cycle, shown in **Figure 29**.[240, 241] The first nucleotide is connected to the solid phase through its 3′-hydroxyl group. Each cycle begins with detritylation (Step 1), where the 5′-dimethoxytrityl (DMT) protecting group is removed to expose a free hydroxyl group. This is followed by coupling, in which an activated phosphoramidite nucleotide reacts with the free 5′-OH of the growing chain (Step 2). Capping (Step 3) then blocks any unreacted hydroxyl groups to prevent formation of truncated sequences. Next, oxidation (Step 4) converts the unstable phosphite triester linkage into a stable phosphate. The cycle is repeated (Step 5) for each nucleotide addition until the desired sequence is complete. After the last nucleotide has been added to the oligonucleotide, the final step of the synthesis (Step 6) is detritylation of the 5′-hydroxyl group. Finally, the oligonucleotide is cleaved from the solid phase and the protecting groups removed under basic conditions to yield the fully deprotected product. Sometimes the final detritylation step (Step 6) is skipped, and the DMT group is kept on (“trityl-on” synthesis) to aid HPLC purification of the oligonucleotide and the final DMT group is removed only after purification.[242]

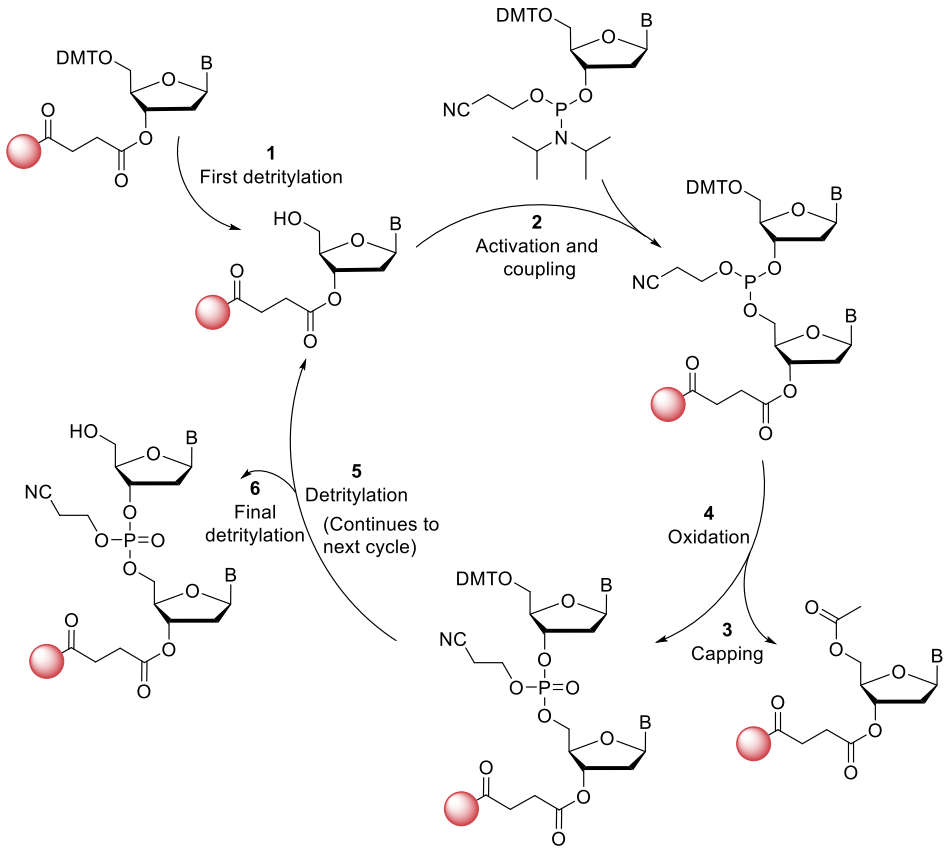

Figure 29. The automated solid-phase oligonucleotide synthesis cycle.

The main advantage of the phosphoramidite method is that it enables precise incorporation of spin labels at specific sites without side-reactions. However, the method is labor-intensive, requiring advanced expertise in synthetic organic chemistry, which may limit its accessibility to researchers without synthesis expertise.

1.4.3 Noncovalent spin labeling

Noncovalent spin labeling is an alternative strategy for SDSL of nucleic acids that avoids the challenges associated with the covalent methods. The most commonly used method for noncovalent SDSL involves specific and reversible binding of a spin-labeled molecule to a pre-designed site, usually an abasic site (**Figure 30A**), in the oligonucleotide. The interaction between the spin-labeled molecule and the abasic site is a ligand-receptor type, governed by noncovalent forces such as hydrogen bonding, π-π stacking or Van der Waals interactions.[228]

One of the early examples utilizing this SDSL strategy was from Sigurdsson group, involving the cytosine-derived nitroxide **ç** (**Figure 30B**), which selectively binds to abasic sites in duplex DNA by pairing with a guanine on the complementary strand through

hydrogen bonding and π-stacking.[233] At low temperatures (e.g., –30 °C), **ç** exhibited high binding specificity and stability, enabling direct EPR measurements without further purification steps. This noncovalent spin labeling strategy offered several advantages over the covalent approaches. It was simpler to synthesize **ç** than spin-labeled phosphoramidites, required smaller amounts of label, and avoided exposing the spin label to harsh oligonucleotide synthesis reagents. Its "mix-and-measure" simplicity also made it accessible to non-specialists. However, the method had limitations: **ç** bound to abasic sites in DNA duplexes only at low temperatures (-30 °C), showed poor binding to RNA duplexes with abasic sites, and binding efficiency was strongly sequence dependent. Furthermore, introducing two binding sites in the same duplex often resulted in incomplete labeling.[243]

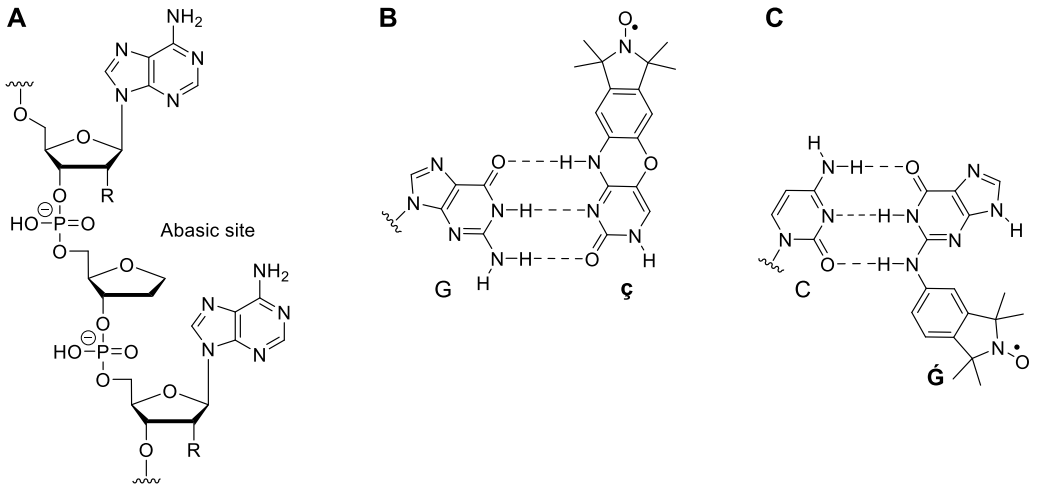

Figure 30. **A**. Structure of an abasic site within an oligonucleotide. **B**. Structure of **ç**[233] base-paired with guanine (G) at an abasic site. **C**. Structure of **Ǵ**[244] base-paired with C at an abasic site.

To overcome the limitations of **ç**, a guanine-derived spin label **Ǵ** (**Figure 30C)** that could base-pair with cytosine was developed, offering high-affinity and specific binding to abasic sites in duplex RNA.[244] Unlike **ç**, which required multistep synthesis, **Ǵ** can be prepared in a single step from readily available materials. It binds efficiently to abasic-site-containing nucleic acids, particularly RNA duplexes, even at higher temperatures, shows minimal sequence dependence, and enables accurate inter-spin distance measurements by PELDOR.

Noncovalent spin-labeling of a completely unmodified RNA has also been reported for a malachite green (MG) binding 38-nucleotide RNA aptamer (**Figure 31**), known to bind the tetramethyl rhodamine (TMR) (**Figure 31**).[232] Therefore, a nitroxide derivative of TMR was used as the spin label.[232] This approach allows for spin-labeling of long RNAs containing

the MG binding motif, prepared by transcription. However, the ligand binding domain may interfere with the structure of the RNA under study.

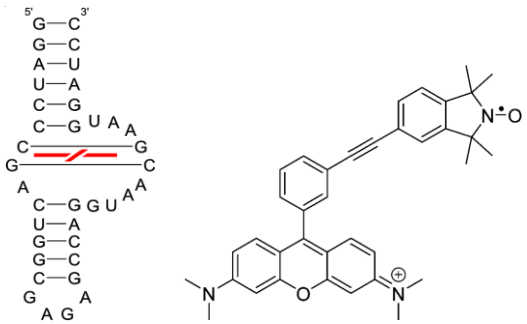

Figure 31. Secondary structure of the MG aptamer showing the position of the ligand in red (left) and TMR derived nitroxide spin label (right).[232]

Base-pairing has also been used for noncovalent spin-labeling, where short, chemically synthesized oligomers containing a nitroxide label were hybridized with a segment of a large RNA (**Figure 32**).[245] However, a complementary spin-labeled sequence needs to be prepared for each target RNA, limiting broader applicability, and making this method less economical.

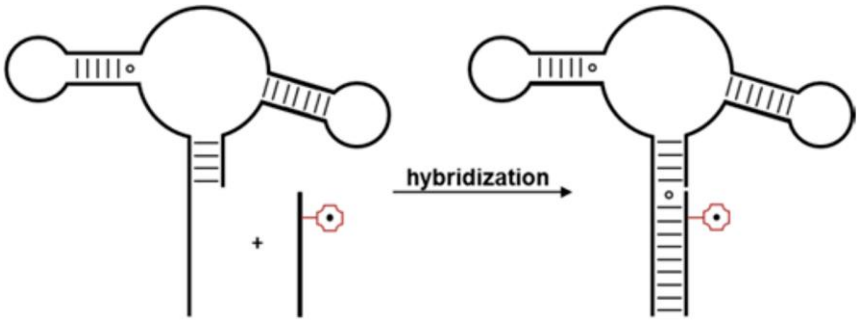

Figure 32. Schematic representation of spin labeling by hybridizing a spin labeled oligomer fragment to a helical section of the RNA of interest. This figure has been reproduced with permission from *ACS Chem. Biol.* **2014**, 9, 6, 1330–1339.

1.5 Nitroxide spin labels

Nitroxides are the most commonly used radicals as spin labels for EPR mainly due to their stability since the unpaired electron is localized mainly on the N–O group and shielding effect of the alkyl groups flanking the radical center.[246, 247] Nitroxides are highly compatible with common nucleic-acid labeling handles like thiols, amines, click-chemistry groups and abasic-site ligands.[228, 248] Various nitroxide spin labels have been developed over the years, and most are linked to the oligonucleotide through a tether. The tether, therefore, governs the mobility of the spin label relative to nucleic acid. Some important spin-labels and the extent of their mobility based on the tether are discussed below.

Flexible spin labels are attached to the nucleotide through rotatable single-bond tethers. They retain their conformational freedom relative to the nucleotide. Such spin labels are usually small in size, non-perturbing to the nucleic acid and also are relatively easier to synthesize. However, since flexible spin labels can adopt multiple rotamers, (**Figure 33**), they produce broader PELDOR/DEER distance distributions and thus complicate EPR analysis.[222, 249]

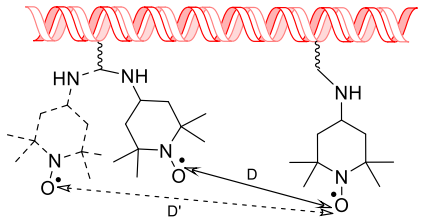

Figure 33. Flexible spin label incorporated into a nucleic acid and its different conformers leading to multiple distances D and D′.

An example of a flexible spin label is a two-atom tethered six-membered ring thymidylate nitroxide DUMTA (**Figure 34**).[250] Spin labels tethered through a semi-rigid linker have lesser motion and therefore give more accurate measurements than flexible spin labels. Some examples are 2'-ureido TEMPO[251] and 2,2,5,5-tetramethyl-pyrrolin-1-oxyl-3-acetylene (TPA)[252] (**Figure 34**).

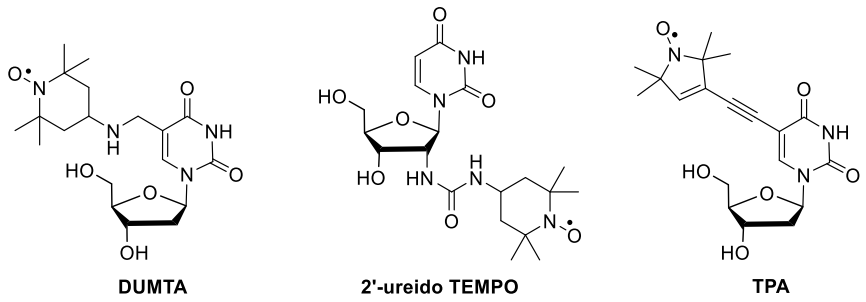

Figure 34. Examples of flexible and semi-rigid nitroxide spin labels.

Rigid spin labels eliminate linker motion by fusing the nitroxide to the nucleobase through two bonds. The spin labels follow nucleic-acid motion rather than moving independently. They yield narrower and more accurate distance distributions.[229] Another advantage of using rigid spin labels is that the relative orientation of two labels can be determined by dipolar EPR.[253] The first reported rigid nucleoside label was **Q**[254, 255] (**Figure 35**) but involved a lengthy synthesis and base pairing with the unnatural base 2-Aminopurine (2-Ap). Rigid

spin labels **Ç**[234] and **Çm**[256] for DNA and RNA, respectively, bearing a phenoxazine scaffold were later introduced (**Figure 35**). They base pair with natural base guanine. **Ç** and **Çm** have enabled efficient study of structure, dynamics, and ligand-induced conformational changes in nucleic acids using EPR spectroscopy.[257-262] However, their syntheses are lengthy and time consuming and their incorporation in the nucleic acid through phosphoramidite approach is tedious. Therefore, spin labeling of nucleic acids with such spin labels is limited to shorter oligonucleotides. More recently, more rigid carbazole-derived rigid spin labels **Ċ** and **Ċm** were introduced (**Figure 35**).[263] While these labels were successfully incorporated into DNA and RNA without significantly perturbing duplex structure, their EPR studies were not reported.

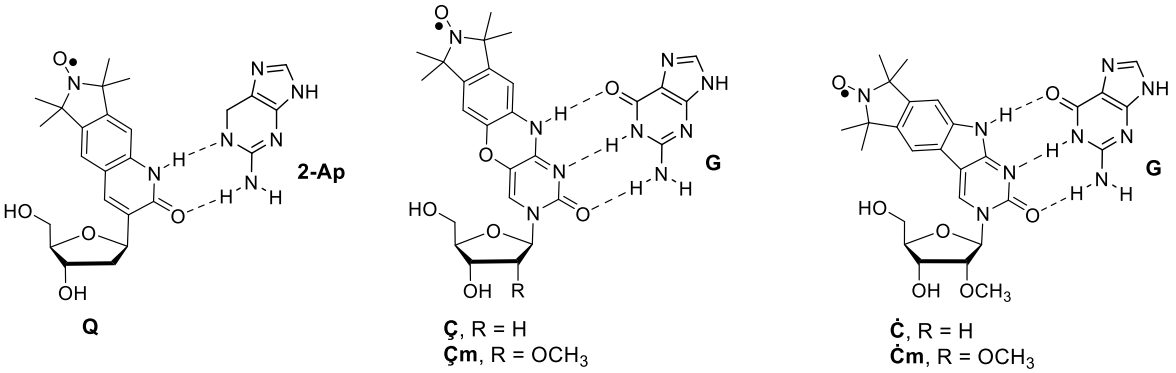

Figure 35. Structures of the rigid nitroxides **Q**, **Ç**, **Çm**, **Ċ** and **Ċm** base-paired with 2-Ap and G, respectively.

1.6 Contribution of Part B of this dissertation

Part B of this PhD thesis contributes to the biophysical studies of nucleic acids through the development of a noncovalent spin labeling approach that is easier to implement while still giving precise structural information as well as through the incorporation of spin labels of various spin- and fluorescent-labels into DNA and RNA for the study of structure and dynamics of nucleic acids by both EPR and fluorescence spectroscopy.

Specifically, in **Chapter B2**, a noncovalent spin labeling approach based on helical stacking is presented, where a short, chemically synthesized RNA hairpin with the rigid **Çm** spin label stack over both ends of a target RNA duplex and positions the spin label at a defined site without covalent modification of the target.

Chapter B3 covers four collaborative projects on labeling of DNA and RNA with spin- and fluorescent-labels. The first part of this chapter describes spin labeling of DNA and RNA with isothiocyanate spin label **M** and rigid spin label **Çm** to study nucleic acid-protein

complexes using PELDOR. The latter part focuses on fluorescence-based studies, including labeling of the neomycin-binding aptamer with the rigid FRET pair **Çmf** and **tCnitro**, as well as incorporation of 2-aminopurine as a fluorescent base analogue into a caffeine-binding aptamer.

B2 Noncovalent spin labeling of RNA through helical stacking

Rigid spin labels like **Ç**[234] and **Çm**[256] are valuable for studying nucleic acids by EPR spectroscopy.[257, 258, 264] They are cytidine analogues, that base pair with the natural base guanine. They give narrow distance distributions[229] in PELDOR experiments and can also provide relative orientational information between two spin labels.[264] This makes rigid spin labels more informative than flexible ones for structural studies of nucleic acids. However, the synthesis and incorporation of such rigid labels is labor intensive and costly, and their use is usually limited to relatively short oligonucleotides prepared by solid-phase synthesis.[229, 265, 266] Consequently, there is a need for simpler and cost-effective methods, preferably a noncovalent approach, to incorporate rigid labels into larger RNAs.

2.1 Helical stacking interactions in nucleic acids

A known noncovalent RNA-RNA association is helical stacking of blunt-ended duplexes through π-π interactions between the terminal base pairs.[267, 268] Helical stacking by CW-EPR was first observed in 2008 by Cekan et al.[234] In that study, a DNA duplex (**a**, **Figure 36**) containing a single **Ç** label at its terminal showed spectral broadening and peculiar features in the CW-EPR spectrum (**Figure 36**). Such changes can arise when two spin-labeled duplexes come into close proximity, because dipolar coupling between the nitroxide radicals alters the EPR line shape. In addition, formation of a larger stacked assembly slows rotational motion, which increases anisotropy and further broadens the spectrum.When increasing amounts of unlabeled duplex **b** were added, the broadening and the additional features disappeared. The experiment, therefore, confirmed that the spin labels on separate duplex molecules were brought into close proximity, and the most plausible explanation for these EPR features was end-to-end stacking of duplexes.

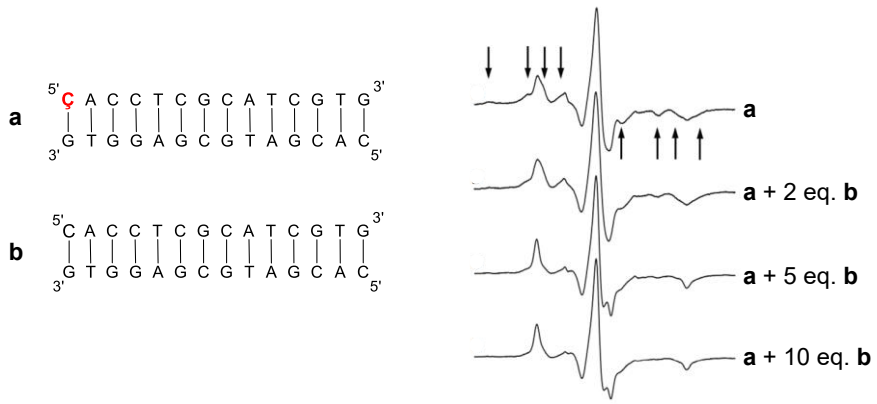

Figure 36. Sequences of the **Ç** labeled DNA duplex **a**, unmodified DNA duplex **b** and the EPR spectrum of the **Ç**-labeled duplex **a**, along with EPR spectra on addition of 2, 5 and 10 eq. of unlabeled DNA duplex **b** in phosphate buffer (10 mM Na_2HPO_4, 100 mM NaCl, 0.1 mM Na_2EDTA, pH 7.0; oligo concentration 200 µM) (Arrows indicate the additional features corresponding to dipolar coupling). This figure has been reproduced with permission from *Nucl. Acids Res.* **2008**, *36* (18), 5946-5954.

RNA stacking was later systematically studied by PELDOR in 2018 by Erlenbach et al.[269] They showed that stacking complicates structural studies of nucleic acids due to additional intermolecular spin-spin distances that appear in the PELDOR distance distribution apart from the expected intramolecular distances. For the study, they used short singly spin-labeled dsRNAs. The stacking was analyzed using two main PELDOR parameters: the distance distributions and the modulation depth. Because each dsRNA contained only a single spin label, any dipolar distance detected by PELDOR (>20 Å) had to arise from intermolecular interactions between separate RNA duplexes. As shown in **Figure 37A** three different stacking arrangements are possible, giving three different PELDOR distances (**Figure 37B)**, thus confirming stacking of duplexes.

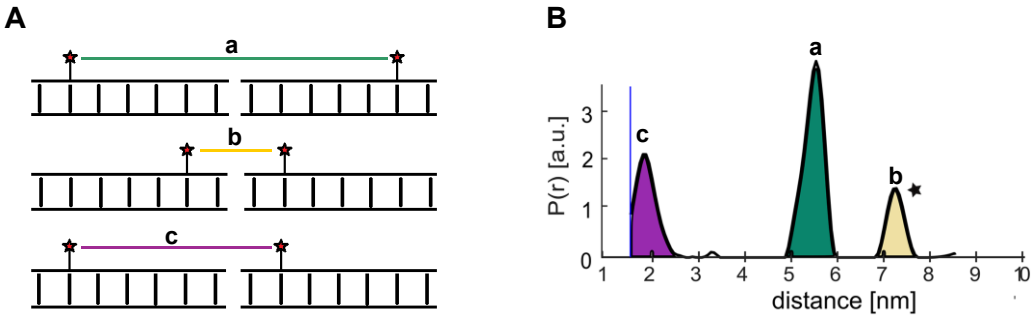

Figure 37. **A**. Three stacking possibilities with three different intermolecular distances between the spin labels of a singly labeled dsRNA sample. **B**. Distance distribution from the four-pulse PELDOR of the singly labeled dsRNA sample. **Figure 37B** has been reproduced with permission from *RNA* **2019**, *25* (2), 239-246.

In addition, the modulation depth of the PELDOR time trace was used as a quantitative measure of stacking. The modulation depth reflects the fraction of spins undergoing dipolar

coupling within an approximately 10 nm sphere. Therefore, a deeper modulation depth indicates more stacking of duplexes, allowing the determination of the stacking probability. This opened the door for studying factors that affect helical stacking, such as RNA and NaCl concentration. The stacking probability was unaffected with the RNA concentration but increased with increased NaCl concentration (**Figure 38A**). They further showed that stacking could be avoided by introducing overhangs at both duplex ends (**Figure 38B**).

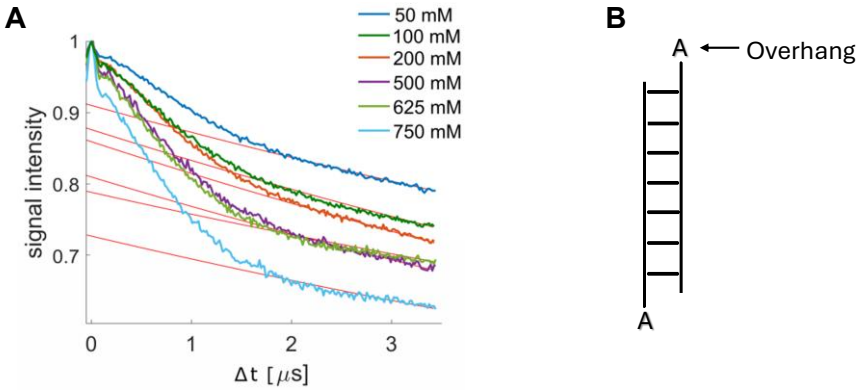

Figure 38. **A**. Time traces of dsRNA samples for six different NaCl concentration as depicted in the figure legend. **B**. dsRNA with an overhang at each end. **Figure 38A** has been reproduced with permission from *RNA* **2019**, *25* (2), 239-246.

These studies suggested that helical stacking could potentially be exploited for noncovalent spin labeling. A small RNA hairpin containing a rigid **Çm** label could, in principle, stack onto both the ends of an RNA duplex and thereby serve as a noncovalent spin-labeling unit. This approach could reduce the synthetic effort required for rigid spin labeling by the phosphoramidite approach and avoiding direct covalent modification of the target RNA, which might be too long for chemical synthesis. This idea formed the basis of the work described in this chapter.

2.2 A blunt-ended Çm-labeled hairpin

Our initial strategy was the synthesis of an 8-nucleotide long RNA hairpin containing the rigid spin label **Çm** (**Figure 39A**). The idea was to have this hairpin stack onto the ends of a duplex and thereby introduce the rigid spin label **Çm** noncovalently into the duplex (**Figure 39B**). The hairpin was designed with three features to ensure stable hairpin formation: a GNRA tetraloop,[270] G and C nucleotides in the stem of the hairpin, and an expected inter-spin distance between two stacked hairpins below the practical lower limit of reliable PELDOR distance determination (<20 Å) so that it does not interfere with distance

measurements.[249] The rigid spin label **Çm** was incorporated by automated chemical synthesis using a protocol previously developed in the Sigurdsson research group,[235] giving a blunt-ended hairpin **I_{HP}** (**Figure 39A**).

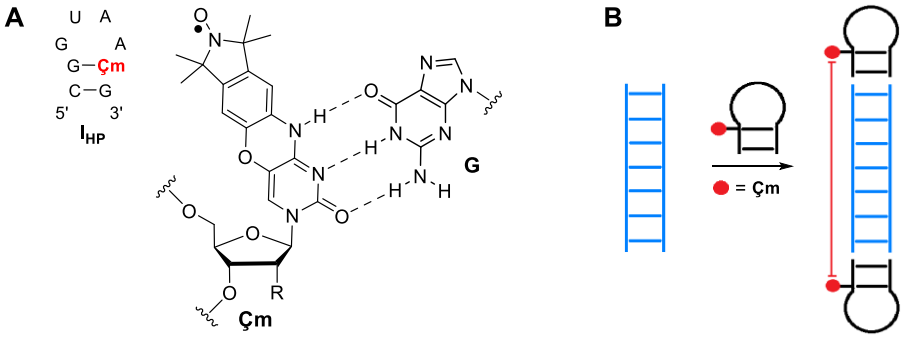

Figure 39. **A**. The sequence of the **Çm**-labeled hairpin **I_{HP}** and the structures of **Çm** shown base-paired with guanine. **B**. Schematic representation of labeling an RNA duplex noncovalently through helical stacking with a **Çm**-labeled hairpin.

2.2.1 EPR analysis of stacking with the Çm-labeled hairpin I_{HP}

As seen in section **2.1**, CW-EPR can be used to monitor stacking, because it is sensitive to intermolecular association, since close proximity of spin labels and slower rotational motion due to biomolecular assembly can alter the EPR line shape. To examine whether the blunt-ended hairpin **I_{HP}** exhibits stacking, temperature-dependent CW-EPR analysis of **I_{HP}** was performed (**Figure 40**). Indeed, broadening and irregular features increased with a decrease in temperature. If the broadening arose from dipolar coupling between two **Çm** labels, brought into close proximity through hairpin self-stacking, these irregular features were expected to disappear upon addition of an excess of an unlabeled duplex.

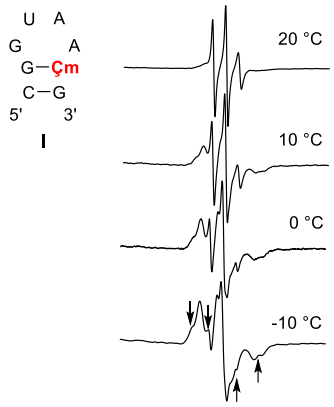

Figure 40. Sequence of the **Çm** labeled hairpin **I_{HP}** and its X-band EPR spectrum as a function of temperature. All data were recorded in a phosphate buffer (10 mM Na_2HPO_4, 100 mM NaCl, 0.1 mM Na_2EDTA, pH 7.0; oligo concentration 200 μM) (Arrows indicate the additional features).

To test this hypothesis, **I_{HP}** was mixed with excess of its corresponding unlabeled duplex **I_{DUPL}** to form the expected stacked assembly **I** (**Figure 41A**). CW-EPR spectra of **I_{HP}** alone and of **I_{HP}** with its duplex **I_{DUPL}** were then compared at 20 and -10 °C (**Figure 41B**). At 20 °C, the spectra of **I_{HP}** and **I_{HP}** + **I_{DUPL}** were essentially identical, indicating little or no detectable association at this temperature. At -10 °C, however, the irregular features observed for **I_{HP}** alone disappeared in the presence of the duplex.

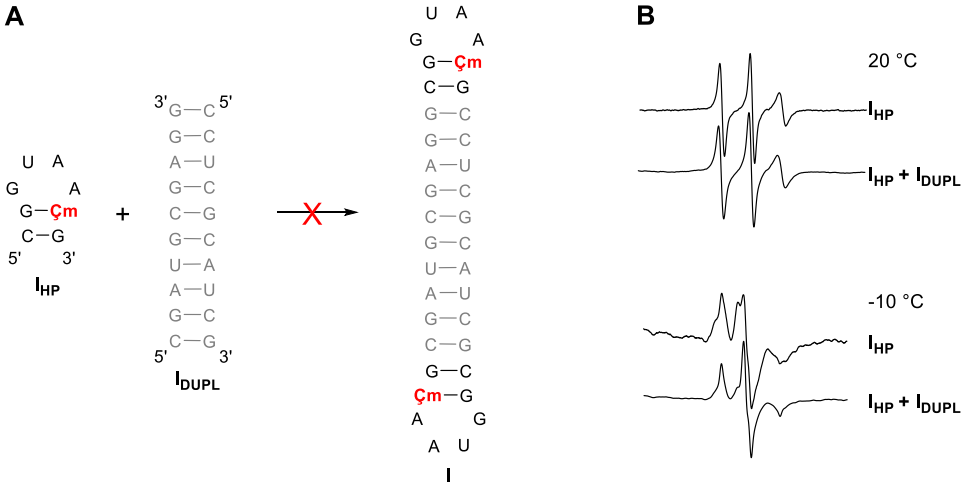

Figure 41. **A**. The sequences of **Çm**-labeled hairpin **I_{HP}**, its corresponding unlabeled RNA duplex **I_{DUPL}** and the expected stacked assembly **I**. **B**. EPR spectra of hairpin **I_{HP}** and assembly **I** obtained on mixing hairpin **I_{HP}** with its 10 eq. duplex **I_{DUPL}** at 20 and -10 °C.

To determine whether the irregular features were indeed caused by stacking, a control experiment was performed in which **I_{HP}** was titrated with a ssRNA. A similar change in the line shape was observed. This showed that the disappearance of the irregular features could not be attributed solely to hairpin-duplex stacking, and that other nonspecific intermolecular interactions also contributed to the observed spectral changes.

An RNA and NaCl concentration dependence was also studied to check if it influences the CW-EPR spectrum of **I_{HP}** (**Figure 42**), as previously observed by PELDOR.[269] Increasing the concentration of **I_{HP}** caused minor changes in the EPR spectra **(Figure 42A)**. In contrast, increasing the NaCl concentration caused changes in the EPR spectra **(Figure 42B)**. However, the effect was more pronounced between 0 and 200 mM NaCl, while further increases in concentration caused only minor additional spectral changes. These observations are in general agreement with the report by Erlenbach et al.[269] and indicate that ionic strength strongly affects stacking. However, in the present case, the CW-EPR data alone did not allow us to conclude with certainty that the observed changes arose solely from

helical stacking, since other nonspecific intermolecular interactions may also contribute to the spectral changes.

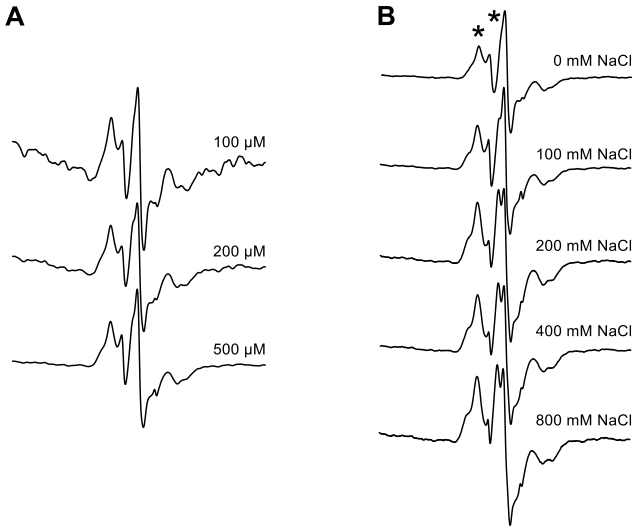

Figure 42. **A**. EPR spectra of the **Çm**-labeled hairpin $\mathbf{I_{HP}}$ with increasing RNA hairpin concentration, performed in a phosphate buffer (10 mM Na_2HPO_4, 100 mM NaCl, 0.1 mM Na_2EDTA, pH 7.0). **B**. EPR spectra of the **Çm**-labeled hairpin $\mathbf{I_{HP}}$ with increasing NaCl concentration in a phosphate buffer (10 mM Na_2HPO_4, 0.1 mM Na_2EDTA, pH 7.0, oligo concentration 200 µM). Asterisk indicates the feature that change with increase in NaCl concentration.

Stacking of $\mathbf{I_{HP}}$ on the ends of $\mathbf{I_{DUPL}}$ was further investigated by PELDOR, in collaboration with Dr. Burkhard Endeward and Prof. Thomas Prisner at Goethe University, Frankfurt. If $\mathbf{I_{HP}}$ stacked on both ends of $\mathbf{I_{DUPL}}$, the expected inter-spin distance from molecular modeling was about 3.0 nm. The distance distribution, however, was dominated by a much shorter distance of ~2.2 nm. This short-distance population was consistent with the modeled distance between two **Çm** labels in a self-stacked hairpin, rather than with the expected hairpin-duplex assembly. These results, therefore, indicate that the blunt-ended hairpin preferentially undergoes self-stacking instead of stacking onto the duplex.

2.3 Çm-labeled hairpins with overhangs

To favor hairpin-duplex stacking over hairpin self-stacking, the strategy was modified by introducing complementary 3′ overhangs on both the **Çm**-labeled hairpins and their corresponding duplexes (**Figure 43A**). Complementary overhangs of hairpin and duplex could base pair and facilitate stacking. **Çm**-labeled hairpins ($\mathbf{II_{HP}}$-$\mathbf{VI_{HP}}$) and duplexes ($\mathbf{II_{DUPL}}$-$\mathbf{VI_{DUPL}}$) with one- to five-nucleotide overhangs were prepared. The overhang

sequences were chosen to minimize undesired intramolecular base pairing in the hairpins (**Figure 43A**).

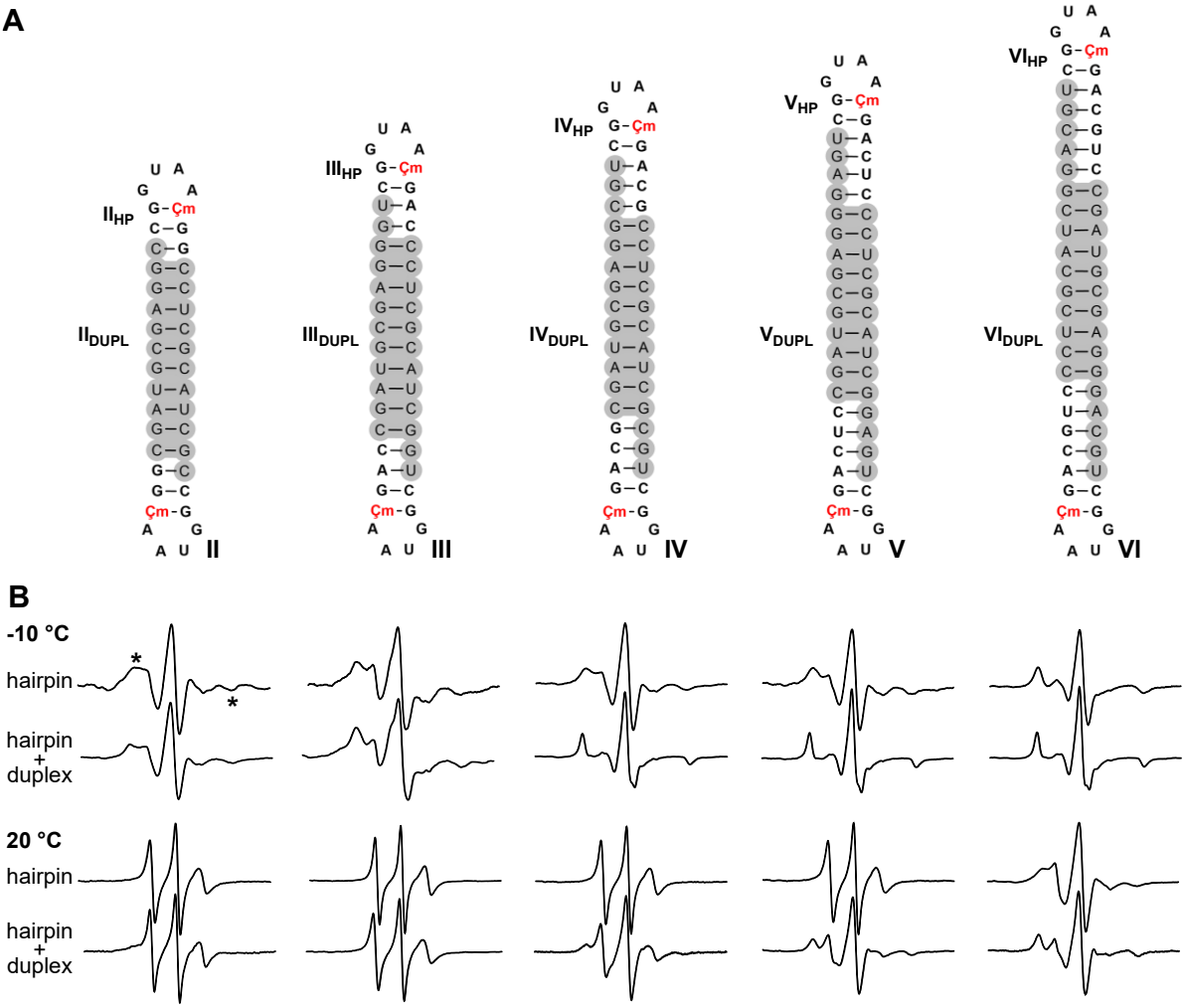

Figure 43. **A**. The sequences of **Çm**-labeled hairpins (**II$_{HP}$-VI$_{HP}$**) shown stacked on their corresponding RNA duplexes (**II$_{DUPL}$-VI$_{DUPL}$**) (in gray), in the order of increasing number of nucleotides in the overhangs (0-5). The overhangs are on the 3'-end of both the hairpins and the duplexes. The hairpin-duplex assemblies are labeled **II-VI**. **B**. X-band EPR spectra of the hairpins (**II$_{HP}$-VI$_{HP}$**) in the absence and presence of their corresponding duplexes (**II$_{DUPL}$-VI$_{DUPL}$**) at -10 °C and 20 °C, recorded in a phosphate buffer (10 mM Na_2HPO_4, 100 mM NaCl, 0.1 mM Na_2EDTA, pH 7.0; concentration of each **Çm**-labeled hairpin was 200 µM and its corresponding duplex 100 µM). Asterisks indicate broad features.

2.3.1 EPR analysis of Çm-labeled hairpins with overhangs

The CW-EPR analysis of the **Çm**-labeled hairpins **II$_{HP}$-VI$_{HP}$** alone and in the presence of their corresponding duplexes **II$_{DUPL}$-VI$_{DUPL}$** was performed (**Figure 43B**). At 20 °C, the spectra of all hairpins except **VI$_{HP}$** appeared very similar and showed little or no broadening. In contrast, the hairpin containing a five-nucleotide overhang, **VI$_{HP}$**, showed noticeable broadening even in the absence of duplex, indicating intermolecular association. At -10 °C,

all hairpins showed significant spectral broadening. This is consistent with increased anisotropy and, therefore, supports intermolecular interaction between the hairpins.

When the hairpins were mixed with their corresponding duplexes, the slow-moving features became more pronounced for assemblies **II**-**VI** at -10 °C. For assemblies **IV**-**VI**, with three-five-nucleotide overhangs, clear spectral broadening was also observed already at 20 °C. These data indicate that efficient hairpin-duplex stacking at 20 °C requires at least three complementary overhang nucleotides. PELDOR measurements of the **Çm**-labeled hairpin-duplex assemblies **II**-**VI** were also performed in collaboration with Dr. Burkhard Endeward and Prof. Thomas Prisner at Goethe University, Frankfurt. The PELDOR results were consistent with the CW-EPR data and showed that stacking efficiency increased with the number of overhang nucleotides.

2.4 Summary of paper II

Paper II described a noncovalent spin labeling strategy in which a small RNA hairpin with the rigid spin label **Çm** was synthesized. The blunt-ended **Çm**-labeled hairpin was expected to stack onto RNA duplex ends, but CW-EPR and PELDOR showed that it mainly formed self-stacked hairpin dimers. The strategy was modified by introducing short complementary overhangs on both the hairpins and the duplexes. These overhangs provided an additional base-pairing interaction between the hairpins and the corresponding duplexes that promoted stacking. The CW-EPR and PELDOR experiments showed that stacking efficiency increased with overhang length. Hairpins with short overhangs showed considerable self-association, whereas hairpins containing three or more complementary overhang nucleotides gave efficient hairpin-duplex stacking.

2.5 Conclusion

This study established helical stacking as a noncovalent spin-labeling strategy for RNA. Earlier EPR and PELDOR studies had shown that blunt-ended nucleic acid duplexes can undergo end-to-end stacking. Based on this vision, a small RNA hairpin containing the rigid spin label **Çm** was designed with one-five nucleotide overhangs along with unmodified duplexes with complementary overhangs. CW-EPR and PELDOR studies showed that

overhangs promoted stacking and that the stacking efficiency increased with overhang length.

An important advantage of this strategy is that it avoids the need to chemically incorporate a rigid spin label into each individual target RNA, thereby reducing the synthetic effort and the cost associated with rigid spin labeling. This proof of concept therefore provides a useful route for spin-labeling longer RNAs prepared by in vitro transcription, provided that they contain accessible duplex ends. This strategy could also potentially be extended to other spectroscopic probes, such as fluorophores.

B3 Miscellaneous projects involving nucleic acid labeling

This chapter presents four collaborative research projects centered on incorporation of spectroscopic probes into nucleic acids to study their structure, dynamics, and interactions with proteins. The first project was in collaboration with Prof. Edwin Antony (Saint Louis University School of Medicine, USA), focusing on protein-DNA interactions. In addition, three projects involved collaborations within the Collaborative Research Centre (CRC) 902, a multidisciplinary consortium comprising 19 research groups from Germany and the Sigurdsson group. The aim of CRC902 was to investigate the structural diversity and conformational dynamics of RNA.

3.1 Spin labeling of nucleic acids

As mentioned in detail in **Chapter B1** and **B2**, rigid spin labels, such as **Ç**[265] and **Çm**[256] provide narrow distance distributions in PELDOR experiments, and allow extraction of relative orientational information between spin pairs.[253, 264] In contrast, semi-flexible spin labels are attached via linkers and, therefore, exhibit a greater conformational freedom. As a result, they often produce broader distance distributions in PELDOR measurements.[249] However, such labels are generally synthetically more accessible, for example, through post-synthetic modification, and tend to introduce minimal perturbation to the native nucleic acid structure. The following sub-sections describe the preparation and application of spin-labeled nucleic acids for investigation of protein-nucleic acid interactions using PELDOR.

3.1.1 Spin-labeled DNA to study the DNA-RPA complex

Replication protein A (RPA) is an essential eukaryotic protein that binds to a ssDNA. It is a heterotrimeric protein consisting of three subunits namely, RPA1 (70 kDa), RPA2 (32 kDa) and RPA3 (14 kDa), and it has multiple DNA binding domains (DBD) and protein interaction domains (**Figure 44**).[271] RPA plays a central role in DNA metabolic processes, like replication, recombination, and repair.[272] Therefore, understanding the precise configuration of ssDNA when bound to RPA is of interest. Two key parameters govern RPA-ssDNA interactions. First, the length of the ssDNA substrate determines how many RPA

molecules can assemble along the DNA, with each RPA heterotrimer occupying approximately 18-30 nucleotides.[273] Second, the structural arrangement of the ssDNA when bound to RPA dictates how DNA-processing proteins access the DNA.[274]

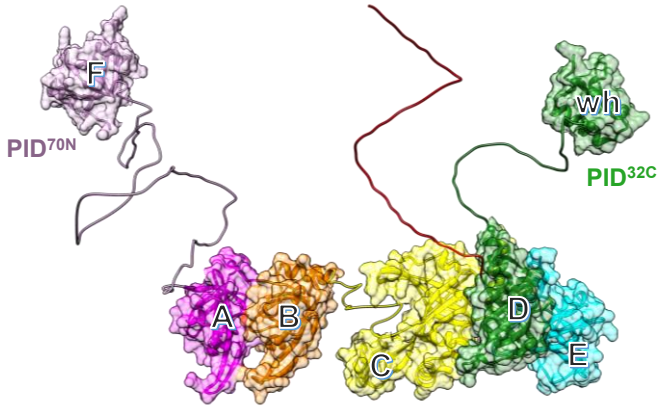

Figure 44. Structural architecture of RPA. A, B, C and D are DNA binding domains. PID70N and PID32C are protein interaction domains.

Two competing models have been proposed to describe the contour of ssDNA in the RPA-ssDNA complex. The classical "linear array" model, which is supported by biochemical and bulk FRET studies, suggests that the DBDs align to stretch the ssDNA into an extended filament.[275] In contrast, more recent structural studies using X-ray and cryo-EM proposed a "wrapping" model, where the DNA curves around the protein surface.[276, 277] However, a clear experimental consensus between these models has not been established. To resolve these structural intricacies, two complementary techniques, namely confocal smFRET and DEER spectroscopy, were employed to measure the end-to-end distance of ssDNA in the absence and presence of RPA. For the DEER experiments, spin-labeled DNA oligonucleotides were synthesized.

Synthesis of the spin-labeled DNA

For the study of the DNA-RPA complex, polyThymidine (polyT) oligonucleotides containing 2′-aminouridine (2′-NH_2U) were labeled with an isothiocyanate derivative of an isoindoline nitroxide. polyT DNA was chosen to avoid intrastrand base-pairing. Two different lengths of spin-labeled polyTs were prepared, 25-mers and 50-mers. The 25-mer, was long enough to bind the primary binding domains of a single RPA molecule. The 50-mer exceeded the 30 nt limit of one RPA molecule, allowing for the investigation of the full complex and its rearrangement after phosphorylation. For each length, three labeled

constructs were synthesized: singly labeled at the 3′-end, singly labeled at the 5′-end, and doubly labeled at both terminals.

The synthesis began with the preparation of 2′-NH_2U-modified 25-mers and 50-mers using automated solid phase oligonucleotide synthesis. The 2′-NH_2U was incorporated at positions shown in **Figure 45** by hand-coupling. The coupling with the 2′-NH_2U modified phosphoramidite was incomplete, yielding only ~50% of 2′-NH_2U modified oligonucleotide. For modifications at the 5′-end, the failure band (n-1) had a very similar electrophoretic mobility to that of the full-length product. This arises because the difference between the 2′-NH_2U modified (full-length) oligonucleotide and the sequence where no coupling occurred (failure band) is only a single nucleotide, resulting in a minimal change in charge and molecular weight. Consequently, the two oligonucleotide bands co-migrate on denaturing polyacrylamide gel electrophoresis (PAGE), making their separation difficult. In contrast, for 3′-end modifications, length difference between the desired and failure sequences resulted in large electrophoretic mobility difference, allowing efficient purification. The 25-mers, however, both with 3′- and 5′-end modifications, were synthesized and purified without difficulty, since the shorter sequence lengths allowed for a better resolution of full-length and failure band.

5' TTT TTT TTT TTT TTT TTT TTT TTU T 3'

5' UTT TTT TTT TTT TTT TTT TTT TTT T 3'

5' UTT TTT TTT TTT TTT TTT TTT TTU T 3'

5' TTT TTT TTT TTT TTT TTT TTT TTT TTT TTT TTT TTT TTT TTT TTT TTT UT 3'

5' UTT TTT TTT TTT TTT TTT TTT TTT TTT TTT TTT TTT TTT TTT TTT TTT TT 3'

5' UTT TTT TTT TTT TTT TTT TTT TTT TTT TTT TTT TTT TTT TTT TTT TTT UT 3'

Figure 45. 2′-NH_2-U modified 50-mer and 25-mer sequences.

To achieve a better resolution between modified and failure sequences for the 50-mers, the position of the modification was optimized by synthesizing shorter unlabeled polyT sequences (46-49 nt) and comparing their electrophoretic mobility with the 50-mer (**Figure 46**). The 47-mer showed a good separation from the 50-mer, therefore, the 4th position from the 5′-end was chosen for modification.

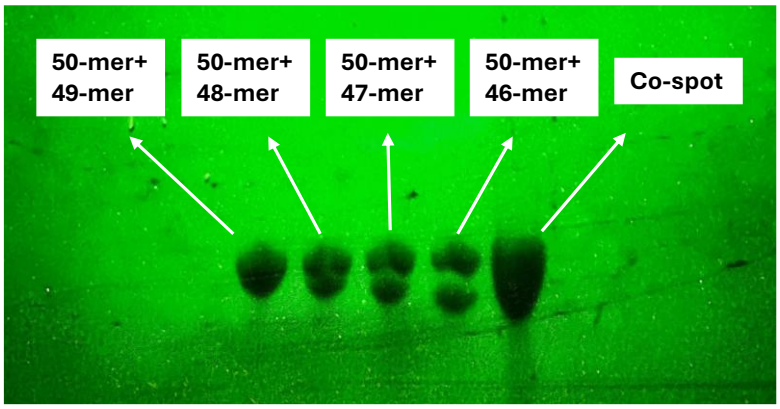

Figure 46. Analytical denaturing PAGE of the polyT 50-mer co-run with the unlabeled 46-49-mer polyTs.

Following successful synthesis and purification of the 2′ NH_2-U modified oligonucleotides, post-synthetic spin-labeling with an isothiocyanate derivative of an isoindoline nitroxide was performed, affording six spin-labeled polyTs (**Figure 47**). The distance between the two spin centers was measured using DEER spectroscopy in the absence and presence of RPA in collaboration with Dr. Reza Dastvan and Prof. Edwin Antony (Saint Louis University School of Medicine, USA). The results obtained from DEER measurements were in agreement with the complementary smFRET experiments performed using fluorophore-labeled oligonucleotides.

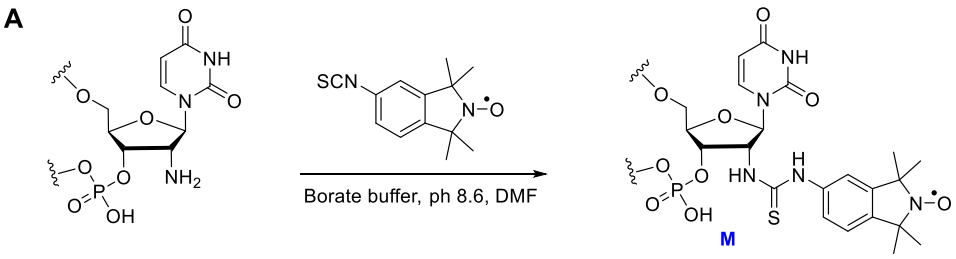

B

5' TTT TTT TTT TTT TTT TTT TTT TTM T 3'

5' MTT TTT TTT TTT TTT TTT TTT TTT T 3'

5' MTT TTT TTT TTT TTT TTT TTT TTM T 3'

5' TTT TTT TTT TTT TTT TTT TTT TTT TTT TTT TTT TTT TTT TTT TTT TTT TTT MT 3'

5' TTT MTT TTT TTT TTT TTT TTT TTT TTT TTT TTT TTT TTT TTT TTT TTT TTT TT 3'

5' TTT MTT TTT TTT TTT TTT TTT TTT TTT TTT TTT TTT TTT TTT TTT TTT TTT MT 3'

Figure 47. **A**. Post-synthetic reaction of the isothiocyanate derivative of an isoindoline nitroxide with the 2′ -NH_2-U modified RNA oligonucleotide to give a spin-labeled oligonucleotide **M**. **B**. 50-mer and 25-mer polyT spin-labeled sequences.

3.1.2 Summary of Paper III

This paper resolves the conformation of ssDNA when bound to the RPA protein, a question that has remained unresolved due to conflicting models proposing either an extended or wrapped DNA arrangement. Two complementary distance measurement techniques were employed, namely smFRET and DEER. For smFRET, fluorophore-labeled oligonucleotides were used, while for DEER experiments, singly and doubly spin-labeled poly-T oligonucleotides, namely $(dT)_{22}$ and $(dT)_{50}$ constructs, were prepared. The results obtained using both experiments were in strong agreement with each other. In the absence of RPA, ssDNA exhibited a broad distribution of distances, consistent with a flexible and dynamic DNA in solution. Upon RPA binding, only a modest increase (~3 nm) in the end-to-end distance was observed. This relatively small change was inconsistent with a linear model and instead supported a partially wrapped conformation, in which ssDNA adopts a curved trajectory along the surface of RPA.

3.1.3 Spin-labeled RNA for the study of Roquin-RNA complex

PELDOR studies are usually performed at cryogenic temperatures, where molecular motion is suppressed, resulting in longer electron relaxation time (T_2) and enabling accurate determination of spin-spin distances. At room temperature, however, rapid molecular tumbling leads to shorter T_2 and loss of dipolar interactions through rotational averaging. However, for studying biomolecules under near-physiological conditions, room-temperature PELDOR is desirable. Some strategies have been applied to enable room-temperature PELDOR, including immobilization of samples using charged surfaces[278-280] or embedding them in viscous matrices such as trehalose.[281, 282] However, such approaches may introduce artificial constraints on molecular motion.

In this work, an alternative strategy to perform room temperature PELDOR was explored, where molecular tumbling could be reduced by forming a complex between an RNA and a larger protein. An example of a heavy protein is Roquin-1 (51 kDa), which is an RNA binding protein that aids in immune homeostasis maintenance.[283] Its interactions with RNA have been extensively studied by X-ray crystallography and NMR spectroscopy[284, 285] and its RNA targets have been identified. One of the efficient binding targets is Ox40 (**Figure 48A**), which is a hexa-loop containing hairpin. Based on Ox40, two RNA hairpin constructs

were proposed based on SELEX by our collaborator Dr. Julia Weigand (TU Darmstadt, Germany) **(Figure 48A)**. Based on the constructs, four **Çm**-labeled hairpin RNA constructs were designed using molecular modeling (**Figure 48B**). The four **Çm**-labeled hairpin RNAs were synthesized by the phosphoramidite approach. However, the binding affinity studies performed by Dr. Jan-Niklas Tant (Goethe University Frankfurt) showed very poor affinity of these **Çm**-labeled RNAs with Roquin-1, perhaps due to steric perturbations introduced by the rigid **Çm** label in the loop.

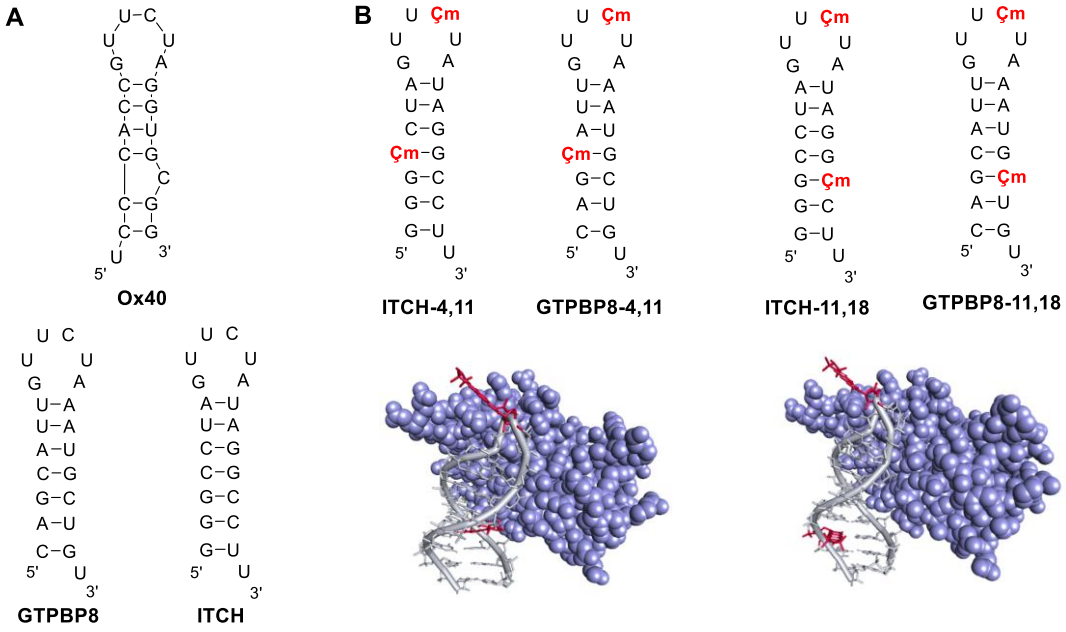

Figure 48. **A**. Sequences of SELEX-derived Roquin-1 binding RNA stem-loop Ox40 and the proposed RNA hairpin constructs. **B**. Sequences of the **Çm**-labeled RNA hairpin constructs and the corresponding molecular models of the **Çm**-labeled hairpins bound to Roquin-1.

To address this issue of poor affinity, the labeling strategy was modified by replacing the rigid **Çm** label in the loop with a smaller, more flexible nitroxide spin label (**M**) (**Figure 49**). Singly **M**-labeled RNA hairpins were prepared by incorporating 2′-NH_2U at positions U10, U11, and U12, followed by post-synthetic spin labeling with **M** (**Figure 47A**). **Çm** was also incorporated into the stem region to assess whether labeling outside the loop interferes with protein binding (**Figure 49**). Binding affinity studies revealed that the **Çm** in the stem did not interfere with binding. Among the **M**-labeled hairpins, hairpin with **M** at position 12 showed the highest binding affinity. However, the binding affinity was still insufficient to ensure stable RNA-Roquin-1 complex formation for reliable room-temperature PELDOR study. Given these limitations, further investigation of this project was not pursued.

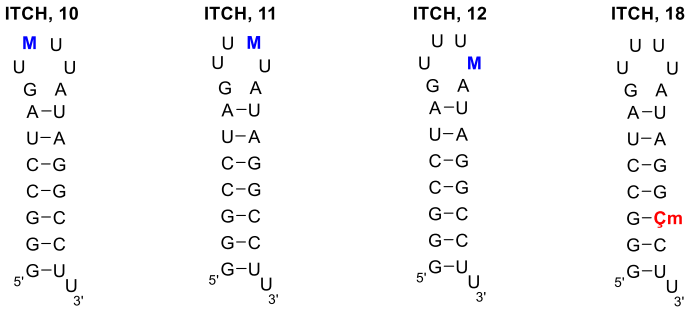

Figure 49. RNA hairpins labeled with **M** and **Çm**.

3.2 Fluorescent labeling of nucleic acids

Fluorescence spectroscopy is a highly sensitive technique for investigating the structure and dynamics of nucleic acids, providing information on local environment, conformational changes, and intermolecular interactions. To enable such studies, nucleic acids require site-specific incorporation of fluorescent probes, just like SDSL. Site-specific labeling with fluorescent probes can be achieved through various labeling strategies, such as post-transcriptional modification, enzymatic incorporation, post-synthetic labeling, and solid-phase synthesis using the phosphoramidite approach.[199, 286] Incorporation of fluorophores by the phosphoramidite approach requires fluorescent base analogues that base-pair with natural nucleobases and do not perturb the overall structure of the nucleic acid.[287] A few examples of such fluorescent base analogues are discussed below.

The adenine analogue 2-aminopurine (**2-AP**)[288] is one of the most used commercially available fluorescent base analogue (**Figure 50**). It base pairs with T and U, and to a lesser extent with C. It is highly fluorescent and is very sensitive to its micro-environment.[289] However, its emission is significantly quenched (~100 times) upon incorporation into nucleic acids due to base stacking interactions. In contrast, tricyclic cytidine analogues such as **tC**[290] and its oxo-derivative **tC^{O}**[291] exhibit higher brightness and are insensitive to their local environment, making them suitable for FRET experiments (**Figure 50**). In addition, cytidine-based analogues such as **Çf**/**Çmf**, that are intermediates in the synthesis of **Ç**/**Çm** spin labels,[256, 265] have been shown to be highly sensitive to their microenvironment[292] and are valuable probes for studying nucleic acid dynamics (**Figure 50**).[293, 294]

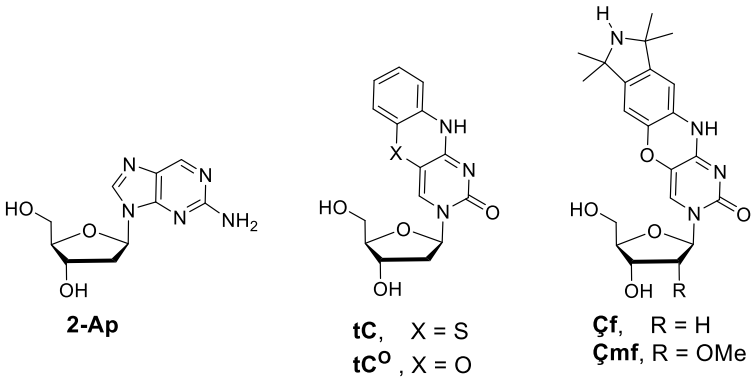

Figure 50. Examples of fluorescent nucleobase analogues.

3.2.1 Fluorescent labeling of the neomycin aptamer

FRET is a widely used technique for probing the structure and dynamics of biomolecules, as it reports on both the distance and the relative orientation between two fluorescent labels. However, a fundamental challenge in conventional FRET is the uncertainty in the orientation factor κ^2, which describes the relative alignment of the donor and acceptor dipoles.[295, 296] κ^2 is difficult to determine experimentally and is usually assumed to be 2/3, a value valid only in the dynamic isotropic limit where both labels tumble freely. One way to overcome this limitation is to use rigid fluorescent nucleobase analogues that are directly incorporated into the nucleic acid scaffold and adopt fixed orientations. Because their orientation relative to the nucleic acid is known, κ^2 can be estimated rather than assumed, enabling more accurate structural interpretation.

Çmf and **tCnitro** are two such rigid nucleobase analogues (**Figure 51**) that were previously validated as a FRET pair, where **Çmf** acts as a donor, while **tCnitro** as a acceptor/quencher.[297] Usually in FRET, the energy absorbed by the donor is transferred to the acceptor, which then emits at a red-shifted wavelength, allowing both donor quenching and acceptor emission to be monitored simultaneously. In the present study, however, **tCnitro** functions not as a conventional fluorescent acceptor but as quencher, meaning that energy transferred from the **Çmf** donor is dissipated non-radiatively rather than re-emitted. As a consequence, the observable fluorescence signal originates exclusively from **Çmf**, and FRET efficiency is reported solely through the quenching of donor emission. A detailed characterization of their energy transfer behavior was performed within a structured RNA system. The neomycin-binding RNA aptamer (N1) was chosen as a model system due to its

well-characterized structure and dynamics, as well as its function as an active riboswitch.[294, 298, 299]

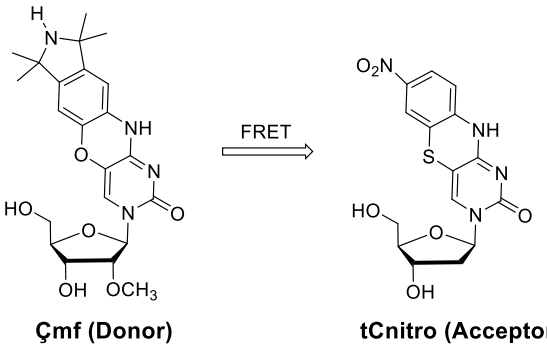

Figure 51. Structures of **Çmf** (FRET donor) and tCnitro (FRET acceptor).

Three doubly labeled variants of the aptamer were synthesized, in which **Çmf** and **tCnitro** were incorporated site-specifically by solid-phase oligonucleotide synthesis to systematically vary the donor-acceptor separation (**Figure 52**). These constructs enabled the investigation of distance-dependent energy transfer within a structured RNA framework. Fluorescence measurements were carried out by Florian Hurter in the group of Prof. Josef Wachtveitl (Goethe University Frankfurt), employing a combination of steady-state and time-resolved fluorescence spectroscopy techniques to characterize the FRET efficiency of the labeled aptamers.

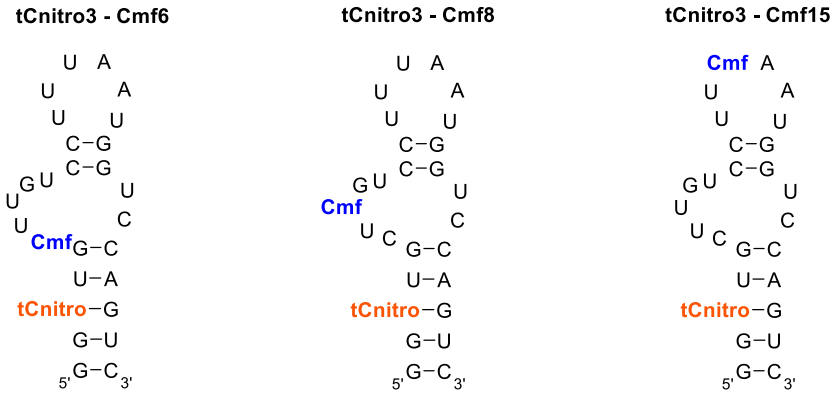

Figure 52. The neomycin aptamer labeled with both **Çmf** (blue) and **tCnitro** (orange) for hetero-FRET measurements.

3.2.2 Summary of Paper IV

This paper explored the use of the rigid nucleobase analogues **Çmf** (donor) and **tCnitro** (quencher) as a FRET pair within the neomycin-sensing RNA aptamer N1, with the aim of

characterizing energy transfer behavior and demonstrating the potential of rigid labels for obtaining precise structural and orientational information in RNA. Three sequences of the neomycin aptamer with the **Çmf** and **tCnitro** were synthesized with increasing donor-acceptor separation. The FRET processes of these labeled neomycin aptamers were characterized using a combination of steady-state fluorescence, time-resolved fluorescence, and ultrafast transient absorption spectroscopy. The FRET efficiencies obtained from all three techniques were in good agreement, with values consistent within approximately 10%, demonstrating the reliability of the measurements. Notably, the transient absorption spectroscopy provided access to ultrafast energy transfer processes that are not detectable using conventional fluorescence methods.

Spectroscopic analysis using static fluorescence, and ultrafast transient absorption spectroscopy revealed a clear distance dependence of the FRET efficiency across the three constructs, with near-complete quenching at the shortest donor-acceptor distance and progressive signal recovery at greater separations. Notably, the energy transfer was found to originate from multiple emitting states of **Çmf** and to span a remarkably wide dynamic range, from the low picosecond to the nanosecond timescale, which required the combined application of several complementary methods for full characterization. The **Çmf-tCnitro** pair proved to be an efficient FRET pair, though as with any FRET experiment, the measured efficiency alone cannot unambiguously report on both distance and orientation simultaneously. By using the known NMR structure of the ligand-bound aptamer as a structural reference, inter-label distances could be approximated and used to estimate κ^2, allowing qualitative conclusions to be drawn about how the relative orientation of the two labels changes upon neomycin binding. This analysis made clear that the commonly used assumption of $\kappa^2 = 2/3$ is not appropriate when rigid labels are used, and that rigidity is in fact an asset rather than a complication, as it enables orientational information to be extracted that would be inaccessible with flexible dyes. The study also pointed to directions for future improvement, noting that a fluorescent acceptor spectrally separated from **Çmf** would open additional avenues for determining label orientations, and that the transient absorption approach used here could be extended to other rigid FRET pairs with more suitable photophysical properties.

3.2.3 2-aminopurine labelled caffeine aptamer

Recently, a caffeine binding aptamer was discovered by Prof. Beatrix Suess (TU Darmstadt, Germany) using RNA Capture-SELEX[300] (**Figure 53**). To investigate the structural dynamics of this aptamer by fluorescence spectroscopy, fluorescent nucleobase analogue **2-AP** was used as a probe (**Figure 53**).

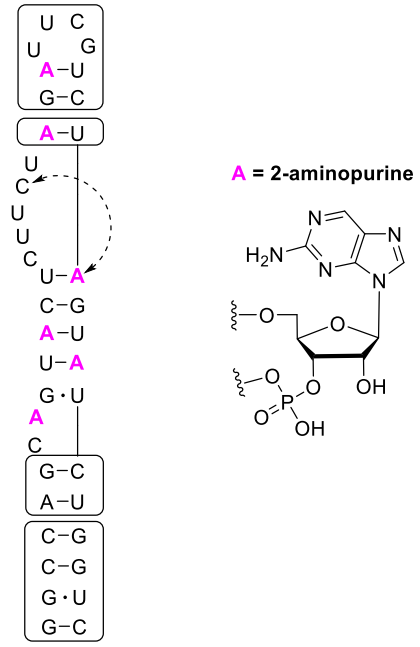

Figure 53. Sequence of the caffeine aptamer with proposed **2-AP** labeling positions.

A series of six caffeine binding aptamers was synthesized, each containing a single **2-AP** at a distinct position within the aptamer sequence (**Figure 53**). The **2-AP** was incorporated in the aptamer by the phosphoramidite approach during automated solid-phase oligonucleotide synthesis. This site-specific fluorescent labeling would enable monitoring of local structural environments and conformational changes through variations in **2-AP** fluorescence. These samples are awaiting fluorescence measurements in the laboratory of Prof. Wachtveitl.

3.3 Conclusion

This chapter described a series of collaborative projects involving labeling of nucleic acids with spectroscopic probes to investigate their structure and interactions. The first part of this chapter involved incorporation of nitroxide spin labels to DNA and RNA for EPR studies. Post-synthetically spin-labeled poly-thymidine DNA constructs were prepared and used to investigate the configuration of ssDNA in the RPA-DNA complex using DEER

spectroscopy. The results were in agreement with complementary smFRET measurements, supporting a partially wrapped configuration of ssDNA with RPA. In addition, **Çm**-labeled and post-synthetically spin-labeled RNA hairpins targeting the Roquin-1 protein were synthesized for room temperature PELDOR studies. However, these spin-labeled hairpins exhibited poor binding affinity with Roquin-1, limiting further structural investigations of this system.

The second part of the chapter focused on the incorporation of fluorescent labels into RNA aptamers. The rigid nucleobase analogues **Çmf** and **tCnitro** were incorporated into the neomycin aptamer and evaluated as a FRET pair, demonstrating their suitability for probing RNA structure with high precision. Furthermore, the widely used fluorescent base analogue **2-AP** was incorporated into a newly identified caffeine-binding aptamer to enable fluorescence-based studies of its structure and dynamics.

B4 Conclusions for Part B

This part of the thesis focused on labeling of nucleic acids for EPR and fluorescence studies. **Chapter B2** emphasizes a simple and efficient noncovalent spin labeling strategy for investigating structure and dynamics of RNA by EPR spectroscopy (Paper II). A small **Çm**-labeled RNA hairpin was first designed as an adaptor for spin labeling various RNA systems through helical stacking. This blunt-ended hairpin mainly formed self-stacked dimers rather than the desired hairpin-duplex assembly. This led to a modified strategy in which complementary overhangs were introduced on both the **Çm**-labeled hairpin and the duplex. CW-EPR and PELDOR (by Dr. Burkhard Endeward at the Goethe University, Frankfurt) studies showed that these overhangs promoted stacking and that stacking efficiency increased with the length of the overhang, with three or more complementary nucleotides giving the most efficient hairpin-duplex assembly. A major advantage of this approach is that it avoids the need to covalently introduce a rigid spin label into each target RNA, thereby reducing the synthetic effort associated with rigid spin labeling. This method could be used for labeling longer RNAs, particularly those prepared by in vitro transcription, provided that suitable duplex ends are accessible. Moreover, this method could be extended to various other spectroscopic probes, such as other rigid spin labels and fluorophores.

Chapter B3 focused on broader collaborative nucleic acid chemistry work involving site-specific spin- and fluorescence-labeling. 2′ NH_2-U modified polyT DNAs, spin-labeled with the isothiocyanate derivative of an isoindoline nitroxide (**M**), were prepared for PELDOR studies of the RPA-ssDNA complex in collaboration with Dr. Reza Dastvan and Prof. Edwin Antony, Saint Louis University School of Medicine, USA. The PELDOR results, together with complementary smFRET data, support the hypothesis of a partially wrapped arrangement of ssDNA on RPA (Paper III). In another project, RNA hairpins labeled with the rigid spin label **Çm** and the semi-rigid nitroxide spin label **M** were prepared for studies of the Roquin-1–RNA complex, although poor binding affinity of the RNA with Roquin-1 precluded the use of these spin-labeled oligonucleotides for PELDOR. In the fluorescence-based studies, in collaboration with Josef Wachtveitl, Goethe University, Frankfurt, the rigid nucleobase analogues **Çmf** and **tCnitro** were incorporated into the neomycin aptamer N1 and were shown to be an efficient FRET pair for probing the neomycin aptamer (Paper IV). In addition, 2-aminopurine-labeled caffeine aptamers were prepared for future fluorescence

studies of the aptamer structure and dynamics. Overall, this part of the thesis introduces a noncovalent spin labeling technique for RNAs. and shows how both rigid and semi-rigid probes can be used to study nucleic acid conformation and biomolecular interactions.

References

1. Llamas-Saiz, A. L.; van Raaij, M. J. X-Ray crystallography of biological macromolecules: Fundamentals and applications. In *Proteins in solution and at interfaces*, 2013; pp 1-22.
2. Smyth, M. S.; Martin, J. H. J. xRay crystallography. *Mol. Pathol.* **2000**, *53* (1), 8.
3. Chayen, N. E.; Saridakis, E. Protein crystallization: from purified protein to diffraction-quality crystal. *Nat. Methods* **2008**, *5* (2), 147-153.
4. Mooers, B. H. M. Crystallographic studies of DNA and RNA. *Methods* **2009**, *47* (3), 168-176.
5. Nelson, J. A.; Uhlenbeck, O. C. When to believe what you see. *Mol. Cell.* **2006**, *23* (4), 447-450.
6. Li, Y.; Huang, W.; Li, Y.; Chiu, W.; Cui, Y. Opportunities for cryogenic electron microscopy in materials science and nanoscience. *ACS Nano* **2020**, *14* (8), 9263-9276.
7. Milne, J. L. S.; Borgnia, M. J.; Bartesaghi, A.; Tran, E. E. H.; Earl, L. A.; Schauder, D. M.; Lengyel, J.; Pierson, J.; Patwardhan, A.; Subramaniam, S. Cryo-electron microscopy - a primer for the non-microscopist. *FEBS J.* **2013**, *280* (1), 28-45.
8. Xu, B. J.; Liu, L. Developments, applications, and prospects of cryo-electron microscopy. *Protein Sci.* **2020**, *29* (4), 872-882.
9. Bai, X. C. Seeing atoms by single-particle cryo-EM. *Trends Biochem. Sci.* **2021**, *46* (4), 253-254.
10. Nakane, T.; Kotecha, A.; Sente, A.; McMullan, G.; Masiulis, S.; Brown, P. M. G. E.; Grigoras, I. T.; Malinauskaite, L.; Malinauskas, T.; Miehling, J.; et al. Single-particle cryo-EM at atomic resolution. *Nature* **2020**, *587* (7832), 152.
11. Yip, K. M.; Fischer, N.; Paknia, E.; Chari, A.; Stark, H. Atomic-resolution protein structure determination by cryo-EM. *Nature* **2020**, *587* (7832), 157.
12. Hamitouche, I.; Jonic, S. DeepHEMNMA: ResNet-based hybrid analysis of continuous conformational heterogeneity in cryo-EM single particle images. *Front. Mol. Biosci.* **2022**, *9*.
13. Shrestha, D.; Jenei, A.; Nagy, P.; Vereb, G.; Szöllosi, J. Understanding FRET as a research tool for cellular studies. *Int. J. Mol. Sci.* **2015**, *16* (4), 6718-6756.
14. Sahoo, H. Förster resonance energy transfer – A spectroscopic nanoruler: Principle and applications. *J. Photochem. Photobiol. C: Photochem. Rev.* **2011**, *12* (1), 20-30.
15. Roy, R.; Hohng, S.; Ha, T. A practical guide to single-molecule FRET. *Nat. Methods* **2008**, *5* (6), 507-516.
16. Yang, Z.; Feng, L. *Electron paramagnetic resonance spectroscopy*; American Chemical Society, 2023. DOI: 10.1021/acsinfocus.7e7031.

17. Jeschke, G. The contribution of modern EPR to structural biology. *Emerg. Top. Life Sci.* **2018**, *2* (1), 9-18.

18. Hofmann, L.; Ruthstein, S. EPR spectroscopy provides new insights into complex biological reaction mechanisms. *J. Phys. Chem. B* **2022**, *126* (39), 7486-7494.

19. Webber, J. B. W. A review of the use of simple time-domain NMR/MRI for material-science. *SN Appl. Sci.* **2021**, *3* (10), 809.

20. Aboalroub, A. A. Advances in NMR Spectroscopy for biological systems: Principles, techniques, and their growing scope. *Biotechnol. Adv.* **2026**, *88*, 108809.

21. Bakhmutov, V. I. Strategies for solid-state NMR studies of materials: From diamagnetic to paramagnetic porous solids. *Chem. Rev.* **2011**, *111* (2), 530-562.

22. Rinaldi, P. L. Three-dimensional solution NMR spectroscopy of complex structures and mixtures. *Analyst* **2004**, *129* (8), 687-699.

23. Zhang, F.; Adnani, N.; Vazquez-Rivera, E.; Braun, D. R.; Tonelli, M.; Andes, D. R.; Bugni, T. S. Application of 3D NMR for structure determination of peptide natural products. *J. Org. Chem.* **2015**, *80* (17), 8713-8719.

24. Palmer, A. G., III. NMR characterization of the dynamics of biomacromolecules. *Chem. Rev.* **2004**, *104* (8), 3623-3640.

25. Tycko, R. Biomolecular solid state NMR: Advances in structural methodology and applications to peptide and protein fibrils. *Annu. Rev. Phys. Chem.* **2001**, *52*, 575-606.

26. Reif, B.; Ashbrook, S. E.; Emsley, L.; Hong, M. Solid-state NMR spectroscopy. *Nat. Rev. Methods. Primers* **2021**, *1* (1), 2.

27. Gullion, T.; Schaefer, J. Rotational-echo double-resonance NMR. *J. Magn. Reson.* **1989**, *81* (1), 196-200.

28. Jaroniec, C. P.; Filip, C.; Griffin, R. G. 3D TEDOR NMR experiments for the simultaneous measurement of multiple carbon−nitrogen distances in uniformly 13C,15N-labeled solids. *J. Am. Chem. Soc.* **2002**, *124* (36), 10728-10742.

29. Haeberlen, U. III - Manifestations of nuclear magnetic shielding in NMR spectra of solids. In *High Resolution Nmr in Solids Selective Averaging*, Haeberlen, U. Ed.; Academic Press, 1976; pp 17-35.

30. Mehring, M. *Principles of high resolution NMR in solids*; Springer Berlin, Heidelberg, 1983.

31. Andrew, E. R.; Bradbury, A.; Eades, R. G. Nuclear magnetic resonance spectra from a crystal rotated at high speed. *Nature* **1958**, *182* (4650), 1659-1659.

32. Lowe, I. J. Free induction decays of rotating solids. *Phys. Rev. Lett.* **1959**, *2* (7), 285-287.

33. Tycko, R. Solid-state NMR studies of amyloid fibril structure. *Annu. Rev. Phys. Chem.* **2011**, *62* (62), 279-299.

34. van der Wel, P. C. A. New applications of solid-state NMR in structural biology. *Emerg. Top. Life Sci.* **2018**, *2* (1), 57-67.

35. Mandala, V. S.; Williams, J. K.; Hong, M. Structure and dynamics of membrane proteins from solid-state NMR. *Annu. Rev. Biophys.* **2018**, *47*, 201-222.

36. Yadav, R.; Patra, B.; Rai, R.; Sinha, N.; Singh, C. Solid-state NMR spectroscopy for unraveling structure and dynamics in biomaterials. *Solid State Nucl. Magn. Reson.* **2025**, *140*, 102045.

37. Zhang, W.; Xu, S.; Han, X.; Bao, X. In situ solid-state NMR for heterogeneous catalysis: a joint experimental and theoretical approach. *Chem. Soc. Rev.* **2012**, *41* (1), 192-210.

38. Thankamony, A. S. L.; Wittmann, J. J.; Kaushik, M.; Corzilius, B. Dynamic nuclear polarization for sensitivity enhancement in modern solid-state NMR. *Prog. Nucl. Magn. Reson. Spectrosc.* **2017**, *102-103*, 120-195.

39. Li, Q.; Xiang, J. Applications of high-field nuclear magnetic resonance (NMR) in chemical research. *J. Magn. Reson. Open* **2025**, *23*, 100199.

40. Hashi, K.; Ohki, S.; Matsumoto, S.; Nishijima, G.; Goto, A.; Deguchi, K.; Yamada, K.; Noguchi, T.; Sakai, S.; Takahashi, M.; et al. Achievement of 1020MHz NMR. *J. Magn. Reson.* **2015**, *256*, 30-33.

41. Kovacs, H.; Moskau, D.; Spraul, M. Cryogenically cooled probes—a leap in NMR technology. *Prog. Nucl. Magn. Reson. Spectrosc.* **2005**, *46* (2), 131-155.

42. Tycko, R. NMR at low and ultralow temperatures. *Acc. Chem. Res.* **2013**, *46* (9), 1923-1932.

43. Weng, G.; Slotboom, J. When more is less: Higher magnetic fields and their limited impact on signal-to-noise ratio per unit of acquisition time in unlocalized and single-voxel magnetic resonance spectroscopy. *Phys. Rev. Appl.* **2025**, *24* (5), 054066.

44. Eills, J.; Budker, D.; Cavagnero, S.; Chekmenev, E. Y.; Elliott, S. J.; Jannin, S.; Lesage, A.; Matysik, J.; Meersmann, T.; Prisner, T.; et al. Spin hyperpolarization in modern magnetic resonance. *Chem. Rev.* **2023**, *123* (4), 1417-1551.

45. Buntkowsky, G.; Theiss, F.; Lins, J.; Miloslavina, Y. A.; Wienands, L.; Kiryutin, A.; Yurkovskaya, A. Recent advances in the application of parahydrogen in catalysis and biochemistry. *RSC Adv.* **2022**, *12* (20), 12477-12506.

46. Reineri, F.; Cerutti, E. Chapter 3 - The chemistry of parahydrogen induced polarization. In *Advances in Magnetic Resonance Technology and Applications*, Suh, E. H., Kovacs, Z. Eds.; Vol. 12; Academic Press, 2024; pp 175-198.

47. Bowers, C. R.; Weitekamp, D. P. Parahydrogen and synthesis allow dramatically enhanced nuclear alignment. *J. Am. Chem. Soc.* **1987**, *109* (18), 5541-5542.

48. Barskiy, D. A.; Knecht, S.; Yurkovskaya, A. V.; Ivanov, K. L. SABRE: Chemical kinetics and spin dynamics of the formation of hyperpolarization. *Prog. Nucl. Magn. Reson. Spectrosc.* **2019**, *114-115*, 33-70.

49. Adams, R. W.; Aguilar, J. A.; Atkinson, K. D.; Cowley, M. J.; Elliott, P. I. P.; Duckett, S. B.; Green, G. G. R.; Khazal, I. G.; López-Serrano, J.; Williamson, D. C. Reversible interactions with para-hydrogen enhance NMR sensitivity by polarization transfer. *Science* **2009**, *323* (5922), 1708-1711.

50. Duckett, S. B.; Mewis, R. E. Application of hydrogen induced polarization techniques in NMR spectroscopy and imaging. *Acc. Chem. Res.* **2012**, *45* (8), 1247-1257.

51. Goez, M. Photo-CIDNP spectroscopy. *Annu. Rep. NMR Spectrosc.* **2009**, *66*, 77-147.

52. Okuno, Y.; Cavagnero, S. Photochemically induced dynamic nuclear polarization: Basic principles and applications. *eMagRes* **2017**, *6* (2), 283-314.

53. Kuhn, L. T. Photo-CIDNP NMR spectroscopy of amino acids and proteins. In *Hyperpolarization Methods in Nmr Spectroscopy*, Kuhn, L. T. Ed.; Vol. 338; 2013; pp 229-300.

54. Consonni, R.; Limiroli, R.; Molinari, H.; Fusi, P.; Grisa, M.; Vanoni, M.; Tortora, P. H-1-Nmr and photo-Cidnp spectroscopies show a possible role for Trp(23) and Phe(31) in nucleic-acid binding by P2 ribonuclease from the Archaeon sulfolobus-solfataricus. *FEBS Lett.* **1995**, *372* (2-3), 135-139.

55. Shapla, U. M.; Smith, J. L.; Halder, A.; Thompson, L.; Buller, A. R.; Cavagnero, S. Highly sensitive detection of tyrosine and neurotransmitters by stereoselective biosynthesis and photochemically Induced dynamic nuclear polarization. *J. Am. Chem. Soc.* **2025**, *147* (46), 42361-42374.

56. Mok, K. H.; Hore, P. J. Photo-CIDNP NMR methods for studying protein folding. *Methods* **2004**, *34* (1), 75-87.

57. Goez, M. Elucidating organic reaction mechanisms ssing photo-CIDNP spectroscopy. In *Hyperpolarization methods in NMR spectroscopy*, Kuhn, L. T. Ed.; Springer Berlin Heidelberg, 2013; pp 1-32.

58. Morozova, O. B.; Ivanov, K. L. Time-resolved chemically induced dynamic nuclear polarization of biologically important molecules. *ChemPhysChem* **2019**, *20* (2), 197-215.

59. Walker, T. G.; Happer, W. Spin-exchange optical pumping of noble-gas nuclei. *Rev. Mod. Phys.* **1997**, *69* (2), 629-642.

60. Fain, S. B.; Korosec, F. R.; Holmes, J. H.; O'Halloran, R.; Sorkness, R. L.; Grist, T. M. Functional lung imaging using hyperpolarized gas MRI. *J. Magn. Reson. Imaging* **2007**, *25* (5), 910-923.

61. Ludlow, A. D.; Boyd, M. M.; Ye, J.; Peik, E.; Schmidt, P. O. Optical atomic clocks. *Rev. Mod. Phys.* **2015**, *87* (2), 637-701.

62. Budker, D.; Romalis, M. Optical magnetometry. *Nat. Phys.* **2007**, *3* (4), 227-234.

63. Hayes, S. E.; Mui, S.; Ramaswamy, K. Optically pumped nuclear magnetic resonance of semiconductors. *J. Chem. Phys.* **2008**, *128* (5), 052203.

64. Goodson, B. M. Nuclear magnetic resonance of laser-polarized noble gases in molecules, materials, and organisms. *J. Magn. Reson.* **2002**, *155* (2), 157-216.

65. Moroz, I. B.; Leskes, M. Dynamic nuclear polarization solid-state NMR spectroscopy for materials research. *Annu. Rev. Mater. Res.* **2022**, *52*, 25-55.

66. Kobayashi, T.; Perras, F. A.; Slowing, I. I.; Sadow, A. D.; Pruski, M. Dynamic nuclear polarization solid-state NMR in heterogeneous catalysis research. *ACS Catal.* **2015**, *5* (12), 7055-7062.

67. Stern, Q.; Verhaeghe, G.; El Daraï, T.; Montarnal, D.; Le, N. H.; Veyre, L.; Thieuleux, C.; Bocquelet, C.; Cala, O.; Jannin, S. Dynamic nuclear polarization with conductive polymers. *Angew. Chem. Int. Ed.* **2024**, *63* (49), e202409510.

68. Biedenbänder, T.; Aladin, V.; Saeidpour, S.; Corzilius, B. Dynamic nuclear polarization for sensitivity enhancement in biomolecular solid-state NMR. *Chem. Rev.* **2022**, *122* (10), 9738-9794.

69. Overhauser, A. W. Polarization of nuclei in metals. *Phys. Rev.* **1953**, *92* (2), 411-415.

70. Corzilius, B. Dynamic Nuclear Polarization. In *Paramagnetism in Experimental Biomolecular NMR*, Luchinat, C., Parigi, G., Ravera, E. Eds.; The Royal Society of Chemistry, 2018; p 0.

71. Abragam, A.; Goldman, M. Principles of dynamic nuclear polarisation. *Rep. Prog. Phys.* **1978**, *41* (3), 395.

72. Mentink-Vigier, F.; Paul, S.; Lee, D.; Feintuch, A.; Hediger, S.; Vega, S.; De Paëpe, G. Nuclear depolarization and absolute sensitivity in magic-angle spinning cross effect dynamic nuclear polarization. *Phys. Chem. Chem. Phys.* **2015**, *17* (34), 21824-21836.

73. Rossini, A. J.; Zagdoun, A.; Hegner, F.; Schwarzwälder, M.; Gajan, D.; Copéret, C.; Lesage, A.; Emsley, L. Dynamic nuclear polarization NMR spectroscopy of microcrystalline solids. *J. Am. Chem. Soc.* **2012**, *134* (40), 16899-16908.

74. Mentink-Vigier, F.; Mathies, G.; Liu, Y. P.; Barra, A. L.; Caporini, M. A.; Lee, D.; Hediger, S.; Griffin, R. G.; De Paëpe, G. Efficient cross-effect dynamic nuclear polarization without depolarization in high-resolution MAS NMR. *Chem. Sci.* **2017**, *8* (12), 8150-8163.

75. Halbritter, T.; Harrabi, R.; Paul, S.; van Tol, J.; Lee, D.; Hediger, S.; Sigurdsson, S. T.; Mentink-Vigier, F.; De Paëpe, G. PyrroTriPol: a semi-rigid trityl-nitroxide for high field dynamic nuclear polarization. *Chem. Sci.* **2023**, *14* (14), 3852-3864.

76. Hediger, S.; Lee, D.; Mentink-Vigier, F.; De Paëpe, G. MAS-DNP enhancements: Hyperpolarization, depolarization, and absolute sensitivity. In *eMagRes*, Harris, R. K., Wasylishen, R. L. Eds.; 2018; pp 105-116.

77. Maly, T.; Debelouchina, G. T.; Bajaj, V. S.; Hu, K. N.; Joo, C. G.; Mak-Jurkauskas, M. L.; Sirigiri, J. R.; van der Wel, P. C.; Herzfeld, J.; Temkin, R. J.; et al. Dynamic nuclear polarization at high magnetic fields. *J. Chem. Phys.* **2008**, *128* (5), 052211.

78. Can, T. V.; Caporini, M. A.; Mentink-Vigier, F.; Corzilius, B.; Walish, J. J.; Rosay, M.; Maas, W. E.; Baldus, M.; Vega, S.; Swager, T. M.; et al. Overhauser effects in insulating solids. *J. Chem. Phys.* **2014**, *141* (6), 064202.

79. Mentink-Vigier, F.; Akbey, U.; Hovav, Y.; Vega, S.; Oschkinat, H.; Feintuch, A. Fast passage dynamic nuclear polarization on rotating solids. *J. Magn. Reson.* **2012**, *224*, 13-21.

80. Smith, A. A.; Corzilius, B.; Barnes, A. B.; Maly, T.; Griffin, R. G. Solid effect dynamic nuclear polarization and polarization pathways. *J. Chem. Phys.* **2012**, *136* (1).

81. Mentink-Vigier, F.; Vega, S.; De Paëpe, G. Fast and accurate MAS–DNP simulations of large spin ensembles. *Phys. Chem. Chem. Phys.* **2017**, *19* (5), 3506-3522.

82. Mentink-Vigier, F.; Akbey, Ü.; Oschkinat, H.; Vega, S.; Feintuch, A. Theoretical aspects of magic angle spinning - Dynamic nuclear polarization. *J. Magn. Reson.* **2015**, *258*, 102-120.

83. Thurber, K. R.; Tycko, R. Theory for cross effect dynamic nuclear polarization under magic-angle spinning in solid state nuclear magnetic resonance: the importance of level crossings. *J. Chem. Phys.* **2012**, *137* (8), 084508.

84. Hovav, Y.; Feintuch, A.; Vega, S. Theoretical aspects of dynamic nuclear polarization in the solid state - spin temperature and thermal mixing. *Phys. Chem. Chem. Phys.* **2013**, *15* (1), 188-203.

85. Hausser, K. H.; Stehlik, D. Dynamic nuclear polarization in liquids. In *Advances in Magnetic and Optical Resonance*, Waugh, J. S. Ed.; Vol. 3; Academic Press, 1968; pp 79-139.

86. Perras, F. A.; Mentink-Vigier, F.; Pylaeva, S. Perspectives on the dynamic nuclear polarization mechanisms of monoradicals: Overhauser effect or thermal mixing? *J. Phys. Chem. Lett.* **2025**, *16* (14), 3420-3432.

87. Jeffries, C. D. Polarization of nuclei by resonance saturation in paramagnetic crystals. *Phys. Rev.* **1957**, *106* (1), 164-165.

88. Can, T. V.; Ni, Q. Z.; Griffin, R. G. Mechanisms of dynamic nuclear polarization in insulating solids. *J. Magn. Reson.* **2015**, *253*, 23-35.

89. Hwang, C. F.; Hill, D. A. New effect in dynamic polarization. *Phys. Rev. Lett.* **1967**, *18* (4), 110-112.

90. Dai, D. H.; Wang, X. W.; Liu, Y. W.; Yang, X. L.; Glaubitz, C.; Denysenkov, V.; He, X.; Prisner, T.; Mao, J. F. Room-temperature dynamic nuclear polarization enhanced NMR spectroscopy of small biological molecules in water. *Nat. Commun.* **2021**, *12* (1).

91. Sezer, D.; Dai, D.; Prisner, T. F. The solid effect of dynamic nuclear polarization in liquids – accounting for g-tensor anisotropy at high magnetic fields. *Magn. Reson.* **2023**, *4* (2), 243-269.

92. Griesinger, C.; Bennati, M.; Vieth, H. M.; Luchinat, C.; Parigi, G.; Höfer, P.; Engelke, F.; Glaser, S. J.; Denysenkov, V.; Prisner, T. F. Dynamic nuclear polarization at high magnetic fields in liquids. *Prog. Nucl. Magn. Reson. Spectrosc.* **2012**, *64*, 4-28.

93. Ardenkjaer-Larsen, J. H.; Fridlund, B.; Gram, A.; Hansson, G.; Hansson, L.; Lerche, M. H.; Servin, R.; Thaning, M.; Golman, K. Increase in signal-to-noise ratio of >10,000 times in liquid-state NMR. *Proc. Natl. Acad. Sci. USA* **2003**, *100* (18), 10158-10163.

94. Pinon, A. C.; Capozzi, A.; Ardenkjær-Larsen, J. H. Hyperpolarization via dissolution dynamic nuclear polarization: new technological and methodological advances. *Magn. Reson. Mater. Phy.* **2021**, *34* (1), 5-23.

95. Rosay, M.; Blank, M.; Engelke, F. Instrumentation for solid-state dynamic nuclear polarization with magic angle spinning NMR. *J. Magn. Reson.* **2016**, *264*, 88-98.

96. Griffin, R. G.; Swager, T. M.; Temkin, R. J. High frequency dynamic nuclear polarization: New directions for the 21st century. *J. Magn. Reson.* **2019**, *306*, 128-133.

97. Blank, M.; Borchard, P.; Cauffman, S.; Felch, K. Demonstration of a 593 GHz gyrotron for DNP. In *2018 43rd International Conference on Infrared, Millimeter, and Terahertz Waves (IRMMW-THz)*, 9-14 Sept, 2018; pp 1-2.

98. Bernard, G. M.; Michaelis, V. K. Instrumentation for high-field dynamic nuclear polarization NMR spectroscopy. *eMagRes* **2019**, *8* (2), 77-85.

99. Rosay, M.; Tometich, L.; Pawsey, S.; Bader, R.; Schauwecker, R.; Blank, M.; Borchard, P. M.; Cauffman, S. R.; Felch, K. L.; Weber, R. T.; et al. Solid-state dynamic nuclear polarization at 263 GHz: spectrometer design and experimental results. *Phys. Chem. Chem. Phys.* **2010**, *12* (22), 5850-5860.

100. Berruyer, P.; Björgvinsdóttir, S.; Bertarello, A.; Stevanato, G.; Rao, Y.; Karthikeyan, G.; Casano, G.; Ouari, O.; Lelli, M.; Reiter, C.; et al. Dynamic nuclear polarization enhancement of 200 at 21.15 T enabled by 65 kHz magic angle spinning. *J. Phys. Chem. Lett.* **2020**, *11* (19), 8386-8391.

101. Chen, P. H.; Albert, B. J.; Gao, C. K.; Alaniva, N.; Price, L. E.; Scott, F. J.; Saliba, E. P.; Sesti, E. L.; Judge, P. T.; Fisher, E. W.; et al. Magic angle spinning spheres. *Sci. Adv.* **2018**, *4* (9).

102. Chen, P.-H.; Gao, C.; Price, L. E.; Urban, M. A.; Popp, T. M. O.; Barnes, A. B. Two millimeter diameter spherical rotors spinning at 68 kHz for MAS NMR. *J. Magn. Reson. Open* **2021**, *8-9*, 100015.

103. Denysenkov, V.; Prisner, T. Liquid state dynamic nuclear polarization probe with Fabry-Perot resonator at 9.2 T. *J. Magn. Reson.* **2012**, *217*, 1-5.

104. Menzildjian, G.; Schlagnitweit, J.; Casano, G.; Ouari, O.; Gajan, D.; Lesage, A. Polarizing agents for efficient high field DNP solid-state NMR spectroscopy under magic-angle spinning: from design principles to formulation strategies. *Chem. Sci.* **2023**, *14* (23), 6120-6148.

105. Corzilius, B. High-field dynamic nuclear polarization. *Annu. Rev. Phys. Chem.* **2020**, *71* (1), 143-170.

106. Zagdoun, A.; Casano, G.; Ouari, O.; Schwarzwälder, M.; Rossini, A. J.; Aussenac, F.; Yulikov, M.; Jeschke, G.; Copéret, C.; Lesage, A.; et al. Large molecular weight nitroxide biradicals providing efficient dynamic nuclear polarization at temperatures up to 200 K. *J. Am. Chem. Soc.* **2013**, *135* (34), 12790-12797.

107. Lange, S.; Linden, A. H.; Akbey, Ü.; Trent Franks, W.; Loening, N. M.; Rossum, B.-J. v.; Oschkinat, H. The effect of biradical concentration on the performance of DNP-MAS-NMR. *J. Magn. Reson.* **2012**, *216*, 209-212.

108. Song, C.; Hu, K.-N.; Joo, C.-G.; Swager, T. M.; Griffin, R. G. TOTAPOL: A biradical polarizing agent for dynamic nuclear polarization experiments in aqueous media. *J. Am. Chem. Soc.* **2006**, *128* (35), 11385-11390.

109. Hu, K. N.; Yu, H. H.; Swager, T. M.; Griffin, R. G. Dynamic nuclear polarization with biradicals. *J. Am. Chem. Soc.* **2004**, *126* (35), 10844-10845.

110. Matsuki, Y.; Maly, T.; Ouari, O.; Karoui, H.; Le Moigne, F.; Rizzato, E.; Lyubenova, S.; Herzfeld, J.; Prisner, T.; Tordo, P.; et al. Dynamic nuclear polarization with a rigid biradical. *Angew. Chem. Int. Ed.* **2009**, *48* (27), 4996-5000.

111. Zagdoun, A.; Casano, G.; Ouari, O.; Lapadula, G.; Rossini, A. J.; Lelli, M.; Baffert, M.; Gajan, D.; Veyre, L.; Maas, W. E.; et al. A slowly relaxing rigid biradical for efficient dynamic nuclear polarization surface-enhanced NMR spectroscopy: Expeditious characterization of functional group manipulation in hybrid materials. *J. Am. Chem. Soc.* **2012**, *134* (4), 2284-2291.

112. Kathirvelu, V.; Smith, C.; Parks, C.; Mannan, M. A.; Miura, Y.; Takeshita, K.; Eaton, S. S.; Eaton, G. R. Relaxation rates for spirocyclohexyl nitroxyl radicals are suitable for interspin distance measurements at temperatures up to about 125 K. *Chem. Commun.* **2009**, (4), 454-456.

113. Sato, H.; Kathirvelu, V.; Fielding, A.; Blinco, J. P.; Micallef, A. S.; Bottle, S. E.; Eaton, S. S.; Eaton, G. R. Impact of molecular size on electron spin relaxation rates of nitroxyl radicals in glassy solvents between 100 and 300 K. *Mol. Phys.* **2007**, *105* (15-16), 2137-2151.

114. Rozantsev, E. G.; Golubev, V. A.; Neiman, M. V.; Kokhanov, Y. V. Some reactions of free iminoxyl radicals with unpaired electron participation. *Izv. Akad. Nauk Arm. SSR Khim. Nauki* **1965**, 572–573.

115. Sauvée, C.; Rosay, M.; Casano, G.; Aussenac, F.; Weber, R. T.; Ouari, O.; Tordo, P. Highly efficient, water-soluble polarizing agents for dynamic nuclear polarization at high frequency. *Angew. Chem. Int. Ed.* **2013**, *52* (41), 10858-10861.

116. Jagtap, A. P.; Geiger, M. A.; Stöppler, D.; Orwick-Rydmark, M.; Oschkinat, H.; Sigurdsson, S. T. bcTol: a highly water-soluble biradical for efficient dynamic nuclear polarization of biomolecules. *Chem. Commun.* **2016**, *52* (43), 7020-7023.

117. Geiger, M.-A.; Jagtap, A. P.; Kaushik, M.; Sun, H.; Stöppler, D.; Sigurdsson, S. T.; Corzilius, B.; Oschkinat, H. Efficiency of water-soluble nitroxide biradicals for dynamic nuclear polarization in rotating solids at 9.4 T: bcTol-M and cyolyl-TOTAPOL as new polarizing agents. *Chem. Eur. J.* **2018**, *24* (51), 13485-13494.

118. Stevanato, G.; Casano, G.; Kubicki, D. J.; Rao, Y.; Esteban Hofer, L.; Menzildjian, G.; Karoui, H.; Siri, D.; Cordova, M.; Yulikov, M.; et al. Open and closed radicals: Local geometry around unpaired electrons governs magic-angle spinning dynamic nuclear polarization performance. *J. Am. Chem. Soc.* **2020**, *142* (39), 16587-16599.

119. Mentink-Vigier, F.; Dubroca, T.; Van Tol, J.; Sigurdsson, S. T. The distance between g-tensors of nitroxide biradicals governs MAS-DNP performance: The case of the bTurea family. *J. Magn. Reson.* **2021**, *329*, 107026.

120. Mentink-Vigier, F.; Marin-Montesinos, I.; Jagtap, A. P.; Halbritter, T.; van Tol, J.; Hediger, S.; Lee, D.; Sigurdsson, S. T.; De Paëpe, G. Computationally assisted design of polarizing agents for dynamic nuclear polarization enhanced NMR: the Asympol family. *J. Am. Chem. Soc.* **2018**, *140* (35), 11013-11019.

121. Harrabi, R.; Halbritter, T.; Aussenac, F.; Dakhlaoui, O.; van Tol, J.; Damodaran, K. K.; Lee, D.; Paul, S.; Hediger, S.; Mentink-Vigier, F.; et al. Highly efficient polarizing agents for MAS-DNP of proton-dense molecular solids. *Angew. Chem. Int. Ed.* **2022**, *61* (12).

122. Lund, A.; Casano, G.; Menzildjian, G.; Kaushik, M.; Stevanato, G.; Yulikov, M.; Jabbour, R.; Wisser, D.; Renom-Carrasco, M.; Thieuleux, C.; et al. TinyPols: a family

of water-soluble binitroxides tailored for dynamic nuclear polarization enhanced NMR spectroscopy at 18.8 and 21.1 T. *Chem. Sci.* **2020**, *11* (10), 2810-2818.

123. Du, X. Z.; Huang, Z. Y.; Shao, Q.; Rockenbauer, A.; Yang, Y.; Song, Y. G.; Ma, Y.; Mao, J. F.; Liu, Y. P. Acrylamide-linked water-soluble nitroxide biradicals with enhanced electron-electron couplings for dynamic nuclear polarization at 14.1 T. *J. Phys. Chem. Lett.* **2025**, *16* (36), 9217-9226.

124. Michaelis, V. K.; Smith, A. A.; Corzilius, B.; Haze, O.; Swager, T. M.; Griffin, R. G. High-Field 13C dynamic nuclear polarization with a radical mixture. *J. Am. Chem. Soc.* **2013**, *135* (8), 2935-2938.

125. Kuhn, R.; Trischmann, H. Über auffallend stabile N-haltige radikale. *Angew. Chem.* **1963**, *75* (6), 294-295.

126. Thurber, K. R.; Le, T. N.; Changcoco, V.; Brook, D. J. R. Verdazyl-ribose: A new radical for solid-state dynamic nuclear polarization at high magnetic field. *J. Magn. Reson.* **2018**, *289*, 122-131.

127. Müller-Warmuth, W.; Vilhjalmsson, R.; Gerlof, P. A. M.; Smidt, J.; Trommel, J. Intermolecular interactions of benzene and carbon tetrachloride with selected free radicals in solution as studied by 13C and 1H dynamic nuclear polarization. *Mol. Phys.* **1976**, *31* (4), 1055-1067.

128. Gomberg, M. An instance of trivalent carbon: Triphenylmethyl. *J. Am. Chem. Soc.* **1900**, *22* (11), 757-771.

129. Ratera, I.; Vidal-Gancedo, J.; Maspoch, D.; Bromley, S. T.; Crivillers, N.; Mas-Torrent, M. Perspectives for polychlorinated trityl radicals. *J. Mater. Chem. C* **2021**, *9* (33), 10610-10623.

130. Poncelet, M.; Huffman, J. L.; Khramtsov, V. V.; Dhimitruka, I.; Driesschaert, B. Synthesis of hydroxyethyl tetrathiatriarylmethyl radicals OX063 and OX071. *RSC Adv.* **2019**, *9* (60), 35073-35076.

131. Ardenkjær-Larsen, J. H.; Laursen, I.; Leunbach, I.; Ehnholm, G.; Wistrand, L. G.; Petersson, J. S.; Golman, K. EPR and DNP properties of certain novel single electron contrast agents intended for oximetric imaging. *J. Magn. Reson.* **1998**, *133* (1), 1-12.

132. Palani, R. S.; Mardini, M.; Quan, Y. F.; Griffin, R. G. Dynamic nuclear polarization with trityl radicals. *J. Magn. Reson.* **2023**, *349*, 107410.

133. Kuzhelev, A. A.; Denysenkov, V.; Ahmad, I. M.; Rogozhnikova, O. Y.; Trukhin, D. V.; Bagryanskaya, E. G.; Tormyshev, V. M.; Sigurdsson, S. T.; Prisner, T. F. Solid-effect dynamic nuclear polarization in viscous liquids at 9.4 T using narrow-line polarizing agents. *J. Am. Chem. Soc.* **2023**, *145* (18), 10268-10274.

134. Koelsch, C. F. Syntheses with triarylvinylmagnesium bromides. α,γ-bisdiphenylene-β-phenylallyl, a stable free radical. *J. Am. Chem. Soc.* **1957**, *79* (16), 4439-4441.

135. Delage-Laurin, L.; Palani, R. S.; Golota, N.; Mardini, M.; Ouyang, Y.; Tan, K. O.; Swager, T. M.; Griffin, R. G. Overhauser dynamic nuclear polarization with selectively deuterated BDPA radicals. *J. Am. Chem. Soc.* **2021**, *143* (48), 20281-20290.

136. Reddy, T. J.; Iwama, T.; Halpern, H. J.; Rawal, V. H. General synthesis of persistent trityl radicals for EPR imaging of biological systems. *J. Org. Chem.* **2002**, *67* (14), 4635-4639.

137. Dane, E. L.; Maly, T.; Debelouchina, G. T.; Griffin, R. G.; Swager, T. M. Synthesis of a BDPA-TEMPO biradical. *Org. Lett.* **2009**, *11* (9), 1871-1874.

138. Haze, O.; Corzilius, B.; Smith, A. A.; Griffin, R. G.; Swager, T. M. Water-soluble narrow-line radicals for dynamic nuclear polarization. *J. Am. Chem. Soc.* **2012**, *134* (35), 14287-14290.

139. Dane, E. L.; Swager, T. M. Synthesis of a water-soluble 1,3-bis(diphenylene)-2-phenylallyl radical. *J. Org. Chem.* **2010**, *75* (10), 3533-3536.

140. Mandal, S.; Sigurdsson, S. T. Water-soluble BDPA radicals with improved persistence. *Chem. Commun.* **2020**, *56* (86), 13121-13124.

141. Atkin, R.; Warr, G. G. The smallest amphiphiles: nanostructure in protic room-temperature ionic liquids with short alkyl groups. *J. Phys. Chem. B* **2008**, *112* (14), 4164-4166.

142. Singh, T.; Kumar, A. Aggregation behavior of ionic liquids in aqueous solutions: effect of alkyl chain length, cations, and anions. *J. Phys. Chem. B* **2007**, *111* (27), 7843-7851.

143. Dutta, R.; Kundu, S.; Sarkar, N. Ionic liquid-induced aggregate formation and their applications. *Biophys. Rev.* **2018**, *10* (3), 861-871.

144. Hu, K. N.; Bajaj, V. S.; Rosay, M.; Griffin, R. G. High-frequency dynamic nuclear polarization using mixtures of TEMPO and trityl radicals. *J. Chem. Phys.* **2007**, *126* (4).

145. Mathies, G.; Caporini, M. A.; Michaelis, V. K.; Liu, Y.; Hu, K. N.; Mance, D.; Zweier, J. L.; Rosay, M.; Baldus, M.; Griffin, R. G. Efficient dynamic nuclear polarization at 800 MHz/527 GHz with trityl-nitroxide biradicals. *Angew. Chem. Int. Ed.* **2015**, *54* (40), 11770-11774.

146. Zhai, W. X.; Paioni, A. L.; Cai, X. Y.; Narasimhan, S.; Medeiros-Silva, J.; Zhang, W. X.; Rockenbauer, A.; Weingarth, M.; Song, Y. G.; Baldus, M.; et al. Postmodification via thiol-click chemistry yields hydrophilic trityl-nitroxide biradicals for biomolecular high-field dynamic nuclear polarization. *J. Phys. Chem. B* **2020**, *124* (41), 9047-9060.

147. Cai, X.; Lucini Paioni, A.; Adler, A.; Yao, R.; Zhang, W.; Beriashvili, D.; Safeer, A.; Gurinov, A.; Rockenbauer, A.; Song, Y.; et al. Highly efficient trityl-nitroxide biradicals for biomolecular high-field dynamic nuclear polarization. *Chem. Eur. J.* **2021**, *27* (50), 12758-12762.

148. Yao, R.; Beriashvili, D.; Zhang, W. X.; Li, S.; Safeer, A.; Gurinov, A.; Rockenbauer, A.; Yang, Y.; Song, Y. G.; Baldus, M.; et al. Highly bioresistant, hydrophilic and rigidly linked trityl-nitroxide biradicals for cellular high-field dynamic nuclear polarization. *Chem. Sci.* **2022**, *13* (47), 14157-14164.

149. Pinto, L. F.; Marín-Montesinos, I.; Lloveras, V.; Muñoz-Gómez, J. L.; Pons, M.; Veciana, J.; Vidal-Gancedo, J. NMR signal enhancement of >50 000 times in fast dissolution dynamic nuclear polarization. *Chem. Commun.* **2017**, *53* (26), 3757-3760.

150. Wisser, D.; Karthikeyan, G.; Lund, A.; Casano, G.; Karoui, H.; Yulikov, M.; Menzildjian, G.; Pinon, A. C.; Purea, A.; Engelke, F.; et al. BDPA-nitroxide biradicals tailored for efficient dynamic nuclear polarization enhanced solid-state NMR at magnetic fields up to 21.1 T. *J. Am. Chem. Soc.* **2018**, *140* (41), 13340-13349.

151. Meckes, J. A.; Schroeder, Z. W.; Sarkar, D.; Hooper, R. W.; Faraday-Smith, C. E.; Brown, A.; Tykwinski, R. R.; Michaelis, V. K. Verdazyl-based radicals for high-field dynamic nuclear polarization NMR. *J. Am. Chem. Soc.* **2025**, *147* (9), 7293-7304.

152. Pylaeva, S.; Marx, P.; Singh, G.; Kuhne, T. D.; Roemelt, M.; Elgabarty, H. Organic mixed-valence compounds and the overhauser effect in insulating solids. *J. Phys. Chem. A* **2021**, *125* (3), 867-874.

153. Liu, W.; Nie, J.; Tan, X.; Liu, H.; Yu, N.; Han, G.; Zhu, Y.; Villamena, F. A.; Song, Y.; Zweier, J. L.; et al. Synthesis and characterization of PEGylated trityl radicals: Effect of PEGylation on physicochemical properties. *J. Org. Chem.* **2017**, *82* (1), 588-596.

154. Liu, Y. P.; Villamena, F. A.; Zweier, J. L. Highly stable dendritic trityl radicals as oxygen and pH probe. *Chem. Commun.* **2008**, (36), 4336-4338.

155. Mardini, M.; Palani, R. S.; Ahmad, I. M.; Mandal, S.; Jawla, S. K.; Bryerton, E.; Temkin, R. J.; Sigurdsson, S. T.; Griffin, R. G. Frequency-swept dynamic nuclear polarization. *J. Mag. Res.* **2023**, *353*, 107511.

156. Dai, D. H.; Denysenkov, V.; Bagryanskaya, E. G.; Tormyshev, V. M.; Prisner, T. F.; Kuzhelev, A. A. ^{13}C hyperpolarization of viscous liquids by transfer of solid-effect ^{1}H dynamic nuclear polarization at high magnetic field. *J. Phys. Chem. Lett.* **2023**, *14* (31), 7059-7064.

157. Sezer, D. The solid effect of dynamic nuclear polarization in liquids. *Magn. Reson.* **2023**, *4* (1), 153-174.

158. Kuzhelev, A. A.; Dai, D.; Denysenkov, V.; Prisner, T. F. Solid-like dynamic nuclear polarization observed in the fluid phase of lipid bilayers at 9.4 T. *J. Am. Chem. Soc.* **2022**, *144* (3), 1164-1168.

159. Dahm, R. Friedrich Miescher and the discovery of DNA. *Dev. Biol.* **2005**, *278* (2), 274-288.

160. Dahm, R. Discovering DNA: Friedrich Miescher and the early years of nucleic acid research. *Hum. Genet.* **2008**, *122* (6), 565-581.

161. Ferry, G. Molecular biology: Of DNA and broken dreams. *Nature* **2014**, *510* (7503), 32-33.

162. Franklin, R. E.; Gosling, R. G. The structure of sodium thymonucleate fibres. I. The influence of water content. *Acta Crystallogr.* **1953**, *6* (8-9), 673-677.

163. Watson, J. D.; Crick, F. H. C. Molecular structure of nucleic acids - A structure for deoxyribose nucleic acid (Reprinted from Nature vol 171, pg 737, 1953). *Clin. Orthop. Relat. Res.* **2007**, (462), 3-5.

164. Fox, A. S. Protein synthesis and genetics. *Nature* **1954**, *173* (4399), 350-351.

165. Sharp, P. A. The centrality of RNA. *Cell* **2009**, *136* (4), 577-580.

166. Kapp, L. D.; Lorsch, J. R. The molecular mechanics of eukaryotic translation. *Annu. Rev. Biochem.* **2004**, *73*, 657-704.

167. Matera, A. G.; Wang, Z. F. A day in the life of the spliceosome. *Nat. Rev. Mol. Cell Bio.* **2014**, *15* (2), 108-121.

168. Yan, C. Y.; Wan, R. X.; Shi, Y. G. Molecular mechanisms of pre-mRNA splicing through structural biology of the spliceosome. *Cold Spring Harb. Perspect. Biol.* **2019**, *11* (1).

169. Duchaine, T. F.; Fabian, M. R. Mechanistic insights into microRNA-mediated gene silencing. *Cold Spring Harb. Perspect. Biol.* **2019**, *11* (3).

170. Dana, H.; Chalbatani, G. M.; Mahmoodzadeh, H.; Karimloo, R.; Rezaiean, O.; Moradzadeh, A.; Mehmandoost, N.; Moazzen, F.; Mazraeh, A.; Marmari, V.; et al. Molecular mechanisms and biological functions of siRNA. *Int. J. Biomed. Sci.* **2017**, *13*, 48 - 57.

171. Bratkovič, T.; Božič, J.; Rogelj, B. Functional diversity of small nucleolar RNAs. *Nucl. Acids Res.* **2020**, *48* (4), 1627-1651.

172. Statello, L.; Guo, C.-J.; Chen, L.-L.; Huarte, M. Gene regulation by long non-coding RNAs and its biological functions. *Nat. Rev. Mol. Cell Bio.* **2021**, *22* (2), 96-118.

173. Park, S. V.; Yang, J. S.; Jo, H.; Kang, B.; Oh, S. S.; Jung, G. Y. Catalytic RNA, ribozyme, and its applications in synthetic biology. *Biotechnol. Adv.* **2019**, *37* (8).

174. Simonović, M.; Steitz, T. A. A structural view on the mechanism of the ribosome-catalyzed peptide bond formation. *Biochim. Biophys. Acta Gene Regul. Mech.* **2009**, *1789* (9), 612-623.

175. Bédard, A. S. V.; Hien, E. D. M.; Lafontaine, D. A. Riboswitch regulation mechanisms: RNA, metabolites and regulatory proteins. *Biochim. Biophys. Acta, Gene Regul. Mech.* **2020**, *1863* (3).

176. Pavlova, N.; Kaloudas, D.; Penchovsky, R. Riboswitch distribution, structure, and function in bacteria. *Gene* **2019**, *708*, 38-48.

177. Garst, A. D.; Edwards, A. L.; Batey, R. T. Riboswitches: Structures and mechanisms. *Cold Spring Harb. Perspect. Biol.* **2011**, *3* (6).

178. Mandal, M.; Boese, B.; Barrick, J. E.; Winkler, W. C.; Breaker, R. R. Riboswitches control fundamental biochemical pathways in Bacillus subtilis and other bacteria. *Cell* **2003**, *113* (5), 577-586.

179. Blouin, S.; Mulhbacher, J.; Penedo, J. C.; Lafontaine, D. A. Riboswitches: Ancient and promising genetic regulators. *ChemBioChem* **2009**, *10* (3), 400-416.

180. Hassibian, S.; Amin, M.; Taghdisi, S. M.; Sameiyan, E.; Ghaffari, R.; Alibolandi, M.; Ramezani, M.; Abnous, K.; Dehnavi, S. M. Aptamers: Design, theory, and applications to diagnosis and therapy for diseases. *MedComm* **2025**, *6* (5), e70180.

181. Etzel, M.; Mörl, M. Synthetic riboswitches: From plug and pray toward plug and play. *Biochem.* **2017**, *56* (9), 1181-1198.

182. Kohlberger, M.; Gadermaier, G. SELEX: Critical factors and optimization strategies for successful aptamer selection. *Biotechnol. Appl. Biochem.* **2022**, *69* (5), 1771-1792.

183. Didarian, R.; Ozbek, H. K.; Ozalp, V. C.; Erel, O.; Yildirim-Tirgil, N. Enhanced SELEX platforms for aptamer selection with improved characteristics: A review. *Mol. Biotechnol.* **2025**, *67* (8), 2962-2977.

184. Dong, Y.; Wang, Z.; Wang, S.; Wu, Y.; Ma, Y.; Liu, J. Introduction of SELEX and important SELEX variants. In *Aptamers for Analytical Applications*, Dong, Y. Ed.; 2018; pp 1-25.

185. Makkar, S. K. Advances in RNA-based therapeutics: current breakthroughs, clinical translation, and future perspectives. *Front. Genet.* **2025**, *16*.

186. Pardi, N.; Hogan, M. J.; Porter, F. W.; Weissman, D. mRNA vaccines — a new era in vaccinology. *Nat. Rev. Drug Discov.* **2018**, *17* (4), 261-279.

187. Hendaus, M. A.; Jomha, F. A. mRNA Vaccines for COVID-19: A simple explanation. *Qatar Med. J.* **2021**, *2021* (1).

188. Dhuri, K.; Bechtold, C.; Quijano, E.; Pham, H.; Gupta, A.; Vikram, A.; Bahal, R. Antisense oligonucleotides: An emerging area in drug discovery and development. *J. Clin. Med.* **2020**, *9* (6), 2004.

189. Lam, J. K. W.; Chow, M. Y. T.; Zhang, Y.; Leung, S. W. S. siRNA Versus miRNA as therapeutics for gene silencing. *Mol. Ther. Nucleic acids* **2015**, *4*, e252.

190. Albrecht, C. Principles of fluorescence spectroscopy, 3rd Edition. In *Analytical and Bioanalytical Chemistry*, Vol. 390; 2008; pp 1223-1224.

191. Sinkeldam, R. W.; Greco, N. J.; Tor, Y. Fluorescent analogs of biomolecular building blocks: Design, properties, and applications. *Chem. Rev.* **2010**, *110* (5), 2579-2619.

192. Roy, S. Fluorescence quenching methods to study protein-nucleic acid interactions. *Methods Enzymol.* **2004**, *379*, 175-187.

193. Klymchenko, A. S. Solvatochromic and fluorogenic dyes as environment-sensitive probes: Design and biological applications. *Acc. Chem. Res.* **2017**, *50* (2), 366-375.

194. Jameson, D. M.; Ross, J. A. Fluorescence polarization/anisotropy in diagnostics and imaging. *Chem. Rev.* **2010**, *110* (5), 2685-2708.

195. Becker, W. Fluorescence lifetime imaging – techniques and applications. *J. Microsc.* **2012**, *247* (2), 119-136.

196. Wilhelmsson, L. M. Förster resonance energy transfer (FRET) between nucleobase analogs – a tool for detailed structure and dynamics investigations. In *Fluorescent Analogues of Biomolecular Building Blocks: Design and Applications*, Wilhelmsson, L. M., Tor, Y. Eds.; 2016; pp 224-241.

197. Sauer, M.; Hofkens, J.; Enderlein, J. Basic Principles of Fluorescence Spectroscopy. In *Handbook of Fluorescence Spectroscopy and Imaging*, 2011; pp 1-30.

198. Lakowicz, J. R. Energy transfer. In *Principles of Fluorescence Spectroscopy*, Lakowicz, J. R. Ed.; Springer US, 1999; pp 367-394.

199. Wood, S.; Rueda, D. Fluorescence labeling of nucleic acids. In *Encyclopedia of Biophysics*, Roberts, G. C. K. Ed.; Springer Berlin Heidelberg, 2013; pp 809-812.

200. Didenko, V. V. DNA probes using fluorescence resonance energy transfer (FRET): Designs and applications. *BioTechniques* **2001**, *31* (5), 1106-1121.

201. Robinson, P. J.; Woolhead, C. A. Implementation of FRET technologies for studying the folding and conformational changes in biological structures. In *FRET – Förster Resonance Energy Transfer*, :Igor Medintz, N. H. Ed.; 2013; pp 357-396.

202. Ghosh, S.; Saha, S.; Goswami, D.; Bilgrami, S.; Mayor, S. Dynamic imaging of homo-FRET in live cells by fluorescence anisotropy microscopy. *Methods Enzymol.* **2012**, *505*, 291-327.

203. Kashida, H.; Kawai, H.; Azuma, H.; Araki, Y.; Wada, T.; Asanuma, H. Quantitative analyses of forster resonance energy transfer between identical pyrene chromophores (Homo-FRET) in DNA scaffolds. *ChemPhotoChem* **2021**, *5* (2), 167-172.

204. Weil, J. A.; Bolton, J. R. Basic principles of paramagnetic resonance. In *Electron Paramagnetic Resonance*, Weil, J. A., Bolton, J. R. Eds.; 2006; pp 1-35.

205. Misra, S. K. Introduction. In *Multifrequency Electron Paramagnetic Resonance*, Misra, S. K. Ed.; 2011; pp 1-22.

206. Zhang, X.; Cekan, P.; Sigurdsson, S. T.; Qin, P. Z. Studying RNA using site-directed spin-labeling and continuous-wave electron paramagnetic resonance spectroscopy. *Methods Enzymol.* **2009**, *469*, 303-328.

207. Kim, N.-K.; Murali, A.; DeRose, V. J. A distance ruler for RNA using EPR and site-directed spin labeling. *Chem. Biol.* **2004**, *11* (7), 939-948.

208. Roessler, M. M.; Salvadori, E. Principles and applications of EPR spectroscopy in the chemical sciences. *Chem. Soc. Rev.* **2018**, *47* (8), 2534-2553.

209. Telser, J. Electron-nuclear double resonance (ENDOR) spectroscopy. In *Encyclopedia of Inorganic Chemistry*, R.B. King, R. H. C., C.M. Lukehart, D.A. Atwood and R.A. Scott Ed.; 2005.

210. McCracken, J. Electron spin echo envelope modulation (ESEEM) spectroscopy. In *Encyclopedia of Inorganic Chemistry*, R.B. King, R. H. C., C.M. Lukehart, D.A. Atwood and R.A. Scott Ed.; 2005.

211. Höfer, P.; Grupp, A.; Nebenführ, H.; Mehring, M. Hyperfine sublevel correlation (hyscore) spectroscopy: a 2D ESR investigation of the squaric acid radical. *Chem. Phys. Lett.* **1986**, *132* (3), 279-282.

212. Milov, A. D.; Maryasov, A. G.; Tsvetkov, Y. D. Pulsed electron double resonance (PELDOR) and its applications in free-radicals research. *Appl. Magn. Reson.* **1998**, *15* (1), 107-143.

213. Martin, R. E.; Pannier, M.; Diederich, F.; Gramlich, V.; Hubrich, M.; Spiess, H. W. Determination of end-to-end distances in a series of TEMPO diradicals of up to 2.8 nm length with a new four-pulse double electron electron resonance experiment. *Angew. Chem. Int. Ed.* **1998**, *37* (20), 2834-2837.

214. Kuzin, S.; Yulikov, M. RIDME Spectroscopy: New topics beyond the determination of electron spin–spin distances. *J. Phys. Chem. Lett.* **2025**, *16* (4), 1024-1037.

215. Jeschke, G.; Pannier, M.; Godt, A.; Spiess, H. W. Dipolar spectroscopy and spin alignment in electron paramagnetic resonance. *Chem. Phys. Lett.* **2000**, *331* (2), 243-252.

216. Mandato, A.; Hasanbasri, Z.; Saxena, S. Double quantum coherence ESR at Q-band enhances the sensitivity of distance measurements at submicromolar concentrations. *J. Phys. Chem. Lett.* **2023**, *14* (40), 8909-8915.

217. Reginsson, Gunnar W.; Schiemann, O. Studying biomolecular complexes with pulsed electron–electron double resonance spectroscopy. *Biochem. Soc. Trans.* **2011**, *39* (1), 128-139.

218. Schiemann, O.; Heubach, C. A.; Abdullin, D.; Ackermann, K.; Azarkh, M.; Bagryanskaya, E. G.; Drescher, M.; Endeward, B.; Freed, J. H.; Galazzo, L.; et al. Benchmark test and guidelines for DEER/PELDOR experiments on nitroxide-labeled biomolecules. *J. Am. Chem. Soc.* **2021**, *143* (43), 17875-17890.

219. Teucher, M.; Bordignon, E. Improved signal fidelity in 4-pulse DEER with Gaussian pulses. *J. Magn. Reson.* **2018**, *296*, 103-111.

220. Fedorova, O. S.; Tsvetkov, Y. D. Pulsed electron double resonance in structural studies of spin-labeled nucleic acids. *Acta Naturae* **2013**, *5* (1), 9-32.

221. Schiemann, O.; Prisner, T. F. Long-range distance determinations in biomacromolecules by EPR spectroscopy. *Q. Rev. Biophys.* **2007**, *40* (1), 1-53.

222. Jeschke, G.; Chechik, V.; Ionita, P.; Godt, A.; Zimmermann, H.; Banham, J.; Timmel, C. R.; Hilger, D.; Jung, H. DeerAnalysis2006 - a comprehensive software package for analyzing pulsed ELDOR data. *Appl. Magn. Reson.* **2006**, *30* (3-4), 473-498.

223. Mett, R. R.; Anilkumar, A.; Garces, A. M.; Wehrley, J. T.; Lerch, M. T.; Klug, C. S.; Sidabras, J. W. Improved electron paramagnetic resonance spectroscopy sensitivity for aqueous biological samples using low-volume multi-channel cells and dielectric resonators. *Rev. Sci. Instrum.* **2026**, *97* (2), 024705.

224. Tamm, L. K.; Lai, A. L.; Li, Y. Combined NMR and EPR spectroscopy to determine structures of viral fusion domains in membranes. *Biochim. Biophys. Acta Biomembr.* **2007**, *1768* (12), 3052-3060.

225. Sahu, I. D.; McCarrick, R. M.; Lorigan, G. A. Use of electron paramagnetic resonance to solve biochemical problems. *Biochem.* **2013**, *52* (35), 5967-5984.

226. Azarkh, M.; Singh, V.; Okle, O.; Seemann, I. T.; Dietrich, D. R.; Hartig, J. S.; Drescher, M. Site-directed spin-labeling of nucleotides and the use of in-cell EPR to determine long-range distances in a biologically relevant environment. *Nat. Protoc.* **2013**, *8* (1), 131-147.

227. Huang, K.; Fang, X. A review on recent advances in methods for site-directed spin labeling of long RNAs. *Int. J. Biol. Macromol.* **2023**, *239*, 124244.

228. Shelke, S. A.; Sigurdsson, S. T. Site-directed spin labelling of nucleic acids. *Eur. J. Org. Chem.* **2012**, *2012* (12), 2291-2301.

229. Shelke, S. A.; Sigurdsson, S. T. Site-directed spin labeling for EPR studies of nucleic acids. In *Modified Nucleic Acids, Springer*, Nakatani K., T. Y. Ed.; Vol. 31; 2016; pp 159-187.

230. Sowa, G. Z.; Qin, P. Z. Site-directed spin labeling studies on nucleic acid structure and dynamics. In *Progress in Nucleic Acid Research and Molecular Biology*, Conn, P. M. Ed.; Vol. 82; Academic Press, 2008; pp 147-197.

231. Kamble, N. R.; Sigurdsson, S. T. Purine-Derived nitroxides for noncovalent spin-labeling of abasic sites in duplex nucleic acids. *Chem. Eur. J.* **2018**, *24* (16), 4157-4164.

232. Saha, S.; Hetzke, T.; Prisner, T. F.; Sigurdsson, S. T. Noncovalent spin-labeling of RNA: the aptamer approach. *Chem. Commun.* **2018**, *54* (83), 11749-11752.

233. Shelke, S. A.; Sigurdsson, S. T. Noncovalent and site-directed spin labeling of nucleic acids. *Angew. Chem. Int. Ed.* **2010**, *49* (43), 7984-7986.

234. Cekan, P.; Smith, A. L.; Barhate, N.; Robinson, B. H.; Sigurdsson, S. T. Rigid spin-labeled nucleoside Ç: a nonperturbing EPR probe of nucleic acid conformation. *Nucl. Acids Res.* **2008**, *36* (18), 5946-5954.

235. Juliusson, H. Y.; Segler, A.-L. J.; Sigurdsson, S. T. Benzoyl-protected hydroxylamines for improved chemical synthesis of oligonucleotides containing nitroxide spin labels. *Eur. J. Org. Chem.* **2019**, *2019* (23), 3799-3805.

236. Michelson, A. M.; Todd, A. R. Nucleotides part XXXII. Synthesis of a dithymidine dinucleotide containing a 3′: 5′-internucleotidic linkage. *J. Chem. Soc.* **1955**, 2632-2638.

237. Beaucage, S. L.; Caruthers, M. H. Deoxynucleoside phosphoramidites - a New class of key intermediates for deoxypolynucleotide synthesis. *Tetrahedron Lett.* **1981**, *22* (20), 1859-1862.

238. Reese, C. B. The chemical synthesis of oligo- and poly-nucleotides: a personal commentary. *Tetrahedron* **2002**, *58* (44), 8893-8920.

239. Beaucage, S. L.; Iyer, R. P. Advances in the synthesis of oligonucleotides by the phosphoramidite approach. *Tetrahedron* **1992**, *48* (12), 2223-2311.

240. Caruthers, M. H. Gene synthesis machines: DNA chemistry and its uses. *Science* **1985**, *230* (4723), 281-285.

241. Ellington, A.; Pollard Jr, J. D. Introduction to the synthesis and purification of oligonucleotides. *Curr. Protoc. Nucleic Acid Chem.* **2000**, *00* (1), A.3C.1-A.3C.22.

242. Mcbride, L. J.; Caruthers, M. H. Nucleotide chemistry .10. An investigation of several deoxynucleoside phosphoramidites useful for synthesizing deoxyoligonucleotides. *Tetrahedron Lett.* **1983**, *24* (3), 245-248.

243. Reginsson, G. W.; Shelke, S. A.; Rouillon, C.; White, M. F.; Sigurdsson, S. T.; Schiemann, O. Protein-induced changes in DNA structure and dynamics observed with noncovalent site-directed spin labeling and PELDOR. *Nucl. Acids Res.* **2013**, *41* (1).

244. Kamble, N. R.; Gränz, M.; Prisner, T. F.; Sigurdsson, S. T. Noncovalent and site-directed spin labeling of duplex RNA. *Chem. Commun.* **2016**, *52* (100), 14442-14445.

245. Helmling, C.; Bessi, I.; Wacker, A.; Schnorr, K. A.; Jonker, H. R. A.; Richter, C.; Wagner, D.; Kreibich, M.; Schwalbe, H. Noncovalent spin labeling of riboswitch

RNAs to obtain long-range structural NMR restraints. *ACS Chem. Biol.* **2014**, *9* (6), 1330-1339.

246. Elajaili, H.; Sedhom, J.; Eaton, S. S.; Eaton, G. R. Persistence of nitroxide radicals in solution. *Appl. Magn. Reson.* **2019**, *50* (10), 1177-1181.

247. Karoui, H.; Moigne, F. L.; Ouari, O.; Tordo, P. Nitroxide radicals: Properties, synthesis and applications. In *Stable Radicals*, 2010; pp 173-229.

248. Klug, C. S.; Lerch, M. T.; Feix, J. B. Applications of nitroxide spin labels to structural biology. In *Nitroxides*, Ouari, O., Gigmes, D. Eds.; The Royal Society of Chemistry, 2021; pp 392-419.

249. Jeschke, G. DEER distance measurements on proteins. *Annu. Rev. Phys. Chem.* **2012**, *63*, 419-446.

250. Keyes, R. S.; Bobst, A. M. Detection of internal and overall dynamics of a two-atom-tethered spin-labeled DNA. *Biochem.* **1995**, *34* (28), 9265-9276.

251. Edwards, T. E.; Okonogi, T. M.; Robinson, B. H.; Sigurdsson, S. T. Site-specific incorporation of nitroxide spin-labels into internal sites of the TAR RNA; Structure-dependent dynamics of RNA by EPR spectroscopy. *J. Am. Chem. Soc.* **2001**, *123* (7), 1527-1528.

252. Fischhaber, P. L.; Reese, A. W.; Nguyen, T.; Kirchner, J. J.; Hustedt, E. J.; Robinson, B. H.; Hopkins, P. B. Synthesis of duplex DNA containing a spin labeled analog of 2′ deoxycytidine. *Nucleosides and Nucleotides* **1997**, *16* (4), 365-377.

253. Schiemann, O.; Cekan, P.; Margraf, D.; Prisner, T. F.; Sigurdsson, S. T. Relative orientation of rigid nitroxides by PELDOR: Beyond distance measurements in nucleic acids. *Angew. Chem. Int. Ed.* **2009**, *48* (18), 3292-3295.

254. Miller, T. R.; Alley, S. C.; Reese, A. W.; Solomon, M. S.; McCallister, W. V.; Mailer, C.; Robinson, B. H.; Hopkins, P. B. A Probe for sequence-dependent nucleic acid dynamics. *J. Am. Chem. Soc.* **1995**, *117* (36), 9377-9378.

255. Miller, T. R.; Hopkins, P. B. Toward the synthesis of a second-generation nitroxide spin probe for DNA dynamics studies. *Bioorg. Med. Chem. Lett.* **1994**, *4* (8), 981-986.

256. Höbartner, C.; Sicoli, G.; Wachowius, F.; Gophane, D. B.; Sigurdsson, S. T. Synthesis and characterization of RNA containing a rigid and nonperturbing cytidine-derived spin label. *J. Org. Chem* **2012**, *77* (17), 7749-7754.

257. Gauger, M.; Duchardt-Ferner, E.; Halbritter, A. L. J.; Hetzke, T.; Sigurdsson, S. T.; Wöhnert, J.; Prisner, T. F. Investigating the conformational diversity of the TMR-3 aptamer. *J. Am. Chem. Soc.* **2025**, *147* (20), 17497-17509.

258. Gauger, M.; Heinz, M.; Halbritter, A. L. J.; Stelzl, L. S.; Erlenbach, N.; Hummer, G.; Sigurdsson, S. T.; Prisner, T. F. Structure and internal dynamics of short RNA duplexes determined by a combination of pulsed EPR methods and MD simulations. *Angew. Chem. Int. Ed.* **2024**, *63* (23), e202402498.

259. Hetzke, T.; Vogel, M.; Halbritter, A. L. J.; Saha, S.; Suess, B.; Sigurdsson, S. T.; Prisner, T. F. Simultaneous localization of two high affinity divalent metal ion binding sites in the tetracycline RNA aptamer with Mn-based pulsed dipolar EPR spectroscopy. *J. Phys. Chem. Lett.* **2023**, *14* (50), 11421-11428.

260. Marko, A.; Denysenkov, V.; Margraft, D.; Cekan, P.; Schiemann, O.; Sigurdsson, S. T.; Prisner, T. F. Conformational flexibility of DNA. *J. Am. Chem. Soc.* **2011**, *133* (34), 13375-13379.

261. Grytz, C. M.; Marko, A.; Cekan, P.; Sigurdsson, S. T.; Prisner, T. F. Flexibility and conformation of the cocaine aptamer studied by PELDOR. *Phys. Chem. Chem. Phys.* **2016**, *18* (4), 2993-3002.

262. Hetzke, T.; Vogel, M.; Gophane, D. B.; Weigand, J. E.; Suess, B.; Sigurdsson, S. T.; Prisner, T. F. Influence of Mg2+ on the conformational flexibility of a tetracycline aptamer. *RNA* **2019**, *25* (1), 158-167.

263. Segler, A. L. J.; Sigurdsson, S. T. A Carbazole-derived nitroxide that is an analogue of cytidine: A rigid spin label for DNA and RNA. *J. Org. Chem.* **2021**, *86* (17), 11647-11659.

264. Prisner, T. F.; Marko, A.; Sigurdsson, S. T. Conformational dynamics of nucleic acid molecules studied by PELDOR spectroscopy with rigid spin labels. *J. Mag. Res.* **2015**, *252*, 187-198.

265. Barhate, N.; Cekan, P.; Massey, A. P.; Sigurdsson, S. T. A nucleoside that contains a rigid nitroxide spin label: a fluorophore in disguise. *Angew. Chem. Int. Ed. Engl.* **2007**, *46* (15), 2655-2658.

266. Haugland, M. M.; Lovett, J. E.; Anderson, E. A. Advances in the synthesis of nitroxide radicals for use in biomolecule spin labelling. *Chem. Soc. Rev.* **2018**, *47* (3), 668-680.

267. Pollack, L. SAXS studies of ion-nucleic acid interactions. *Annu. Rev. Biophys.* **2011**, *40*, 225-242.

268. Ryter, J. M.; Schultz, S. C. Molecular basis of double-stranded RNA-protein interactions: structure of a dsRNA-binding domain complexed with dsRNA. *EMBO J.* **1998**, *17* (24), 7505-7513.

269. Erlenbach, N.; Grünewald, C.; Krstic, B.; Heckel, A.; Prisner, T. F. "End-to-end" stacking of small dsRNA. *Rna* **2019**, *25* (2), 239-246.

270. Heus, H. A.; Pardi, A. Structural features that give rise to the unusual stability of RNA hairpins containing GNRA loops. *Science* **1991**, *253* (5016), 191-194.

271. Bochkareva, E.; Korolev, S.; Lees-Miller, S. P.; Bochkarev, A. Structure of the RPA trimerization core and its role in the multistep DNA-binding mechanism of RPA. *EMBO J.* **2002**, *21* (7), 1855-1863.

272. Caldwell, C. C.; Spies, M. Dynamic elements of replication protein A at the crossroads of DNA replication, recombination, and repair. *Crit. Rev. Biochem. Mol.* **2020**, *55* (5), 482-507.

273. Kumaran, S.; Kozlov, A. G.; Lohman, T. M. Saccharomyces cerevisiae replication protein a binds to single-stranded DNA in multiple salt-dependent modes. *Biochem.* **2006**, *45* (39), 11958-11973.

274. Wang, Q. M.; Yang, Y. T.; Wang, Y. R.; Gao, B.; Xi, X. G.; Hou, X. M. Human replication protein A induces dynamic changes in single-stranded DNA and RNA structures. *J. Biol. Chem.* **2019**, *294* (38), 13915-13927.

275. Yates, L. A.; Aramayo, R. J.; Pokhrel, N.; Caldwell, C. C.; Kaplan, J. A.; Perera, R. L.; Spies, M.; Antony, E.; Zhang, X. D. A structural and dynamic model for the assembly of Replication Protein A on single-stranded DNA. *Nat. Commun.* **2018**, *9*.

276. Fan, J.; Pavletich, N. P. Structure and conformational change of a replication protein A heterotrimer bound to ssDNA. *Genes Dev.* **2012**, *26* (20), 2337-2347.

277. Madru, C.; Martinez-Carranza, M.; Laurent, S.; Alberti, A. C.; Chevreuil, M.; Raynal, B.; Haouz, A.; Le Meur, R. A.; Delarue, M.; Henneke, G.; et al. DNA-binding mechanism and evolution of replication protein A. *Nat. Commun.* **2023**, *14* (1).

278. Gränz, M.; Erlenbach, N.; Spindler, P.; Gophane, D. B.; Stelzl, L. S.; Sigurdsson, S. T.; Prisner, T. F. Dynamics of nucleic acids at room temperature revealed by pulsed EPR spectroscopy. *Angew. Chem. Int. Ed.* **2018**, *57* (33), 10540-10543.

279. Shevelev, G. Y.; Krumkacheva, O. A.; Lomzov, A. A.; Kuzhelev, A. A.; Rogozhnikova, O. Y.; Trukhin, D. V.; Troitskaya, T. I.; Tormyshev, V. M.; Fedin, M. V.; Pyshnyi, D. V.; et al. Physiological-temperature distance measurement in nucleic acid using triarylmethyl-based spin labels and pulsed dipolar EPR spectroscopy. *J. Am. Chem. Soc.* **2014**, *136* (28), 9874-9877.

280. Yang, Z. Y.; Liu, Y. P.; Borbat, P.; Zweier, J. L.; Freed, J. H.; Hubbell, W. L. Pulsed ESR dipolar spectroscopy for distance measurements in immobilized spin labeled proteins in liquid solution. *J. Am. Chem. Soc.* **2012**, *134* (24), 9950-9952.

281. Kuzhelev, A. A.; Shevelev, G. Y.; Krumkacheva, O. A.; Tormyshev, V. M.; Pyshnyi, D. V.; Fedin, M. V.; Bagryanskaya, E. G. Saccharides as prospective immobilizers of nucleic acids for room-temperature structural EPR studies. *J. Phys. Chem. Lett.* **2016**, *7* (13), 2544-2548.

282. Meyer, V.; Swanson, M. A.; Clouston, L. J.; Boratynski, P. J.; Stein, R. A.; Mchaourab, H. S.; Rajca, A.; Eaton, S. S.; Eaton, G. R. Room-temperature distance measurements of immobilized spin-labeled protein by DEER/PELDOR. *Biophys. J.* **2015**, *108* (5), 1213-1219.

283. Schaefer, J. S.; Klein, J. R. Roquin--a multifunctional regulator of immune homeostasis. *Genes Immun.* **2016**, *17* (2), 79-84.

284. Binas, O.; Tants, J.-N.; Peter, S. A.; Janowski, R.; Davydova, E.; Braun, J.; Niessing, D.; Schwalbe, H.; Weigand, J. E.; Schlundt, A. Structural basis for the recognition of transiently structured AU-rich elements by Roquin. *Nucl. Acids Res.* **2020**, *48* (13), 7385-7403.

285. Braun, J.; Fischer, S.; Xu, Z. Z.; Sun, H.; Ghoneim, D. H.; Gimbel, A. T.; Plessmann, U.; Urlaub, H.; Mathews, D. H.; Weigand, J. E. Identification of new high affinity targets for Roquin based on structural conservation. *Nucl. Acids Res.* **2018**, *46* (22), 12109-12125.

286. Klöcker, N.; Weissenboeck, F. P.; Rentmeister, A. Covalent labeling of nucleic acids. *Chem. Soc. Rev.* **2020**, *49* (23), 8749-8773.

287. Xu, W.; Chan, K. M.; Kool, E. T. Fluorescent nucleobases as tools for studying DNA and RNA. *Nat. Chem.* **2017**, *9* (11), 1043-1055.

288. Ward, D. C.; Reich, E.; Stryer, L. Fluorescence studies of nucleotides and polynucleotides: I. Formycin, 2-Aminopurine riboside, 2,6-Diaminopurine riboside, and their derivatives. *J. Biol. Chem.* **1969**, *244* (5), 1228-1237.

289. Lobsiger, S.; Blaser, S.; Sinha, R. K.; Frey, H. M.; Leutwyler, S. Switching on the fluorescence of 2-aminopurine by site-selective microhydration. *Nat. Chem.* **2014**, *6* (11), 989-993.

290. Wilhelmsson, L. M.; Holmén, A.; Lincoln, P.; Nielsen, P. E.; Nordén, B. A highly fluorescent DNA base analogue that forms Watson−Crick base pairs with guanine. *J. Am. Chem. Soc.* **2001**, *123* (10), 2434-2435.

291. Sandin, P.; Börjesson, K.; Li, H.; Martensson, J.; Brown, T.; Wilhelmsson, L. M.; Albinsson, B. Characterization and use of an unprecedentedly bright and structurally non-perturbing fluorescent DNA base analogue. *Nucl. Acids Res.* **2008**, *36* (1), 157-167.

292. Sigurdsson, S. T.; Gardarsson, H.; Cekan, P. Single base interrogation by a fluorescent nucleotide: Each of the DNA bases identified by fluorescence spectroscopy. *Biophys. J.* **2009**, *96* (3), 348a.

293. Cekan, P.; Sigurdsson, S. T. Conformation and dynamics of nucleotides in bulges and symmetric internal loops in duplex DNA studied by EPR and fluorescence spectroscopies. *Biochem. Biophys. Res. Commun.* **2012**, *420* (3), 656-661.

294. Gustmann, H.; Segler, A. L. J.; Gophane, D. B.; Reuss, A. J.; Grünewald, C.; Braun, M.; Weigand, J. E.; Sigurdsson, S. T.; Wachtveitl, J. Structure guided fluorescence labeling reveals a two-step binding mechanism of neomycin to its RNA aptamer. *Nucl. Acids Res.* **2019**, *47* (1), 15-28.

295. van der Meer, B. W. Kappa-squared: from nuisance to new sense. *Rev. Mol. Biotechnol.* **2002**, *82* (3), 181-196.

296. Vogel, S. S.; van der Meer, B. W.; Blank, P. S. Estimating the distance separating fluorescent protein FRET pairs. *Methods* **2014**, *66* (2), 131-138.

297. Segler, A. L. J. Synthesis of DNA and RNA containing rigid spin- and fluorescent labels for studies by EPR and fluorescence spectroscopies. Ph.D. Dissertation, University of Iceland, 2021.

298. Weigand, J. E.; Sanchez, M.; Gunnesch, E. B.; Zeiher, S.; Schroeder, R.; Suess, B. Screening for engineered neomycin riboswitches that control translation initiation. *RNA* **2008**, *14* (1), 89-97.

299. Heel, S. V.; Bartosik, K.; Juen, F.; Kreutz, C.; Micura, R.; Breuker, K. Native top-down mass spectrometry uncovers two distinct binding motifs of a functional neomycin-sensing riboswitch aptamer. *J. Am. Chem. Soc.* **2023**, *145* (28), 15284-15294.

300. Lyu, C.; Khan, I. M.; Wang, Z. Capture-SELEX for aptamer selection: A short review. *Talanta* **2021**, *229*, 122274.

Paper I

Paper I. Tetra-substituted BDPA radicals via click-chemistry and application to liquid-state DNP

Ahmad IM, Roy P, Kuzhelev A and Sigurdsson ST, *Chem. Commun*. **2026**, 62, 10685-10689.

ChemComm

COMMUNICATION

View Article Online
View Journal | View Issue

Cite this: *Chem. Commun.*, 2026, **62**, 10685

Received 20th February 2026,
Accepted 2nd May 2026

DOI: 10.1039/d6cc01089j

rsc.li/chemcomm

Tetra-substituted BDPA radicals *via* click-chemistry and application to liquid-state DNP

Iram M. Ahmad, [a] Pralambika Roy, [a] Andrei Kuzhelev *[b] and Snorri Th. Sigurdsson *[a]

The 1,3-bisdiphenylene-2-phenylallyl (BDPA) radical is a promising polarizing agent for DNP NMR, but is limited by poor persistence. A divergent synthetic strategy, using copper(I)-catalyzed azide–alkyne cycloaddition, is presented for preparing tailored BDPA derivatives. A high-molecular-weight, sterically shielded BDPA-dendrimer showed improved persistence and the highest liquid-state DNP enhancement reported thus far.

Nuclear magnetic resonance (NMR) spectroscopy is an important analytical technique for investigating the structure and dynamics of biomolecules and materials.[1–4] However, a major drawback of NMR is its low sensitivity, which is due to the small energy difference between the ground and excited states of nuclear spins in a magnetic field. Dynamic nuclear polarization (DNP) NMR has emerged as a powerful technique to overcome this drawback, by transferring the much higher polarization of unpaired electrons to the nuclei of interest.[5–7] In DNP NMR, the sample is doped with a paramagnetic molecule, referred to as a polarizing agent, and irradiated with microwaves (μw) during signal acquisition.[8,9] Persistent organic radicals are the most commonly used polarizing agents.

Bis-nitroxide biradicals are a class of polarizing agents that are fairly easy to synthesize and have extensively been used for DNP at magnetic fields of 9.4 and 14.1 T.[10–14] AsymPol-POK (Fig. 1) is a prominent example for solid-state DNP in aqueous solutions, offering high DNP performance at these magnetic fields.[12,15] With recent technological advances, DNP NMR has been extended to even higher magnetic fields (≥18.8 T) in order to improve both the signal-to-noise ratio and signal resolution.[16] However, the performance of nitroxides drops at very high magnetic fields due to shorter electronic relaxation times and a concomitant broader EPR signal, which broadens linearly with the external magnetic field.[16,17] This results in reduced excitation of the electronic spins and thus, lower DNP enhancement. Moreover, loss of nuclear polarization through depolarization becomes prominent for nitroxides at very high fields.[18]

To overcome the drawbacks associated with nitroxides, carbon-based radicals like Finland trityl[18–20] and 1,3-bisdiphenylene-2-phenylallyl (BDPA)[21] (Fig. 1) have attracted attention as promising radicals for high field DNP-NMR. The isotropic *g*-values of carbon lead to a much lower or even non-existing depolarization.[18,21] Furthermore, the narrow EPR line of carbon radicals in the solid-state and their long electron spin–lattice relaxation times (T_{1e}) enable efficient saturation at comparatively lower microwave power.[16,22]

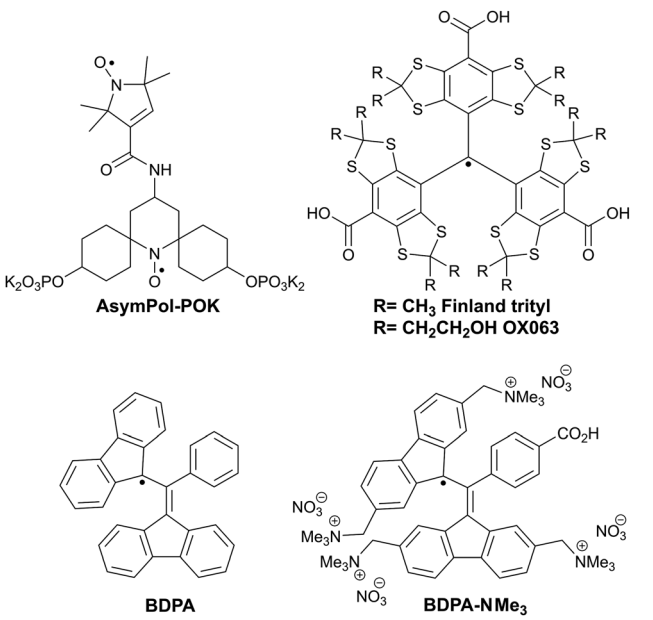

Fig. 1 Persistent radicals used as polarizing agents for DNP NMR: AsymPol-POK, Finland trityl, OX063, BDPA and trimethylammonium BDPA (BDPA-NMe_3).

[a] *University of Iceland, Department of Chemistry, Science Institute, Dunhaga 3, Reykjavik 107, Iceland. E-mail: snorrisi@hi.is*

[b] *Institute of Physical and Theoretical Chemistry and Center for Biomolecular Magnetic Resonance (BMRZ), Goethe University, 60438, Frankfurt am Main, Germany*

An advantage of the BDPA radical over the Finland trityl is its relative ease of synthesis.[23,24] Moreover, its EPR signal is narrower and more isotropic than the Finland trityl radical.[22] BDPA radicals have been used for DNP in both liquids and solids,[22,25–31] where they exhibit multiple polarization pathways. Traditionally, the Overhauser effect (OE) was considered exclusive to liquids, relying on fast molecular motion to mediate electron-nuclear cross-relaxation.[32,33] However, BDPA was shown to have the ability to operate in solids through the OE.[26,27] This behaviour has been linked to its mixed-valence character and intramolecular charge-transfer dynamics.[34] Furthermore, Kuzhelev *et al*. have also shown that BDPA monoradicals can polarize fluid lipid membranes and analytes in viscous solutions through the solid effect (SE) mechanism at high magnetic fields, previously only observed in solids.[29,30] When molecular tumbling of an analyte in solution is reduced,[30,35] electron-nuclear dipolar interactions slow down, which allows efficient polarization transfer and sizable signal enhancements.[36] Such polarization can also be observed for large molecules (with a long rotational correlation time) in aqueous solutions.[29,37] Thus, BDPA radicals exhibit versatile and interesting DNP properties for solid- and solution-state alike. Nonetheless, BDPA radicals have limitations.

Two major drawbacks of BDPA-based radicals have been their low persistence and limited solubility in aqueous solutions for use in structural biology.[38] A new class of tetraalkylammonium BDPA derivatives has partially addressed these shortcomings by providing more persistent radicals with tuneable solubility.[39] However, the water-soluble trimethylammonium BDPA derivative (BDPA-NMe_3) (Fig. 1), has limited persistence in aqueous solutions, probably due to the tendency of tetraalkylammonium salts to aggregate in water,[40–42] leading to dimerization.[38,39] Attaching bulky substituents to BDPA should reduce its tendency to aggregate and thereby enhance its stability.[43,44] Here we describe a convergent synthetic strategy that enables conjugation of a variety of different substituents to BDPA by Cu-catalyzed azide–alkyne cycloaddition (CuAAC) with a focus on the incorporation of hydrophilic and sterically demanding groups. This approach provides flexibility in preparing various substituted BDPA derivatives with tailored properties and complements the strategy of increasing the persistence of BDPA by changing the electronic properties of the aromatic rings.[45,46] Of the BDPA derivatives described here, a BDPA-conjugated dendrimer was particularly promising, with improved persistence in water and the highest reported DNP enhancement thus far in viscous liquids.

The synthetic strategy was based on the known tetrabromo BDPA derivative **1**[39] and its conversion to tetraazide BDPA **2** (Scheme 1). This tetraazide can be readily conjugated to various alkyne-bearing substituents by CuAAC, including hydrophilic and sterically demanding groups. We chose four different alkynes with distinct properties: propargyl alcohol (**3a**), which can be further derivatized; a polyhydroxyamide derivative (**3b**)[47] to use in sorbitol-based glass matrices for DNP; a glucose derivative (**3c**)[48] as a neutral and hydrophilic moiety that could provide some steric shielding; and a dendrimer alkyne (**3d**) to impart solubility and extensive steric effects (Scheme 1).

The synthesis began with the azidation of the tetrabromide **1**[39] to give the tetraazide BDPA derivative **2** in excellent yield (Scheme 1). The click reaction of **2** with the alkynes (**3a–d**) was straightforward, however, the purification of BDPA derivatives **4a–d** was challenging due to either limited solubility (**4a** and **4b**) or very high polarity (**4c** and **4d**). For derivatives **4a**, **4b** and **4c**, precipitation with Et_2O gave fairly pure products with good yields. Compound **4d** was purified by flash column chromatography. The corresponding BDPA radicals **5a–d** were prepared

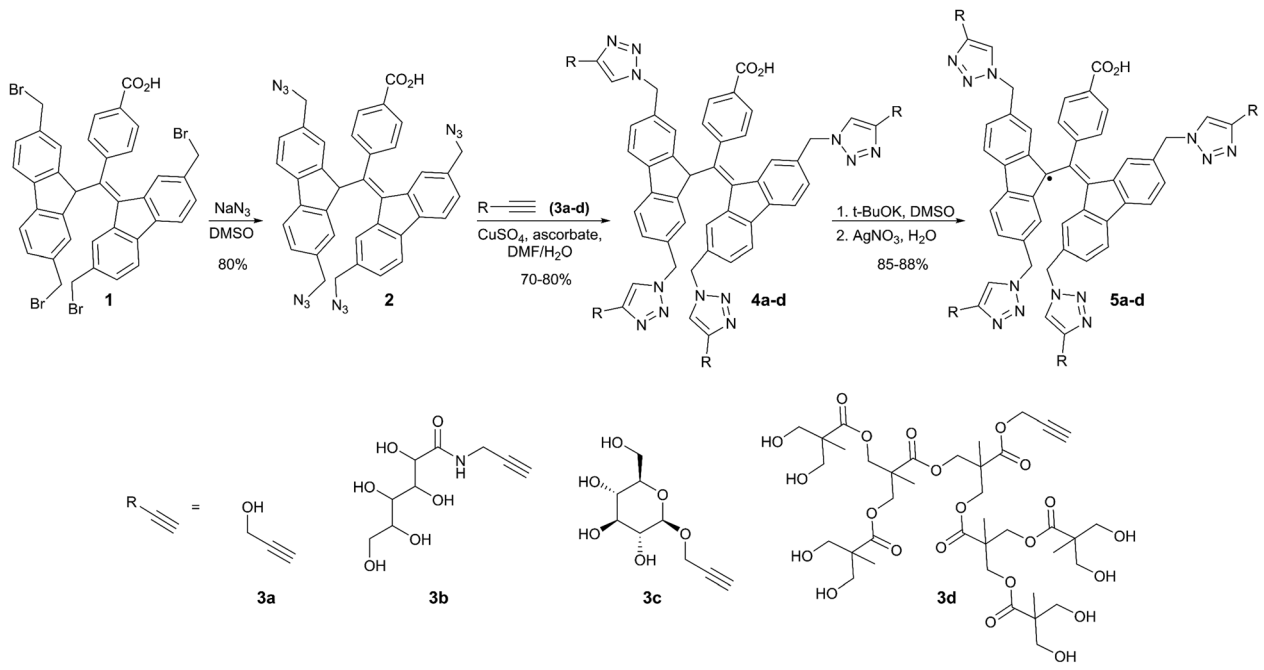

Scheme 1 Synthesis of water-soluble BDPA radicals **5a–d** *via* CuAAC of tetraazide **2** and their corresponding alkyne substrates **3a–d**.

by treating derivatives **4a–d** sequentially with *t*-BuOK and $AgNO_3$ (Scheme 1). Since compound **4d** was prone to hydrolysis in the presence of base, a shorter reaction time was used for the deprotonation with *t*-BuOK (see SI for details).

BDPA radicals **5a–d** were all soluble in DMSO, while only **5c** and **5d** were soluble in water. On the other hand, compound **5b** was unexpectedly insoluble in water, despite being a sugar-based derivative like **5c**. The insolubility of **5b** in water is likely due to a combination of intermolecular hydrogen bonding involving the carbohydrate moieties and π–π stacking of the BDPA cores. As anticipated, the tetrahydroxyl BDPA radical **5a** exhibited negligible solubility in water. However, the hydroxyl groups can be readily phosphorylated[12] or converted to sulfates to dramatically increase hydrophilicity.[49] Thus, the tetrasulfate derivative of **4a** was prepared and subsequently converted to the corresponding radical **7** in good overall yield (Scheme 2). The sulfate derivative **7** showed excellent solubility in water.

Based on its high molecular weight and good solubility in aqueous solutions, the BDPA-dendrimer radical (**5d**) was chosen for investigation of persistence and for evaluation as a polarizing agent. The persistence of **5d** in DMSO and water was determined by monitoring the radical concentration as a function of time by UV-Vis spectroscopy (Fig. 2).[39] Interestingly, the radical concentration **5d** unexpectedly increased in DMSO during the first three days, before reaching a plateau (Fig. 2A). This indicated that the that the radical precursor **4d**, which was still present in the sample of **5d**, was converted to the radical under these conditions. DMSO plays a key role, facilitating formation of the BDPA anion (change in color), which then converts to the radical. The same behaviour was also observed when **4d** was dissolved in DMSO, which ruled out possibility of oxidation of **5d** by residual oxidizing agent from the previous step (Fig. S27). Once the anion had been converted to the radical, it remained persistent in DMSO for at least 25 days (Fig. 2A).[39] The estimated half-life of **5d** in water was ~2 days, which was substantially longer that of BDPA-NMe_3 (<24 h (Fig. 2B). Since the liquid DNP experiments were performed in glycerol (see below), the persistence of **5d** in glycerol was also investigated (Fig. 2C); it showed a gradual degradation with an estimated half-life of ~8 days. No detectable

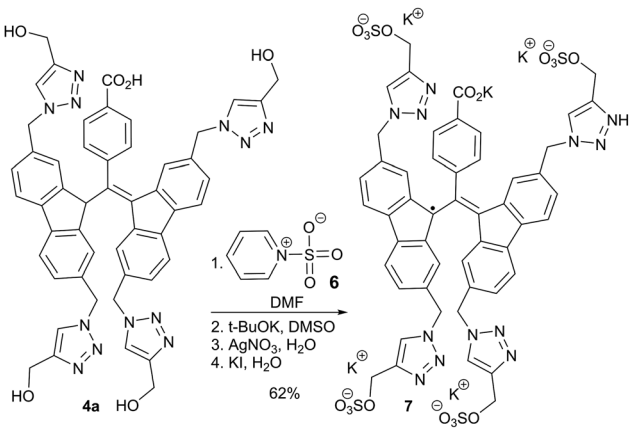

Scheme 2 Synthesis of BDPA-sulfate **7** from **4a**.

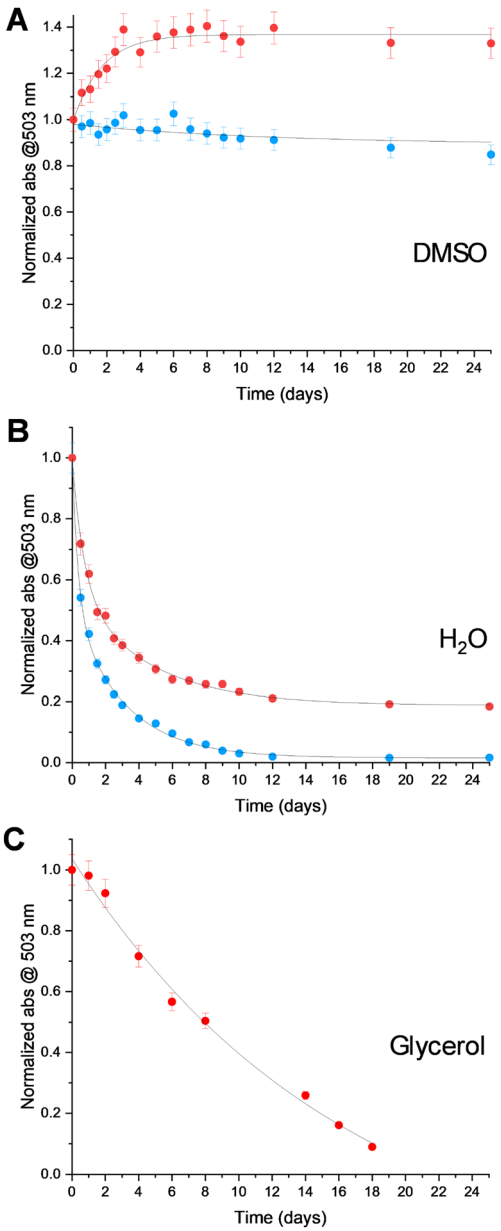

Fig. 2 Persistence of the trimethyl derivative of trialkylammonium BDPA (BDPA-NMe_3) (●) and BDPA-dendrimer **5d** (●) in DMSO (A) and H_2O (B), as well as **5d** in glycerol (C) at 23 °C, monitored by UV-Vis spectroscopy.[39] The concentration of the radicals were 10 mM by weight, but the absolute radical concentration, determined by spin-counting was 7.5 mM and 5.6 mM for BDPA-NMe_3 and BDPA-dendrimer **5d**, respectively.

decrease in the DNP enhancement (see below) was observed during measurements at 315 K over a period of 4 h.

As mentioned above, DNP NMR in viscous liquids is emerging as a valuable approach for solution-state NMR studies at high magnetic fields and room temperature.[35] When molecular tumbling of an analyte in solution is reduced, for example in viscous solvents,[30,35] electron-nuclear dipolar interactions slow down, which allows efficient polarization transfer and sizable signal enhancements.[36] Such polarization can also be observed for large molecules (with a long rotational correlation time) in

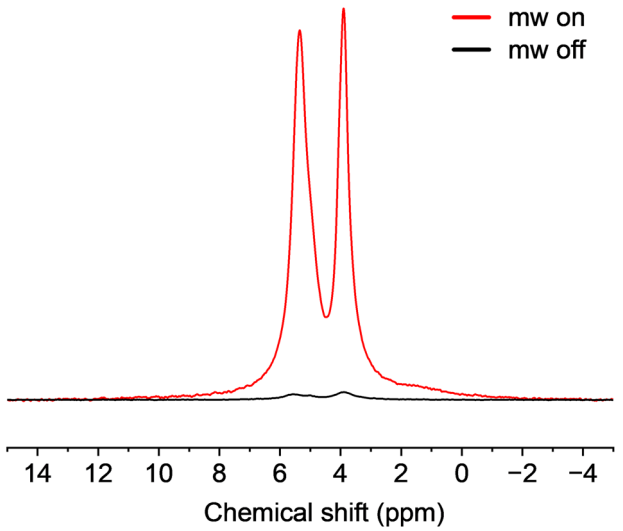

Fig. 3 ^{1}H-DNP-enhanced NMR signal of glycerol with BDPA-dendrimer **5d** at a concentration of 20 mM. Spectra were recorded at ∼315 K and 9.4 T with (red) and without (black) microwave irradiation at 263 GHz and 5 W of microwave power. The NMR signals are normalized with respect to the number of acquisitions.

aqueous solutions.[29,37] Carbon-based radicals like BDPA-NMe$_3$ and OX063 (Fig. 1) give enhancements through the SE pathway using this approach, correlating with molecular weight, with OX063 (M_W = 1360.8) showing the highest DNP performance.[30] Given the high molecular weight of BDPA-dendrimer **5d** (M_W = 4157.2), we investigated its DNP performance. At 9.4 T and 315 K, **5d** produced a ^{1}H DNP enhancement of 40 ± 5 at a concentration of 20 mM in glycerol (Fig. 3), a roughly twofold increase in DNP enhancement relative to OX063 (ε = 20 ± 3, 20 mM).[30] DNP performance was also evaluated at radical concentrations of 10 and 40 mM for **5d**, giving DNP enhancements of 18 ± 3 and 57 ± 6, respectively (Table S1). Although high viscosity leads to an increase in transverse relaxation rates and subsequent line broadening, using a viscous solvent is not a requirement for the DNP mechanism itself. Efficient polarization of small molecules, like ATP, can be achieved at viscosities only six times that of water, while larger biomolecules (∼15 kDa) possess sufficiently long rotational correlation times to exhibit sizable enhancements in pure aqueous solutions.[37] Glycerol was chosen here to enable a direct and quantitative comparison with the trityl-based radical OX063.[30]

In summary, we have developed a versatile click-based approach to prepare tetrasubstituted BDPA radicals, giving access to BDPA derivatives with tuneable size, solubility and stability. Among the four derivatives, BDPA-dendrimer **5d** stood out, showing improved persistence in both water and DMSO. Importantly, **5d** exhibited the best DNP performance reported thus far for ^{1}H DNP NMR in viscous liquids, with enhancements of 57 at 40 mM, making the BDPA-dendrimer a promising polarizing agent for liquid-state DNP NMR.

Conflicts of interest

There are no conflicts to declare.

Data availability

Data for this article are available at Zenodo.org at https://doi.org/10.5281/zenodo.17975646. The supporting data has been provided as part of the supplementary information (SI). Supplementary information is available. See DOI: https://doi.org/10.1039/d6cc01089j.

Acknowledgements

We thank Dr S. Jonsdottir and Dr Gunnar W. Reginsson for assistance with collecting analytical data for structural characterization of new compounds and members of the Sigurdsson research group for helpful discussions. S. Th. S. acknowledges financial support from the Icelandic Research Fund (239662). I. M. A. acknowledges the Aðalsteinn Kristjánsson Memorial Fund for providing the doctoral research fellowship. A. K. acknowledges the financial support from the European Union (ERC, LiquidStateDNP, 101219713). Views and opinions expressed are however those of the author(s) only and do not necessarily reflect those of the European Union or the European Research Council. Neither the European Union nor the granting authority can be held responsible for them.

References

1 A. G. M. Rankin, J. Trébosc, F. Pourpoint, J. P. Amoureux and O. Lafon, *Solid State Nucl. Magn. Reson.*, 2019, **101**, 116–143.
2 A. R. Camacho-Zarco, V. Schnapka, S. Guseva, A. Abyzov, W. Adamski, S. Milles, M. R. Jensen, L. Zidek, N. Salvi and M. Blackledge, *Chem. Rev.*, 2022, **122**, 9331–9356.
3 M. J. Zheng, Y. Y. Chu, Q. Wang, Y. X. Wang, J. Xu and F. Deng, *Prog. Nucl. Magn. Reson. Spectrosc.*, 2024, **140**, 1–41.
4 X. Lu, W. Myint, C. S. Muli, M. Larion, H. Matsuo and K. J. Walters, *J. Mol. Biol.*, 2025, **437**, 169302.
5 A. S. Lilly Thankamony, J. J. Wittmann, M. Kaushik and B. Corzilius, *Prog. Nucl. Magn. Reson. Spectrosc.*, 2017, **102–103**, 120–195.
6 B. Corzilius, *Annu. Rev. Phys. Chem.*, 2020, **71**, 143–170.
7 T. Biedenbänder, V. Aladin, S. Saeidpour and B. Corzilius, *Chem. Rev.*, 2022, **122**, 9738–9794.
8 M. Rosay, M. Blank and F. Engelke, *J. Magn. Reson.*, 2016, **264**, 88–98.
9 T. Maly and T. J. Keller, *Eur. Phys. J. A*, 2025, **61**, 18.
10 C. Sauvée, M. Rosay, G. Casano, F. Aussenac, R. T. Weber, O. Ouari and P. Tordo, *Angew. Chem., Int. Ed.*, 2013, **52**, 10858–10861.
11 A. Zagdoun, G. Casano, O. Ouari, M. Schwarzwälder, A. J. Rossini, F. Aussenac, M. Yulikov, G. Jeschke, C. Copéret, A. Lesage, P. Tordo and L. Emsley, *J. Am. Chem. Soc.*, 2013, **135**, 12790–12797.
12 F. Mentink-Vigier, I. Marin-Montesinos, A. P. Jagtap, T. Halbritter, J. van Tol, S. Hediger, D. Lee, S. T. Sigurdsson and G. De Paëpe, *J. Am. Chem. Soc.*, 2018, **140**, 11013–11019.
13 M.-A. Geiger, A. P. Jagtap, M. Kaushik, H. Sun, D. Stöppler, S. T. Sigurdsson, B. Corzilius and H. Oschkinat, *Chem. – Eur. J.*, 2018, **24**, 13485–13494.
14 A. Lund, G. Casano, G. Menzildjian, M. Kaushik, G. Stevanato, M. Yulikov, R. Jabbour, D. Wisser, M. Renom-Carrasco, C. Thieuleux, F. Bernada, H. Karoui, D. Siri, M. Rosay, I. V. Sergeyev, D. Gajan, M. Lelli, L. Emsley, O. Ouari and A. Lesage, *Chem. Sci.*, 2020, **11**, 2810–2818.
15 T. Maly, G. T. Debelouchina, V. S. Bajaj, K. N. Hu, C. G. Joo, M. L. Mak-Jurkauskas, J. R. Sirigiri, P. C. van der Wel, J. Herzfeld, R. J. Temkin and R. G. Griffin, *J. Chem. Phys.*, 2008, **128**, 052211.
16 G. Menzildjian, J. Schlagnitweit, G. Casano, O. Ouari, D. Gajan and A. Lesage, *Chem. Sci.*, 2023, **14**, 6120–6148.
17 G. Mathies, M. A. Caporini, V. K. Michaelis, Y. Liu, K. N. Hu, D. Mance, J. L. Zweier, M. Rosay, M. Baldus and R. G. Griffin, *Angew. Chem., Int. Ed.*, 2015, **54**, 11770–11774.

18 F. Mentink-Vigier, G. Mathies, Y. Liu, A.-L. Barra, M. A. Caporini, D. Lee, S. Hediger, R. G. Griffin and G. De Paëpe, *Chem. Sci.*, 2017, **8**, 8150–8163.
19 Y. Liu, F. A. Villamena, A. Rockenbauer, Y. Song and J. L. Zweier, *J. Am. Chem. Soc.*, 2013, **135**, 2350–2356.
20 K. Sato, R. Hirao, I. Timofeev, O. Krumkacheva, E. Zaytseva, O. Rogozhnikova, V. M. Tormyshev, D. Trukhin, E. Bagryanskaya, T. Gutmann, V. Klimavicius, G. Buntkowsky, K. Sugisaki, S. Nakazawa, H. Matsuoka, K. Toyota, D. Shiomi and T. Takui, *J. Phys. Chem. A*, 2019, **123**, 7507–7517.
21 D. Wisser, G. Karthikeyan, A. Lund, G. Casano, H. Karoui, M. Yulikov, G. Menzildjian, A. C. Pinon, A. Purea, F. Engelke, S. R. Chaudhari, D. Kubicki, A. J. Rossini, I. B. Moroz, D. Gajan, C. Copéret, G. Jeschke, M. Lelli, L. Emsley, A. Lesage and O. Ouari, *J. Am. Chem. Soc.*, 2018, **140**, 13340–13349.
22 O. Haze, B. Corzilius, A. A. Smith, R. G. Griffin and T. M. Swager, *J. Am. Chem. Soc.*, 2012, **134**, 14287–14290.
23 T. J. Reddy, T. Iwama, H. J. Halpern and V. H. Rawal, *J. Org. Chem.*, 2002, **67**, 4635–4639.
24 E. L. Dane, T. Maly, G. T. Debelouchina, R. G. Griffin and T. M. Swager, *Org. Lett.*, 2009, **11**, 1871–1874.
25 L. Lumata, S. J. Ratnakar, A. Jindal, M. Merritt, A. Comment, C. Malloy, A. D. Sherry and Z. Kovacs, *Chem. – Eur. J.*, 2011, **17**, 10825–10827.
26 T. V. Can, M. A. Caporini, F. Mentink-Vigier, B. Corzilius, J. J. Walish, M. Rosay, W. E. Maas, M. Baldus, S. Vega, T. M. Swager and R. G. Griffin, *J. Chem. Phys.*, 2014, **141**, 064202.
27 S. R. Chaudhari, D. Wisser, A. C. Pinon, P. Berruyer, D. Gajan, P. Tordo, O. Ouari, C. Reiter, F. Engelke, C. Copéret, M. Lelli, A. Lesage and L. Emsley, *J. Am. Chem. Soc.*, 2017, **139**, 10609–10612.
28 A. Radaelli, H. A. I. Yoshihara, H. Nonaka, S. Sando, J. H. Ardenkjaer-Larsen, R. Gruetter and A. Capozzi, *J. Phys. Chem. Lett.*, 2020, **11**, 6873–6879.
29 A. A. Kuzhelev, D. Dai, V. Denysenkov and T. F. Prisner, *J. Am. Chem. Soc.*, 2022, **144**, 1164–1168.
30 A. A. Kuzhelev, V. Denysenkov, I. M. Ahmad, O. Y. Rogozhnikova, D. V. Trukhin, E. G. Bagryanskaya, V. M. Tormyshev, S. T. Sigurdsson and T. F. Prisner, *J. Am. Chem. Soc.*, 2023, **145**, 10268–10274.
31 M. Levien, L. M. Yang, A. van der Ham, M. Reinhard, M. John, A. Purea, J. Ganz, T. Marquardsen, I. Tkach, T. Orlando and M. Bennati, *Nat. Commun.*, 2024, **15**, 5904.
32 N. M. Loening, M. Rosay, V. Weis and R. G. Griffin, *J. Am. Chem. Soc.*, 2002, **124**, 8808–8809.
33 C. Griesinger, M. Bennati, H. M. Vieth, C. Luchinat, G. Parigi, P. Höfer, F. Engelke, S. J. Glaser, V. Denysenkov and T. F. Prisner, *Prog. Nucl. Magn. Reson. Spectrosc.*, 2012, **64**, 4–28.
34 S. Pylaeva, P. Marx, G. Singh, T. D. Kuhne, M. Roemelt and H. Elgabarty, *J. Phys. Chem. A*, 2021, **125**, 867–874.
35 D. H. Dai, V. Denysenkov, E. G. Bagryanskaya, V. M. Tormyshev, T. F. Prisner and A. A. Kuzhelev, *J. Phys. Chem. Lett.*, 2023, **14**, 7059–7064.
36 D. Sezer, *Magn. Reson.*, 2023, **4**, 153–174.
37 A. Kuzhelev, *Anal. Chem.*, 2025, **97**, 14890–14893.
38 S. Mandal and S. T. Sigurdsson, *Chem. – Eur. J.*, 2020, **26**, 7486–7491.
39 S. Mandal and S. T. Sigurdsson, *Chem. Commun.*, 2020, **56**, 13121–13124.
40 T. Singh and A. Kumar, *J. Phys. Chem. B*, 2007, **111**, 7843–7851.
41 R. Atkin and G. G. Warr, *J. Phys. Chem. B*, 2008, **112**, 4164–4166.
42 R. Dutta, S. Kundu and N. Sarkar, *Biophys. Rev.*, 2018, **10**, 861–871.
43 Y. P. Liu, F. A. Villamena and J. L. Zweier, *Chem. Commun.*, 2008, 4336–4338, DOI: 10.1039/b807406b.
44 W. Liu, J. Nie, X. Tan, H. Liu, N. Yu, G. Han, Y. Zhu, F. A. Villamena, Y. Song, J. L. Zweier and Y. Liu, *J. Org. Chem.*, 2017, **82**, 588–596.
45 A. R. Birge, M. J. Piper, K. J. Painter and G. T. Sazama, *Results Chem.*, 2022, **4**, 100393.
46 H. Hamamoto, D. Shimizu and K. Matsuda, *Chem. – Eur. J.*, 2024, **30**, e202401353.
47 E. H. Ryu and Y. Zhao, *Org. Lett.*, 2005, **7**, 1035–1037.
48 A. L. M. Morotti, K. L. Lang, I. Carvalho, E. P. Schenkel and L. S. C. Bernardes, *Tetrahedron Lett.*, 2015, **56**, 303–307.
49 J. A. Alshehri and A. M. Jones, *Essays Biochem.*, 2024, **68**, 449–466.

Supporting Information

Tetra-substituted BDPA radicals via click-chemistry and application to liquid-state DNP

Iram M. Ahmad,[a] Pralambika Roy,[a] Andrei Kuzhelev,[b] Snorri Th. Sigurdsson*[a]

[a] *Department of Chemistry, Science Institute, University of Iceland, 107 Reykjavik, Iceland*
[b] *Institute of Physical and Theoretical Chemistry and Center for Biomolecular Magnetic Resonance (BMRZ), Goethe University, 60438 Frankfurt am Main, Germany*

Table of Contents

List of Figures

List of abbreviations

Aq.	Aqueous
ATR	Attenuated Total Reflection
BDPA	1,3- Bisdiphenylene-2- phenylallyl
Calcd.	Calculated
CuAAC	Cu-catalyzed azide-alkyne cycloaddition
CW	Continuous wave
DMF	*N,N*-dimethylformamide
DMSO	Dimethylsulfoxide
DNP	Dynamic nuclear polarization
EPR	Electron paramagnetic resonance
ESI	Electrospray ionization
HPLC	High-performance liquid chromatography
HRMS	High resolution mass spectrometry
NMR	Nuclear magnetic resonance
Pet-ether	Petroleum ether
ppm	Parts per million
RP	Reverse phase
Satd.	Saturated
R_f	Retention factor
TLC	Thin layer chromatography

Synthetic procedure

General materials and methods

All commercially available reagents were purchased from Sigma-Aldrich Co., abcr GmbH, and Polymer Factory, and were used without further purification. Polyester-8-hydroxyl-1-acetylene bis-MPA dendron, Gen-3 (**3d**) was purchased from Polymer Factory. All moisture sensitive reactions were carried out in oven-dried glassware under an inert atmosphere of Ar. CH_2Cl_2 was dried over calcium hydride and freshly distilled before use. Reagent grade DMSO and DMF were dried over molecular sieves (3 Å). Thin layer chromatography (TLC) was carried out using glass plates pre-coated with silica gel (Kieselgel 60 F_{254}, 0.2 mm, Silicycle) and compounds were visualized using UV light. Column chromatography was performed using 230–400 mesh silica gel (Silicycle). ^{1}H- and ^{13}C-NMR spectra were recorded at the frequencies stated, using deuterated solvents as internal standards on a Bruker Avance 400 MHz and 600 MHz spectrometers. Radicals show broadening and loss of NMR signals due to their paramagnetic nature and therefore, those NMR spectra are not shown. Mass spectrometric analyses of all organic compounds were performed on an ESI-HRMS (Bruker, MicrOTOF-Q). EPR spectra were recorded on a MiniScope MS200 with following experimental parameters: 9.43 GHz, microwave power 1 mW, sweep width 12 mT, modulation 0.2 mT, 23 °C. Purity of all radicals was analysed on an analytical Agilent 1200 HPLC system using a NUCLEODUR C18 Pyramid 4.6 x 150 mm analytical column with UV detection at λ = 254 nm. Solvent gradients for analytical RP-HPLC were run at 1.0 mL/min using the following gradient: solvent A, 0.1% TFA in H_2O; solvent B, CH_3CN; 0-2 min isocratic 0% B, 10 min linear gradient to 100% B, 2 min linear gradient to 0% B, 2 min isocratic 0% B. The UV-Vis spectra were recorded on an Agilent Cary UV-Vis Multicell Peltier spectrophotometer. The IR spectra were recorded on a Thermo Scientific Nicolet iS50-ATR IR spectrometer.

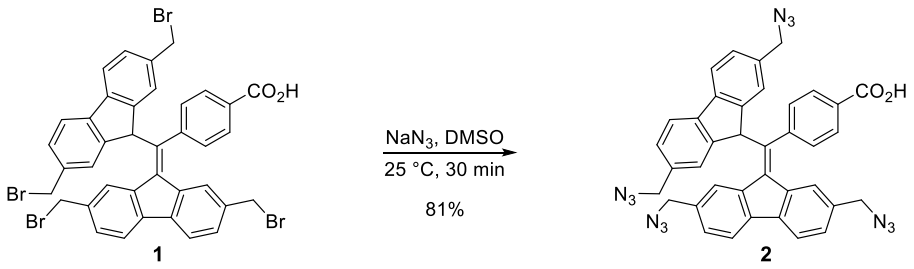

BDPA tetraazide 2. To a solution of compound **1**[1] (500 mg, 0.6 mmol) in DMSO (6 mL), was added NaN_3 (194.8 mg, 3.0 mmol) and the resulting solution was stirred at 23 °C for 30 min. The reaction was acidified with aq. HCl (1 N, 10 mL) and extracted with EtOAc (3 x 10 mL). The combined organic layers were washed with brine (2 x 20 mL), dried over Na_2SO_4 and concentrated *in vacuo*. The crude product was purified by flash-column chromatography using a gradient elution (CH_2Cl_2:MeOH; 100:0 to 98:02) to give **2** (331 mg, 81%) as an orange solid.

R_f (**1**) = 0.5, R_f (**2**) = 0.4 (CH_2Cl_2/MeOH 98:02); ^{1}H NMR (400 MHz, DMSO-d_6) δ 8.62 (s, 1H), 8.08 (d, J = 7.8 Hz, 1H), 7.93 (d, J = 7.8 Hz, 1H), 7.84 (d, J = 7.8 Hz, 2H), 7.71 (s, 2H), 7.56 (d, J = 8.2 Hz, 3H), 7.41 (dd, J = 7.8 Hz, 1.1 Hz, 2H), 7.25 (dd, J = 9.0 Hz, 1.1 Hz, 1H), 6.79 (d, J = 8.3 Hz, 2H), 6.62 (s, 1H), 5.61 (s, 1H), 4.56 (s, 2H), 4.46 (q, J = 7.8 Hz 2H), 4.02 (s, 2H) ppm; ^{13}C NMR (101 MHz, DMSO-d_6) δ 166.74, 144.38, 144.29, 142.35, 141.08, 140.12, 138.83, 138.48, 138.10, 135.33, 134.99, 134.76, 134.20, 129.81, 129.36, 128.73, 128.59, 128.44, 128.04, 126.37, 125.86, 124.52, 120.66, 119.97, 53.94, 53.71, 53.55, 51.89 ppm; IR (ATR, cm^{-1}): $\tilde{\nu}$ 2926.88 (s) (C-H), 2100 (vs) (N_3), 1694.06 (s) (C=O), 1417.13 (m) (C-C, aromatic) and 1240.41 (s) (C-O); HRMS (ESI): *m/z* calcd. for $C_{38}H_{26}N_{12}O_2$+Na$^+$ [M+Na$^+$] 705.2194, found 705.1864.

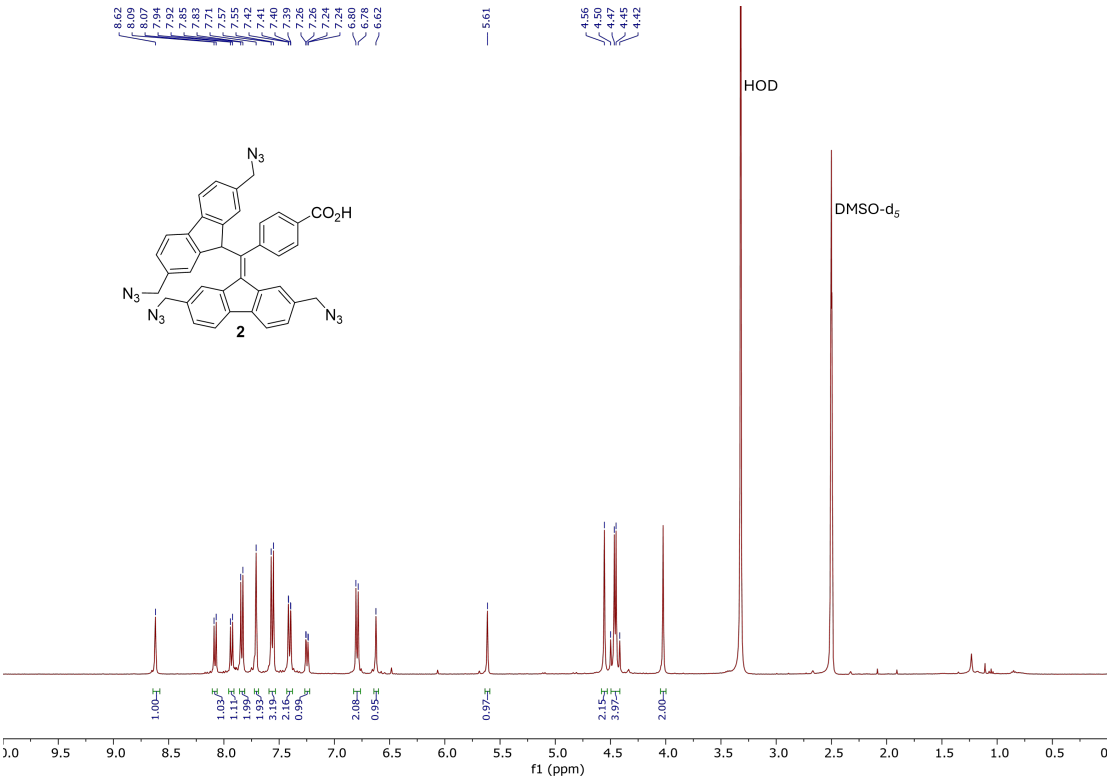

Figure S1. ^{1}H-NMR spectrum of compound BDPA tetraazide **2**.

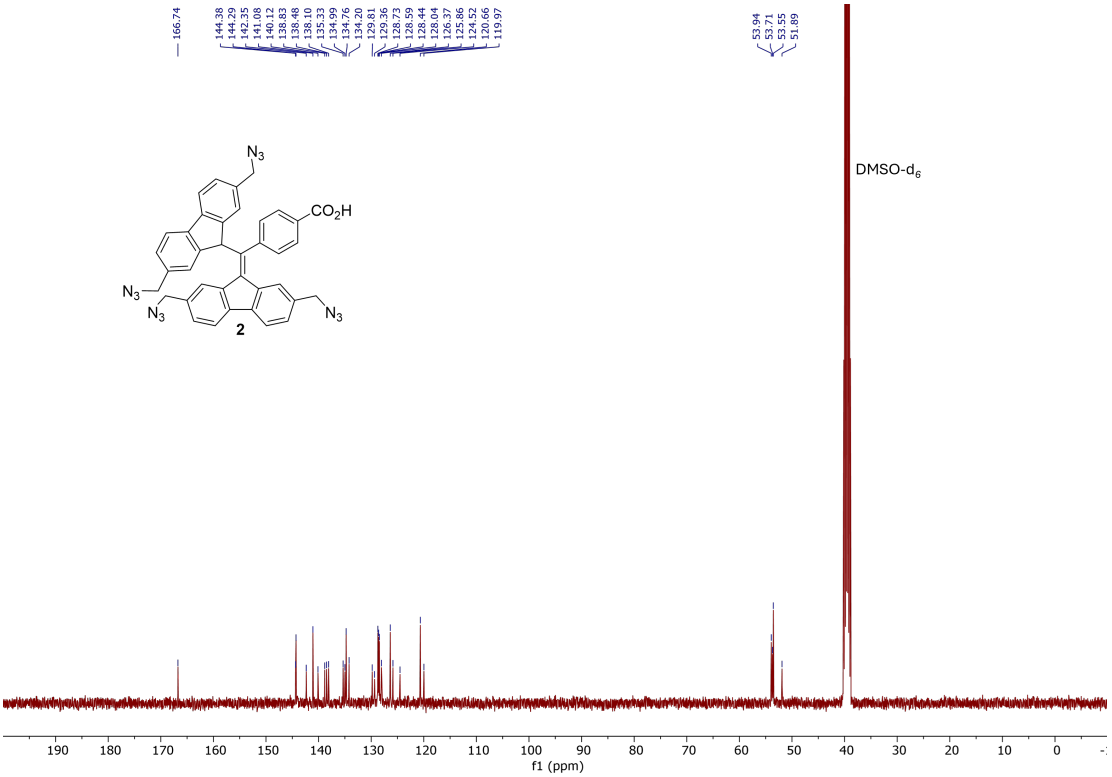

Figure S2. ^{13}C-NMR spectrum of BDPA tetraazide **2**.

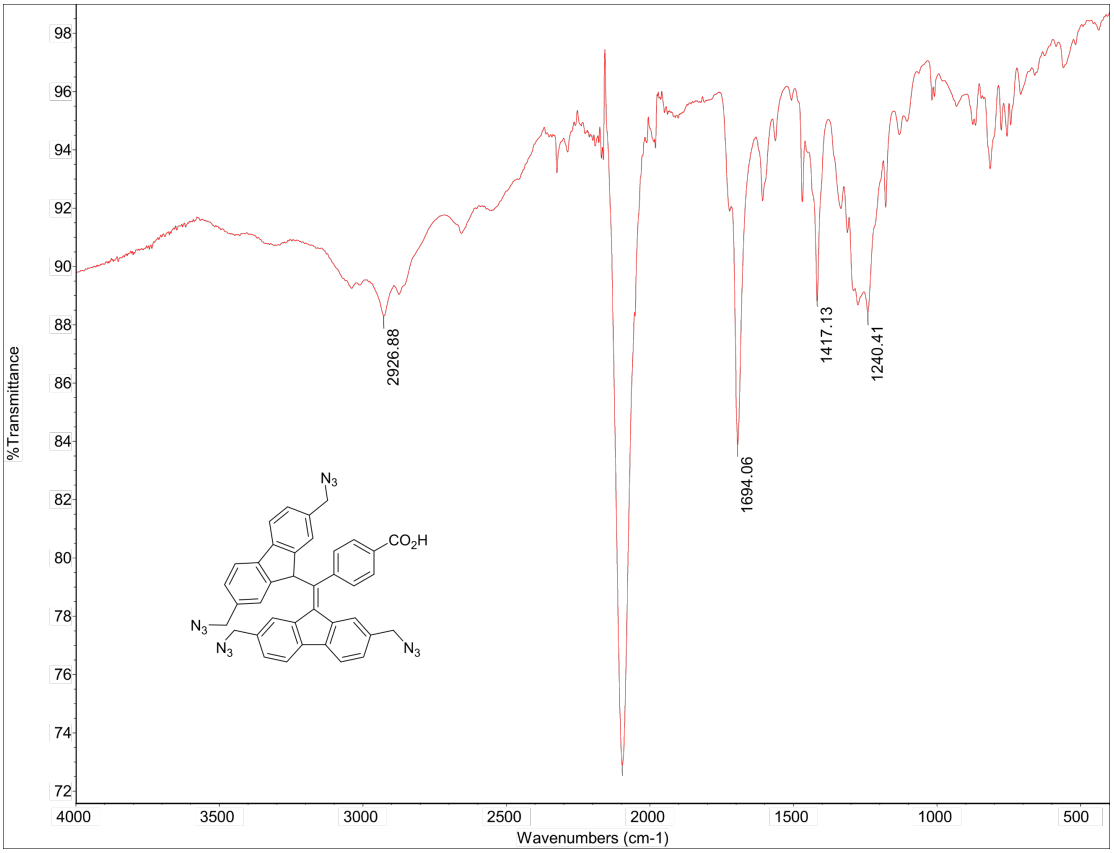

Figure S3. IR spectrum of BDPA tetraazide **2**.

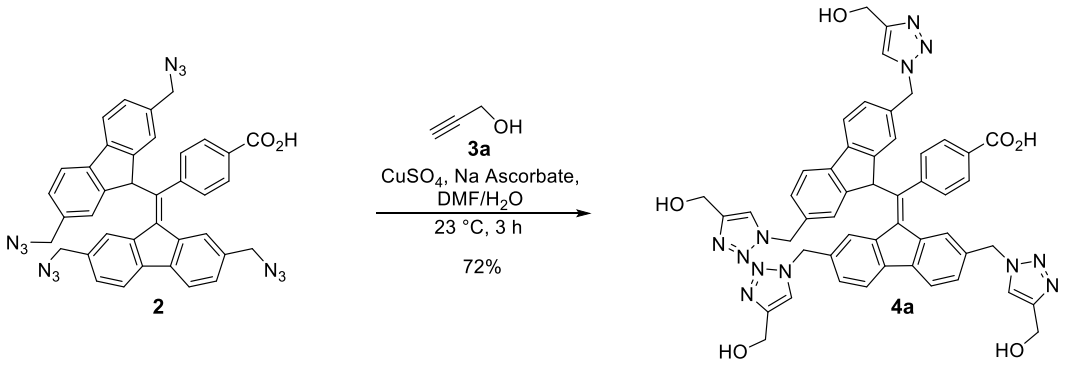

BDPA-OH 4a. To a solution of tetraazide **2** (60 mg, 0.088 mmol) in DMF (0.6 mL), was added a solution of sodium ascorbate (17.4 mg, 0.088 mmol) and $CuSO_4$ (4.4 mg, 0.018 mmol) in H_2O (0.2 mL) and the reaction mixture was stirred at 23 °C. After 5 min, propargyl alcohol **3a** (0.23 mL, 0.395 mmol) was added and the reaction mixture was stirred at 23 °C for 3h. The solvent was removed *in vacuo*, and the crude was washed with Et_2O (2 x 10 mL). The precipitate was collected by centrifugation, followed by decantation of the solvent. The precipitate was washed with H_2O (2 x 5 mL) and isolated again by centrifugation and decantation of the solvent. The precipitate was dissolved in DMSO (0.5 mL) and re-precipitated with Et_2O (10 mL). This step was repeated, and the precipitate was dried to give **4a** (57 mg, 72%) as a yellow solid.

^{1}H NMR (600 MHz, DMSO-d_6): δ 8.52 (s, 1H), 8.02 (d, *J* = 7.4 Hz, 2H), 7.97 (s, 2H), 7.90 (d, *J* = 7.9 Hz, 1H), 7.76 (d, *J* = 7.7 Hz, 2H), 7.63 (s, 2H), 7.50 (s, 1H), 7.47 (d, *J* = 7.9 Hz, 2H), 7.43 (d, *J* = 8.0 Hz, 1H), 7.32 (dd, *J* = 7.9, 1.5 Hz, 2H), 7.26 (dd, *J* = 7.9, 1.5 Hz, 1H), 6.59 (d, *J* = 7.9 Hz, 2H), 6.48 (s, 1H), 5.66 (s, 2H), 5.62 – 5.56 (m, 5H), 5.10 (s, 2H), 4.50 (s, 4H), 4.48 (s, 2H), 4.42 (s, 2H) ppm; ^{13}C NMR (151 MHz, DMSO-d_6): δ 148.28, 147.95, 144.44, 144.16, 140.81, 139.82, 138.81, 138.48, 138.04, 135.90, 135.30, 134.90, 134.47, 128.71, 128.49, 128.07, 128.04, 127.88, 125.97, 122.83, 122.60, 122.27, 120.55, 119.97, 55.00, 54.93, 54.82, 52.94, 52.84, 52.75, 51.88 ppm; IR (ATR, cm^{-1}): $\tilde{\nu}$ 3288.04 (s,b) (O-H, alcohol), 3145.06, 1654.88 (s) (C=O), 2930.58 (C-H), 1654.06 (s) (C=O), 1418.36 (m) (C-C, aromatic) and 1135.11 (s) (C-O); HRMS (ESI): *m/z* calcd. for $C_{50}H_{42}N_{12}O_6$+Na$^+$ [M+Na$^+$] 929.3242, found 929.3119.

HPLC:

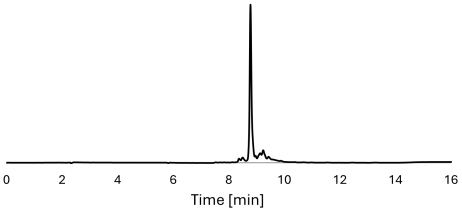

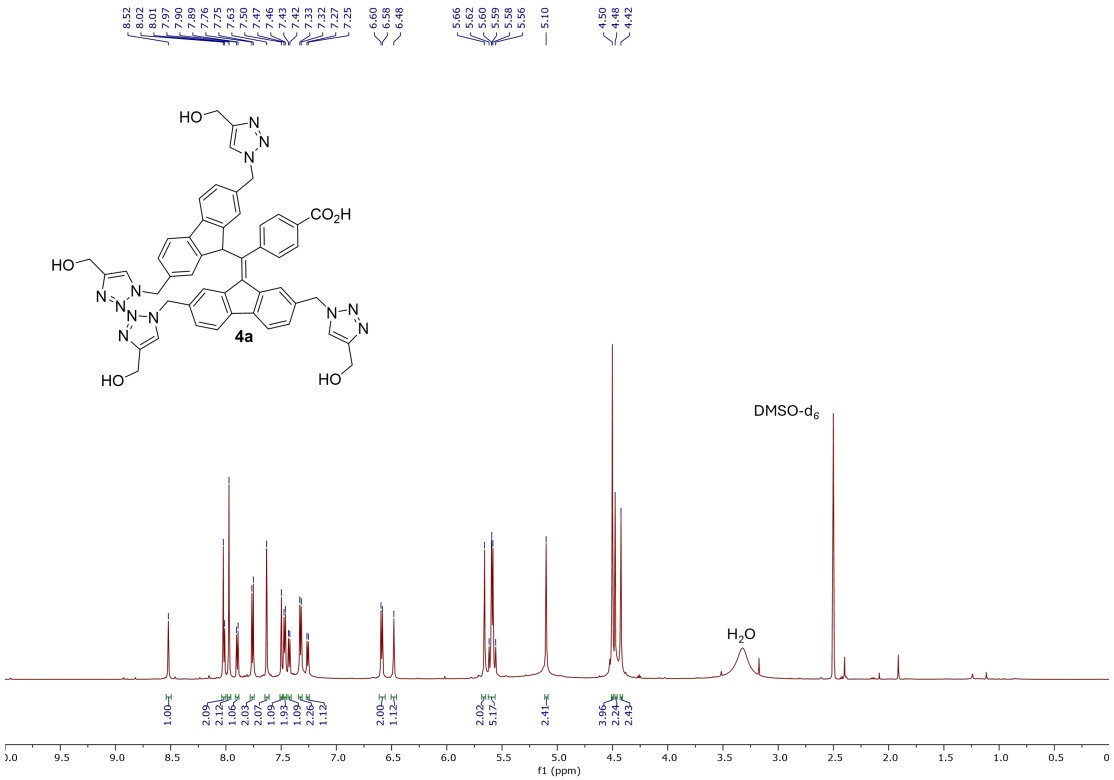

Figure S4. ^{1}H-NMR spectrum of compound **4a**.

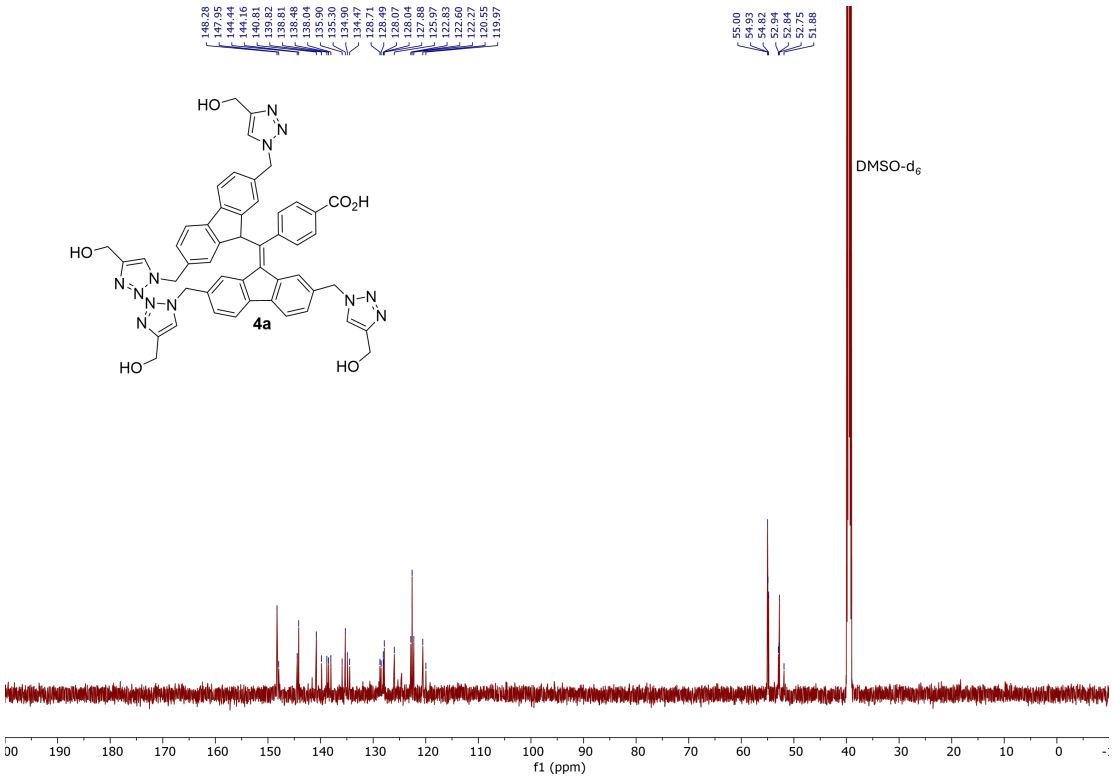

Figure S5. ^{13}C-NMR spectrum of compound **4a**.

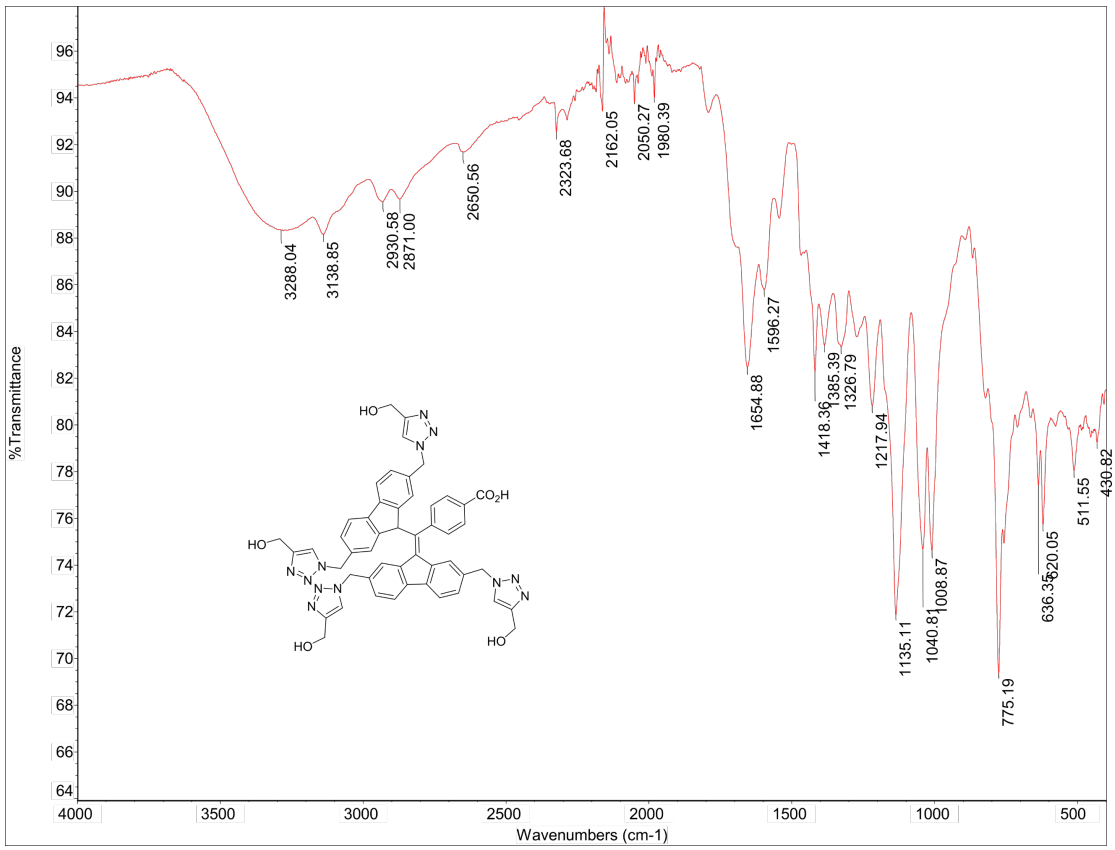

Figure S6. IR spectrum of compound **4a**.

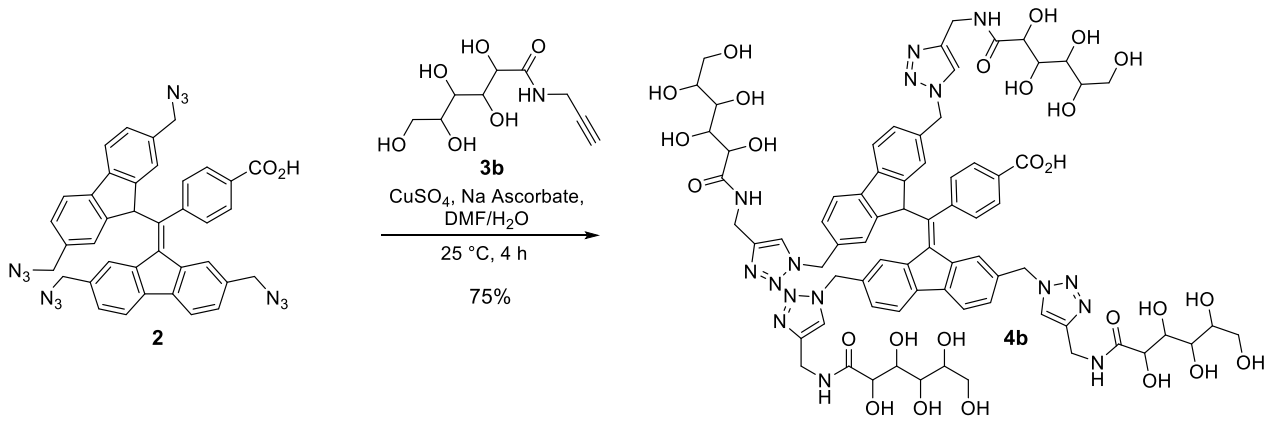

BDPA-hydroxyamide 4b. To a solution of tetraazide **2** (30 mg, 0.0439 mmol) in DMF (0.4 mL), was added a solution of sodium ascorbate (8.7 mg, 0.0439 mmol) and $CuSO_4$ (2.2 mg, 0.009 mmol) in H_2O (0.2 mL) at 23 °C. After 2 min a solution of *N*-2-propyn-1-yl-D-gluconamide **3b**[2] (40 mg, 0.198 mmol) in DMF (0.2 mL) was added and the reaction mixture was stirred at 23 °C for 4 h. The solvent was removed *in vacuo*, and the crude was washed with Et_2O (2 x 10 mL). The precipitate formed was collected by centrifugation, followed by decantation of the solvent. The precipitate was washed with H_2O (2 x 5 mL) and isolated again by centrifugation and decantation of the solvent. The precipitate was dissolved in 0.1% TFA H_2O: CH_3CN (7:1) and passed through C18 silica, followed by drying to afford **4b** (53 mg, 75%) as a brownish red solid.

^{1}H NMR (600 MHz, DMSO-d_6): δ 8.53 (s, 1H), 8.09-8.05 (m, , 3H), 8.03 – 7.98 (m, 3H), 7.95 (s, 2H), 7.89 (d, *J* = 7.8 Hz, 1H), 7.75 (d, *J* = 7.9 Hz, 2H), 7.63 (s, 2H), 7.55 (s, 1H), 7.48 (d, *J* = 7.9 Hz, 2H), 7.39 (d, *J* = 7.9 Hz, 1H), 7.29 (d, *J* = 7.9 Hz, 2H), 7.22 (d, *J* = 7.9 Hz, 1H), 6.63-6.61 (m, 2H), 6.49 (s, 1H), 5.66 (s, 2H), 5.61 – 5.56 (m, 5H), 5.38 (d, *J* = 4.7 Hz, 3H), 5.09 (s, 2H), 4.53 (s, 4H), 4.48 – 4.43 (m, 8H), 4.39-4.24 (m, 12H), 4.11 – 4.00 (m, 8H), 3.93 (s, 4H), 3.57 (d, *J* = 11.0 Hz, 4H), 3.48 (s, 9H) ppm; ^{13}C NMR (151 MHz, DMSO-d_6) δ 172.58, 166.83, 145.26, 145.22, 144.99, 144.41, 144.13, 141.90, 140.81, 139.84, 138.83, 138.46, 138.02, 135.84, 135.24, 134.91, 134.49, 134.42, 129.83, 128.74, 128.41, 128.17, 128.14, 127.89, 127.83, 126.03, 125.37, 124.52, 123.11, 122.93, 122.43, 120.64, 120.62, 120.58, 120.02, 118.03, 73.61, 72.25, 71.52, 70.16, 63.30, 52.99, 52.90, 52.82, 51.87 ppm; IR (ATR, cm^{-1}): $\tilde{\nu}$ 3296.48 (s,b) (O-H, alcohol), 2935.38 (C-H), 1647.66 (s) (C=O), 1418.83 (m) (C-C, aromatic) and 1123.61 (s) (C-O), 1051.19 (m) (C-N); HRMS (ESI): *m/z* calcd. for $C_{74}H_{86}N_{16}O_{26}$+2Na$^+$ [M+2Na$^+$] 830.2842, found 830.2794.

HPLC:

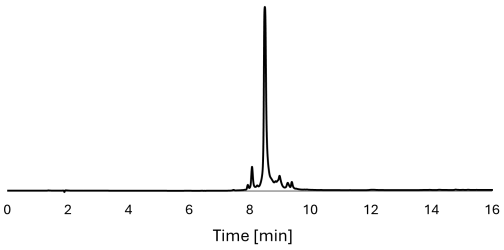

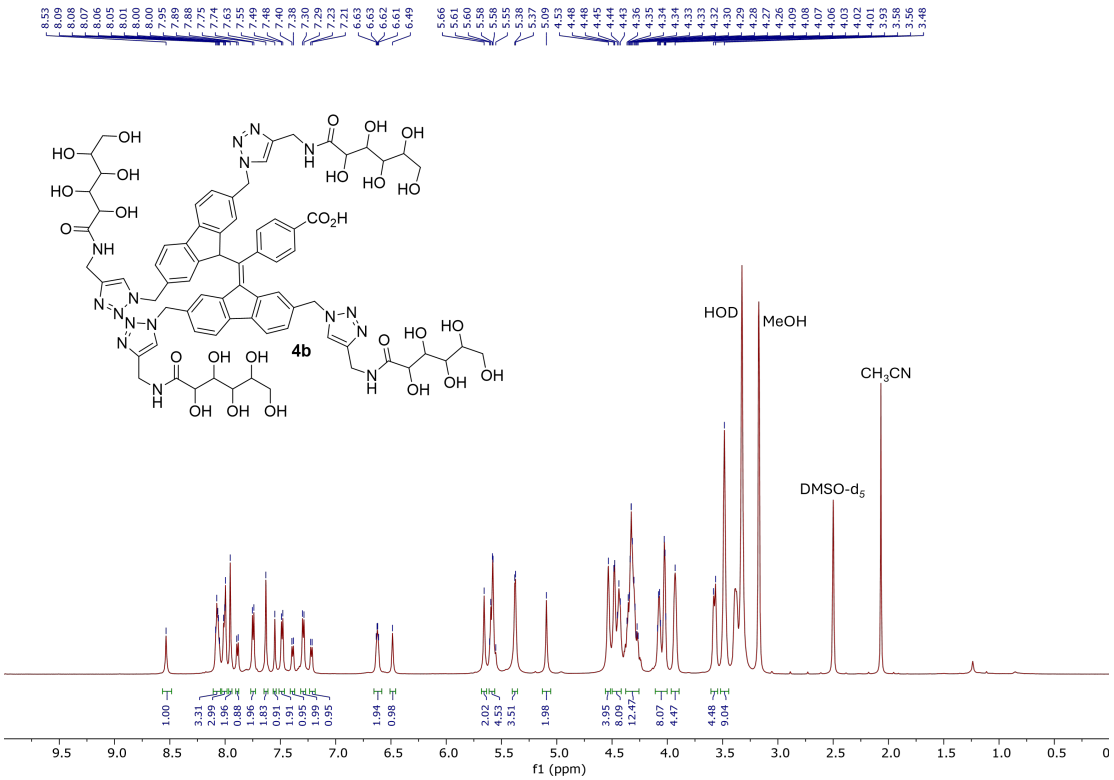

Figure S7. ^{1}H-NMR spectrufm of compound **4b**.

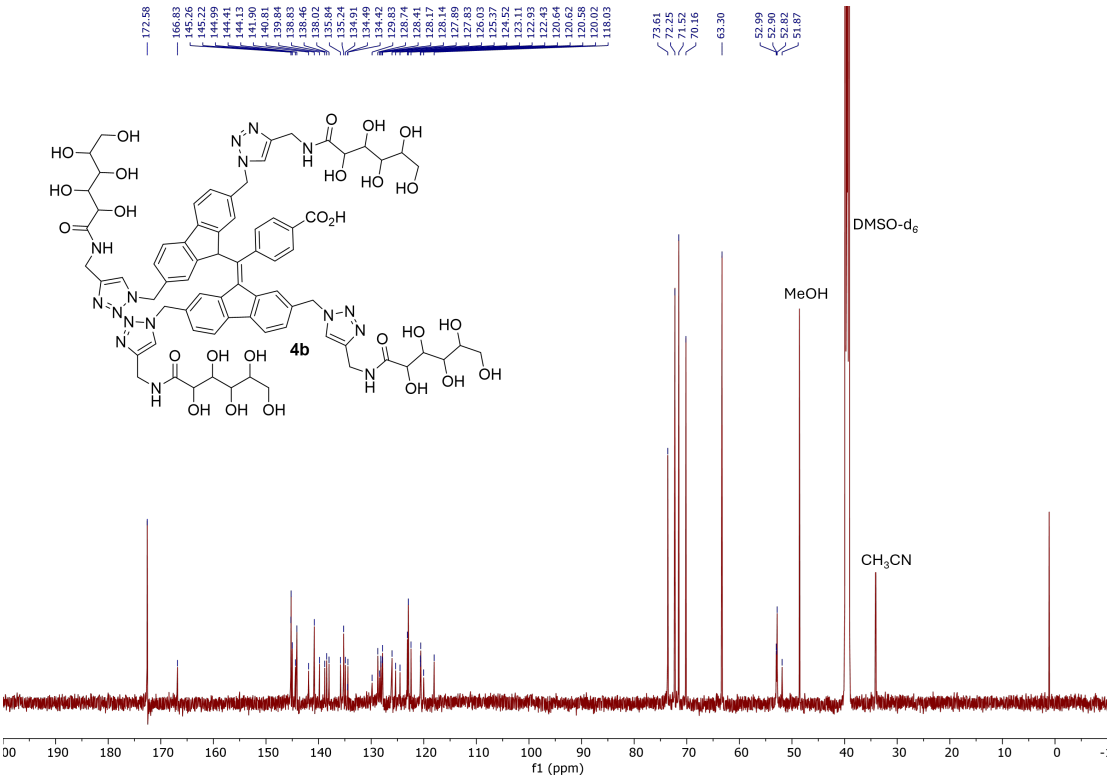

Figure S8. ^{13}C-NMR spectrum of compound **4b**.

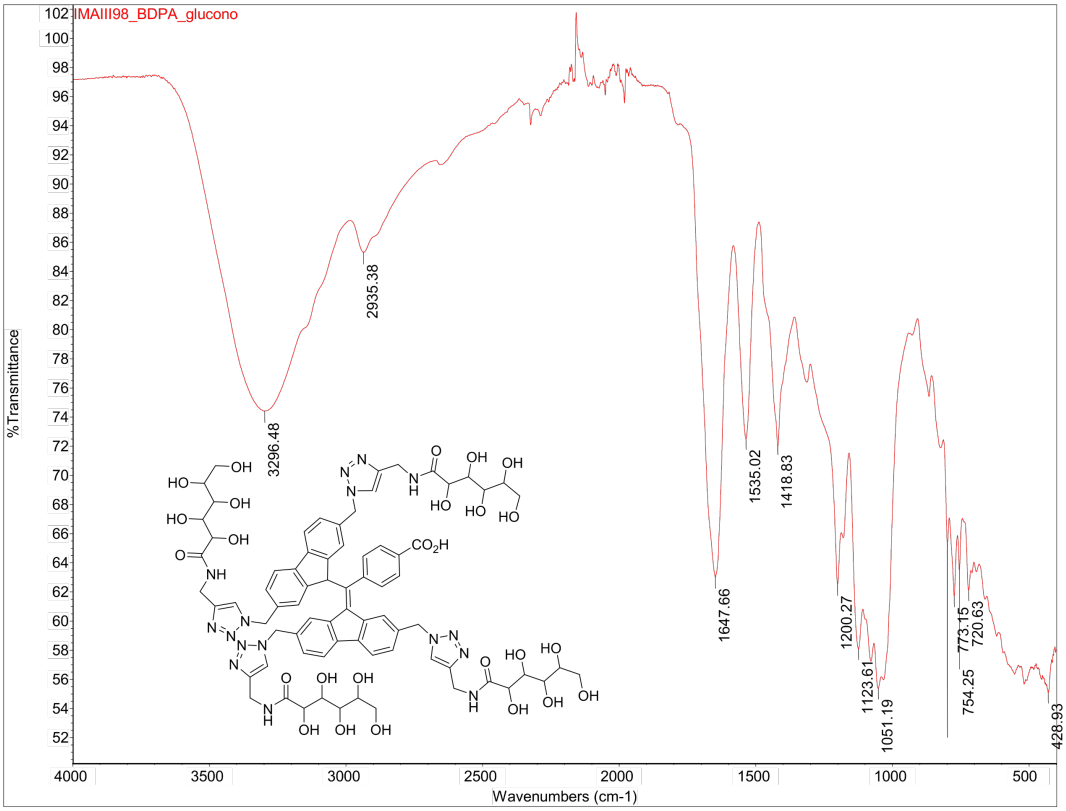

Figure S9. IR spectrum of compound **4b**.

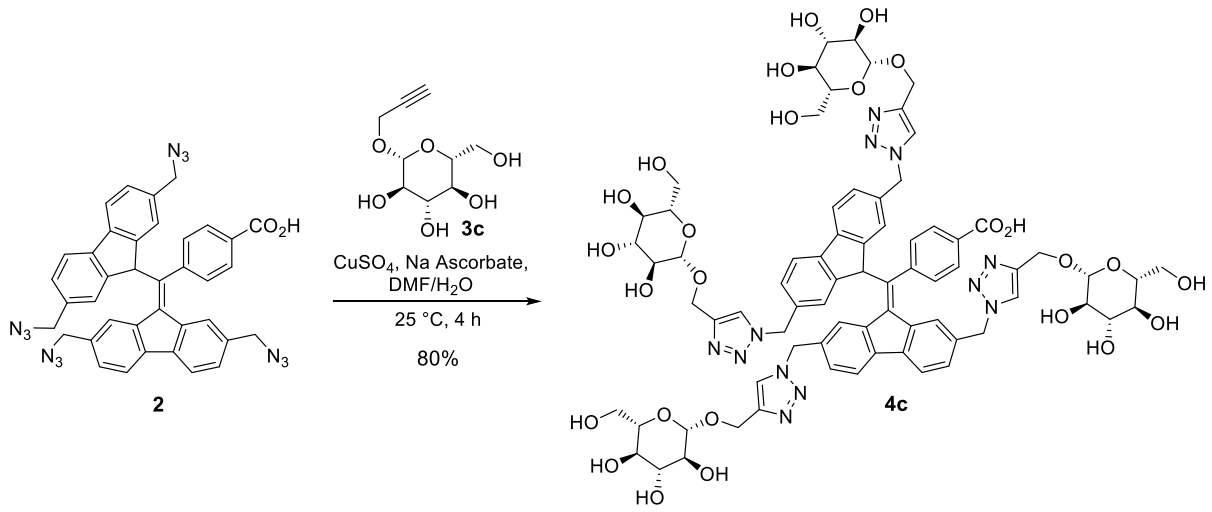

BDPA-glucose 4c. To a solution of tetraazide **2** (30 mg, 0.0439 mmol) in DMF (0.4 mL), was added a solution of sodium ascorbate (8.7 mg, 0.0439 mmol) and $CuSO_4$ (2.2 mg, 0.009 mmol) in H_2O (0.2 mL) at 23 °C. After 2 min a solution of 2-propyn-1-yl-β-D-glucopyranoside **3c**[3] (43.15 mg, 0.198 mmol) in DMF (0.2 mL) was added and the reaction mixture stirred at 23 °C for 4 h. The solvent was removed *in vacuo* and the crude was washed with Et_2O (20 mL). The precipitate was collected by centrifugation, followed by decantation of the solvent. The precipitate was dissolved in H_2O (0.25 mL) and re-precipitated with Et_2O (10 mL). The precipitate was dissolved in H_2O: CH_3CN (7:1) and passed through C18 silica, followed by drying *in vacuo* to afford **4c** (54.5 mg, 80%) as a reddish-orange solid.

^{1}H NMR (600 MHz, DMSO-d_6): δ 8.53 (s, 1H), 8.24 (s, 1H), 8.19 (s, 2H), 8.03 (d, *J* = 7.9 Hz, 1H), 7.90 (d, *J* = 7.8 Hz, 1H), 7.75 (dd, *J* = 7.9, 2.0 Hz, 2H), 7.73 (s, 1H), 7.63 (d, *J* = 7.3 Hz, 2H), 7.46-7.44 (m,, 3H), 7.32 (t, *J* = 7.9 Hz, 2H), 7.25 (d, *J* = 7.9 Hz, 1H), 6.64 – 6.59 (m, 2H), 6.49 (s, 1H), 5.69 (s, 2H), 5.69-5.58 (m, 6H), 5.14 (s, 2H), 4.85 – 4.81 (m, 5H), 4.77 (d, *J* = 12 Hz, 3H), 4.65 – 4.56 (m, 9H), 4.27 – 4.23 (m, 6H), 3.70-3.67 (m, 5H), 3.47 – 3.43 (m, 5H), 3.15-3.10 (m, 10H), 3.06-3.03 (m, 5H), 2.98-2.94 (m, 4H) ppm; ^{13}C NMR (151 MHz, DMSO-d_6) δ 166.69, 162.23, 144.29, 141.82, 140.77, 140.74, 139.80, 138.74, 138.38, 137.95, 135.64, 135.10, 135.08, 134.78, 134.33, 129.60, 128.66, 128.15, 128.08, 127.91, 127.81, 125.97, 125.34, 124.44, 124.01, 120.61, 120.52, 119.94, 102.20, 102.14, 102.12, 102.05, 76.82, 76.77, 76.59, 76.56, 73.27, 70.03, 70.00, 61.52, 61.44, 61.41, 61.25, 61.06, 61.04, 52.96, 52.86, 51.81 ppm; IR (ATR, cm^{-1}): $\tilde{\nu}$ 3297.29 (s,b) (O-H, alcohol), 2878.16 (C-H), 1652.92 (s) (C=O), 1050.19 (m) (C-O); HRMS (ESI): *m/z* calcd. for $C_{74}H_{82}N_{12}O_{26}$+Na^+ [M+Na^+] 1577.5355, found 1577.5250.

HPLC:

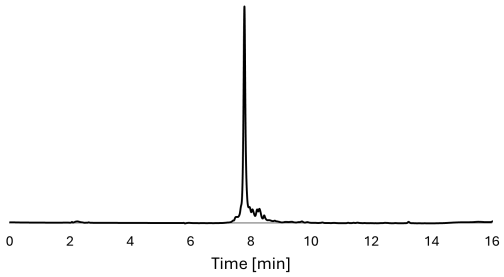

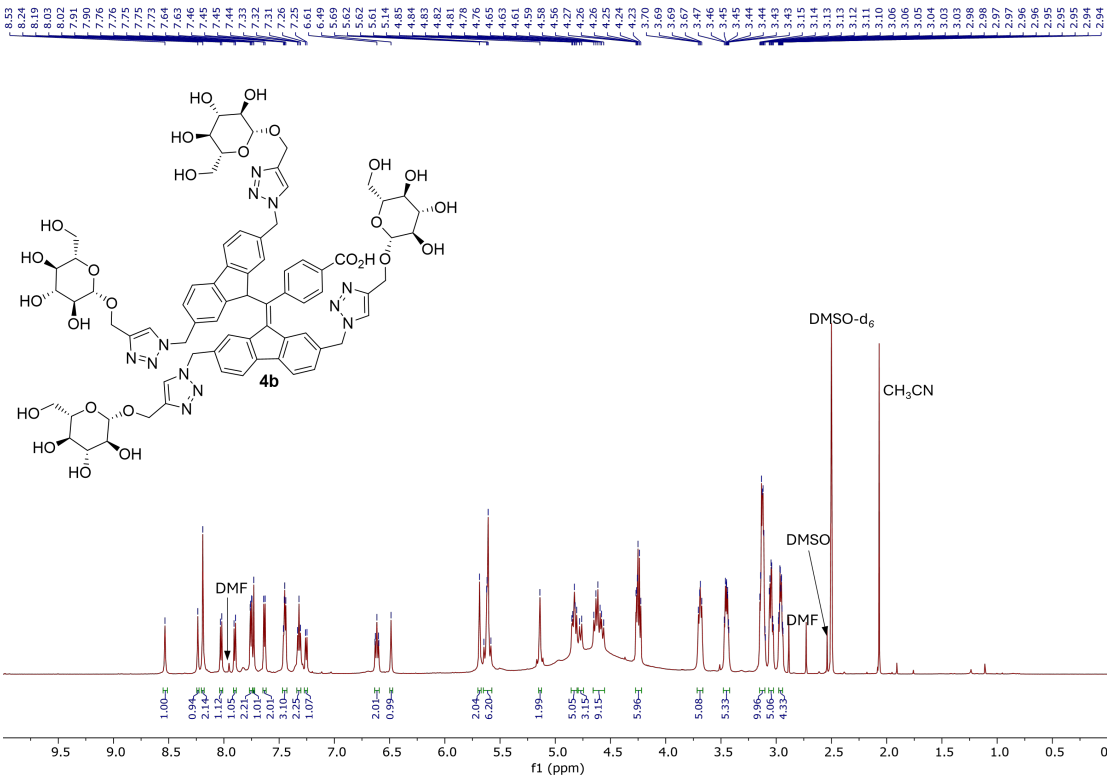

Figure S10. ^{1}H-NMR spectrum of compound **4c**.

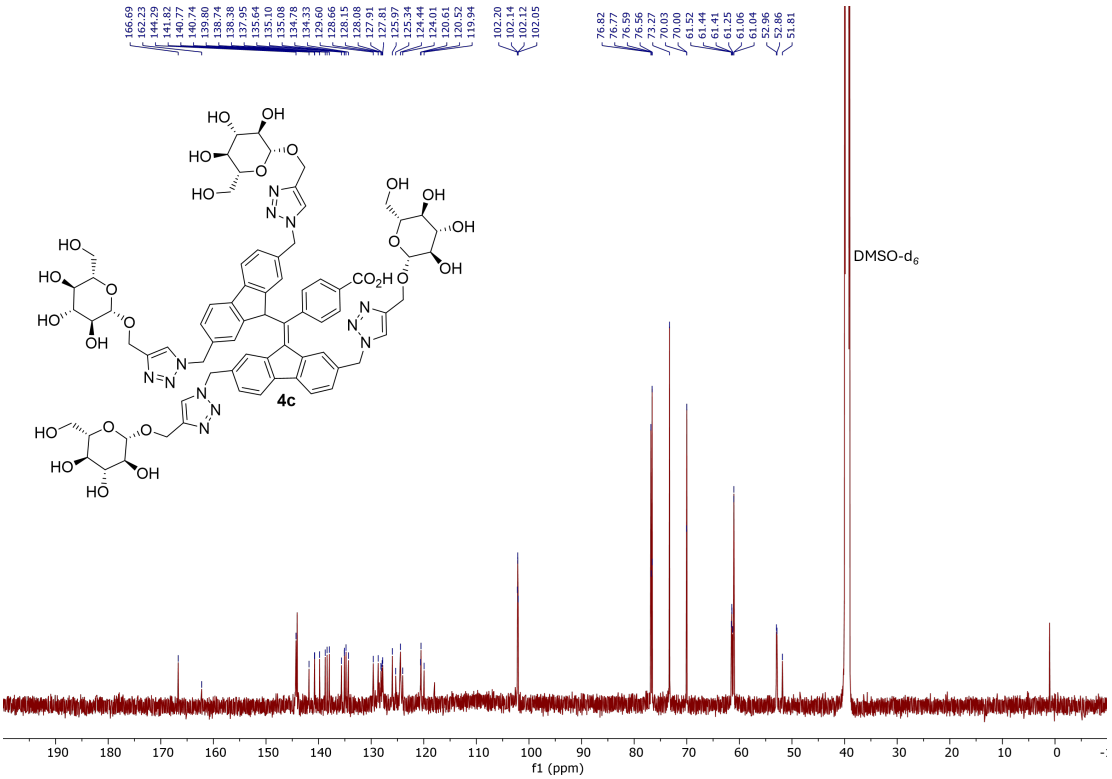

Figure S11. ^{13}C-NMR spectrum of compound **4c**.

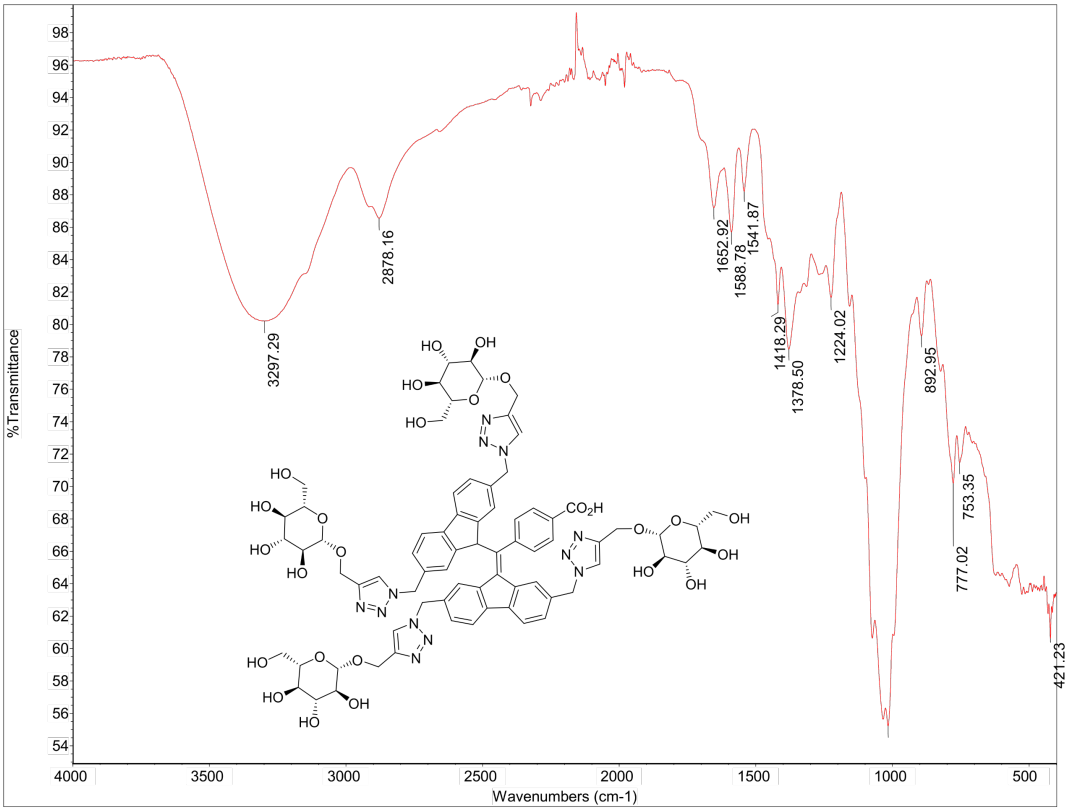

Figure S12. IR spectrum of compound **4c**.

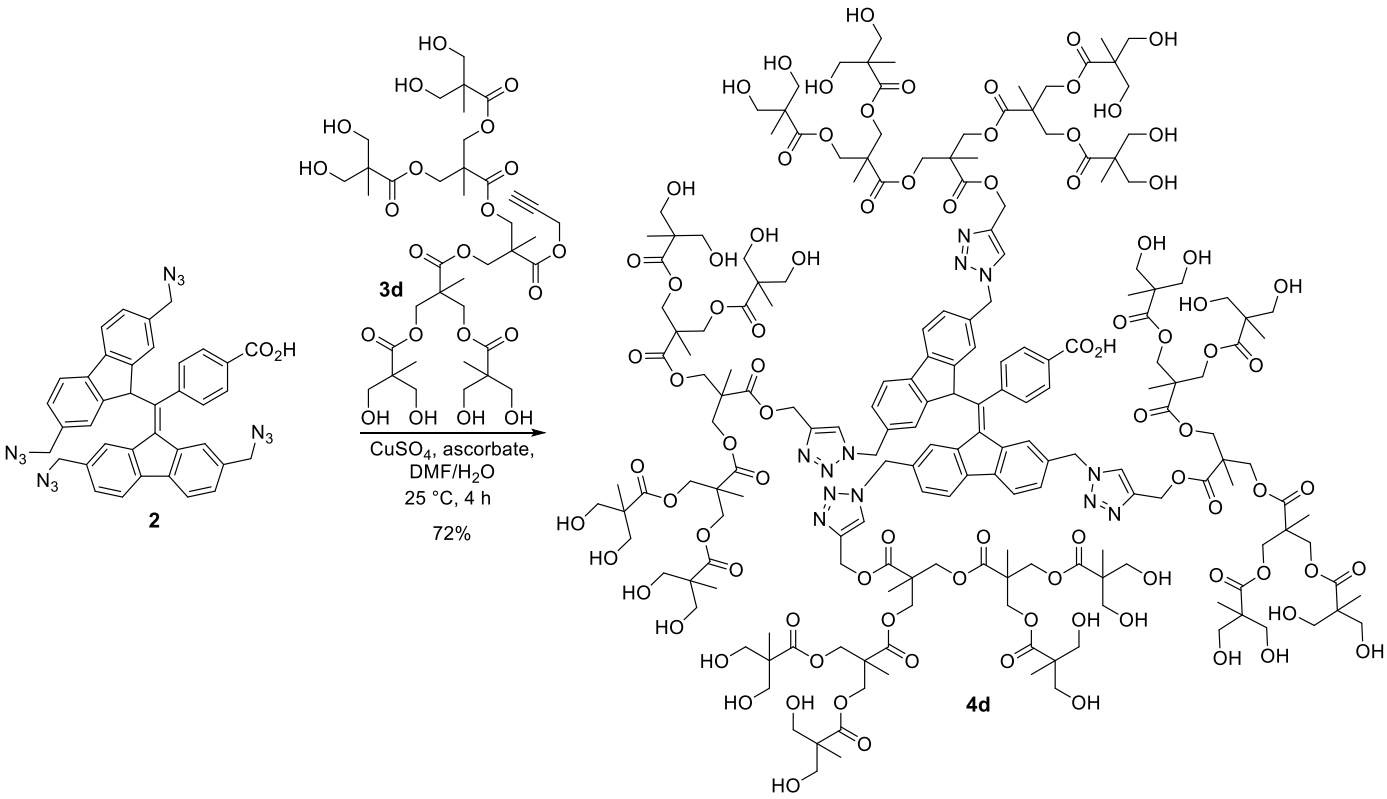

BDPA-dendrimer 4d. To a solution of compound **2** (20 mg, 0.029 mmol) in DMF (0.3 mL), was added a solution of sodium ascorbate (5.8 mg, 0.029 mmol) and $CuSO_4$ (1.5 mg, 0.0058 mmol) in H_2O (0.2 mL) at 23 °C. After 2 min a solution of alkyne dendrimer **3d** (112 mg, 0.1289 mmol) in DMF (0.3 mL) was added and the reaction mixture was stirred at 23 °C for 4 h. The solvent was removed *in vacuo,* and the crude was washed with Et_2O (20 x 2 mL). The reaction mixture was poured into Et_2O (10 mL), the precipitate collected by centrifugation, followed by decantation of the solvent. The precipitate was redissolved in MeOH (1 mL) and re-precipitated by addition of Et_2O (10 mL). The product was further purified by flash-column chromatography using a gradient elution (CH_2Cl_2:MeOH; 85:15 to 65:35) to give **4d** (1.08 g, 90%) as an orange solid.

R_f (**4d**) = 0.3 (CH_2Cl_2/ MeOH 7:3); ^{1}H NMR (400 MHz, Methanol-d_4): δ 8.26 (s, 1H), 8.18 (s, 1H), 8.10 (s, 2H), 8.00 (d, *J* = 7.9 Hz, 1H), 7.85 (d, *J* = 7.8 Hz, 1H), 7.77 (s, 1H), 7.74 (d, *J* = 2.3 Hz, 2H), 7.54 (t, *J* = 8.5 Hz, 3H), 7.48 (s, 2H), 7.38 (d, *J* = 7.9 Hz, 2H), 7.23 (d, *J* = 7.8 Hz, 1H), 6.55 (d, *J* = 8.1 Hz, 2H), 6.38 (s, 1H), 5.77 (d, *J* = 3.3 Hz, 3H), 5.73-5.64 (m, 5H), 5.32 (s, 2H), 5.27 (s, 4H), 5.19 (s, 2H), 5.09 (s, 2H), 4.34 – 4.15 (m, 63H), 3.71 – 3.65 (m, 40H), 3.62-3.57 (m, 32H), 1.31 – 1.28 (m, 10H), 1.26 – 1.19 (m, 39H), 1.14 (s, 33H), 1.13 (s, 10H).ppm; ^{13}C NMR (101 MHz, Methanol-d_4): δ 175.98, 175.95, 173.73, 173.69, 173.68, 173.63, 173.61, 146.97, 146.17, 143.85, 143.84, 143.44, 142.96, 141.98, 141.37, 140.73,

140.64, 140.32, 138.44, 136.54, 136.51, 136.13, 135.20, 132.36, 129.96, 129.48, 129.02, 128.98, 128.90, 126.88, 126.64, 126.54, 125.75, 121.95, 121.91, 121.16, 71.12, 69.19, 68.55, 67.21, 67.17, 66.88, 66.12, 65.78, 59.03, 58.94, 55.16, 54.96, 53.66, 51.78, 47.88, 47.86, 39.42, 33.04, 30.74, 25.98, 23.70, 19.51, 18.20, 18.16, 18.09, 18.04, 17.37, 15.43, 14.42 and 13.99 ppm; IR (ATR, cm^{-1}): $\tilde{\nu}$ 3369.88 (s,b) (O-H, alcohol), 2882.91 (C-H), 1723.61 (s) (C=O, ester), 1466.11 (m) (C-C), 1029.75 (m) (C-O); HRMS (ESI): *m/z* calcd. for $C_{190}H_{266}N_{12}O_{90}$ +4Na^+ [M+4Na^+] 1062.4060, found 1062.3909.

HPLC:

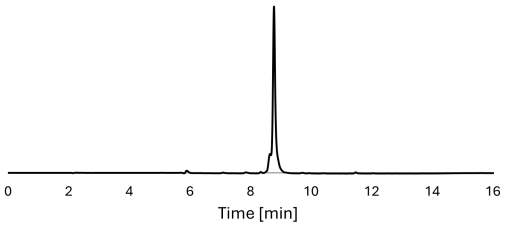

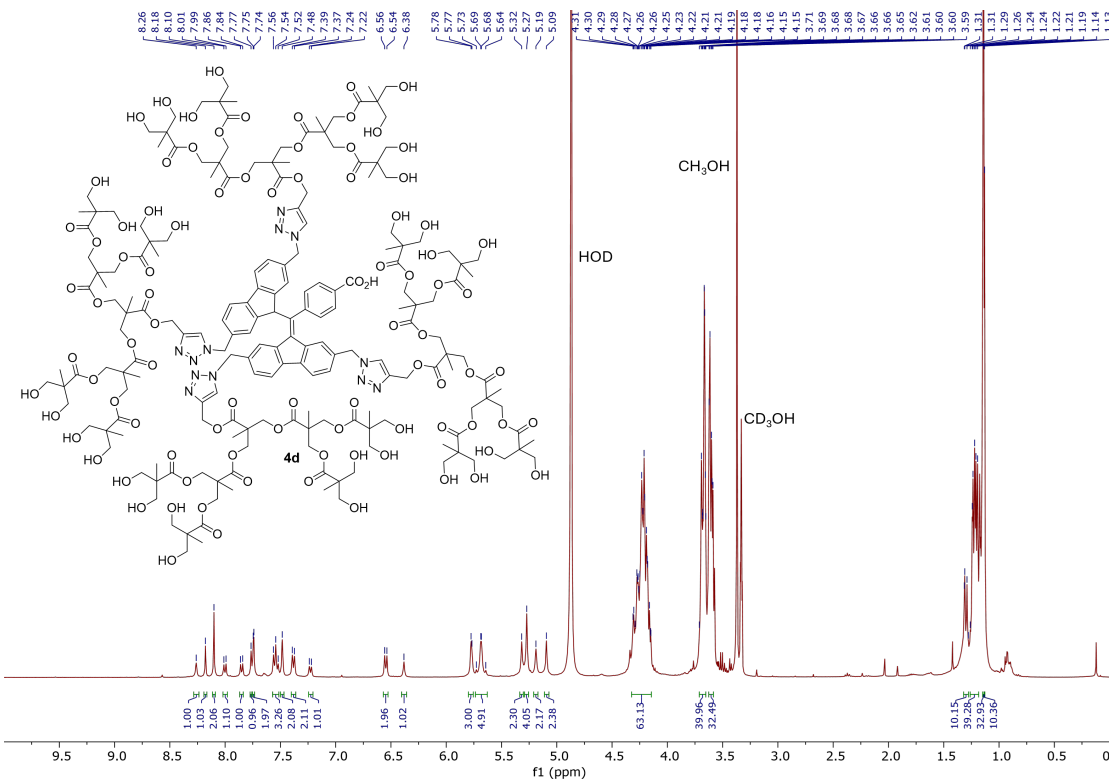

Figure S13. ^{1}H-NMR spectrum of compound **4d**.

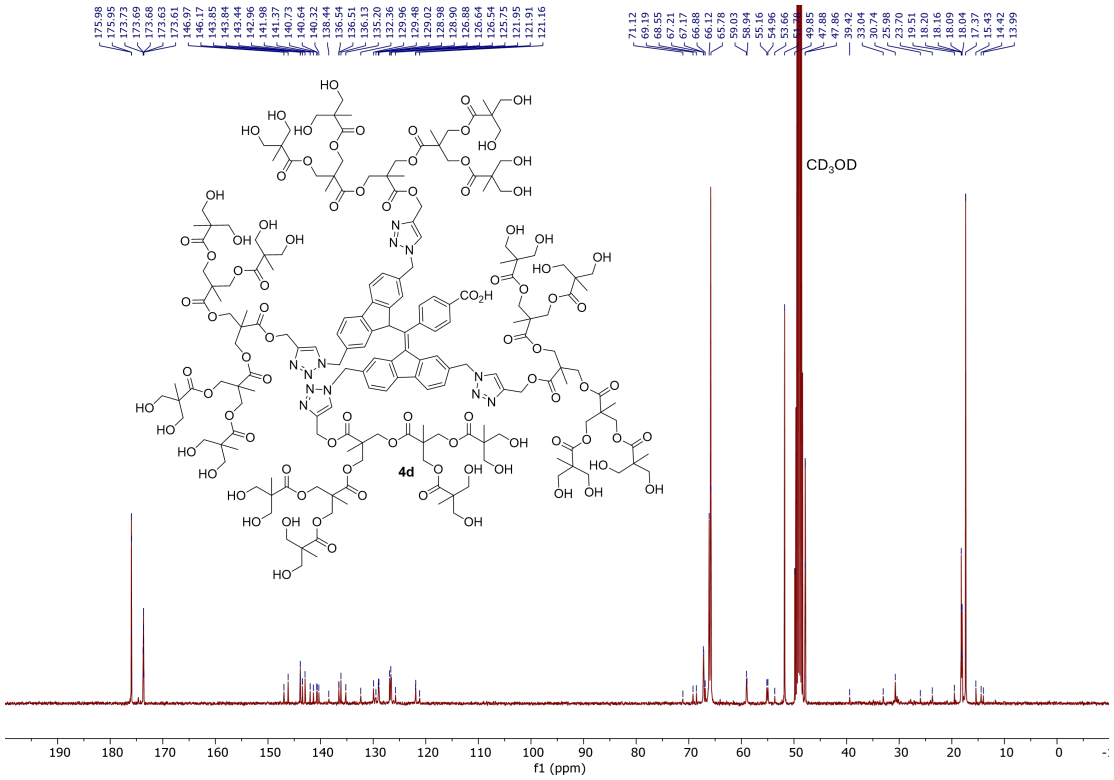

Figure S14. ^{13}C-NMR spectrum of compound **4d**.

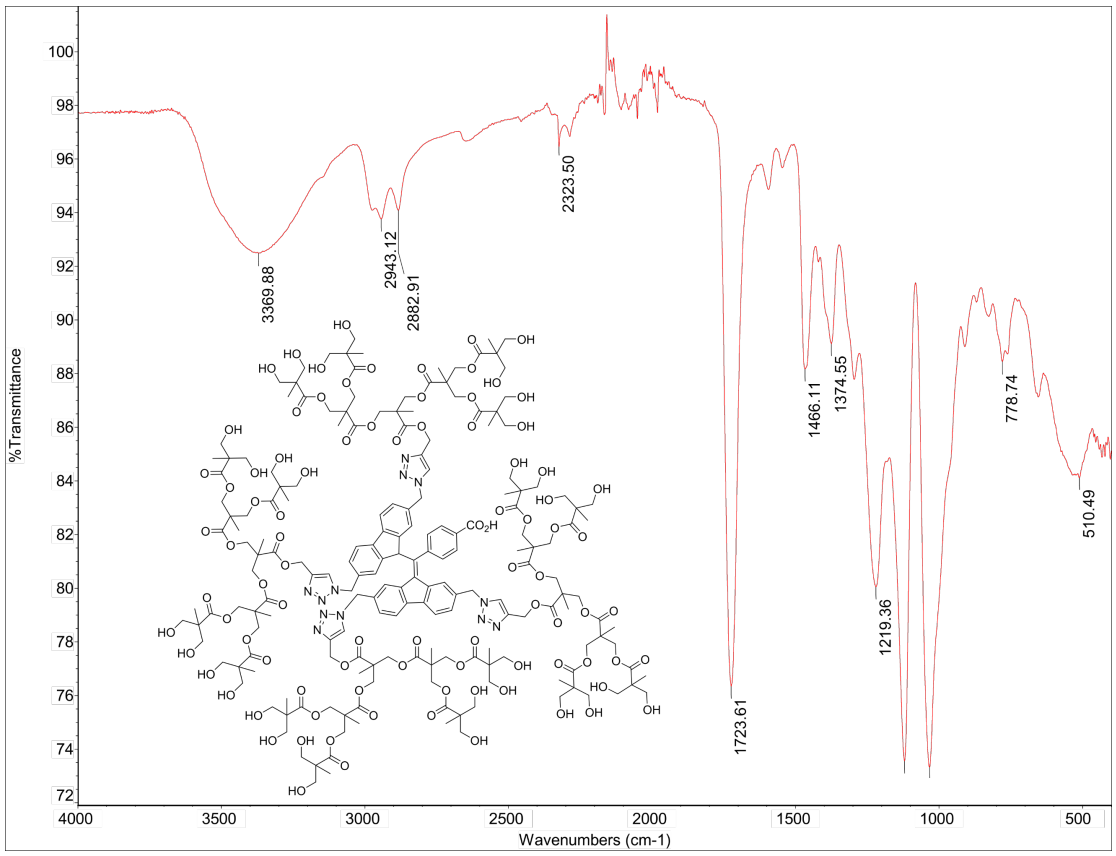

Figure S15. IR spectrum of compound **4d**.

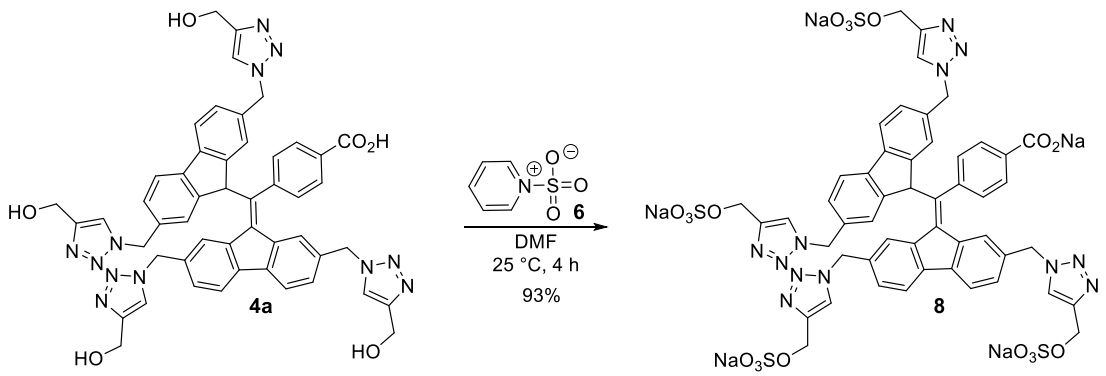

BDPA-sulfate 8. Sulfur trioxide pyridine complex **6** (28 mg, 0.176 mmol) was taken in an oven dried round bottom flask. To this, a solution of compound **4a** (20 mg, 0.022 mmol) in DMF (1.0 mL), was added and the resulting solution was stirred at 23 °C for 3 h. Satd. $NaHCO_3$ (0.5 mL) was added to the solution and stirred for 15 min. Water was evaporated *in vacuo* and the residue was precipitated using MeOH:Et_2O (1:10). The precipitate was dissolved in MeOH and filtered. The filtrate was dried and re-precipitated. The precipitate was dried in vacuo to give **8** (27 mg, 93%) as a blue solid.

^{1}H NMR (600 MHz, Methanol-d_4): δ 8.25 (s, 1H), 8.10 (s, 1H), 8.02 (s, 2H), 7.95 (d, J = 7.9 Hz, 1H), 7.80 (d, J = 7.8 Hz, 1H), 7.70 (d, J = 8.0 Hz, 2H), 7.67 (s, 1H), 7.56 (d, J = 8.1 Hz, 2H), 7.49 (d, J = 6.6 Hz, 3H), 7.31 (dd, J = 7.9, 1.6 Hz, 2H), 7.16 (dd, J = 7.9, 1.6 Hz, 1H), 6.57 (d, J = 8.0 Hz, 2H), 6.39 (s, 1H), 5.81 (d, J = 1.6 Hz, 1H), 5.73 (s, 2H), 5.64 (s, 4H), 5.15 (s, 2H), 5.11 (s, 2H), 5.08 (s, 4H), 4.94 (s, 2H) ppm;^{13}C NMR (151 MHz, Methanol-d_4): δ 174.94, 161.49, 146.94, 146.18, 144.97, 144.87, 144.60, 142.94, 141.98, 141.38, 140.78, 140.65, 140.31, 138.56, 136.57, 136.14, 135.02, 129.97, 129.42, 128.91, 128.80, 128.73, 126.84, 126.56, 126.02, 125.81, 125.72, 125.65, 121.72, 120.91, 61.80, 61.73, 61.67, 55.08, 54.88, 53.67 ppm; IR (ATR, cm^{-1}): $\tilde{\nu}$ 3409.33 (s,b) (O-H, alcohol), 2882.91 (C-H), 1599.84 (s) (C-C), 1382.67 (s) (S=O), 1250.11 (s) (C-N), 1050.19 (m) (C-O); HRMS (ESI): calcd. for $C_{50}H_{37}N_{12}O_{18}S_4Na$ [M^{4-}] 305.5333, found 305.5472.

HPLC:

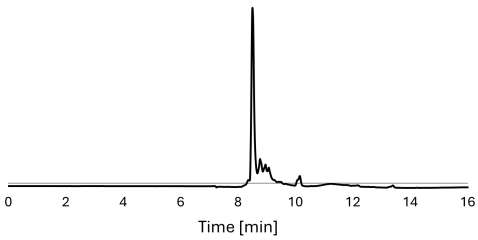

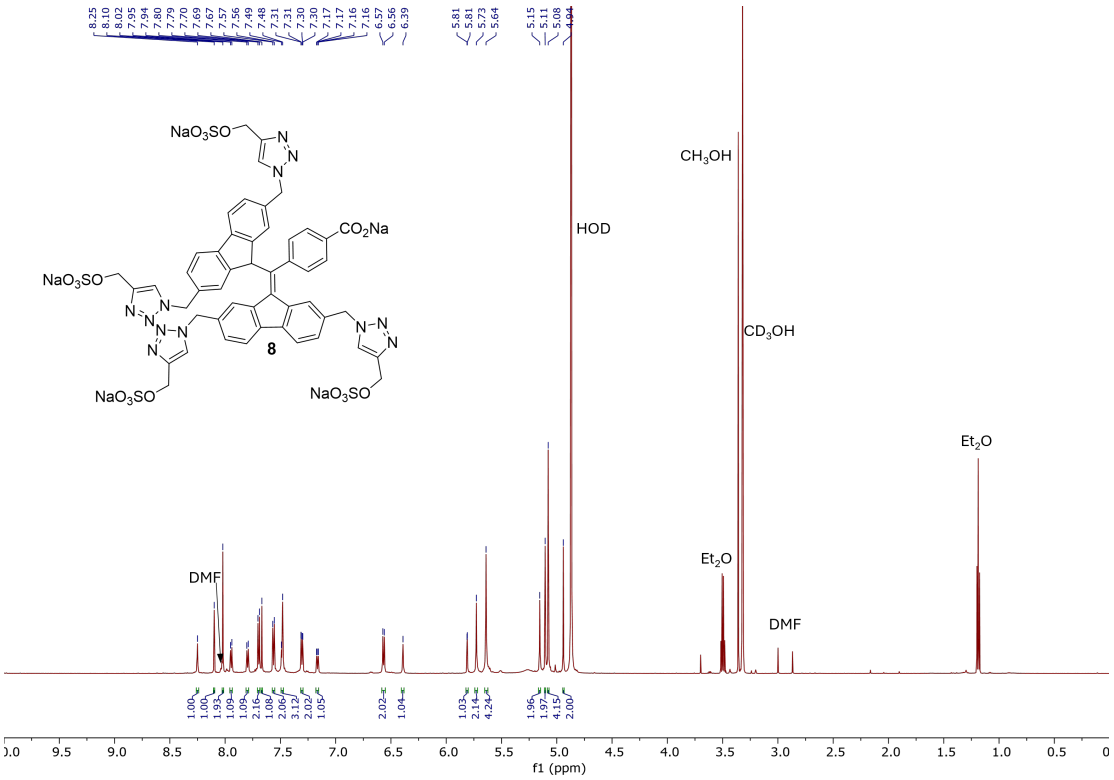

Figure S16. ^{1}H NMR spectrum of compound **8**.

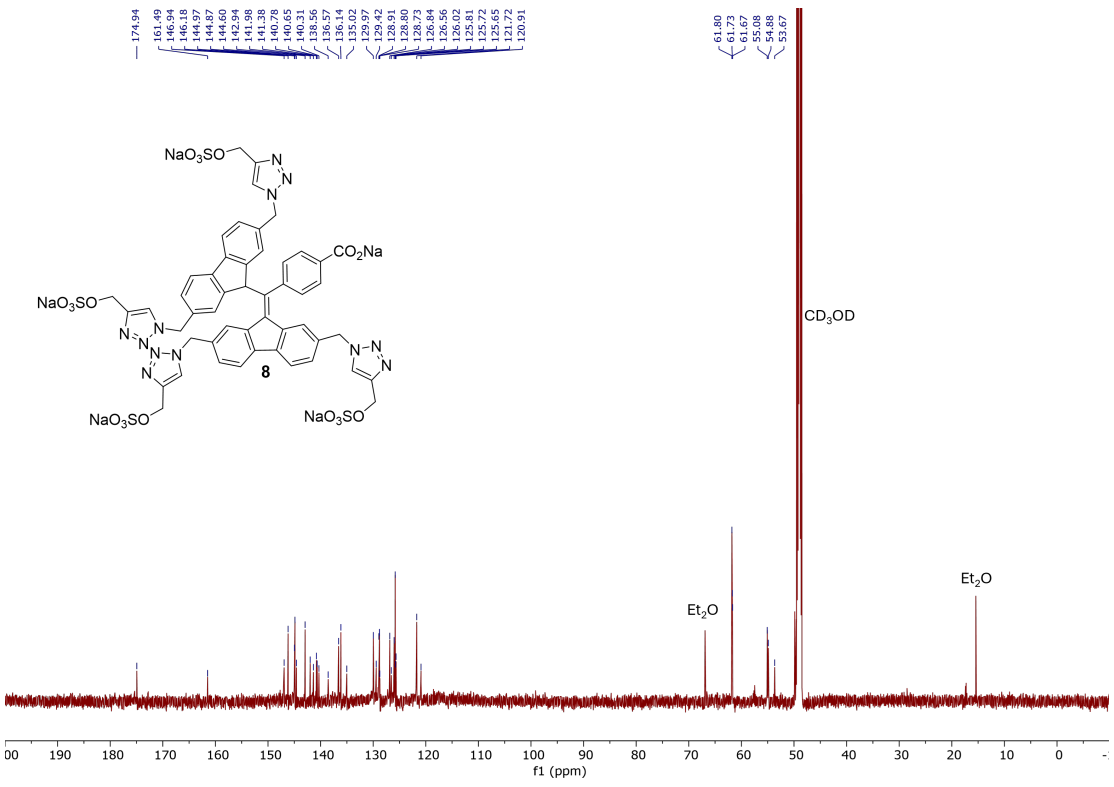

Figure S17. ^{13}C NMR spectrum of compound **8**.

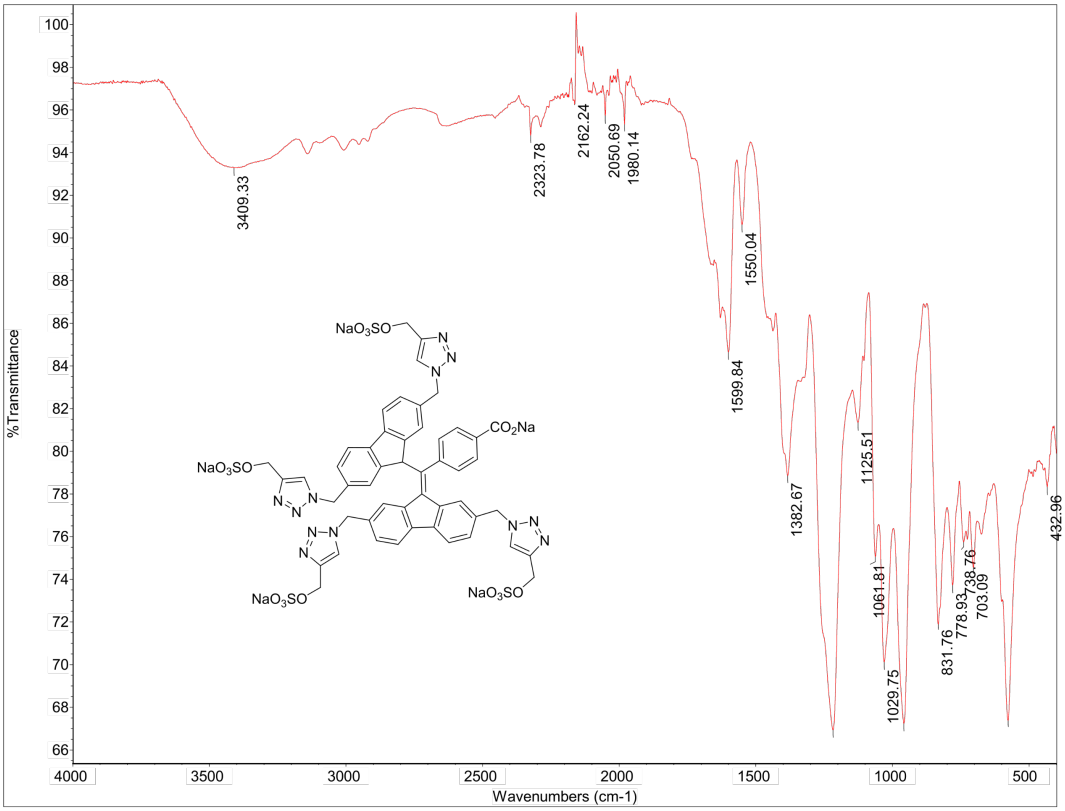

Figure S18. IR spectrum of compound **8**.

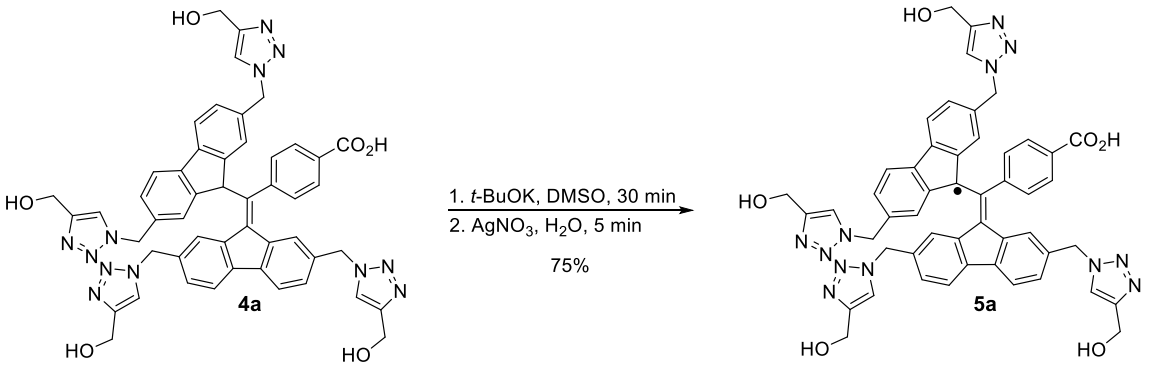

BDPA-OH radical 5a. To a solution of compound **4a** (20 mg, 0.022 mmol) in DMSO (1.0 mL), was added a freshly prepared solution of *t*-BuOK (0.176 mL, 0.044 mmol, 0.25M in DMSO) and the resulting solution was stirred at 23 °C for 30 min. A solution of $AgNO_3$ (18.8 mg, 0.110 mmol) in H_2O (0.1 mL) was added and the red solution was stirred for 5 min. The mixture was centrifuged, the solution was decanted and poured into Et_2O (10 mL), followed by centrifugation and decantation of the Et_2O layer. This was repeated until a precipitate was obtained and DMSO was removed. The precipitate was washed with H_2O (1 mL), centrifuged and decanted. The precipitate was dissolved in DMSO (0.5 mL), re-precipitated with Et_2O (10 mL) and dried to give **5a** (15 mg, 75%) as a reddish brown solid.

IR (ATR, cm^{-1}): $\tilde{\nu}$ 3308.25 (s,b) (O-H, alcohol), 3138.62 (O-H), 1581.72 (s) (C=O); HRMS (ESI): *m/z* calcd. for $C_{50}H_{41}N_{12}O_6$ [M-H^-] 904.3199, found 904.3186.

EPR (DMSO):

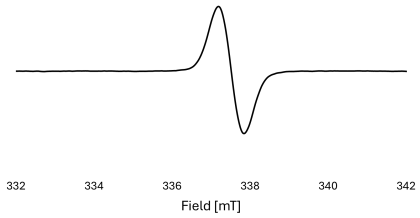

HPLC:

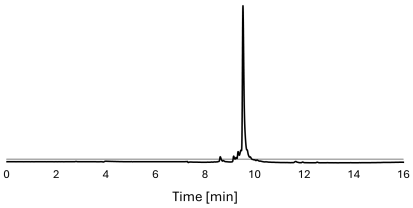

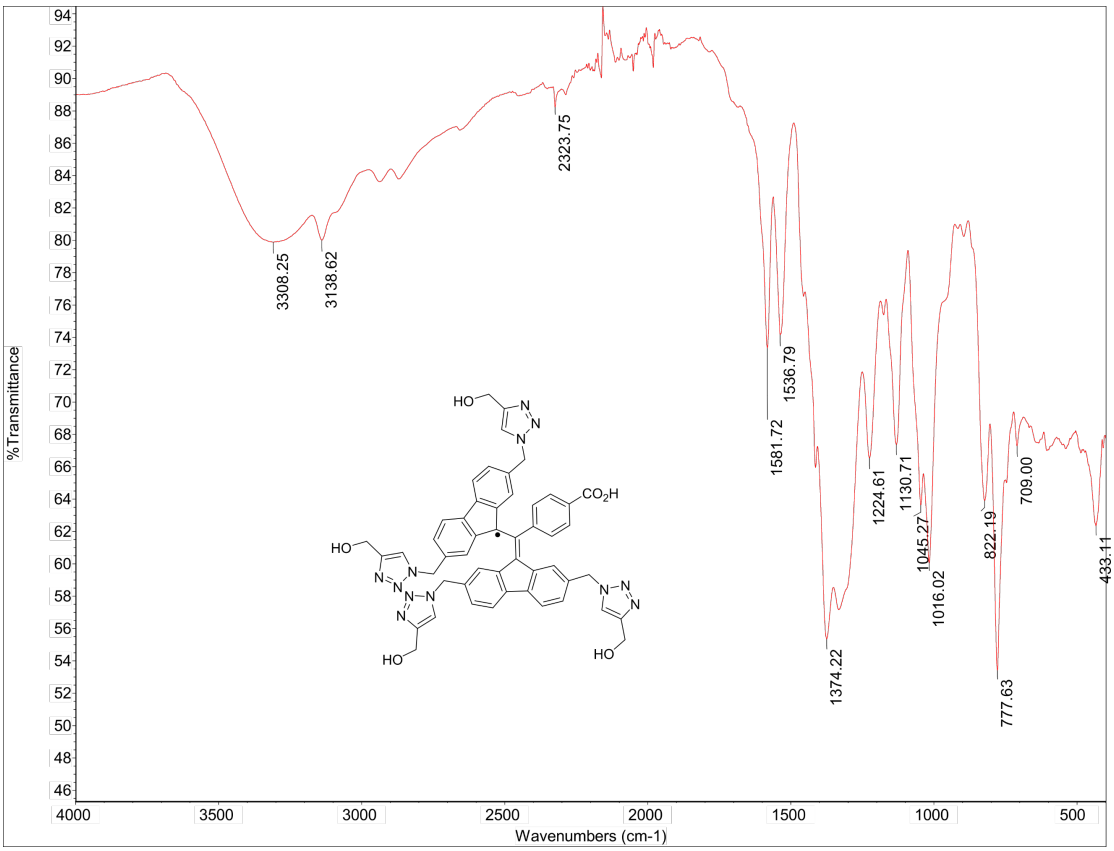

Figure S19. IR spectrum of compound **5a.**

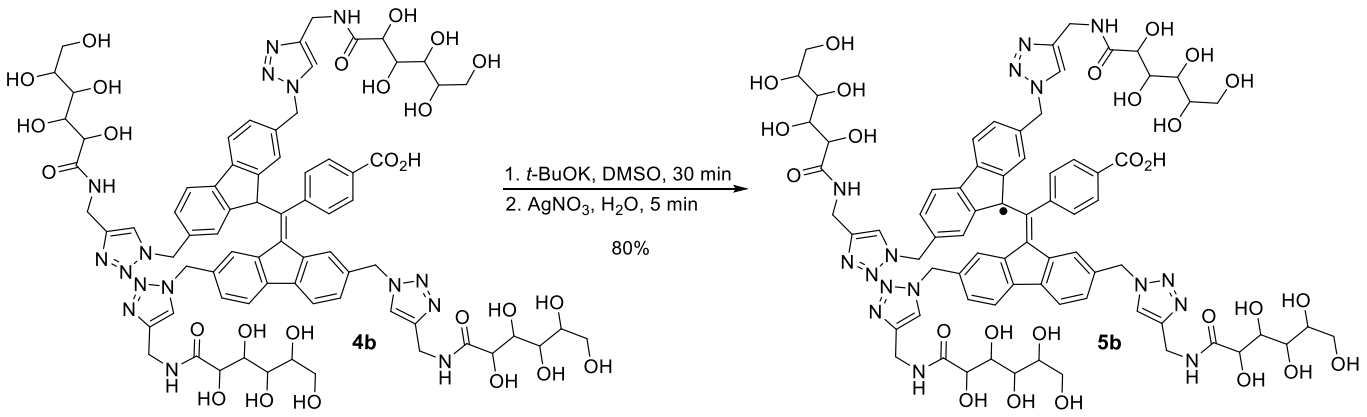

BDPA-hydroxyamide radical 5b. To a solution of compound **4b** (10 mg, 0.006 mmol) in DMSO (0.75 mL), was added a freshly prepared solution of *t*-BuOK (0.05 mL, 0.012 mmol, 0.25M in DMSO) and the resulting solution was stirred at 23 °C for 30 min. A solution of $AgNO_3$ (5.3 mg, 0.031 mmol) in H_2O (0.05 mL) was added and the red solution was stirred for 5 min. The mixture was centrifuged, the solution was decanted and poured into Et_2O (10 mL), followed by centrifugation and decantation of the Et_2O layer. This was repeated until a precipitate was obtained and DMSO was removed. The precipitate was washed with H_2O (1 mL), centrifuged and decanted. The precipitate was dissolved in DMSO (0.5 mL), re-precipitated with Et_2O (10 mL) and dried to give **5b** (8 mg, 80%) as a reddish brown solid.

IR (ATR, cm^{-1}): $\tilde{\nu}$ 3308.20 (s,b) (O-H, alcohol), 2932.20 (C-H), 1654.47 (s) (C=O), 1532.07 (s) (N-H), 1418.83 (m) (C-C, aromatic), 1072.40 (s) (C-O), 1022.53 (m) (C-N); HRMS (ESI): *m/z* calcd. for $C_{74}H_{86}N_{16}O_{26}+2Na^+$ [M+2Na$^+$] 830.2842, found 830.2676.

EPR(DMSO):

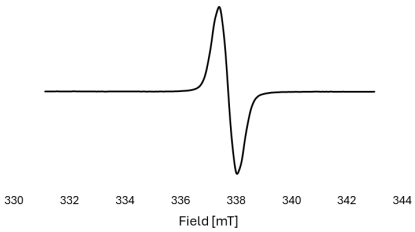

HPLC:

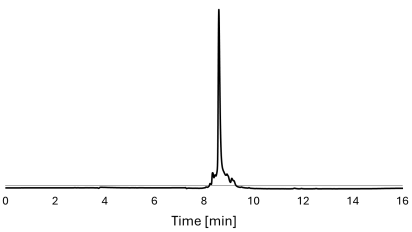

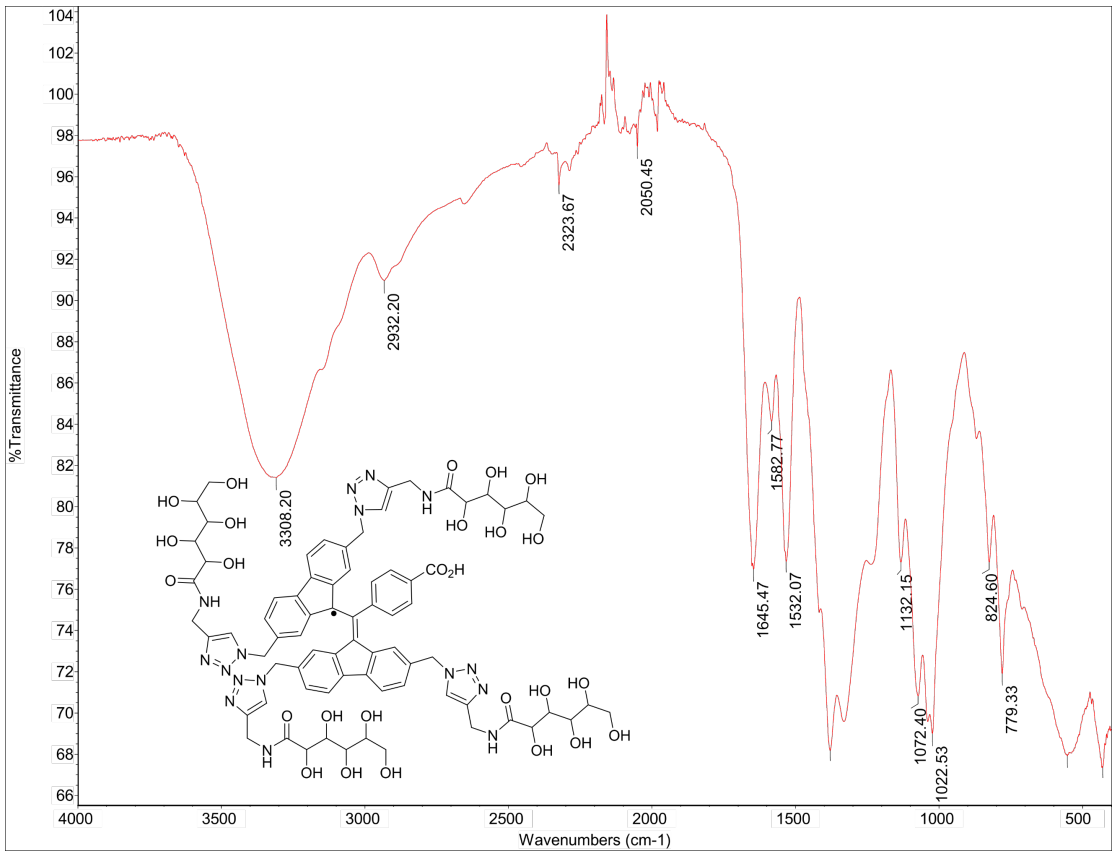

Figure S20. IR spectrum of compound **5b**.

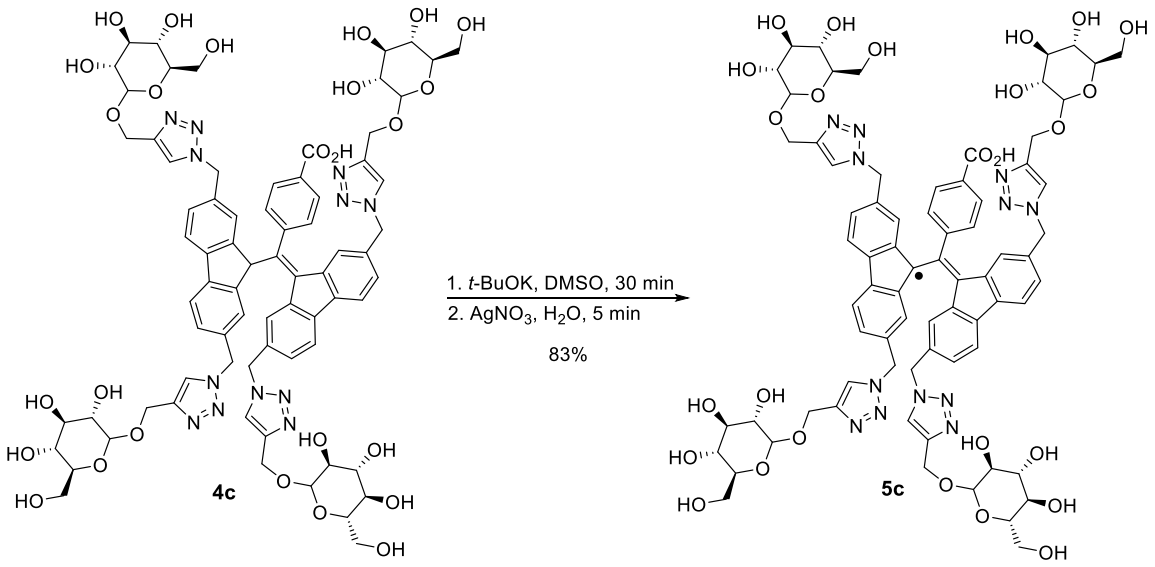

BDPA-glucose radical 5c. To a solution of compound **4c** (20 mg, 0.013 mmol) in DMSO (1.5 mL), was added a freshly prepared solution of *t*-BuOK (0.1 mL, 0.0257 mmol, 0.25M in DMSO) and the resulting solution was stirred at 23 °C for 30 min. A solution of $AgNO_3$ (10.9 mg, 0.0643 mmol) in H_2O (0.1 mL) was added and the red solution was stirred for 5 min. The mixture was centrifuged, the solution was decanted and poured into Et_2O (10 mL), followed by centrifugation and decantation of the Et_2O layer. This was repeated until a precipitate was obtained and DMSO was removed. The precipitate was dissolved in H_2O (0.5 mL), centrifuged and decanted. To the decanted solution, MeOH (2 mL) was added, followed by Et_2O (10 mL). The precipitate was collected by centrifugation, followed by decantation of the solvent and was dried to give **5c** (16.6 mg, 83%) as a reddish brown solid.

IR (ATR, cm^{-1}): $\tilde{\nu}$ 3353.00 (s,b) (O-H, alcohol), 2881.71 (C-H), 1583.61 (s) (C=O), 1374.82 (s) (C-N) 1038.58 (m) (C-O); HRMS (ESI): *m/z* calcd. for $C_{74}H_{81}N_{12}O_{26}$+2Na^+ [M+2Na^+] 799.7585, found 799.7495.

EPR (DMSO):

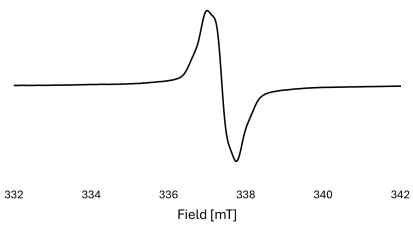

HPLC:

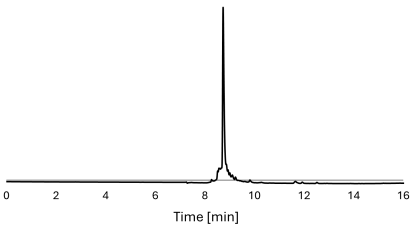

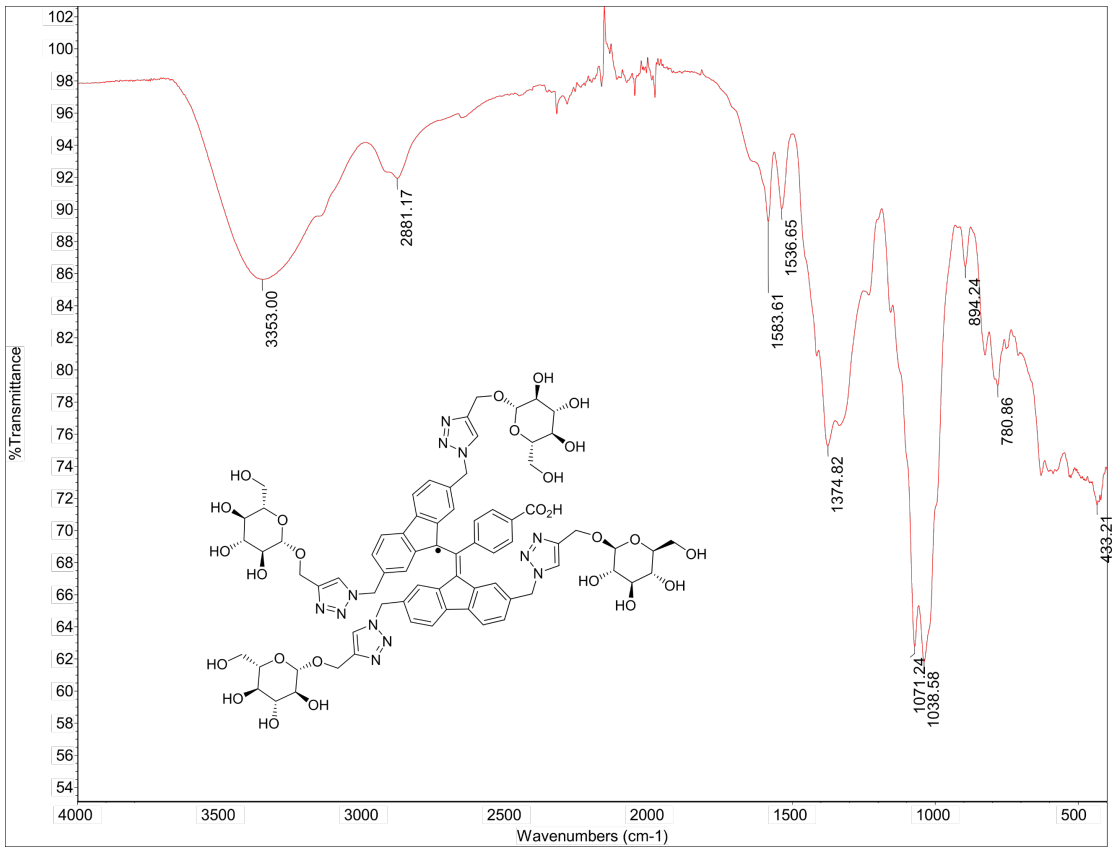

Figure S21. IR spectrum of compound **5c**.

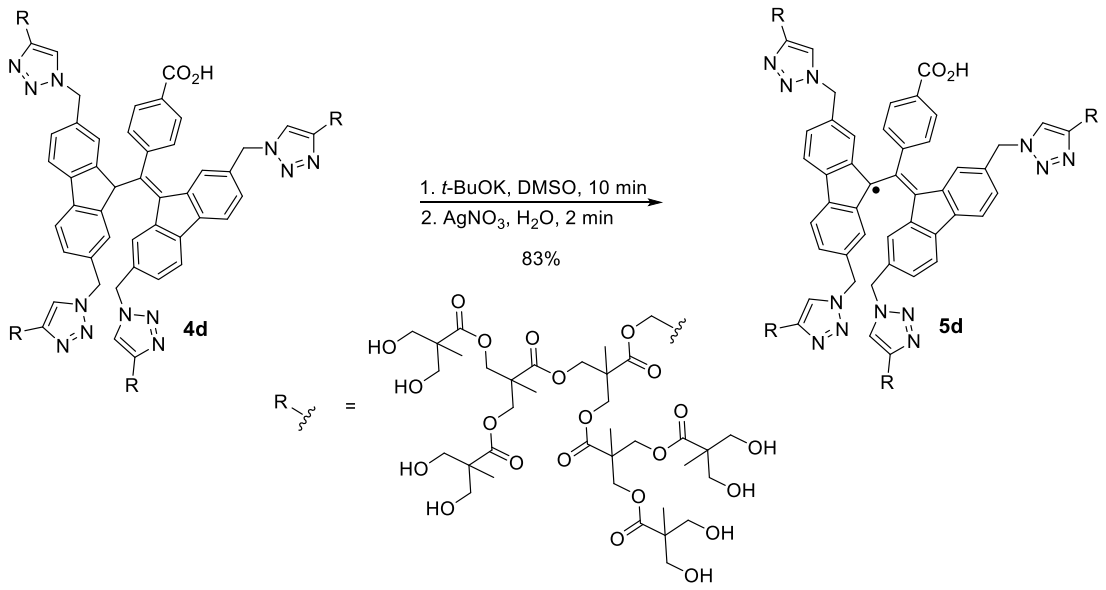

BDPA-dendrimer radical 5d. To a solution of compound **4d** (20 mg, 0.0048 mmol) in DMSO (1.5 mL), was added a freshly prepared solution of *t*-BuOK (0.04 mL, 0.0096 mmol, 0.25M in DMSO) and the resulting solution was stirred at 23 °C for 10 min. A solution of $AgNO_3$ (4 mg, 0.024 mmol) in H_2O (0.1 mL) was added and the red solution was stirred for 2 min. The mixture was centrifuged; the solution was decanted and poured into Et_2O (10 mL). The precipitate formed was collected by centrifugation followed by decantation of the solvent. The precipitate was redissolved in MeOH (1 mL) and re-precipitated by addition of Et_2O (10 mL) twice. The precipitate was dissolved in MeOH (1 mL) and centrifuged to remove the Ag residue and decanted and dried to give **5d** (14 mg, 70%) as a reddish brown solid.

IR (ATR, cm^{-1}): $\tilde{\nu}$ 3378.89 (s,b) (O-H, alcohol), 2882.93 (C-H), 1723.02 (s) (C=O, ester), 1461.22 (m) (C-C), 1031.54 (m) (C-O); ESI-HRMS: *m/z* calcd. for $C_{190}H_{265}N_{12}O_{90}$+4Na$^+$ [M+4Na$^+$] 1061.6524, found 1061.6410.

EPR (DMSO):

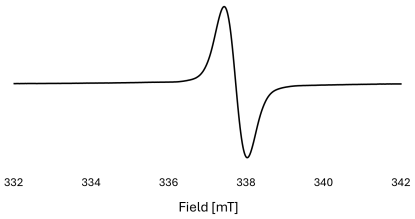

HPLC:

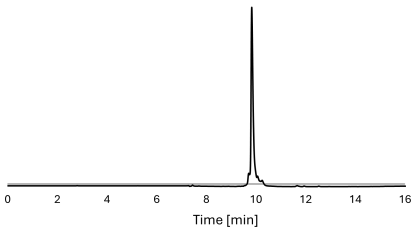

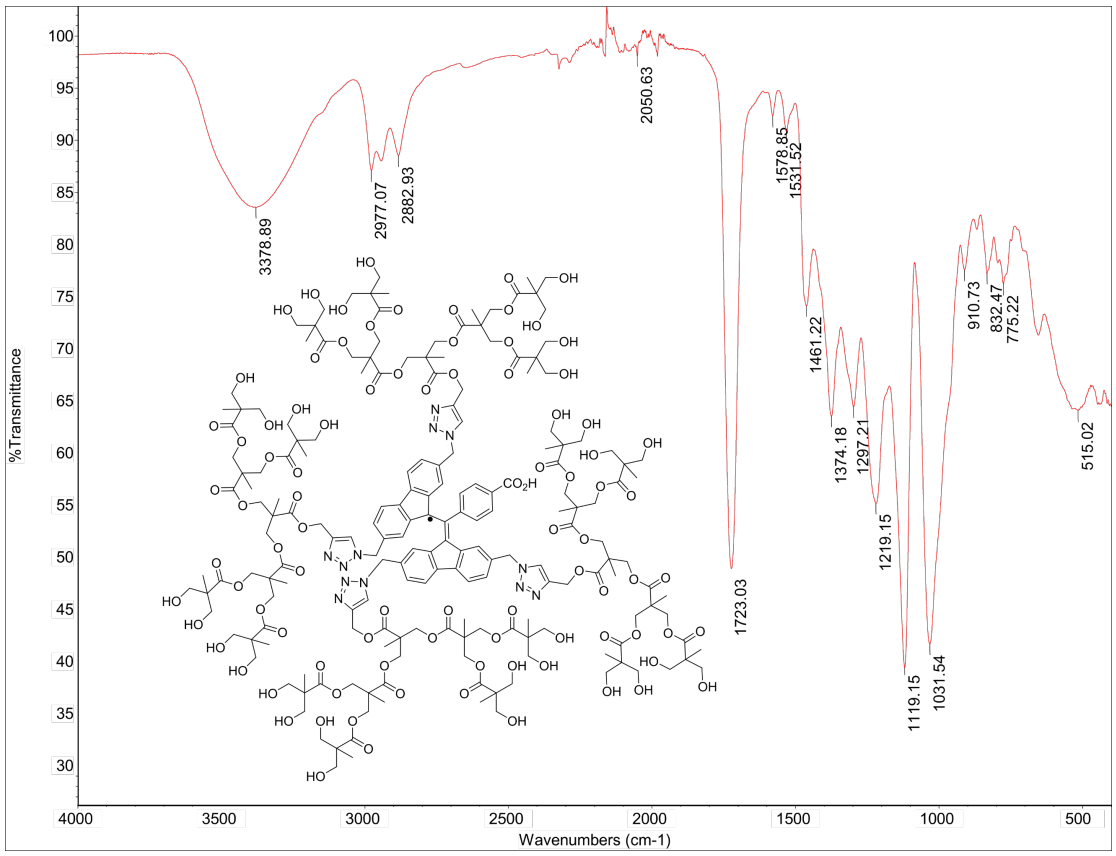

Figure S22. IR spectrum of compound **5d**.

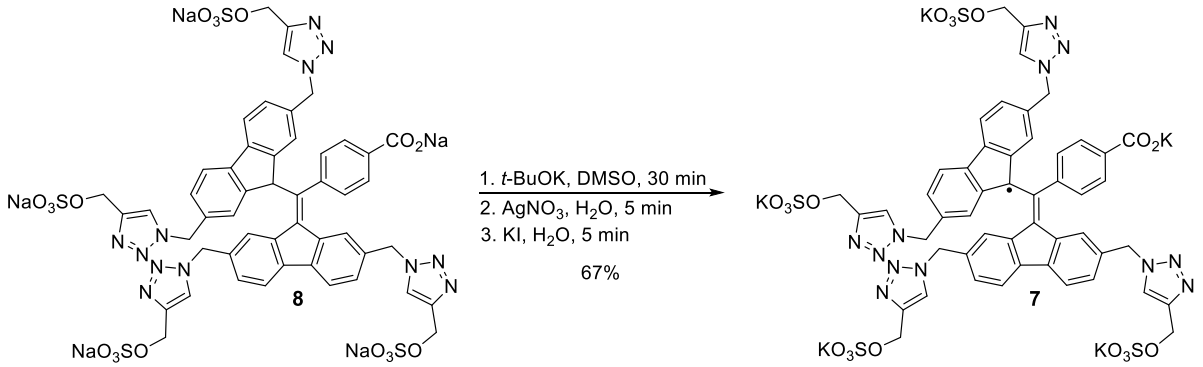

BDPA-sulfate radical 7. To a solution of compound **8** (20 mg, 0.015 mmol) in DMSO (1.0 mL), was added a freshly prepared solution of *t*-BuOK (0.12 mL, 0.029 mmol, 0.25M in DMSO) and the resulting solution was stirred at 23 °C for 45 min. A solution of $AgNO_3$ (12.7 mg, 0.075 mmol) in H_2O (0.06 mL) was added and the red solution was stirred for 5 min. A solution KI in H_2O (60 µL) was added, and the solution was stirred for 5 min. The mixture was centrifuged; the solution was decanted and poured into Et_2O (10 mL). The precipitate formed was collected by centrifugation followed by decantation of the solvent. The precipitate was redissolved in MeOH:H_2O (1:1) and re-precipitated by addition of Et_2O (10 mL) twice. The precipitate was dissolved in MeOH (1 mL) and centrifuged again to remove the Ag residue and decanted and dried to give **5d** (14 mg, 67%) as a reddish brown solid.

IR (ATR, cm^{-1}): $\tilde{\nu}$ 3442.06 (s,b) (O-H, alcohol), 2882.91 (C-H), 1593.14 (s) (C-C), 1382.67 (s) (S=O), 1216.95 (s) (C-O); ESI-HRMS: *m/z* calcd. for $C_{50}H_{37}N_{12}O_{18}S_4$ [M^{4-}] 305.2813, found 305.2828.

EPR (H_2O):

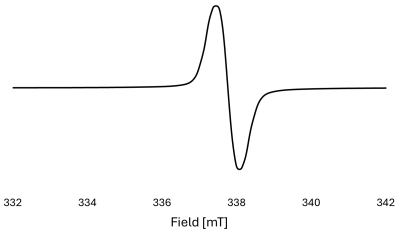

HPLC:

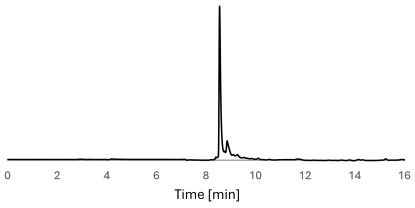

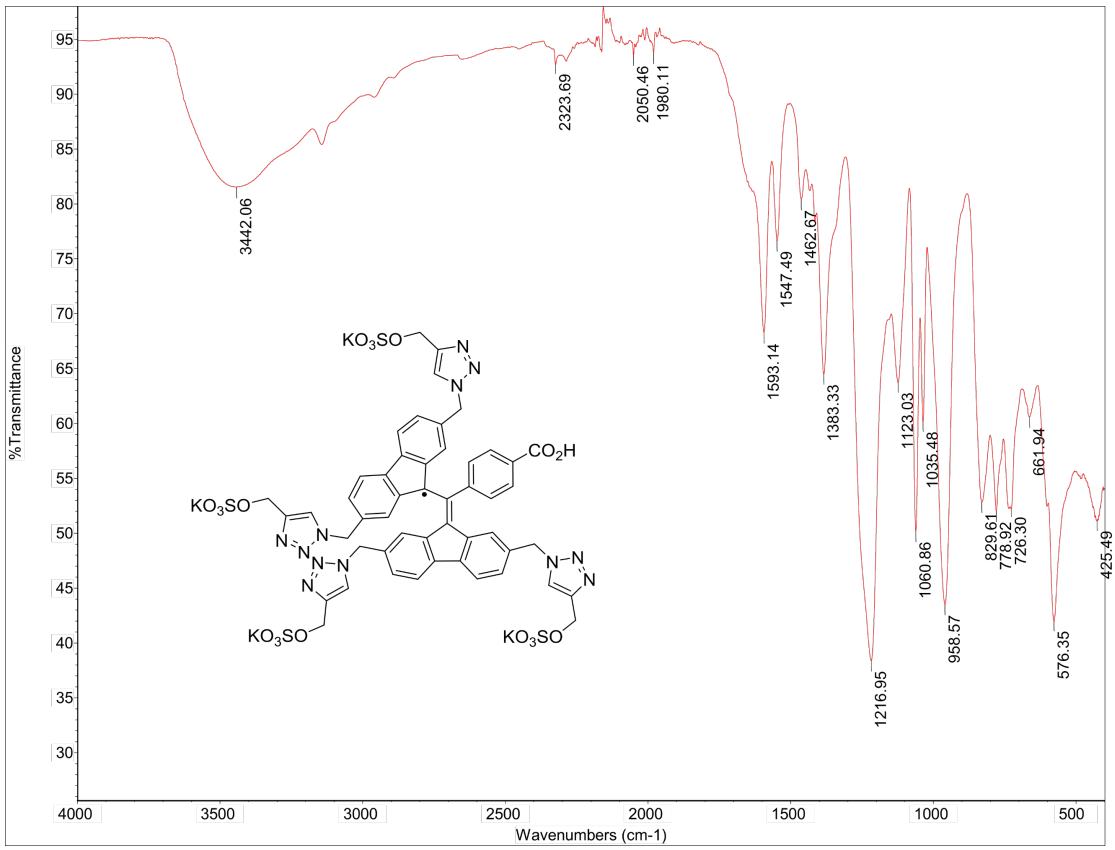

Figure S23. IR spectrum of compound **7**.

Quantification of BDPA radicals

The amount of radical present in the BDPA radicals **5a**-**d** and **7** was determined by spin counting using EPR spectroscopy. A stock solution of 4-hydroxy-TEMPO (1.0 M) was prepared in DMSO. The stock solution was diluted into a series of concentrations (0.1–1.5 mM), and each sample was measured by EPR spectroscopy. The area under the peaks of each spectrum, obtained by double integration, was plotted against its concentration to yield a standard curve. Solutions of BDPA radicals **5a**-**d** and **7** (1 mM) in DMSO were measured under same conditions and double-integrated to obtain the area under the peaks. Comparison with the TEMPO calibration curve showed that the radical content was approximately 83% (**5a**), 82% (**5b**), 80% (**5c**), 56% (**5d**) and 89% (**7**) with an error margin of 5–10%.

Persistence of BDPA-dendrimer 5d

Solvent-dependent persistence

The persistence of BDPA-dendrimer **5d** was investigated by monitoring its absorption at 503 nm using UV-vis spectroscopy. UV-Vis spectroscopy was used to monitor the radical persistence since it allowed easier and more accurate quantification of the radical than EPR spectroscopy. The concentrations of **5d** in H_2O, DMSO and glycerol were 10 mM (by weight) The solutions were kept at 23 °C and the UV-vis spectra were recorded at different time intervals by removing aliquots (3 µL) and diluting with H_2O (0.5 mL). Commercially purchased solvents were used without further drying and purification for these experiments, except for DMSO which was dried over molecular sieves (3 Å).

The UV-vis spectra of BDPA-dendrimer radical **5d** in DMSO, H_2O and glycerol as a function of time are shown in **Figure S24**. The characteristic radical absorption band between 440 – 550 nm (λ_{max} = 503 nm), decreases as the radical decomposes. In DMSO (**Figure S24A**), the absorbance of **5d** increases with time for about 3 days and then becomes constant. In H_2O, the absorbance decreases exponentially with time, yielding a half-life of about 2 days (**Figure S24B**). In glycerol, **5d** shows a gradual decrease in the absorbance at 503 nm, while the absorbance in the 360 - 440 nm region gradually increases with time, unlike the measurements in DMSO or H_2O. The normalized absorbance at 503 nm, as a function of time, shows a half-life of ca. 8 days in glycerol (**Figure S24C**).

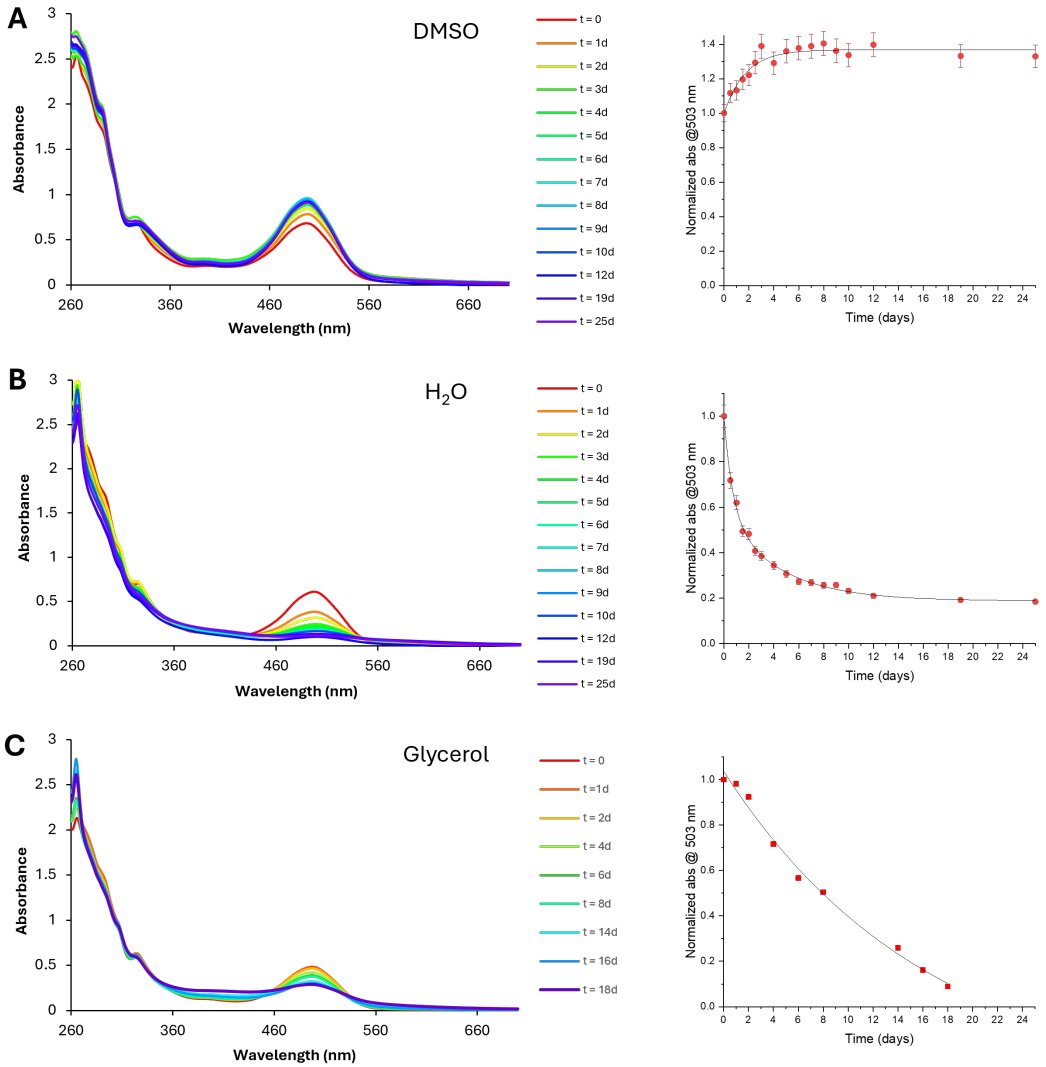

Figure S24. The UV-vis absorbance spectra of **5d** (left) and its corresponding normalized absorbance at 503 nm (right), plotted as a function of time in DMSO (**A**), H_2O (**B**) and glycerol (**C**).

One possible explanation of the unexpected increase of absorbance of **5d** in DMSO could be low solubility that might result in slow dissolution. To rule out this explanation, a 10 mM solution of **5d** in DMSO was prepared and an aliquot was immediately filtered through a 0.2 μm membrane filter. Its persistence was subsequently compared with the unfiltered solution (**Figure S25**). The material in the two solutions showed identical persistence curves, indicating that solubility of **5d** in DMSO was not responsible for the increase in absorbance of radical with time.

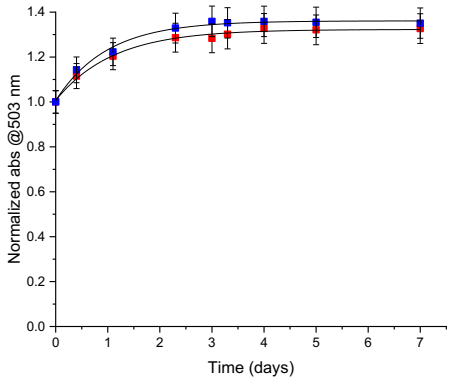

Figure S25. Comparison of persistence of filtered (■) and unfiltered (■) **5d** solution in DMSO (10 mM) at 23 °C, monitored by UV-vis spectroscopy at 503 nm.

We also determined whether the increase in absorbance was concentration dependent, by comparing the persistence of 5d at different concentrations (1 mM, 5mM, 10 mM and 20 mM, **Figure S26**). All concentrations exhibited similar persistence curve profiles, with each showing an initial increase in absorbance.

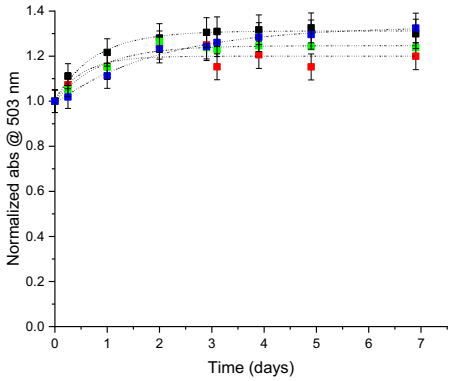

Figure S26. Persistence of 5d for 1 mM (■), 5mM (■), 10 mM (■) and 20 mM (■) solutions in DMSO at 23 °C monitored by UV-vis spectroscopy at 503 nm.

To determine if the initial increase in concentration of radical **5d** in DMSO originated from presence of the non-radical precursor **4d** in the sample of **5d**, a solution of **4d** in DMSO was monitored by UV-vis spectroscopy (**Figure S27A**). Initially, formation of the anion was observed (λ_{max} = 630 nm), which subsequently decreased as the radical gradually formed over a period of 4 days (**Figure S27A**,**B**). The increase in radical content for **5d** is shown for comparison (**Figure S27B**).

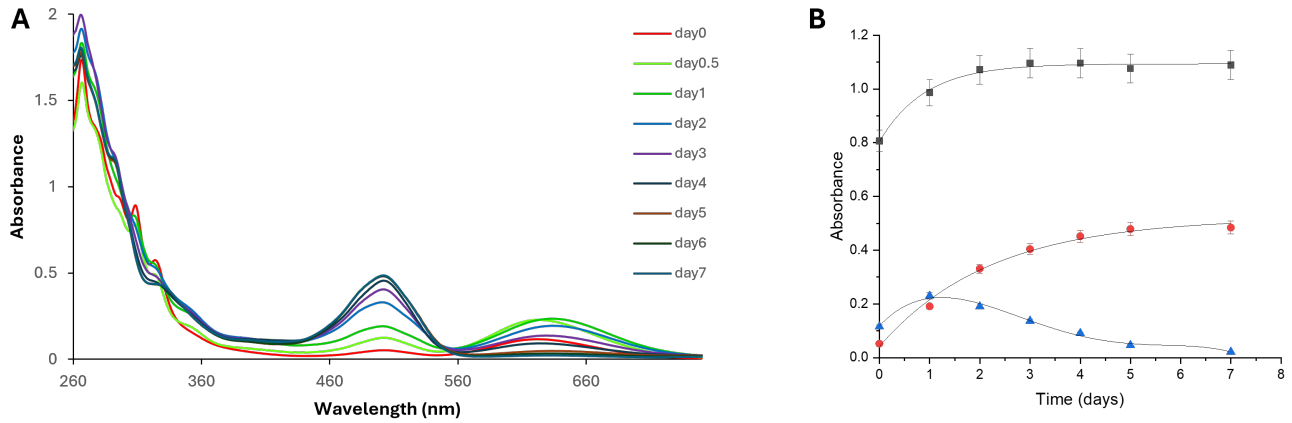

Figure S27. **A**. The UV-vis absorbance of BDPA-dendrimer **4d** in DMSO over 7 days at 23 °C. **B**. Comparison of effect of DMSO on radical **5d** (■) with its non-radical **4d**. Anion formed in non-radical is shown by (▲) while the radical formed over time in the **4d** is indicated by (●).

To assess whether dissolved oxygen in DMSO plays a role in the oxidation of the BDPA anion to the radical, conversion of **4d** in DMSO to the radical **5d** was monitored in the presence and absence of oxygen (**Figure S28**). The radical formation was comparable in both cases, indicating that dissolved oxygen is not required for radical formation.

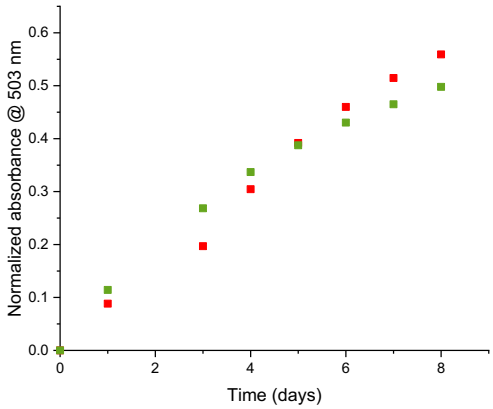

Figure S28. Normalized absorbance (503 nm) of **4d** in DMSO (10 mM) plotted as a function of time, in the presence (■) and absence of oxygen (■).

Liquid DNP NMR measurements

Experimental setup

^{1}H DNP NMR experiments were performed on a home-built DNP spectrometer, which was a modified Bruker Avance II wide-bore spectrometer operating at 9.4 T. Microwaves were generated by a 12 W gyrotron operating at 263 GHz.[4] The DNP probehead was a homemade Fabry-Perot/stripline double resonance structure operating at 263 GHz/400 MHz.[5] DNP-enhanced (mw on) and reference (mw off) NMR FID signals were recorded using standard 90° RF pulse excitation. The pulse length was 25 µs,

and the repetition time was optimized for each radical concentration and set to one second for each experiment. DNP enhancement was measured by integrating all glycerol protons. Enhancement was calculated according to $\varepsilon = (I/I_0) - 1$, where I and I_0 are the dynamic and Boltzmann nuclear polarizations, respectively. Temperature calibration was performed by monitoring the distance between the CH_2 and OH groups in the NMR spectrum, as previously described.[6]

J-band EPR experiments were carried out using an ELEXSYS E780 at temperatures of 298 K and 100 K with the following parameters for CW EPR: a microwave frequency of 262.75 GHz, a microwave power of 0.02377 mW, a sweep width of 20 mT, a field modulation frequency of 100 kHz, a field modulation amplitude of 0.3 mT, a time constant of 1 s, 201 points, and one scan. The echo detected (ED) spectrum was measured at 100 K using a pulse sequence of 70–250–140 ns with a repetition time of 100 ms. The number of shot per point was 10 ns, and the number of scans was 1.

The BDPA dendrimer radical **5d** concentration was between 10 and 40 mM, as determined by X-band CW EPR at room temperature **(Figure S28A)**. The J-band CW and ED EPR spectra are shown in **Figures S28B** and **S28C**, respectively.

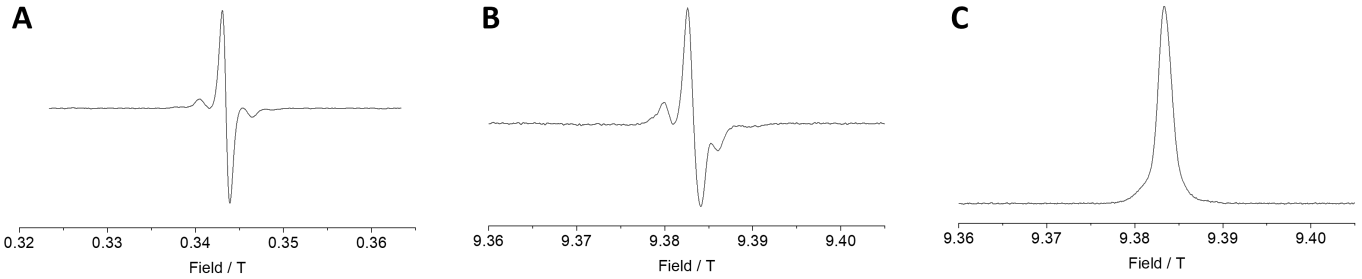

Figure S29. X-band and J-band EPR of BDPA-dendrimer. **A**. X-band CW EPR spectrum of 20 mM **5d** in glycerol at 298 K. **B**. J-band CW EPR of 20 mM **5d** in glycerol at 298 K. **C.** J-band ED EPR of 0.3 mM **5d** at 100 K.

^{1}H DNP Field Profile

The ^{1}H DNP field profile of the glycerol is antisymmetric (**Figure S29**), with peaks located at magnetic field strengths that are displaced by two nuclear Larmor frequency ($2\omega_H/\gamma_e$). This is characteristic of the SE mechanism.

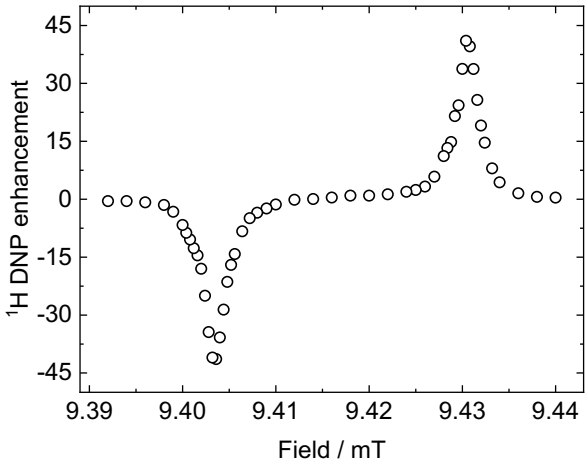

Figure S30. Field profile of the ^{1}H DNP enhancement for a solution of BDPA-dendrimer **5d** (20 mM) in glycerol at 9.4T and 315 K.

DNP measurements at different concentrations of 5d

To evaluate the effect of radical concentration on DNP performance, ^{1}H DNP was measured for **5d** at concentrations of 10, 20 and 40 mM, showing a clear concentration-dependent increase in DNP performance (**Table S1**).

Table S1. ^{1}H DNP enhancement at three different concentrations of **5d**.

Concentration	^{1}H DNP enhancement
10 mM	18 ± 3
20 mM	40 ± 5
40 mM	57 ± 6

References

1. S. Mandal and S. T. Sigurdsson, *Chem. Commun.*, 2020, **56**, 13121-13124.
2. E. H. Ryu and Y. Zhao, *Org. Lett.*, 2005, **7**, 1035-1037.
3. A. L. M. Morotti, K. L. Lang, I. Carvalho, E. P. Schenkel and L. S. C. Bernardes, *Tetrahedron Lett.*, 2015, **56**, 303-307.
4. V. Denysenkov, M. J. Prandolini, M. Gafurov, D. Sezer, B. Endeward and T. F. Prisner, *Phys. Chem. Chem. Phys.*, 2010, **12**, 5786-5790.
5. V. Denysenkov, D. H. Dai and T. F. Prisner, *J. Mag. Res.*, 2022, **337**.
6. A. A. Kuzhelev, V. Denysenkov, I. M. Ahmad, O. Y. Rogozhnikova, D. V. Trukhin, E. G. Bagryanskaya, V. M. Tormyshev, S. T. Sigurdsson and T. F. Prisner, *J. Am. Chem. Soc.*, 2023, **145**, 10268-10274.

Paper II

Paper II. Non-covalent spin-labeling of RNA with short hairpins containing the rigid spin label Çm

Ahmad IM, Endeward B, Prisner TF and Sigurdsson ST, *Chem. Eur. J.* **2025**, 32, e03253.

Chemistry – A European Journal

ChemEurJ Chemistry Europe European Chemical Societies Publishing

RESEARCH ARTICLE

Non-Covalent Spin-Labeling of RNA With Short Hairpins Containing the Rigid Spin Label Çm

Iram M. Ahmad[1] | Burkhard Endeward[2] | Thomas F. Prisner[2] | Snorri Th. Sigurdsson[1]

[1]Department of Chemistry, Science Institute, University of Iceland, Reykjavik, Iceland | [2]Institute of Physical and Theoretical Chemistry, Goethe University, Frankfurt am Main, Germany

Correspondence: Snorri Th. Sigurdsson (snorrisi@hi.is)

Received: 27 October 2025 | **Revised:** 11 December 2025 | **Accepted:** 17 December 2025

Keywords: DEER | EPR spectroscopy | nucleic acids | PELDOR | spin labeling

ABSTRACT

Understanding the structure and dynamics of nucleic acids is essential for elucidating their complex biological functions. Electron Paramagnetic Resonance (EPR) spectroscopy is a valuable technique to extract such information. However, its application to nucleic acids requires the incorporation of spin labels, usually nitroxides. Rigid spin labels are more informative EPR probes than flexible ones, since they offer high-precision distance measurements and can provide information about the relative orientation of spin labels. However, the synthesis and incorporation of such rigid labels is nontrivial. Here we describe a strategy in which the rigid spin label **Çm** is incorporated into a small hairpin, which in turn can be used to label several different oligonucleotides noncovalently through helical stacking. We have studied the noncovalent assembly of spin-labeled RNA hairpins with RNA duplexes by both continuous wave (CW) and pulsed dipolar EPR spectroscopy, specifically pulsed electron-electron double resonance (PELDOR, also called DEER). Our data shows that short complementary overhangs facilitate efficient helical stacking, opening the possibility of using noncovalent labeling with **Çm**-modified hairpins in conjunction with pulsed dipolar EPR spectroscopy for structural studies of larger RNAs and RNA-protein complexes.

1 | Introduction

Electron Paramagnetic Resonance (EPR) spectroscopy has emerged as a valuable technique for studying paramagnetic molecules and molecular assemblies, for example, to gain insights into the structure and dynamics of complex biomolecules, such as proteins and nucleic acids [1–7]. Continuous wave (CW) EPR spectroscopy gives information about dynamics through line shape analysis [8] and can also be used to determine distances between paramagnetic centers in the range of 5 to 25 Å [9–11]. Pulsed dipolar EPR methods, such as pulsed electron-electron double resonance (PELDOR), also known as double electron–electron resonance (DEER), have been used to measure distances from 15–160 Å [12–16]. In addition to distance measurements, PELDOR can provide information about orientations of paramagnetic centers [17–19].

For the application of EPR spectroscopy to study nucleic acids, spin labels need to be incorporated into the biopolymer [20, 21]. Stable aminoxyl radicals, usually called nitroxides, are the most commonly used spin labels [20–22]. Short linkers between the nucleic acid and the spin label are desirable to limit the conformational ensemble of the label and thus give a narrow distance distribution [23–24]. Even better are rigid spin labels, such as the cytidine analogues **Ç** [25] and **Çm** [26] that can form base pairs with guanine in DNA and RNA helices, respectively (Figure 1A). In addition to providing precise inter-spin distances, PELDOR with such rigid labels also yields relative orientations

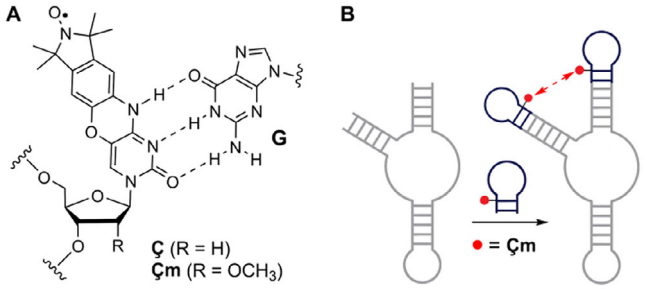

FIGURE 1 | **A**. The **Ç** and **Çm** spin labels are shown base-paired with guanine. **B**. Schematic representation of labeling a large RNA noncovalently through helical stacking with a **Çm**-labeled hairpin.

between the spin labels [18–19]. Thus, rigid spin labels give more detailed information about both the structure and dynamics of nucleic acids. However, both **Ç** and **Çm** have the drawback of requiring a labor-intensive multi-step synthesis and subsequent incorporation into nucleic acids using the phosphoramidite approach, which is limited to the synthesis of relatively short oligonucleotides [21, 24, 27].

Spin labels can also be incorporated into nucleic acids through noncovalent spin-labeling. One example is the binding of pyrimidine- and purine-derived nitroxides to abasic sites in DNA and RNA duplexes [28, 29]. However, such spin labels require the presence of abasic sites that need to be incorporated by chemical synthesis of oligonucleotides. Moreover, in some cases, they have poor affinity to the binding sites [28]. A ligand-binding RNA molecule (aptamer) has also been spin-labeled noncovalently through binding to its nitroxide-modified malachite green (MG) ligand [30]. This approach allows for spin-labeling of long RNAs containing the MG binding motif, prepared by transcription. However, the ligand-binding domain may interfere with the structure of the RNA under study. Base-pairing has also been used for noncovalent spin-labeling, where short, chemically synthesized oligomers containing a nitroxide label were hybridized to a segment of a large RNA [31]. Nonetheless, such an approach would require chemical synthesis of a spin-labeled oligomer of a certain sequence for each target RNA.

Another known noncovalent nucleic acid binding interaction is helical stacking of blunt-ended duplexes, observed by EPR spectroscopy [25, 32, 33]. In this paper, we describe end-to-end helical stacking of RNA for noncovalent spin-labeling with short hairpins containing the rigid spin label **Çm**. This approach minimizes the synthetic effort and cost of using rigid spin labels for RNA (Figure 1B). This involves the synthesis of a small **Çm**-labeled hairpin that can be used as a universal adaptor to spin label different RNAs noncovalently through helical stacking. Thus, this approach yields spin-labeled RNA without chemical modification of the RNA to be studied. We show that the affinity of stacking, and thereby the labeling efficiency, can be improved by using complementary overhangs.

2 | Results and Discussion

Although our strategy is for labeling long and structured RNAs, we used stacking of spin-labeled hairpins to duplexes for proof-of-principle experiments (Figure 2). The oligonucleotide constructs were designed such that the core sequences of the hairpins and duplexes were kept constant (Figure 2A). The hairpins were designed to minimize complementarity for duplex formation and contained the hairpin-stabilizing GNRA tetraloop [34]. We began by synthesizing a short blunt-ended hairpin ($\mathbf{I_{HP}}$) containing **Çm** [35] and its corresponding RNA duplex ($\mathbf{I_{DUPL}}$, Figure 2A). Incorporation of **Çm** into the hairpins was achieved through automated solid-phase synthesis as previously described [35]. The spin-labeled hairpins were enzymatically digested, and the digests were analyzed by high-performance liquid chromatography (HPLC) to demonstrate incorporation of intact **Çm** (Figure S1) [27, 35]. The spin-labeling efficiency was quantified by spin counting using CW-EPR spectroscopy (Figure S2).

Helical stacking in solution can be monitored by CW-EPR through line shape analysis [25]. Biomolecular assembly increases the rotational correlation time of spin-labeled RNAs and thereby the anisotropy and the associated line-broadening of the EPR spectra. Moreover, any association of two spin-labeled hairpins that brings two spin labels into close proximity (<15 Å) may alter the line shape through dipolar coupling between the nitroxide radicals if the rotational correlation time of the assembly is long, relative to the time scale of the EPR experiment [2, 25]. The EPR spectrum of the hairpin $\mathbf{I_{HP}}$ alone at -10°C shows some broadening and some irregular features (Figure 2B) that might arise from dipolar coupling due to self-stacking of the hairpins. Adding an unmodified duplex ($\mathbf{I_{DUPL}}$) resulted in the disappearance of the irregular features in the EPR spectrum, which might have been due to hairpin-duplex stacking and thereby reduced dipolar coupling. However, when the hairpin was titrated with an unmodified single-stranded RNA, a similar change in the line shape was observed (Figure S4C). This suggests that the disappearance of the irregular features may not solely be due to stacking between duplexes but also due to other nonspecific intermolecular interactions. The line shape of the EPR spectrum of $\mathbf{I_{HP}}$ alone at 20°C shows no broadening (Figure S3).

The stacking of two hairpins on the ends of the same duplex can be monitored by PELDOR. If $\mathbf{I_{HP}}$ stacks on each end of $\mathbf{I_{DUPL}}$, as in **I** (Figure 2A), the distance between the spin labels is expected to be ca. 3.0 nm, as predicted by molecular modeling (Figure S7, I, Table S2), ideal for a PELDOR measurement. However, the PELDOR data of **I** showed a broad distance distribution that was dominated by shorter distances (~ 2.2 nm) and some longer distances of much lower probability between 3 and 6 nm (Figure S6, B). The shorter distances are consistent with the modeled distance between two **Çm**s in a hairpin dimer (Figure S7, I, Table S2). Taken together, the data indicate that the blunt-ended $\mathbf{I_{HP}}$ prefers self-stacking rather than stacking with its duplex ($\mathbf{I_{DUPL}}$).

To favor hairpin-duplex stacking over hairpin-hairpin stacking, overhangs were incorporated at the 3'-end of the spin-labeled hairpins ($\mathbf{II_{HP}}$-$\mathbf{VI_{HP}}$) and the corresponding duplexes ($\mathbf{II_{DUPL}}$-$\mathbf{VI_{DUPL}}$) (Figure 2A). The overhangs were one to five nucleotides long and complementary to overhangs on the corresponding duplexes. Significant broadening (indicated by asterisks in Figure 2B) became prominent at -10°C in the CW-EPR spectra of the **Çm**-labeled hairpins $\mathbf{II_{HP}}$-$\mathbf{VI_{HP}}$. These features are consistent with increased anisotropy due to intermolecular association. On

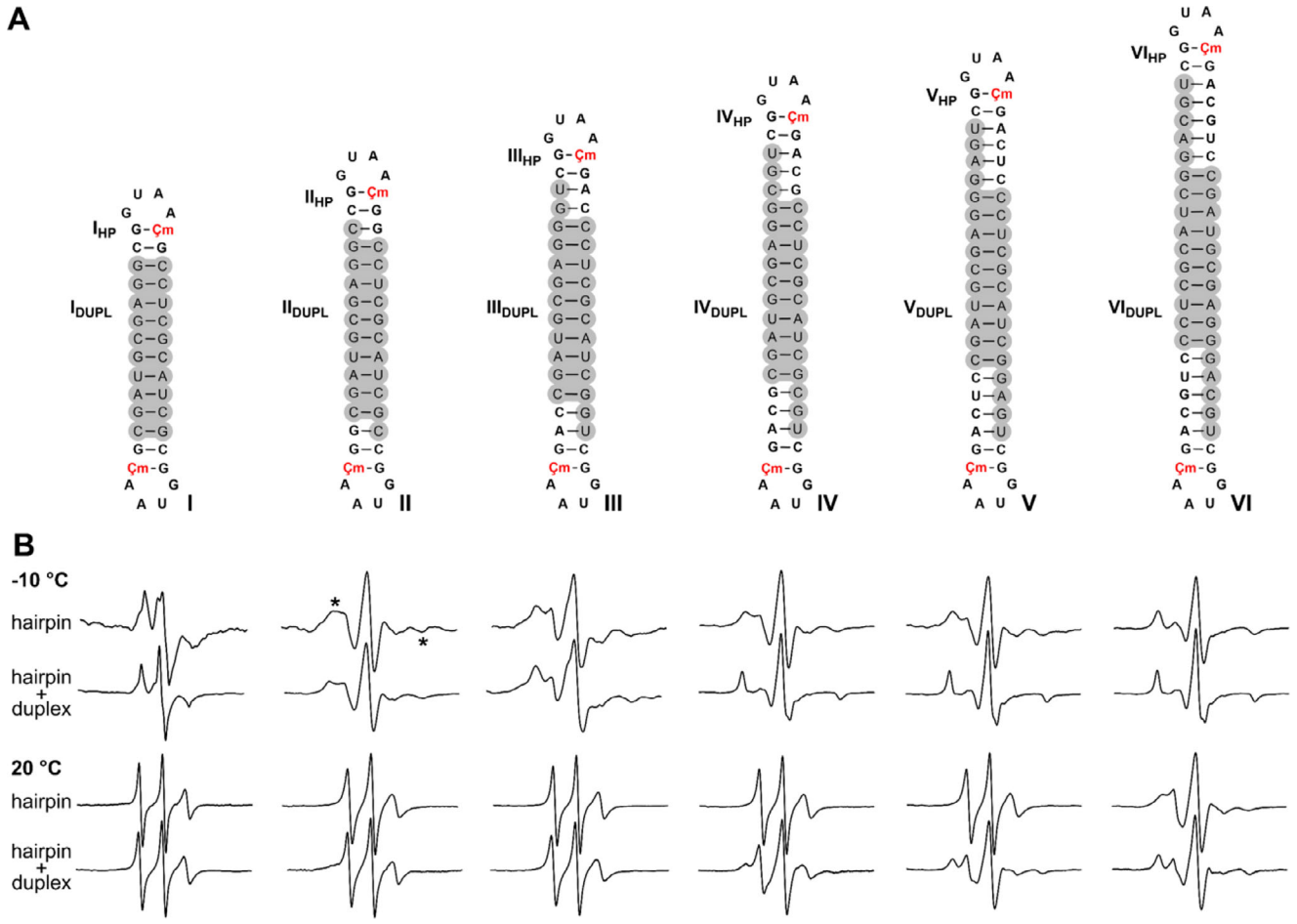

FIGURE 2 | **A**. The sequences of **Çm**-labeled hairpins ($\mathbf{I_{HP}}$-$\mathbf{VI_{HP}}$) shown stacked on their corresponding RNA duplexes ($\mathbf{I_{DUPL}}$-$\mathbf{VI_{DUPL}}$) (in gray), in the order of increasing number of nucleotides in the overhangs (0-5). The overhangs are on the 3'-end of both the hairpins and the duplexes. The hairpin-duplex assemblies are labeled **I**-**VI**. **B**. X-band EPR spectra of the hairpins ($\mathbf{I_{HP}}$-$\mathbf{VI_{HP}}$) in the absence and presence of their corresponding duplexes ($\mathbf{I_{DUPL}}$-$\mathbf{VI_{DUPL}}$) at -10°C and 20°C, recorded in a phosphate buffer (10 mM $NaHPO_4$, 100 mM NaCl, 0.1 mM Na_2EDTA, pH 7.0; concentration of each **Çm**-labeled hairpin was 200 μM and its corresponding duplex 100 μM). Asterisks indicate broad features.

mixing the hairpins with their corresponding duplexes, the slow-moving features became more pronounced, in particular for three-, four-, and five-nucleotide overhangs (**IV**-**VI**), consistent with hairpin-duplex stacking. Moreover, the EPR spectra for the assemblies containing three-to five-nucleotide-long overhangs look nearly identical, suggesting a similar extent of stacking at -10°C. As expected, the EPR spectra for hairpins $\mathbf{II_{HP}}$-$\mathbf{V_{HP}}$ alone at 20°C showed no detectable broadening (Figure 2B), since overhangs are known to prevent RNA stacking [33]. However, the EPR spectrum of the hairpin with a five-nucleotide overhang ($\mathbf{VI_{HP}}$) at 20°C indicated intermolecular association.

Interestingly, the hairpins with three-, four-, or five-nucleotide overhangs ($\mathbf{IV_{HP}}$-$\mathbf{VI_{HP}}$) showed significant spectral broadening upon addition of their corresponding duplexes ($\mathbf{IV_{DUPL}}$-$\mathbf{VI_{DUPL}}$) at 20°C, indicating that hairpin-duplex stacking at this temperature requires a minimum of 3-base overhangs for base-pairing. Indeed, this broad feature increases with the length of the overhang.

The hairpin-duplex stacking of assemblies **II**-**VI** was further studied by PELDOR. The depth of the oscillation pattern (modulation depth) in the PELDOR time traces (Figure 3A) reflects the extent of dipolar coupling between interacting spin pairs [36]. Therefore, a larger modulation depth would indicate more double-stacking of the **Çm**-labeled hairpins on the duplex ends. However, modulation depth also depends on the excitation bandwidth, as strong dipolar coupling at very short spin-spin distances can lead to incomplete excitation of all spin pairs, resulting in a lower observed modulation depth [14, 37]. However, the modulation depth does reflect the same general trend as observed in the CW-EPR data: it increases as the length of the overhang increases. The time traces for oligonucleotides with three- and more overhangs (**IV**, **V,** and **VI**) display the highest modulation depth (Figure 3A), suggesting efficient hairpin-duplex stacking. For one- or two-nucleotide overhangs (**II**, **III**), the modulation depth is noticeably smaller. This is presumably due to a very strong dipolar coupling resulting from hairpin self-association, which contributes only partly to the modulation depth. To partly compensate for the limited excitation due to dipolar coupling, we recorded PELDOR time traces using short (strong) pulses to broaden the excitation bandwidth (Figure S5A). The stronger pulses yielded a higher modulation depth for **III** than **II**, presumably reflecting a high degree of self-association for **II**.

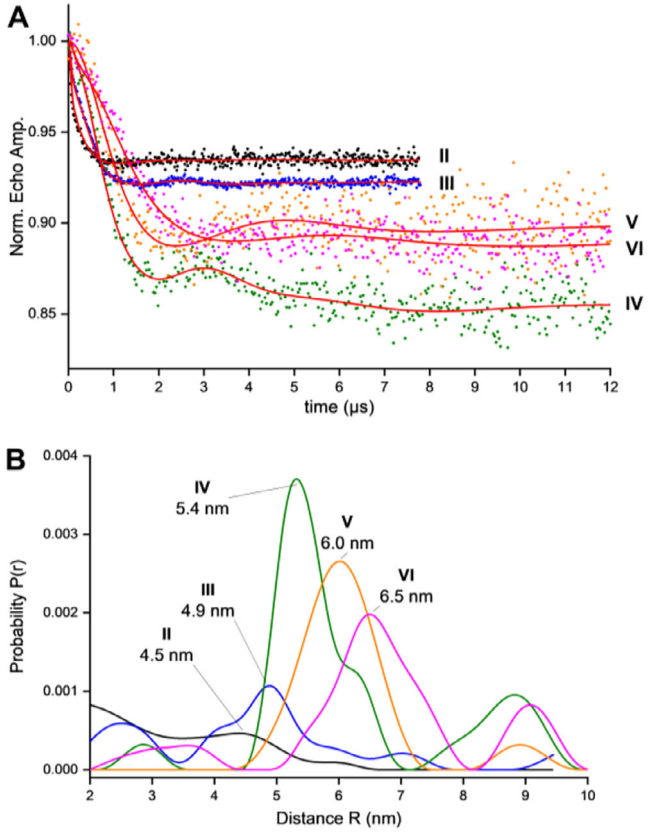

FIGURE 3 | **A**. PELDOR time-traces for the **Çm**-labeled hairpins with one to five nucleotide overhangs, mixed with their complementary RNA duplexes (**II**-**VI**). (10 mM $NaHPO_4$, 100 mM NaCl, 0.1 mM Na_2EDTA, 20% ethylene glycol, pH 7.0) **B**. Distance distribution derived from a Tikhonov regularization of the background-corrected PELDOR time traces using DeerAnalysis [38].

Although the modulation depth for assemblies **V** and **VI** is lower than for **IV**, it is not due to less stacking. The short transversal relaxation time only allowed a short time trace to be collected, relative to the longer oscillation of the PELDOR time trace [36]. This can lead to artifacts, such as a too-short distance distribution and wrong background correction, which in turn affects the modulation depth. As a result, the modulation is not as deep and the estimated distance is less accurate. However, hairpin-hairpin association can be excluded with certainty.

Tikhonov regularization of the time traces yielded the corresponding distance distributions (Figure 3B), further supporting the trends observed in the modulation depths. Assembly **II** and **III** show prominent short-distance populations (<3.5 nm), suggesting hairpin-hairpin association rather than stacking to the duplex ends. However, longer distances of 4.5 and 4.9 nm also appear, which agree with the expected modeled distances with the hairpins stacked on the duplex ends (3.9 and 4.6 nm, respectively) (Figure S5B). For the assembly with three- to five-nucleotide overhangs (**IV**-**VI**), the short-distance population is negligible, and a dominant distance distribution appears at ~5.4 nm, 6.0 nm, and 6.5 nm, respectively, close to that of the modeled distances of 5.0 nm, 5.5 nm, and 6.2 nm, respectively (Figure S5B). Overall, the PELDOR data aligns well with the CW-EPR results, further asserting that hairpins with three- or more overhangs exhibit the most efficient stacking.

3 | Conclusion

In conclusion, we have described a noncovalent spin-labeling strategy with the rigid spin label Çm that utilizes end-to-end helical stacking of RNAs. While blunt-ended hairpins did not result in appreciable stacking on RNA duplexes, CW-EPR and PELDOR experiments showed that inclusion of three or more complementary overhang nucleotides on the hairpins and duplexes resulted in efficient assembly. A great advantage of this spin-labeling strategy is that it circumvents the need to chemically incorporate a rigid spin label into each target RNA. Although the spin-labeled hairpin was prepared by chemical synthesis, each preparation can be used for multiple labeling; the spin-labeled RNA was prepared on a µmol scale, while only a few nmols are required for each PELDOR experiment. Thus, this labeling strategy reduces the synthetic effort and cost associated with rigid spin labeling.

Although the proof-of-principle experiments described here utilized hairpin-duplex stacking, this approach should be applicable for long RNAs produced by *in vitro* transcription, provided that accessible RNAs contain helix-loops that could be replaced with Çm-labeled hairpins. Potential applications include the study of helical arrangements within complex RNAs and interactions of RNA with other biomolecules, such as proteins. This labeling strategy can also be extended to other spectroscopic probes, such as fluorophores. Applications of this noncovalent spin-labeling approach, in conjunction with PELDOR, with structured RNAs will be reported in due course.

Acknowledgments

We acknowledge financial support from the Icelandic Research Fund (206708). I.M.A acknowledges the Aðalsteinn Kristjánsson Memorial Fund for providing the doctoral research fellowship. We thank Dr. Gunnar W. Reginsson for assistance with simulations of EPR spectra and for valuable suggestions, and members of the Sigurdsson research group for helpful discussions.

Conflicts of Interest

The authors declare no conflict of interest.

References

1. M. Bennati and T. Prisner, "New Developments in High Field Electron Paramagnetic Resonance With Applications in Structural Biology," *Reports on Progress in Physics* 68 (2005): 411.

2. P. Nguyen and P. Z. Qin, "RNA Dynamics: Perspectives From Spin Labels," *Wiley Interdiscip Rev RNA* 3 (2012): 62–72.

3. B. Endeward, A. Marko, V. P. Denysenkov, S. T. Sigurdsson, and T. F. Prisner, "Advanced EPR Methods for Studying Conformational Dynamics of Nucleic Acids," *Methods in Enzymology* 564 (2015): 403–425.

4. L. Hofmann and S. Ruthstein, "EPR Spectroscopy Provides New Insights Into Complex Biological Reaction Mechanisms," *The Journal of Physical Chemistry B* 126 (2022): 7486–7494.

5. P. C. Brennan, J. D. Grosskopf, A. M. Garces, C. L. Trier, and M. T. Lerch, "Capturing Protein Dynamics Across Timescales With Site-directed Spin Labeling Electron Paramagnetic Resonance Spectroscopy," *Current Opinion in Structural Biology* 93 (2025): 103073.

6. L. Galazzo and E. Bordignon, "Electron Paramagnetic Resonance Spectroscopy in Structural-dynamic Studies of Large Protein Complexes," *Progress in Nuclear Magnetic Resonance Spectroscopy* 134-135 (2023): 1–19.

7. A. Shah, J. L. Wort, Y. Ma, and C. Pliotas, "Enabling Structural Biological Electron Paramagnetic Resonance Spectroscopy in Membrane Proteins Through Spin Labelling," *Current Opinion in Chemical Biology* 84 (2025): 102564.

8. X. Zhang, P. Cekan, S. T. Sigurdsson, and P. Z. Qin, "Studying RNA Using Site-directed Spin-labeling and Continuous-wave Electron Paramagnetic Resonance Spectroscopy," *Methods in Enzymology* 469 (2009): 303–328.

9. N. K. Kim, A. Murali, and V. J. DeRose, "A Distance Ruler for RNA Using EPR and Site-directed Spin Labeling," *Chemistry & Biology* 11 (2004): 939–948.

10. J. E. Banham, C. M. Baker, S. Ceola, et al., "Distance Measurements in the Borderline Region of Applicability of CW EPR and DEER: A Model Study on a Homologous Series of Spin-labelled Peptides," *Journal of Magnetic Resonance* 191 (2008): 202–218.

11. J. A. Cooke and L. J. Brown, *Protein Folding, Misfolding, and Disease: Methods and Protocols*, ed. A. F. Hill, K. J. Barnham, S. P. Bottomley, and R. Cappai, (Humana Press, 2011), 73–96.

12. O. Schiemann and T. F. Prisner, "Long-range Distance Determinations in Biomacromolecules by EPR Spectroscopy," *Quarterly Reviews of Biophysics* 40 (2007): 1–53.

13. G. W. Reginsson and O. Schiemann, "Studying Biomolecular Complexes With Pulsed Electron–Electron Double Resonance Spectroscopy," *Biochemical Society Transactions* 39 (2011): 128–139.

14. G. Jeschke, "DEER Distance Measurements on Proteins," *Annual Review of Physical Chemistry* 63 (2012): 419–446.

15. T. Schmidt, M. A. Wälti, J. L. Baber, E. J. Hustedt, and G. M. Clore, "Long Distance Measurements up to 160 Å in the GroEL Tetradecamer Using Q-band DEER EPR Spectroscopy ," *Angewandte Chemie International Edition* 55 (2016): 15905–15909.

16. B. Endeward, Y. Hu, G. Bai, G. Liu, T. F. Prisner, and X. Fang, "Long-range Distance Determination in Fully Deuterated RNA with Pulsed EPR Spectroscopy," *Biophysical Journal* 121 (2022): 37–43.

17. V. P. Denysenkov, T. F. Prisner, J. Stubbe, and M. Bennati, "High-Field Pulsed Electron–Electron Double Resonance Spectroscopy to Determine the Orientation of the Tyrosyl Radicals in Ribonucleotide Reductase," *Proceedings of the National Academy of Sciences* 103 (2006): 13386–13390.

18. O. Schiemann, P. Cekan, D. Margraf, T. F. Prisner, and S. T. Sigurdsson, "Relative Orientation of Rigid Nitroxides by PELDOR: Beyond Distance Measurements in Nucleic Acids," *Angewandte Chemie International Edition* 48 (2009): 3292–3295.

19. T. F. Prisner, A. Marko, and S. T. Sigurdsson, "Conformational Dynamics of Nucleic Acid Molecules Studied by PELDOR Spectroscopy With Rigid Spin Labels," *Journal of Magnetic Resonance* 252 (2015): 187–198.

20. S. A. Shelke and S. T. Sigurdsson, "Site-Directed Spin Labelling of Nucleic Acids," *European Journal of Organic Chemistry* 2012 (2012): 2291–2301.

21. M. M. Haugland, J. E. Lovett, and E. A. Anderson, "Advances in the Synthesis of Nitroxide Radicals for Use in Biomolecule Spin Labelling," *Chemical Society Reviews* 47 (2018): 668–680.

22. H. Karoui, F. L. Moigne, O. Ouari, and P. Tordo, *Stable Radicals* (2010): 173–229.

23. G. Z. Sowa and P. Z. Qin, *Progress in Nucleic Acid Research and Molecular Biology*, ed. P. M. Conn, (Academic Press, 2008), 147–197.

24. S. A. Shelke and S. T. Sigurdsson, *Modified Nucleic Acids*, ed. T. Yitzhak and K. Nakatani (Springer, 2016), 159–187.

25. P. Cekan, A. L. Smith, N. Barhate, B. H. Robinson, and S. T. Sigurdsson, "Rigid Spin-labeled Nucleoside Ç: A Nonperturbing EPR Probe of Nucleic Acid Conformation," *Nucleic Acids Research* 36 (2008) : 5946–5954.

26. C. Höbartner, G. Sicoli, F. Wachowius, D. B. Gophane, and S. T. Sigurdsson, "Synthesis and Characterization of RNA Containing a Rigid and Nonperturbing Cytidine-derived Spin Label," *The Journal of Organic Chemistry* 77 (2012): 7749–7754.

27. N. Barhate, P. Cekan, A. P. Massey, and S. T. Sigurdsson, "A Nucleoside That Contains a Rigid Nitroxide Spin Label: A Fluorophore in Disguise," *Angewandte Chemie International Edition* 46 (2007): 2655–2658.

28. S. A. Shelke and S. T. Sigurdsson, "Noncovalent and Site-Directed Spin Labeling of Nucleic Acids," *Angewandte Chemie International Edition* 49 (2010): 7984–7986.

29. N. R. Kamble, M. Gränz, T. F. Prisner, and S. T. Sigurdsson, "Noncovalent and Site-directed Spin Labeling of Duplex RNA," *Chemical Communications* 52 (2016): 14442–14445.

30. S. Saha, T. Hetzke, T. F. Prisner, and S. T. Sigurdsson, "Noncovalent Spin-labeling of RNA: The Aptamer Approach," *Chemical Communications* 54 (2018): 11749–11752.

31. C. Helmling, I. Bessi, A. Wacker, et al., "Noncovalent Spin Labeling of Riboswitch RNAs to Obtain Long-range Structural NMR Restraints," *ACS Chemical Biology* 9 (2014): 1330–1339.

32. L. Pollack, "SAXS Studies of Ion–Nucleic Acid Interactions," *Annual Review of Biophysics* 40 (2011): 225–242.

33. N. Erlenbach, C. Grünewald, B. Krstic, A. Heckel, and T. F. Prisner, ""End-to-end" stacking of small dsRNA," *Rna* 25 (2019): 239–246.

34. H. A. Heus and A. Pardi, "Structural Features That Give Rise to the Unusual Stability of RNA Hairpins Containing GNRA Loops," *Science* 253 (1991): 191–194.

35. H. Y. Juliusson, A.-L. J. Segler, and S. T. Sigurdsson, "Benzoyl-Protected Hydroxylamines for Improved Chemical Synthesis of Oligonucleotides Containing Nitroxide Spin Labels," *European Journal of Organic Chemistry* 2019 (2019): 3799–3805.

36. O. Schiemann, C. A. Heubach, D. Abdullin, et al., "Benchmark Test and Guidelines for DEER/PELDOR Experiments On Nitroxide-labeled Biomolecules," *Journal of the American Chemical Society* 143 (2021): 17875–17890.

37. G. Jeschke, "Distance Measurements in the Nanometer Range by Pulse EPR," *Chemphyschem* 3 (2002): 927–932.

38. G. Jeschke, V. Chechik, P. Ionita, et al., "DeerAnalysis2006 – a Comprehensive Software Package for Analyzing Pulsed ELDOR Data," *Applied Magnetic Resonance* 30 (2006): 473–498.

39. Y. Polyhach, E. Bordignon, R. Tschaggelar, S. Gandra, A. Godt, and G. Jeschke, "High Sensitivity and Versatility of the DEER Experiment On Nitroxide Radical Pairs at Q-band Frequencies," *Physical Chemistry Chemical Physics* 14 (2012): 10762–10773.

Supporting Information

Additional supporting information can be found online in the Supporting Information section.

The authors have cited additional references within the Supporting Information [38, 39]. **Supporting File:** chem70626-sup-0001-SuppMat.docx

NON-COVALENT SPIN-LABELING OF RNA THROUGH HELICAL STACKING

Iram M. Ahmad,[a] Burkhard Endeward,[b] Thomas F. Prisner,[b] and Snorri Th. Sigurdsson*[a]

[a] *Department of Chemistry, Science Institute, University of Iceland, 107 Reykjavik, Iceland*
[b] *Institute of Physical and Theoretical Chemistry, Goethe University, D-60438 Frankfurt am Main, Germany*

Supporting Information

Table of contents

List of abbreviations

CPG	Controlled pore glass
EPR	Electron paramagnetic resonance
DMF	*N*,*N*-Dimethylformamide
EDTA	Ethylenediaminetetraacetic acid
ESI-TOF	Electrospray Ionization Time-of-Flight
HPLC	High-performance liquid chromatography
RP-HPLC	Reversed phase high-performance liquid chromatography
UV	Ultraviolet
CW	Continuous wave
ss	single-stranded
TBDMS	tert-Butyldimethylsilyl
DPAGE	Denaturing Polyacrylamide Gel Electrophoresis

RNA synthesis and purification

All commercial phosphoramidites, controlled pore glass (CPG) solid support, the activators 5-benzylthiotetrazole and 5-ethylthiotetrazole, as well as CH_3CN for oligonucleotide synthesis, were purchased from ChemGenes Corp. Columns for the CPG solid-support were purchased from BioAutomation. All other reagents and solvents were purchased from Sigma-Aldrich Co. RNA solid-phase oligonucleotide syntheses were performed on an automated ASM-800 DNA/RNA synthesizer (BIOSSET Ltd., Russia) using phosphoramidite chemistry. CH_2Cl_2 and CH_3CN were dried over calcium hydride and freshly distilled before use. Unmodified 2'O-TBDMS phosphoramidites were dissolved in CH_3CN (0.1 M), while the **Çm** phosphoramidite was dissolved in 1,2-dichloroethane (0.1 M). 5-benzylthiotetrazole (0.25 M in CH_3CN) was used as a coupling agent for the unmodified RNA phosphoramidites, and 5-ethylthiotetrazole (0.25 M in CH_3CN) was used for **Çm**. The coupling time was 7 min for the unmodified RNA phosphoramidites, and the **Çm** phosphoramidite was coupled manually for 10 min. Oxidation was performed with tert-butylhydroperoxide in toluene (1.0 M). Capping and detritylation were performed under standard conditions for RNA

oligonucleotide synthesis. The RNAs were deprotected and cleaved from the resin in a 1:1 solution (2 mL) of CH_3NH_2 (8 M in EtOH) and saturated aqueous NH_3 at 65 °C for 1 h. The solvent was removed *in vacuo*, and the 2'O-TBDMS groups were removed by incubation in a solution of $Et_3N\cdot 3HF$ (300 µL) in DMF (100 µL) at 55 °C for 1.5 h, followed by addition of sterilized water (100 µL). This solution was transferred to a Falcon tube (50 mL), and *n*-butanol (20 mL) was added. The mixture was stored at −20 °C for 14 h and centrifuged (4000 rpm) at 4 °C for 1 h. The solvent was decanted from the RNA pellet, and the pellet was dried *in vacuo*.

All oligonucleotides were purified by 20% denaturing polyacrylamide gel electrophoresis (DPAGE) and extracted twice from the gel slices using the "crush and soak method" with Tris buffer (250 mM NaCl, 10 mM Tris, 1 mM Na_2EDTA, pH 7.5). The solutions were filtered through GD/X syringe filters (0.45 µm, 25 mm diameter, Whatman) and were subsequently desalted using Sep-Pak cartridges (Waters), following the instructions provided by the manufacturer. The dried oligonucleotides were dissolved in deionized and sterilized water (200 µL for each oligonucleotide). Concentrations of the oligonucleotides were determined by measuring UV absorbance at 260 nm on an Agilent Cary UV-Vis Multicell Peltier spectrophotometer and calculated using Beer's law.

Molecular weights of the oligonucleotides were determined by LC-MS on a Waters Acuity Premier Peptide BEH C18 column (300 Å, 1.7 µm, 150 x 2.1 mm) using the following gradient: Solvent A, MeOH; Solvent B, DEPC-treated H_2O, 400 mM HFIP and 16 mM Et_3N; 0-18 min, 5%-100% A at 40 °C. An Orbitrap Exploris 120 mass spectrometer was operated in negative-ion mode.

HPLC analyses of enzymatic digests were carried out on an analytical Agilent 1200 HPLC system using a GL Science Inc. C18 4.6 × 150 mm analytical column with UV detection at 260 nm. Solvent gradients for analytical RP-HPLC were run at 1.0 mL/min using the following gradient: solvent A, triethylammonium acetate (TEAA) buffer (50 mM, pH 7.0), solvent B, CH_3CN; 0–4 min isocratic 4% B, 26 min linear gradient to 100% B, 4 min isocratic 100% B, 2 min linear gradient to 100% B, and isocratic for 4 min.

MS analysis of the synthesized oligonucleotides

Table S1. Monoisotopic masses of the synthesized oligonucleotides. $\mathbf{I_{HP}}$-$\mathbf{VI_{HP}}$ are the **Çm**-labeled hairpins. Subscripts **SSa** and **SSb** denote the complementary single strands that make up duplexes $\mathbf{I_{DUPL}}$-$\mathbf{VI_{DUPL}}$.

Sequence ID	Sequence	Calculated mass	Observed mass
$\mathbf{I_{HP}}$	5'-CGG UAA **Çm**G-3'	2764.508	2763.491
$\mathbf{II_{HP}}$	5'-CGG UAA **Çm**GG-3'	3109.555	3109.465
$\mathbf{III_{HP}}$	5'-CGG UAA **Çm**GA C-3'	3398.601	3398.503
$\mathbf{IV_{HP}}$	5'-CGG UAA **Çm**GA CG -3'	3743.648	3743.540
$\mathbf{V_{HP}}$	5'-CGG UAA **Çm**GA CUC-3'	4009.667	4009.546
$\mathbf{VI_{HP}}$	5'-CGG UAA **Çm**GA CGU C-3'	4354.714	4354.589
$\mathbf{I_{SSa}}$	5'-CCU CGC AUC G-3'	3095.453	3095.326
$\mathbf{I_{SSb}}$	5'-CGA UGC GAC G-3'	3198.493	3238.493
$\mathbf{II_{SSa}}$	5'-CCU CGC AUC GC-3'	3400.494	3400.396
$\mathbf{II_{SSb}}$	5'-CGA UGC GAG GC-3'	3543.540	3543.438
$\mathbf{III_{SSa}}$	5'-CCU CGC AUC GGU-3'	3746.525	3746.417
$\mathbf{III_{SSb}}$	5'-CGA UGC GAG GGU-3'	3889.571	3889.458
$\mathbf{IV_{SSa}}$	5'-CCU CGC AUC GCG U-3'	4051.566	4051.451
$\mathbf{IV_{SSb}}$	5'-CGA UGC GAG GCG U-3'	4194.612	4194.494
$\mathbf{V_{SSa}}$	5'-CCU CGC AUC GGA GU-3'	4420.625	4420.500
$\mathbf{V_{SSb}}$	5'-CGA UGC GAG GGA GU-3'	4563.671	4563.534
$\mathbf{VI_{SSa}}$	5'-CCU CGC AUC GGA CGU-3'	4725.666	4726.529
$\mathbf{VI_{SSb}}$	5'-CGA UGC GAG GGA CGU-3'	4868.712	4869.572

HPLC analyses of enzymatically digested Çm labeled hairpins

To an oligonucleotide (4 nmol) in sterile water (8 µL) was added calf intestinal alkaline phosphatase (1 µL, 2 U), snake venom phosphodiesterase I (4 µL, 0.2 U), nuclease P1 from Penicillium citrinum (5 µL, 1.5 U), and Tris buffer (2 µL, 500 mM Tris and 100 mM $MgCl_2$). The samples were incubated at 37 °C for 24 h, after which they were analyzed by HPLC chromatography (**Figure S1**). The HPLC chromatograms for digests of $\mathbf{I_{HP}}$–$\mathbf{VI_{HP}}$ each showed five peaks, one for each natural nucleoside and a more strongly retained peak for the **Çm** nucleoside peak (**Figure S1**).

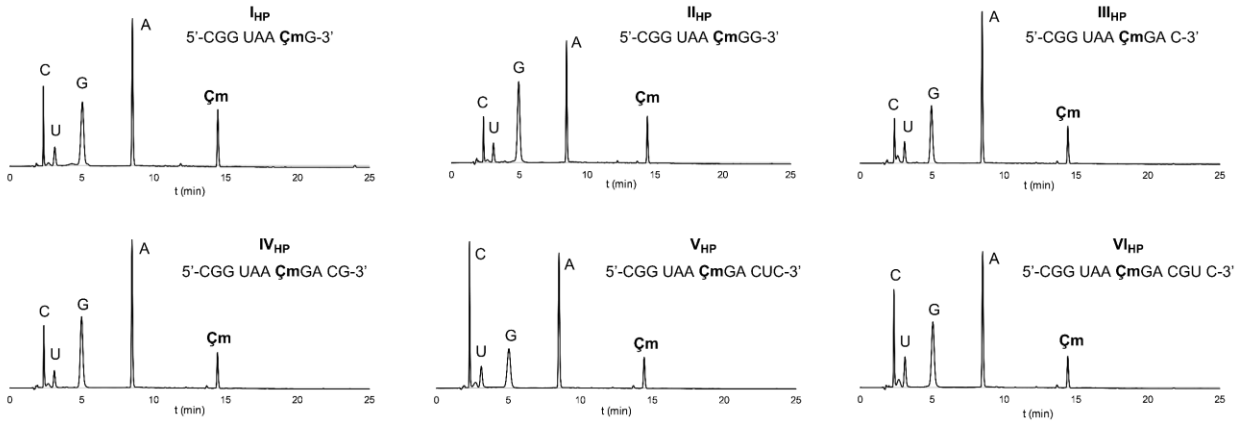

Figure S1. HPLC chromatograms of the **Çm** labeled RNA oligonucleotide digests $\mathbf{I_{HP}}$–$\mathbf{VI_{HP}}$.

EPR analyses

CW-EPR measurements

Instrument and settings

The EPR spectra were recorded on a MiniScope MS200 (Magnettech Germany) spectrometer (100 kHz modulation frequency, 1.0 G modulation amplitude and 2.0 mW microwave power). Magnettech temperature controller M01 (± 0.5 °C) was used as temperature regulator. The samples were placed in a quartz capillary (BLAUBRAND intraMARK) prior to EPR measurements.

CW-EPR measurements of the Çm-labeled hairpins and spin-counting

Samples of the **Çm**-labeled oligonucleotides for EPR measurements were prepared by dissolving the RNA (2.0 nmol) in phosphate buffer (10 µL, 10 mM phosphate, 100 mM NaCl, 0.1 mM Na_2EDTA, pH 7.0; oligonucleotide final concentration 200 µM), annealing at 90 °C for 2 min, 60 °C for 5 min, 50 °C for 5 min, 22 °C for 15 min and placing the sample in a 50 µL quartz capillary . The amount of spin label in each oligonucleotide was determined by spin counting. A stock solution of 4-hydroxy-TEMPO (1.0 M) was prepared in phosphate buffer (10 mM phosphate, 100 mM NaCl, 0.1 mM Na_2EDTA, pH 7.0). The stock solution was diluted into samples of different concentrations (0–0.5 mM), and each sample was measured by EPR spectroscopy. The area under the peaks of each spectrum, obtained by double integration,

was plotted against its concentration to yield a standard curve and was used to determine the spin labeling efficiency with an error margin of 5–10%.

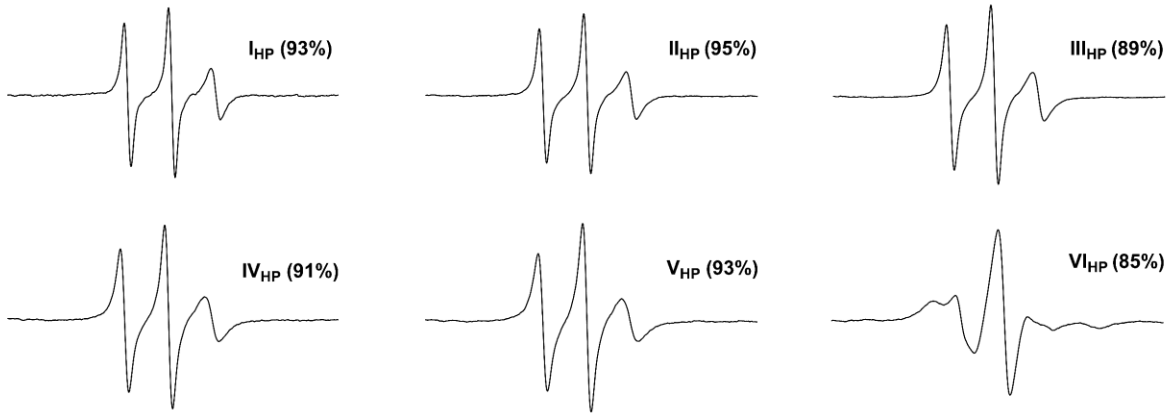

Figure S2. EPR spectra of the **Çm** labeled hairpin RNAs with the corresponding spin-counts in parenthesis.

CW-EPR measurements of the spin-labeled hairpin and duplex assemblies

Solutions for CW-EPR experiments were prepared by mixing each **Çm**-labeled RNA hairpin (2.0 nmol) with its corresponding unlabeled RNA duplex (1 nmol). The solvent was evaporated in vacuo, the resulting residue was dissolved in a phosphate buffer (10 µL; 10 mM Na_2HPO_4, 100 mM NaCl, 0.1 mM Na_2EDTA, pH 7.0; oligonucleotide final spin concentration 200 µM), annealed as described above and placed in a 50 µL quartz capillary.

Temperature-dependent CW-EPR spectra of the Çm-labeled hairpin I_{HP}

Temperature-dependent EPR studies were performed with the **Çm**-labeled hairpin **I_{HP}** alone to monitor the change in the line-shape of the EPR spectra upon gradually lowering the temperature (**Figure S3**). The arrows indicate the additional features that become prominent as the temperature decreases.

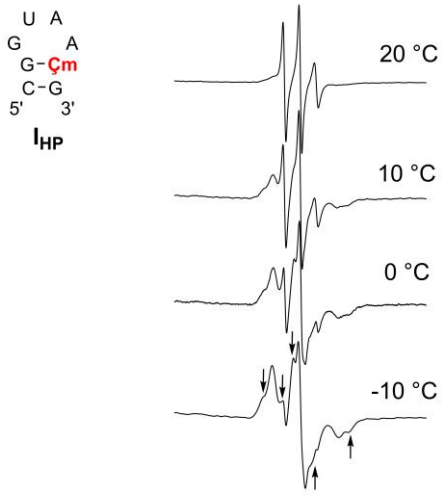

Figure S3. Sequence of the **Çm** labeled hairpin $\mathbf{I_{HP}}$ and its X-band EPR spectra as a function of temperature. All data were recorded a phosphate buffer (10 mM Na_2HPO_4, 100 mM NaCl, 0.1 mM Na_2EDTA, pH 7.0; oligo concentration 200 µM). (Arrows indicate the additional features).

Effect of duplex and ssRNA on the Çm-labeled hairpin $\mathbf{I_{HP}}$

We hypothesized that the additional broad features observed in the EPR spectrum of hairpin $\mathbf{I_{HP}}$ arouse from dipolar coupling between stacked hairpins. If this is the case, these features should diminish and eventually disappear upon addition of an unmodified duplex, as the labeled hairpin would preferentially stack on the duplex instead of on another hairpin. **Figure S4B** shows the EPR spectra with increasing amounts of unmodified duplex $\mathbf{I_{DUPL}}$ on the **Çm** labeled hairpin $\mathbf{I_{HP}}$ at -10 °C, while **Figure S4C** shows a similar experiment with an unmodified ssRNA $\mathbf{I_{DUPLa}}$. Both the experiments yield the same result, i.e. the disappearance of the additional features.

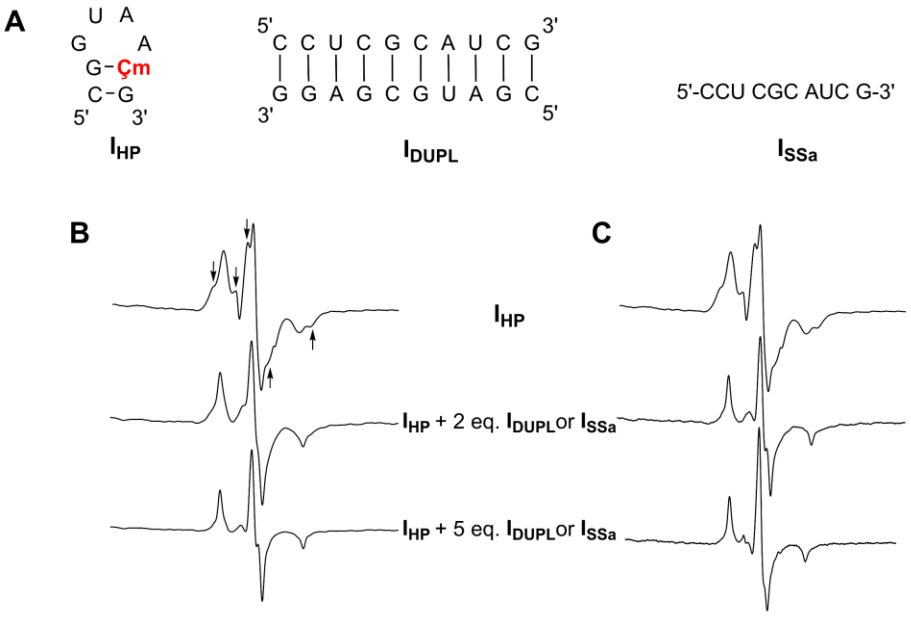

Figure S4. A. Sequences of the **Çm** labeled hairpin $\mathbf{I_{HP}}$, RNA duplex $\mathbf{I_{DUPL}}$ and ssRNA $\mathbf{I_{DUPLa}}$. **B**. EPR spectra of the **Çm**-labeled hairpin **I** on addition of 2 and 10 eq. of unlabeled RNA duplex $\mathbf{I_{DUPL}}$ at -10 °C. **C**. EPR spectra of the **Çm**-labeled hairpin on addition of 2 and 10 eq. of unlabeled ssRNA $\mathbf{I_{SSa}}$ at -10 °C. (Arrows indicate the additional features).

PELDOR measurements

Sample preparation

Each sample was prepared by annealing each **Çm**-labeled hairpin (20.5 nmol), mixed with each strand of the corresponding RNA duplex (10 nmol) in 100 µL of PNE buffer (10 mM Na_2HPO_4, pH 7.0; 100 mM NaCl; 0.1 mM Na_2EDTA), followed by evaporation of water. Solutions for PELDOR measurements were prepared by dissolving the sample in 20% ethylene glycol in sterile water (100 µL) to yield a spin-pair concentration of 100 µM. An aliquot of each sample (10 µL, 30 µL) was subsequently transferred into Suprasil tubes (10 µL: 1.6 mm OD; Wilmad WG-222T-RB, 30 µL: 2.8 mm OD; Wilmad Q-2M-2.8M-0-120M/RB). Samples were shock-frozen in liquid nitrogen prior to being inserted into the resonator within a cryostat at 50 K.

Instrumentation and settings

PELDOR data were recorded on an Elexsys E580 EPR spectrometer (Bruker) at Q-band frequencies (34 GHz), equipped with a TE102 rectangular resonator for the long pulses suitable for oversized sample tubes (2.8 mm OD)[39] and a EN 5107D2 from Bruker for the short pulse (1.6 mm OD), a continuous-flow helium cryostat (CF935, Oxford Instruments) and a temperature control system (ITC 502, Oxford Instruments). Experiments were performed at 50 K. A TWT amplifier (150 W; Bruker) was used for microwave amplification. The pump pulse was chosen to coincide with the maximum of the field-swept spectrum. Detection was performed at a frequency offset of $\Delta\nu$ = -80 MHz.

PELDOR experiments with 'short' pulses: The detection pulses had a length of 32 ns and the pump pulses were optimized for a length of 14 ns. Tau values of τ_1 = 232 ns were used, with a tau averaging cycle of 8 × 16 ns, to suppress deuterium modulations. The shot repetition time was set to 2 µs. The time increment of 8 ns up to 6 µs were chosen for the length of the PELDOR time traces.

PELDOR experiments with 'long' pulses: The detection pulses had a length of 84 ns and the pump pulses were optimized for a length of 36 ns. Tau values of τ_1 = 232 ns were used, with a tau averaging cycle of 8 × 16 ns, to suppress deuterium modulations. The shot repetition time was set to 3 µs. The time increment of 32 ns up to 16 µs were chosen for the length of the PELDOR time traces.

Primary PELDOR data were background-corrected by a mono exponential decay function (3D background). Tikhonov regularization was subsequently performed on the background-corrected PELDOR data, to obtain the distance probability function P(r). Data processing was done using the MATLAB toolbox DeerAnalysis 2022.[38]

To obtain more information on the shorter distances, PELDOR was performed using the short (strong) pulses on **Çm** labeled hairpins ($\mathbf{II_{HP}}$-$\mathbf{IV_{HP}}$, one- to three-nucleotide overhangs), mixed with their corresponding duplexes ($\mathbf{II_{DUPL}}$-$\mathbf{IV_{DUPL}}$). The resulting PELDOR time traces and distance distributions are shown in **Figure S5**. The PELDOR time traces show that the modulation depth increases from the one- to three-nucleotide overhang oligonucleotides,

reflecting a larger proportion of spin pairs contributing to the expected dipolar interaction (**Figure S5A**).

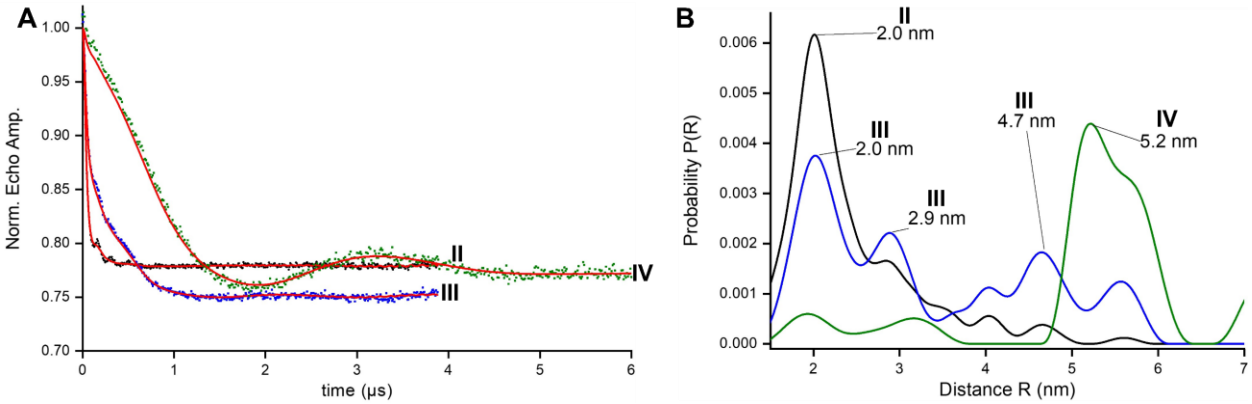

Figure S5. **A**. PELDOR time traces with short (strong) pulses for the **Çm** labeled hairpin-duplex assembly **II-IV** with one to three nucleotide overhangs. **B**. Distance distribution derived from a Tikhonov regularization of the background corrected PELDOR time traces.

The distance distributions (**Figure S5B**) show a clear progression in stacking behavior with the number of nucleotides in the overhang. With only one-nucleotide overhang (**II**), the majority of the distance distribution lies below 3.5 nm, indicating that most spin-labeled hairpins are in close proximity, presumably due to self-association rather than stacked on the duplex. With two-nucleotide overhang assembly (**III**), the intensity of short distances decreases, and a broader distribution begins to emerge around 4.7 nm, reflecting an increase in the hairpin-duplex stacking. With three-nucleotide overhang (**IV**), the short-distance population became negligible, and a dominant distance distribution appears at ~5.2 nm, consistent with specific stacking of the hairpins on both ends of the duplex.

Detailed PELDOR data for all hairpin-duplex assemblies

Figure S7 shows the detailed PELDOR data of all the hairpin-duplex assemblies (**I-VI**). It includes the raw data and background corrected time traces the PELDOR measurements, performed with both short and long pulses.

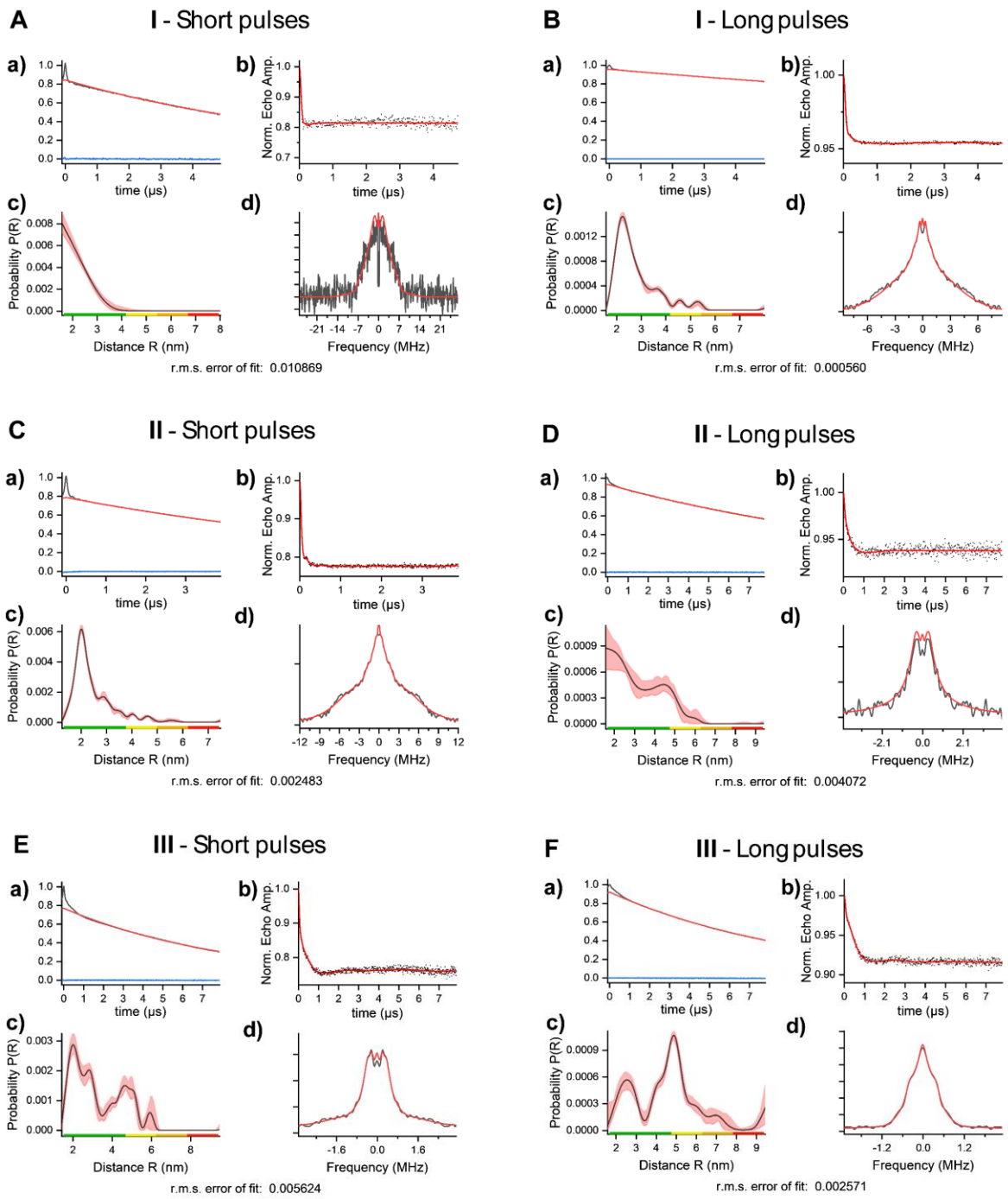
A
I - Short pulses
a)
b)
c)
d)
time (µs)
Norm. Echo Amp.
Probability P(R)
Distance R (nm)
Frequency (MHz)
r.m.s. error of fit: 0.010869
B
I - Long pulses
r.m.s. error of fit: 0.000560
C
II - Short pulses
r.m.s. error of fit: 0.002483
D
II - Long pulses
r.m.s. error of fit: 0.004072
E
III - Short pulses
r.m.s. error of fit: 0.005624
F
III - Long pulses
r.m.s. error of fit: 0.002571

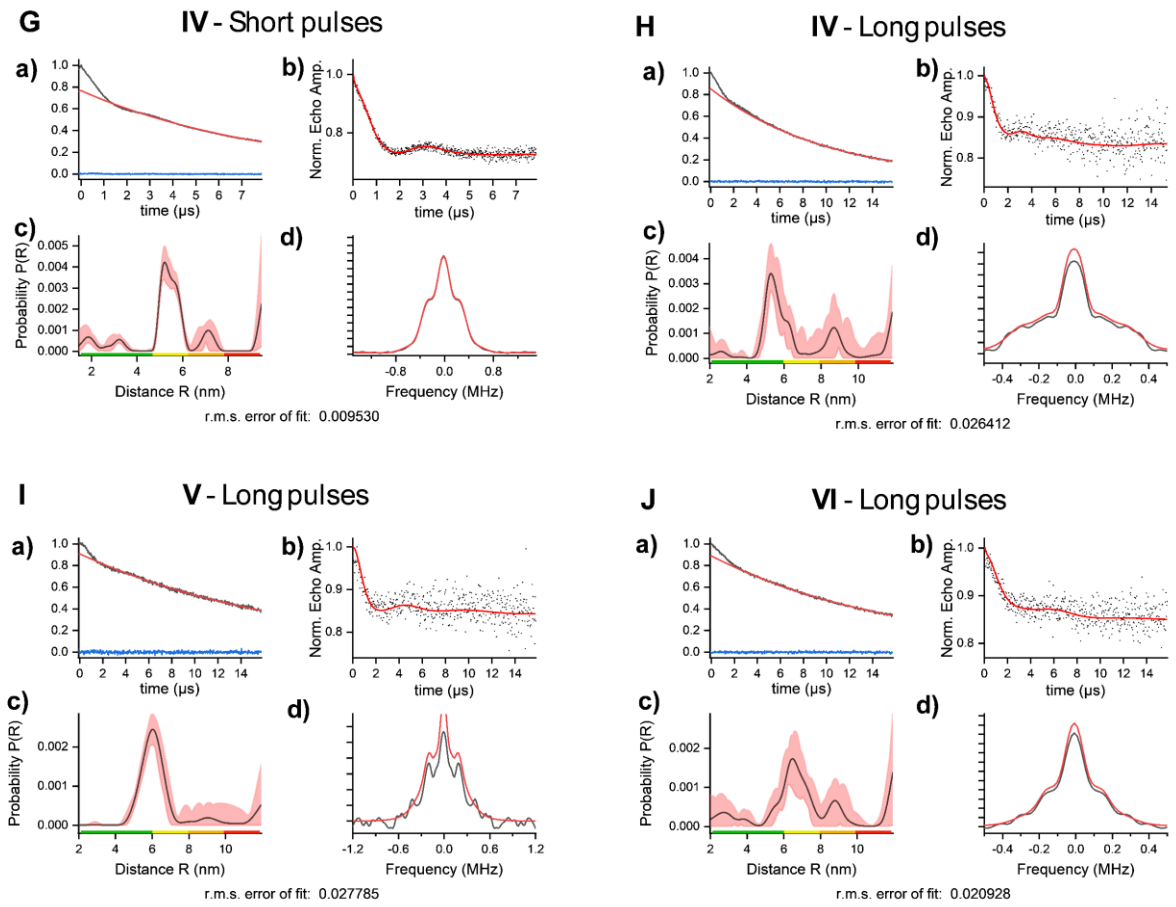

Figure S6. PELDOR time traces and distance distributions for assemblies **I**-**VI**, using short and long pulses (**A**-**J**). **a**) Normalized PELDOR time traces. The background fits are indicated as a red line. **b**) Background-corrected PELDOR time traces and fits of the signal (red). **c**) Distance distributions from PELDOR time trace (black). The red shadow is the estimated uncertainty. **d**) Fourier transform data from the PELDOR formfactors (black) and the fitted model (red).

Molecular models of the hairpin-duplex stacked assemblies

To determine the expected distances between the spin-centers for hairpins stacked on the duplexes, we used molecular modeling (BIOVIA, Dassault Systèmes, Discovery Studio Visualizer, v24.1.0.23298, San Diego: Dassault Systèmes, 2024). To model the hairpins stacked on each other or on the duplexes would require manual stacking, which could give inaccurate measurements. Therefore, for simplification, we modeled only the duplexes by extending their sequences to include the **Çm**-labeled hairpin helix sequences at both ends (**Figure S7**).

To estimate the expected inter-spin distances in the assemblies, we modeled stacked assemblies by extending duplex sequences to include the hairpin stem and positioning **Çm** labels at both ends (**Figure S7**).

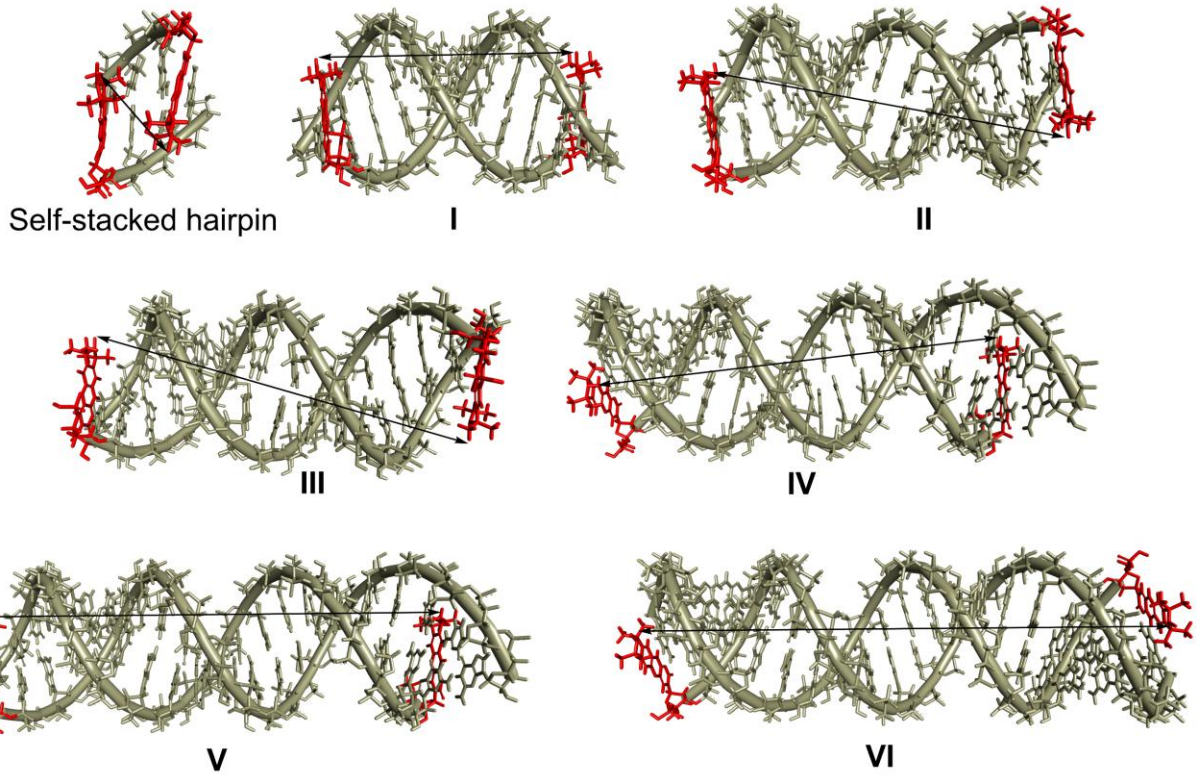

Figure S7. Molecular models of self-stacked hairpin **I** and the duplexes extended with the **Çm**-containing helical region of the hairpins, on both the ends of duplex (**I-VI**). The double-headed arrows show the distance determination (distances listed in **Table S2**).

The expected distances between the spin-centers along with the distances measured by PELDOR are shown in **Table S2**. The data show a clear trend of increasing inter-spin distance with increase in the length of the spin-labeled assembly, and the measured values agree closely with the modeled expectations, generally deviating by less than ~0.5 nm.

Table S2. Expected distances from molecular modeling

Hairpin-duplex assembly	Expected distances (nm)	Measured distances (nm)
I	3.0	(2.2)
II	3.9	4.5
III	4.6	4.9
IV	5	5.4
V	5.5	6.0
VI	6.2	6.5
Self-stacked Hairpin	1.5	-

Paper III

Paper III. Partial wrapping of single-stranded DNA by Replication Protein A and modulation through phosphorylation

Chadda R, Kaushik V, Ahmad IM, Deveryshetty J, Holehouse A, Sigurdsson ST, Biswas G, Levy Y, Bothner B, Cooley R, Mehl R, Dastvan R, Origanti S and Antony E, *Nucleic Acids Res*. **2024**, 52, 11626–40.

Nucleic Acids Research, 2024, **52**, 11626–11640
https://doi.org/10.1093/nar/gkae584
Advance access publication date: 11 July 2024
Genome integrity, repair and replication

Partial wrapping of single-stranded DNA by replication protein A and modulation through phosphorylation

Rahul Chadda[1,†], Vikas Kaushik[1,†], Iram Munir Ahmad[2], Jaigeeth Deveryshetty[1], Alex S. Holehouse[3], Snorri Th. Sigurdsson[2], Gargi Biswas[4], Yaakov Levy[4], Brian Bothner[5], Richard B. Cooley[6], Ryan A. Mehl[6], Reza Dastvan[1], Sofia Origanti[7] and Edwin Antony[1,*]

[1]Department of Biochemistry and Molecular Biology, Saint Louis University School of Medicine, St. Louis, MO 63104, USA
[2]Department of Chemistry, Science Institute, University of Iceland, 107 Reykjavik, Iceland
[3]Department of Biochemistry and Molecular Biophysics, Washington University in Saint Louis School of Medicine, St. Louis, MO 63110, USA
[4]Department of Chemical and Structural Biology, Weizmann Institute of Science, Rehovot, Israel
[5]Department of Chemistry and Biochemistry, Montana State University, Bozeman, MT 59717, USA
[6]Department of Biochemistry and Biophysics, Oregon State University, Corvallis, OR 97331, USA
[7]Department of Biology, Saint Louis University, St. Louis, MO 63103, USA

[*]To whom correspondence should be addressed. Tel: +1 314 977 9257; Fax: +1 314 977 9206; Email: edwin.antony@health.slu.edu
[†]The first two authors should be regarded as Joint First Authors.

Abstract

Single-stranded DNA (ssDNA) intermediates which emerge during DNA metabolic processes are shielded by replication protein A (RPA). RPA binds to ssDNA and acts as a gatekeeper to direct the ssDNA towards downstream DNA metabolic pathways with exceptional specificity. Understanding the mechanistic basis for such RPA-dependent functional specificity requires knowledge of the structural conformation of ssDNA when RPA-bound. Previous studies suggested a stretching of ssDNA by RPA. However, structural investigations uncovered a partial wrapping of ssDNA around RPA. Therefore, to reconcile the models, in this study, we measured the end-to-end distances of free ssDNA and RPA–ssDNA complexes using single-molecule FRET and double electron–electron resonance (DEER) spectroscopy and found only a small systematic increase in the end-to-end distance of ssDNA upon RPA binding. This change does not align with a linear stretching model but rather supports partial wrapping of ssDNA around the contour of DNA binding domains of RPA. Furthermore, we reveal how phosphorylation at the key Ser-384 site in the RPA70 subunit provides access to the wrapped ssDNA by remodeling the DNA-binding domains. These findings establish a precise structural model for RPA-bound ssDNA, providing valuable insights into how RPA facilitates the remodeling of ssDNA for subsequent downstream processes.

Graphical abstract

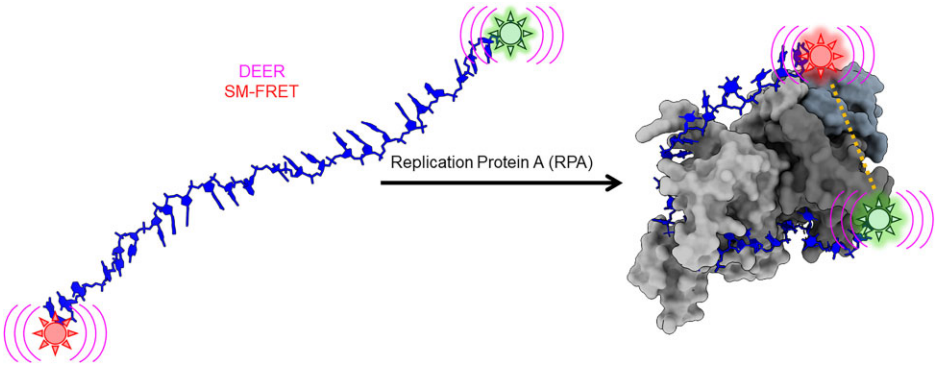

Introduction

Replication protein A (RPA) is an essential eukaryotic single-stranded DNA (ssDNA) binding protein that sequesters transiently exposed ssDNA during various DNA metabolic processes (1–4). RPA binds to ssDNA with high affinity (K_d ~10^{-10} M) (5,6), resolves secondary structures, and shields it from nucleolytic degradation (7–10). Notably, the assembly of RPA filaments on ssDNA acts as a trigger for the DNA damage checkpoint (11–14). RPA–ssDNA filaments also function as an interaction hub by recruiting over thirty proteins/enzymes

Received: April 1, 2024. **Revised:** May 30, 2024. **Editorial Decision:** June 18, 2024. **Accepted:** June 25, 2024

and promoting their assembly on DNA with correct binding polarity (15–17). This multifaceted functionality is enacted through six oligonucleotide/oligosaccharide binding (OB) domains housed within a heterotrimeric complex (Figure 1A) (18–20).

Human RPA is a constitutive heterotrimer composed of three subunits RPA70, RPA32 and RPA14. Six OB domains (A–F) are spread across the three subunits. OB-F, A, B and C reside in RPA70 and are connected by disordered linkers. RPA32 harbors OB-D and a winged helix (wh) motif. OB-E is a structural domain in RPA14 and holds the three subunits together as part of a trimerization core (Tri-C) along with OB-C & OB-D (21). Domains A, B, C & D primarily coordinate ssDNA interactions and are termed DNA-binding domains (DBDs). OB-F and wh coordinate protein-protein interactions and are called protein-interaction domains (PIDs). Dynamic rearrangements of the DBDs and PIDs are observed upon binding to DNA and in response to post-translational modifications (22–25). Each DBD exhibits a moderate affinity for ssDNA binding. Consequently, their collective action engenders a remarkably high affinity and stoichiometric binding of RPA to ssDNA (1). The intrinsic dynamic binding/dissociation characteristics of each DBD transiently unveil pockets within the buried ssDNA, enabling access for incoming proteins while the RPA complex remains attached to the ssDNA (19,26,27).

One fascinating aspect of RPA–ssDNA interactions and the proposed roles in DNA metabolism is the sequestration of the DNA. If the ssDNA is buried under RPA due to the high-affinity interactions, how do incoming proteins gain access to the DNA? This problem is enhanced when specific structures associated with the DNA need to be recognized. For example, during homologous recombination (HR), a double strand break is corrected by resection of one strand and thus producing a DNA substrate with a long 3′ overhang and a ss–dsDNA junction (28,29). The ssDNA is coated by RPA and a Rad51 nucleoprotein must be formed on the ssDNA to promote subsequent steps in HR. So, the position of RPA on the DNA with respect to the ss–dsDNA junction likely plays a key role in initiating Rad51 binding. These ssDNA overhangs can be up to 2000 nt long (30,31), thus positioning of the 3′ end of the ssDNA and the ss–dsDNA junction are critical. Two crucial parameters play a pivotal role in unravelling the intricate RPA–ssDNA interactions: a) the length of the ssDNA, and b) the shaping or contour of the RPA–ssDNA complex. The length of the ssDNA determines the number of assembled RPA molecules, subsequently influencing the variety and number of interactors recruited during a specific cellular DNA metabolic process (6). Concurrently, the shape of the complex determines the positioning of the ss-ds junction, or fork, respective to the 3′ or 5′ termini. If the DNA is stretched by RPA, then the spacing between two positions on the DNA will be distant. Conversely, if DNA is wrapped by RPA, then this distance would be much closer. On average, the occluded site-size for a single human RPA heterotrimer is ∼18–25 nucleotides (nt) (32). Therefore, the density of RPA molecules can be reasonably inferred to be proportional to the length of the ssDNA. Additionally, employing poly-pyrimidine (dT) ssDNA as experimental substrates further mitigates interference arising from secondary structures.

Surprisingly, there is a lack of experimental consensus regarding the configuration of ssDNA within the RPA–ssDNA complex. In both X-ray and CryoEM structures of diverse RPA–ssDNA complexes, the ssDNA displays a 'C' shape, exhibiting end-to-end distances typically ranging between ∼5 and 8 nm (Figure 1B) (18–20). Remarkably, in all these structures, the contour of the ssDNA along the DBDs of RPA is similar including comparable end-to-end distances. However, the structural findings could be influenced by the utilization of truncated RPA (18), or a limited subset of its DBDs (21), alongside potential artifacts originating from crystal packing (crystallography), or dynamics-induced factors (CryoEM) (19). In contrast, biochemical and bulk FRET measurements suggest a complete linearization of even short 30 nucleotide (nt) long ssDNA (19). However, bulk FRET assays are often a readout of multiple underlying populations, especially at relatively high protein to ssDNA ratios.

To mitigate experimental biases or limitations, and accurately determine the contour of ssDNA bound to RPA, we employed solution-based single-molecule confocal FRET and double electron–electron resonance (DEER) spectroscopy (33–36) to directly measure the end-to-end distance of ssDNA, both in the absence and presence of RPA. On average, we observe only a small ∼3 nm increase in the ssDNA end-to-end distance in the RPA-bound complex. Our results suggest a partial wrapping of ssDNA around RPA, exhibiting a contour closer to that observed in the crystal structure (18). Therefore, models depicting RPA–ssDNA interactions during DNA metabolism should consider the significant curvature induced in the DNA lattice upon RPA binding. Furthermore, we show that the post-translational modification of RPA through phosphorylation at Ser-384 in the RPA70 subunit introduces substantial changes in the arrangement of the DBDs and PIDs while causing only minimal changes in the pattern of ssDNA wrapping. Thus, access to internal ssDNA segments can be made available by remodeling the RPA domains to serve specific DNA metabolic roles without substantially altering the path, or shape, of DNA.

Materials and methods

Preparation of oligonucleotides

Unlabeled, Cyanine-5, and Cyanine-3 end-labeled poly- (dT) ssDNA oligonucleotides of various lengths $(dT)_n$ ($n = 15$, 30, 45, 60, 80 or 97 thymidine bases; Supplementary Table S1) were purchased from Integrated DNA Technologies (Iowa). For the synthesis of the doubly spin-labeled $(dT)_{22}$ and $(dT)_{50}$ oligonucleotides, 2′-aminouridine nucleotides were incorporated at specific sites (Supplementary Table S1) and post-synthetically spin labeled with an isothiocyanate derivative of an isoindoline nitroxide as described (37).

Purification of RPA and site-specific phosphoserine incorporation

Human RPA was produced using plasmid pET-Duet1-hRPA^{syn}-70C-His coding for a poly-His affinity tag at the C-terminus of RPA70. The open reading frames for RPA70, RPA32 and RPA14 were codon-optimized for overexpression in *E. coli* (GenScript Inc). RPA70 was engineered into multiple cloning site (MCS) 1 while RPA32 and RPA14 were cloned into MCS2. RPA was purified as described (38) with the following modifications. Briefly, the plasmid was transformed into BL21 (DE3) cells and transformants were selected

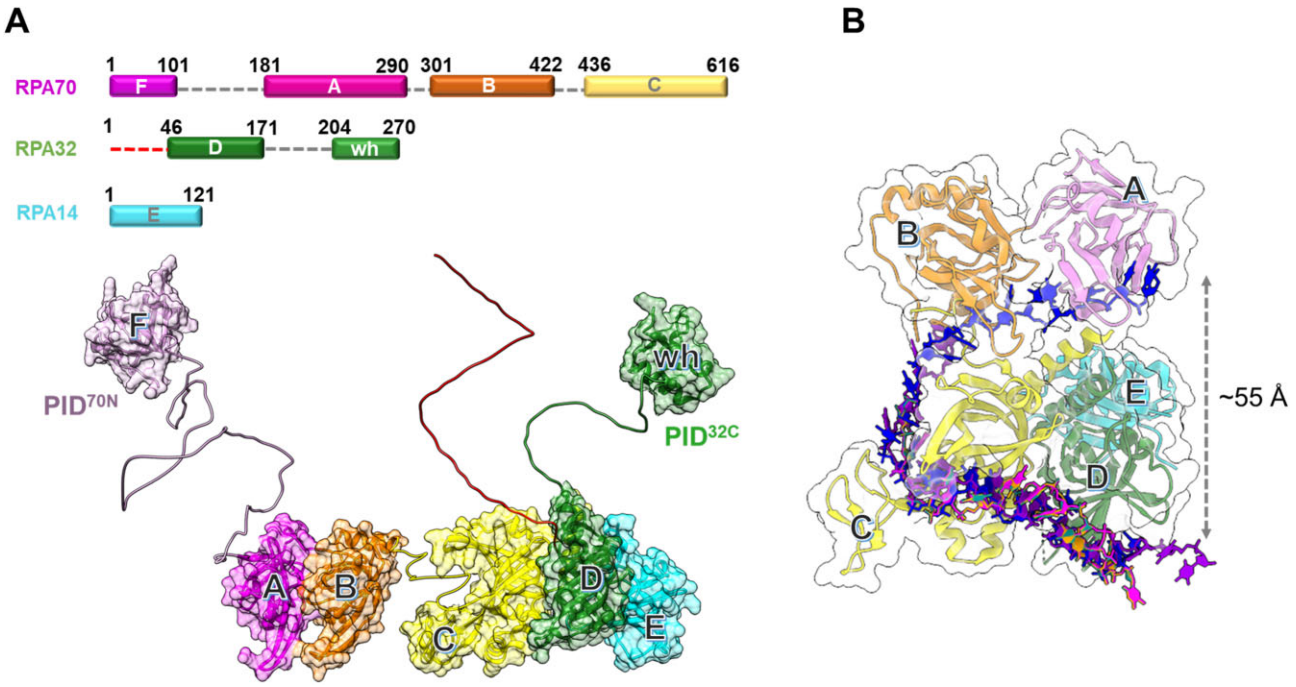

Figure 1. Architecture of the replication protein A (RPA) – ssDNA complex. (**A**) The three subunits of RPA—RPA70, RPA32 and RPA14 house several oligonucleotide/oligosaccharide binding (OB) domains that are classified as either DNA binding domains (DBDs: DBD-A, DBD-B, DBD-C and DBD-D) or protein-interaction domains (OB-F/PID^{70N} and winged helix (wh)/PID^{32C}). A structural model of RPA is shown and was generated using information from known structures of the OB-domains and AlphaFold2 models of the linkers. (**B**) Crystal structure of *Ustilago maydis* RPA bound to ssDNA is shown (PDB 4GNX). This structure lacks OB-F, the F-A linker, wh and the D-wh linker. ssDNA from CryoEM structures of *Saccharomyces cerevisiae* RPA (PDB 6I52) and *Pyrococcus abyssi* RPA (8OEL) are superimposed and reveal an end-to-end DNA distance of ∼55 Å. Structural data supports partial wrapping of ssDNA around the OB domains.

using ampicillin (100 μg/ml). A single colony was inoculated in 1 L of Luria Broth and incubated at 37°C without shaking for 20-24 hrs. Cells were then grown at 37°C with shaking at 250 rpm, until the OD_{600} reached 0.6 and then induced with 0.4 mM isopropyl β-D-1-thiogalactopyranoside (IPTG). Induction was carried out at 37°C for 3 h. Harvested cells were resuspended in 30 ml/l cell resuspension buffer (30 mM HEPES, pH 7.8, 300 mM KCl, 0.02% v/v Tween-20, 1.5× protease inhibitor cocktail, 1 mM PMSF and 10% (v/v) glycerol). Cells were lysed with 0.4 mg/ml lysozyme for 30 min at 4°C followed by sonication in the cold room. The samples were maintained at 4°C through the entirety of the remaining purification. The clarified lysate was fractionated over a Ni^{2+}-NTA agarose column (Gold Biotechnology Inc.). RPA was eluted using cell resuspension buffer containing 400 mM imidazole following a wash with lysis buffer containing 2M NaCl to remove any trace non-specifically bound nucleic acids. Fractions containing RPA were pooled and diluted with H_0 buffer (30 mM HEPES, pH 7.8, 0.02% v/v Tween-20, 1.5× protease inhibitor cocktail, 10% (v/v) glycerol and 0.25 mM EDTA pH 8.0) to match the conductivity of buffer H_{100} (H_0 + 100 mM KCl), and further fractionated over a fast-flow Heparin column (Cytiva Inc.). RPA was eluted using a linear gradient of H_{100}–H_{1500} buffers (subscripts denote the mM concentrations of KCl), and fractions containing RPA were pooled and concentrated using an Amicon spin concentrator (30 kDa molecular weight cut-off). The concentrated RPA was fractionated over a HiLoad 26/600 Superdex-200 column (Cytiva Inc.) using RPA storage buffer (30 mM HEPES, pH 7.8, 200 mM KCl, 0.25 mM EDTA, 0.01% v/v Tween-20 and 10% (v/v) glycerol). Purified RPA was flash frozen using liquid nitrogen and stored at –80°C. RPA concentration was measured spectroscopically using $\epsilon_{280} = 87\,410\ M^{-1}cm^{-1}$.

Human RPA-pSer^{384}, carrying a phospho-serine at position 384 in RPA70, was expressed and purified using genetic code expansion (39,40). First, a fragment containing the RPA70, RPA32 and RPA14 open reading frames was subcloned into an RSF-Duet1 plasmid and an amber suppression codon (TAG) was engineered at the position corresponding to Ser-384 in the RPA70 subunit using Q5 site-directed mutagenesis (NEB). pRSF-Duet1-hRPA-70C-His-S384TAG and pKW2-EFSep (41) plasmids were co-transformed in to BL21 (DE3) Δ*serB E. coli* cells and transformants were selected using chloramphenicol (25 μg/ml) and kanamycin (50 μg/ml). A starter culture was prepared by inoculating colonies into ZY-non inducing media (ZY-NIM; Supplementary Table S2A) followed by overnight growth with shaking at 250 rpm at 37°C. 1% of the overnight starter culture was added to ZY-auto induction media (ZY-AIM; Supplementary Table S2B) and grown until the OD_{600} reached 1.5. The temperature was reduced to 20°C and the cultures were grown for an additional 20 h. Cells were then harvested by centrifugation at 2057 xg for 20 min and the cell pellet was resuspended with cell-resuspension buffer (30 mM HEPES, pH 7.8, 300 mM KCl, 0.02% v/v Tween-20, 1.5× protease inhibitor cocktail, 1 mM PMSF, 10% (v/v) glycerol, 50 mM sodium fluoride, 10 mM sodium pyrophosphate, and 1 mM sodium orthovanadate). RPA-pSer^{384} was purified as described above for wild type RPA. Typical yields for RPA-pSer^{384} are ∼6.8 mg of pure protein/L of culture compared to ∼20–25 mg/l for wild-type unmodified RPA. Phosphoserine incorporation was confirmed using mass spectrometry and analysis on Phos-tag SDS PAGE.

Analysis of pSer incorporation using Phos-Tag SDS-PAGE

Incorporation of pSer into RPA70 was assessed using Phos-tag SDS PAGE (Fujifilm Inc.). A gradient SDS-PAGE gel (10–14%) was prepared by adding 0.05 mM of the Phos-tag reagent and 0.1 mM $MnCl_2$ to the resolving gel (before pouring the gel). Other steps for preparing the resolving and stacking gels, and running the gel, are as defined for standard SDS-PAGE analysis. Gels are stained using Coomassie stain. The band carrying pSer in RPA70 runs with slower electrophoretic mobility in Phos-tag SDS PAGE analysis.

Single-molecule FRET measurements

smFRET data were collected on an EI-FLEX bench-top microscope from Exciting Instruments Ltd (Sheffield, UK). For measurement, 100 μl of a fluorescent sample droplet was placed onto a no.1 thickness coverslip and excited with alternating 520 and 638 nm lasers at 0.22 and 0.15 mW power, respectively. Experiments were carried out in buffer containing 50 mM Tris–acetate, pH 7.5, 50 mM KCl, 5 mM $MgCl_2$, 10% (v/v) glycerol and 0.1 mg/ml BSA. Lasers were sequentially turned ON for 45 μs for each measurement and separated by a dark period of 5 μs for a total of 40 mins of acquisition. Fluorescence emission photons from freely diffusing molecules were collected using an Olympus 60× (1.2 N.A.) water-immersion objective, focused onto a 20 μm pinhole. 20 pM of fluorescent sample was suitable for a burst rate of 1 Hz. After passing through the pinhole, the photons were split using a 640 nm long-pass filter, cleaned up using 572 and 680 nm band-pass filters, and focused onto respective avalanche photodiodes. The photon arrival times, and respective detector were saved in HDF5 data format for offline analysis.

After photoirradiation, the background counts from the buffer were comparable to that of DI water at 2–3 counts per second (cps), whereas typical bursts comprised of 50–100 photons. The photoirradiation of buffer was performed using a 100W LED flood light. The entire set-up (i.e. flood light and buffers taken in covered glass beakers) was placed in a cold-room to minimize heating of samples. Analysis of smFRET data was performed in an Anaconda environment, with Jupyter notebooks, using FRETBursts Python package (42). Single molecule photon emission bursts were identified using a dual channel burst search (DCBS) algorithm as previously described (L = 10, and F = 45 for both channels). The background estimated from an exponential fit to inter-photon delays greater than 1.5 ms was subtracted. The compensation for spectral crosstalk (a), compensation factor for different detection efficiencies between donor and acceptor channel (g), and compensation for direct excitation (d) for EI-FLEX were estimated as 0.0938, 1.591 and 0.05824, respectively. The same factors for measurements on the Picoquant Micro Time (MT200; Picoquant Inc., Germany) instrument were 0.05, 0.85 and 0.1, respectively.

Continuous wave (CW)-EPR and DEER spectroscopy

Continuous wave (CW)-EPR spectra of spin-labeled ssDNA samples ± RPA were collected at room temperature on a Bruker EMX spectrometer operating at X-band frequency (9.5 GHz) using 2 mW incident power and a modulation amplitude of 1 G. DEER spectroscopy was performed on an Elexsys E580 EPR spectrometer operating at Q-band frequency (33.9 GHz) with the dead-time free four-pulse sequence at 83 K. Pulse lengths were 20 ns (π/2) and 40 ns (π) for the probe pulses and 40 ns for the pump pulse. The frequency separation was 63 MHz. Samples for DEER analysis were cryoprotected with 24% (vol/vol) glycerol and flash-frozen in liquid nitrogen. Primary DEER decays were analyzed using a home-written software (DeerA, Dr Richard Stein, Vanderbilt University) operating in the Matlab (MathWorks) environment as previously described (43). Briefly, the software carries out analysis of the DEER decays obtained under different conditions for the same spin-labeled pair. The distance distribution is assumed to consist of a sum of Gaussians, the number and population of which are determined based on a statistical criterion.

Confocal smFRET with alternating-laser excitation (ALEX)

The photons emitted during a transit through confocal volume are called a burst and can be used to estimate FRET efficiency (E).

$$E = \frac{f_{Dex}^{Aem}}{(f_{Dex}^{Dem} + f_{Dex}^{Aem})} \quad (1)$$

This uncorrected *E* is a ratio of number of sensitized acceptor emission photons i.e. via energy transfer (f_{Dex}^{Aem}) and the sum of number of photons in the donor channel after donor excitation (f_{Dex}^{Dem}) and the number of photons in the acceptor channel after donor excitation (f_{Dex}^{Aem}). However, to convert the E into distances, spectral crosstalk must be taken into account. This especially poses a problem in the low E regimen, i.e. distinguishing low E species from donor alone species is a huge challenge. And this is where alternating laser excitation (ALEX) solves the problem. During an ALEX scheme, both donor and acceptor fluorophores are rapidly excited in alternating fashion. The diffusion coefficient of biomolecules in dilute solutions isof the order of hundreds of $\mu m^2/_s$. And, so typically an alternation frequency of 20KHz is more than sufficient to excite both donor and acceptor fluorophores multiple times during the transit of a single molecule through the confocal volume (∼1 ms). The f_{Aex}^{Aem} thus estimated can be used to calculate another informative quantity about the population of diffusing single molecules named raw stoichiometry.

$$S = \frac{(f_{Dex}^{Aem} + f_{Dex}^{Dem})}{(f_{Dex}^{Dem} + f_{Dex}^{Aem} + f_{Aex}^{Aem})} \quad (2)$$

Stoichiometry can be best understood in terms of ratio of total fluorescence photons recorded after donor wavelength excitation to total fluorescence photons recorded after direct donor and acceptor excitation. For donor-only and acceptor-only species the S is close to 1 and 0, respectively. Similarly, the donor and acceptor laser intensity are tuned such that double-labeled molecules scale to an *S* value of 0.5. Furthermore, binding of a protein like RPA to Cy5/Cy3 labeled ssDNA could lead to a reduction in E (i.e. DNA ends are brought further apart), or an increase in S (increase in donor quantum yield due to PIFE) or both. Finally, in order to convert E into distances, three additional steps were taken: (1) Background intensity in all three photon streams f_{Dex}^{Aem}, f_{Dex}^{Dem}, and f_{Aex}^{Aem} is estimated via mean count rate and subtracted taking the length of burst into account. (2) Two channel cross-talk factors are estimated (a) bleed-through of donor-emission into

the acceptor channel and (b) the direct excitation of acceptor molecules by the donor-laser. These are estimated from the donor-, and acceptor- only molecules in the background-corrected ES histogram, and finally (3) gamma correction, which takes into account the differences in the detection efficiencies of donor and acceptor, their quantum, and the transmission efficiencies of the optical elements etc. The corrected FRET values were converted into distance following the relationship between energy transfer efficiency (E) and donor-to-acceptor separation (r):

$$E = \frac{1}{1 + \left(\frac{r}{R_0}\right)^6} \quad (3)$$

The R_0 or the donor–acceptor distance at which the energy transfer efficiency is 50% was taken to be 5.4 nm. The end-to-end distance for a fully linearized ssDNA molecule was estimated simply by multiplying l_d or rise per base, taken to be 0.67 nm, with the number of the bases in the dT polymer.

Crosslinking mass spectrometry (XL-MS) analysis

RPA or RPApSer^{384} (10 μM) in the absence or presence of ssDNA [$(dT)_{25}$] (10 μM) were incubated with 5 mM BS3 crosslinker at room temperature for 15 min in 20 μl reaction buffer (50 mM HEPES pH 7.8, 100 mM KCl, 10% glycerol). The crosslinking reaction was quenched with 2 μl of 1M ammonium acetate for 15 min and the samples were separated on SDS-PAGE. Gel bands were excised and destained with a 50 mM ammonium bicarbonate and 50% acetonitrile mixture and reduced with a mixture of 100 mM dithiothreitol and 25 mM bicarbonate for 30 min at 56°C. The reaction was subsequently exchanged for the alkylation step with 55 mM iodoacetamide and 25 mM ammonium bicarbonate and incubated in the dark at room temperature for 25 min. The solution was then washed with the 50 mM ammonium bicarbonate and 50% acetonitrile mixture. The gel pieces were then first dehydrated with 100% acetonitrile and then rehydrated with sequence grade trypsin solution (0.6 μg, Promega) and incubated overnight at 37°C. The reaction was quenched with 10 μl of 50% acetonitrile and 0.1% formic acid (FA, Sigma) and transferred to new microfuge tubes, vortexed for 5 min, and centrifuged at 15 000 rpm for 30 min. The extracted and dried peptide was reconstituted with 0.1% FA in water and injected onto a Neo trap cartridge coupled with an analytical column (75 μm ID × 50 cm PepMap Neo C18, 2 μm). Samples were separated using a linear gradient of solvent A (0.1% formic acid in water) and solvent B (0.1% formic acid in ACN) over 120 mins using a Vanquish Neo UHPLC System coupled to an Orbitrap Eclipse Tribrid Mass Spectrometer with FAIMS Pro Duo interface (Thermo Fisher Scientific). The acquired MS/MS data was queried for cross-link identification against the sequence of five target proteins using Proteome Discoverer v3.0 with the XlinkX node, applying a 1% FDR for cross-link validation. Data were visualized using xiVIEW (44) and plotted in Inkscape.

Mass photometry (MP) measurements

All measurements were carried out on a TwoMP instrument (Refeyn Ltd.) as described before (45). Briefly, glass coverslips (No. 1.5*H* thickness, 24 × 50 mm, VWR) were cleaned by sonication in isopropanol followed by deionized water and dried using a nitrogen gas stream. For each round of measurement, a clean coverslip was placed on the oil-immersion objective lens (Olympus PlanApo N, 1.42 NA, 60×), with a holey-silicone gasket (Refeyn Ltd) adhered on the top surface of the coverslip. All dilutions and measurements were performed at room temperature (23 ± 2°C) in 1× Mg^{2+}/Ca^{2+} buffer (20 mM HEPES, pH 7.5, 150 mM KCl, 5 mM $MgCl_2$, 5 mM $CaCl_2$) supplemented with 1 mM DTT. Samples of DNA alone, RPA alone, or DNA–RPA mixtures were allowed to equilibrate at 23 ± 2°C for 5 min after which 1 μl of the respective sample was quickly diluted in 15 μl of buffer. The newly adhered spots were video recorded for 1 min. High contrast (light-scattering) events corresponding to single particle landings on the coverslip were analyzed further. A known mass standard (β-amylase, Sigma A8781-1VL) was used to convert image contrast-signal into mass units. Histograms were plotted from all the data gathered during the 1 min video interval and non-linear least squares fit to single gaussian function to extract mean mass and error.

Coarse-grained molecular dynamics (MD) simulations

To explore the interaction between RPA and ssDNA at the molecular level, a coarse-grained model has been utilized. In this model, each protein residue was represented by two beads positioned at the C_α and C_β locations. For charged amino acids (K, R, H, D and E), charges were placed at the C_β position. The coarse-grained model for ssDNA comprised three beads representing each nucleotide: one at the geometric center of phosphate (P), one at sugar (S) and one at base (B). While the S and B beads were neutrally charged, the P bead carried a negative charge. Simulations were conducted using a native topology-based model, where the internal energy of the protein, ssDNA and protein–ssDNA interaction was denoted as E_{prot}, E_{ssDNA} and $E_{ssDNA\text{-}Protein}$, respectively. These energies can be expressed by the following equations:

$$E_{prot}\ (\Gamma, \Gamma_0) = E_{prot}^{Bond} + E_{prot}^{Angle} + E_{prot}^{Dihedral} + E_{prot}^{Native\ Contacts} + E_{prot}^{Electrostatics} + E_{prot}^{Repulsions}$$

$$E_{ssDNA}\ (\Gamma, \Gamma_0) = E_{ssDNA}^{Bond} + E_{ssDNA}^{Angle} + E_{ssDNA}^{Dihedral} + E_{ssDNA}^{Stacking} + E_{ssDNA}^{Repulsions}$$

$$E_{ssDNA-Protein}\ (\Gamma, \Gamma_0) = E_{ssDNA-Protein}^{Electrostatics} + E_{ssDNA-Protein}^{Aromatic} + E_{ssDNA-ssDNA}^{Repulsions}$$

The potential energy of E^{Bond}, E^{Angle}, E^{Dihedral}, $E^{\text{Electrostatics}}$, $E^{\text{Repulsions}}$ can be expressed by $\sum_{bonds} K_{bonds}\ (b_{ij} - b_{ij}^0)^2$, $\sum_{angles} K_{angles}\ (\theta_{ijk} - \theta_{ijk}^0)^2$, $\sum_{dihedrals} K_{dihedrals}\ [1 - \cos(\phi_{ijkl} - \phi_{ijkl}^0) - \cos\ (3\Phi_{ijkl} - \Phi_{ijkl}^0)]$, $\sum_{i,j} K_{electrostatics}\ B\ (\kappa) \frac{q_i q_j exp^{-\kappa r}}{\varepsilon_r r_{ij}}$ and $\sum_{i \neq j} K_{contacts}\ \left(\frac{C_{ij}}{r_{ij}}\right)^{12}$ respectively. The $E_{ssDNA-Protein}^{Aromatic}$, $E_{prot}^{Native\ Contacts}$, $E_{ssDNA}^{Stacking}$, $E_{ssDNA-Protein}^{Aromatic}$ are expressed by a Lennard–Jones interaction term designated by, $\sum_{i \neq j} K_{contacts}\ [5\ (\frac{A_{ij}}{r_{ij}})^{12} - 6\ (\frac{A_{ij}}{r_{ij}})^{10}]$. All parameters described in these equations are adopted from previous studies (46,47). The repulsion radius of P, S and B beads is set to 1.9 Å. The stacking interaction potential between protein and ssDNA beads in contact in the crystal structure (PDB: 4GNX) (18) is denoted as $K_{\text{contacts}} = 3.0$,

while for those not in contact in the crystal structure, it is set to 0.5. This configuration ensures that RPA does not diffuse through ssDNA. The salt concentration in the Debye–Hückel model of electrostatics is set to 0.01 M. Additionally, the flexibility of ssDNA in response to salt concentration is represented by the dihedral potential ($K_{dihedral}$) between four consecutive phosphate beads in the ssDNA, set to either 0.0 or 0.4 to simulate high and low salt conditions, respectively.

Results

Solution based single molecule FRET with alternating-laser excitation (ALEX) provides an excellent read out of end-to-end ssDNA distances

Single molecule FRET (smFRET) has been used to obtain accurate end-to-end distances for double-stranded nucleic acids (48). Similar measurements of conformational flexibility for ssDNA have been measured using single molecule total internal reflection (smTIRF) microscopy where overhang DNA with varying length of ssDNA were tethered to glass slides (49). Here, we used a benchtop microscope that uses ALEX (50) for in-solution smFRET measurements to capture the conformations of ssDNA and RPA–ssDNA complexes (51). First, to test whether this instrumental setup accurately captures the conformational sampling of ssDNA, we measured the changes in FRET as a function of ssDNA length. For these experiments, all ssDNA substrates carried Cy3 (donor) and Cy5 (acceptor) fluorophores at the 3′ versus 5′ ends, respectively (3′-Cy3-$(dT)_{xx}$-Cy5-5′, where xx = number of nucleotides). A plot of the FRET efficiency versus length of end-labeled poly (dT) substrates shows an excellent monotonic relationship with high and low FRET captured for $(dT)_{15}$ and $(dT)_{95}$, respectively (Figure 2). These measurements obtained using a benchtop EI-FLEX microscope are in excellent agreement with similar data collected using a Picoquant MicroTime 200 confocal microscope (Supplementary Figure S1 and Supplementary Table S3).

RPA binding does not produce a complete linearization of ssDNA

To assess the change in ssDNA shape upon RPA binding, we quantified the FRET changes in the RPA–ssDNA complex. First, in these assays, DNA alone produces a FRET signal proportional to the length (Figure 2A). Upon binding to RPA, the FRET signal decreases because of an increase in distance between the donor and acceptor (Figure 3). In addition, since the concentration of RPA and ssDNA used in these experiments are low (pM range), we collected data on each ssDNA substrate as a function of increasing RPA concentrations (Figures 3A–H, S2–S4 and Supplementary Tables S4 and S5). Furthermore, to ensure that we only assessed 1:1 RPA:DNA complexes (molar ratios of RPA trimer bound to one molecule of DNA), we performed parallel mass photometry analysis of the complexes (Figures 3I–L). Under all RPA concentrations tested, we captured predominantly stoichiometric RPA–ssDNA complexes. Thus, our interpretation of end-to-end ssDNA distances from the FRET measurements is not influenced by the binding of multiple RPA molecules. The RPA:DNA binding stoichiometries measured using MP (nM concentrations) are recapitulated in analytical ultracentrifugation analysis at higher protein concentrations (μM; data not shown).

smFRET measurements were performed on four ssDNA substrates of varying lengths [$(dT)_{xx}$, xx = 15, 25, 30 or 45 nt]. When these measurements are plotted as a function of ssDNA length, the results mirror the data for DNA alone (Figure 4A). However, for every ssDNA substrate, an overall increase in end-to-end distance of ∼3.1 ± 0.2 nm is observed (Supplementary Table S5 and Figure 4B). This surprising result does not agree with the canonical models described for RPA where the DBDs are arranged in a sequential fashion with the ssDNA stretched in a linear manner. Instead, the shorter end-to-end distance measurements better agree with observations in the structural studies where DNA is wrapped around the DBDs, as shown in Figure 1B (18–20). Thus, ssDNA is not linearized, but rather follows the intrinsic curvature of RPA (Figure 1B). The second observation is that the ∼3.1 nm shift in distance is observed across the increasing length of ssDNA (Figure 4B). This suggests that DNA occupancy along the curvature of the DBDs is uniform and there is no looping or extrusion of the ssDNA. Finally, the minimal change in distances between the shortest $(dT)_{15}$ and the longest $(dT)_{45}$ ssDNA substrates supports our model that the trimerization core (Tri-C) of RPA contributes most to ssDNA binding stability (and in this case contour or path of wrapping) whereas the F–A–B domains are intrinsically more dynamic.

DEER spectroscopy confirms wrapping of DNA along the curvature dictated by the DNA binding domains of RPA

To obtain another independent experimental validation of our findings from the smFRET analysis, we performed double electron-electron resonance (DEER) spectroscopy (52,53). This experiment requires the incorporation of two spin labels, one on each end of the oligonucleotide. 2′-aminouridine was introduced during chemical synthesis of the oligonucleotides and post-synthetically spin-labeled with an isothiocyanate derivative of an isoindoline nitroxide (Figure 5A and Supplementary Table S1) (37). The distance between the two spin centers was measured using DEER spectroscopy in the absence and presence of RPA. For a $(dT)_{22}$ substrate, DNA alone produces a broad distribution of distances with two populations (Figure 5B and Supplementary Table S6) and these measurements are in excellent agreement with our smFRET data. When RPA is added in equimolar amounts to form a stoichiometric RPA:DNA (1:1) complex, the end-to-end distance increases to ∼6.83 ± 1.5 nm (Figure 5C). This measurement is again in very good agreement with our smFRET observations (Figures 4 and 5). We also checked if this phenomenon was specific to human RPA by performing DEER and smFRET measurements for the *Saccharomyces cerevisiae* RPA–ssDNA complex. On a $(dT)_{22}$ oligonucleotide, the end-to-end distance in DEER measurements was 6.9 ± 1.8 nm (Figure 4). In smFRET measurements on a $(dT)_{25}$ oligonucleotide, we observed an end-to-end distance of 8.5 ± 0.82 nm (Figure 4). These distances agree well with the smFRET measurements. These distances are similar between the human and yeast RPA, suggesting that the mechanism of ssDNA wrapping is likely conserved across eukaryotic RPA.

Computational prediction of the shape of the wrapped ssDNA

In principle, ssDNA should behave as a flexible polymer, in particular when the sequence cannot form secondary structures through intra-strand base-pairing; thus the choice of

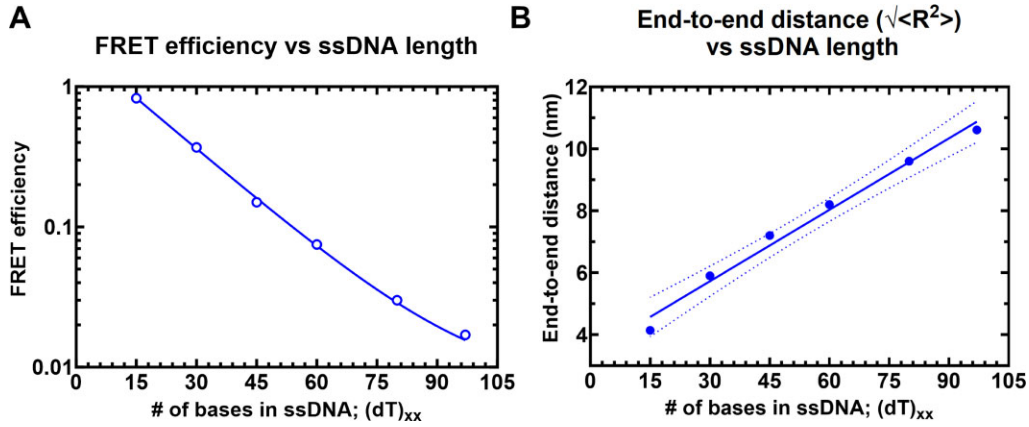

Figure 2. Solution confocal-based FRET measurements accurately report on ssDNA end-to-end distances. (**A**) FRET efficiencies were calculated based on single molecule measurements of Cy3 (donor) and Cy5 (acceptor) fluorescence. Data were collected on a series of ssDNA substrates (30 pM) of increasing lengths. Energy transfer events were detected as bursts of photons as the molecules transited the confocal volume. The mean of the distribution is plotted in panel A as a function of length of poly-thymidine (dT_{xx}). (**B**) The end-to-end distances were calculated based on a R_0 value of 5.4 nm for the Cy3/Cy5 pair and Eq. (3) described in the Methods. The dotted lines represent a 95% confidence interval for the linear fit.

poly-dT (49). The dependence of the end-to-end distance for a flexible polymer on the number of monomer units (here nucleotides) generally can be described in terms of polymer scaling laws. These laws define the dimensions of unfolded and intrinsically disordered macromolecules and are modeled based on the composition of the nucleotides and salt conditions (54). We therefore sought to determine if our unbound dT constructs showed characteristic polymer scaling behavior. Fitting the root-mean-squared end-to-end distance against the number of bases reveals extremely good agreement with a polymer scaling law of $R_e = R_0 N^{\nu}$, where R_0 is 1.07 nm and ν is 0.50 (Figure 6A). This would suggest that under the solution conditions examined, ssDNA (dT) behaves as a flexible chain that conforms to the statistical properties of a Gaussian chain. To further assess the validity of our experimental measurements and conclusions, we compared end-to-end distance obtained previously using a confocal-based smFRET set up by Chen *et al.* (55). Gratifyingly, for $(dT)_{40}$ under matching solution conditions (50 mM NaCl), the data from Chen et. al. lies directly over the polymer fit generated from our smFRET data (Figure 6A).

If the bound-state conformation were to form a stretched linear extension, we would expect major deviations from the polymer scaling and an increase in distance between the DNA ends. Instead, bound-state derived distances reveal an identical dependency on the number of nucleotides, shifted by ~3 nm more expanded than the unbound state (Figure 6B). Both bound and unbound distances are far from the trend expected for fully linearized DNA. Taken together, our results suggest the configurational/conformational properties of the RPA-bound ssDNA are relatively similar to unbound, with the exception of a systematic shift in the end-to-end distance, consistent with dT wrapping around RPA in a dynamic state that preserves the DNA's intrinsic flexibility (Figure 6C).

Post-translational modification of human RPA by Aurora kinase B rearranges the domains without affecting the wrapping of ssDNA

Since ssDNA wraps around the contour of the DNA-binding domains (DBDs) of RPA, we wondered how RPA-interacting proteins might gain access to the buried ssDNA. There are two important features that need to be considered: The first is the intrinsic dynamic interactions between the DBDs and ssDNA, and the second is the configurational rearrangements of the domains with respect to each other and the ssDNA. We, and others, have shown that the domains possess different dynamic properties, with DBD-A and DBD-B being more dynamic on ssDNA compared to DBD-C and DBD-D (19,22,23,26). Using C-trap experiments, we recently showed that the rates of diffusion for RPA on long stretches of ssDNA are regulated by the trimerization core (46). Thus, incoming proteins can access the buried ssDNA through transient dissociation of one or more DBDs. The second mode of ssDNA access might be provided through post-translational modifications of the DBDs or the disordered linkers (22,26). Using hydrogen-deuterium exchange mass spectrometry, we recently showed that the domains of RPA are not splayed apart but are tightly organized along with the protein-interaction domains and this configuration is altered upon phosphorylation by Aurora kinase B (22). This modification is specific to RPA functions during mitosis. To gain a better understanding of these configurational changes and how the phosphorylated RPA alters the wrapping of ssDNA, we performed crosslinking mass spectrometry (XL-MS) of RPA and phosphorylated-RPA in the absence/presence of ssDNA. Aurora kinase B phosphorylates RPA at a single Ser-384 position in the large RPA70 subunit (22). Using genetic code expansion (39,40) we generated site-specific phospho-serine (pSer) modified RPA at Ser-384 (RPA-$pSer^{384}$). This approach produced 100% phosphorylated RPA as seen by complete shift of the RPA-$pSer^{384}$ band in Phos-Tag SDS-PAGE analysis (Figure 7A). Site-specific incorporation was also confirmed through mass spectrometry (Supplementary Figure S5) and by western blotting using a pSer-384 specific antibody (Figure 7B) (22). XL-MS of RPA or RPA-$pSer^{384}$ were performed with a bis (sulfosuccinimidyl)suberate (BS3) crosslinker in the absence or presence of a $(dT)_{25}$ ssDNA substrate. BS3 crosslinks primary amines (Lys residues) that are within 15 Å (56).

We made several key observations: (i) Extensive crosslinks (XLs) are captured between the three subunits (RPA70, RPA32 and RPA14) and between the DNA binding do-

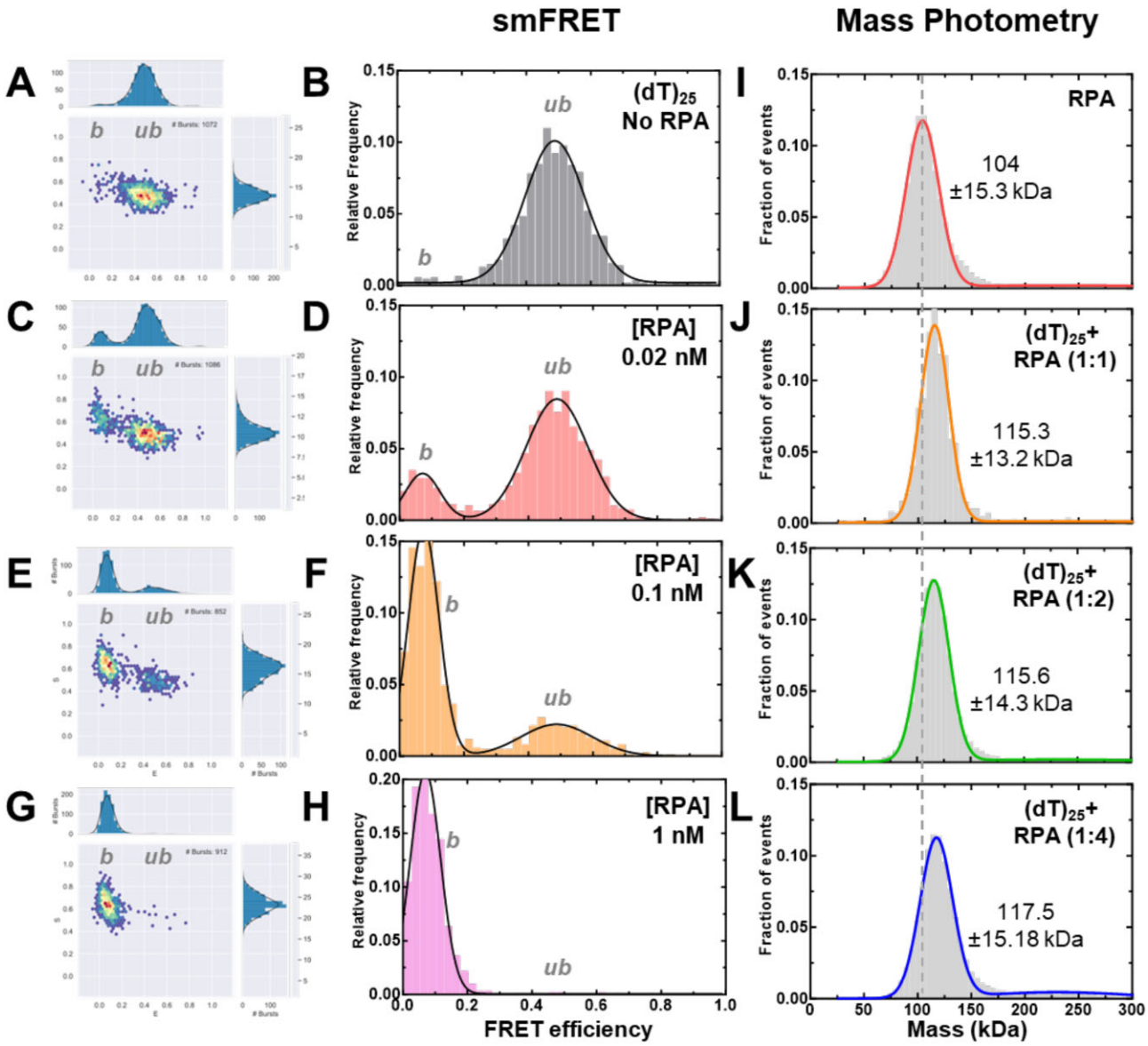

Figure 3. Concentration dependence of RPA–ssDNA complexes. **A-H**) FRET analysis of $(dT)_{25}$ ssDNA bound to increasing concentrations of RPA show a shift from the unbound to bound complex. As RPA concentrations are increased, a complete shift to the bound population is observed. Ratios are defined as one molecule of ssDNA: number of RPA trimers (molar ratio). **I-L**) Mass photometry analysis of RPA and RPA-$(dT)_{25}$ complexes show formation of predominantly single RPA bound $(dT)_{25}$ complexes. The dotted line serves as a reference point for the mass of free RPA in solution as seen in panel I. The measured mass for RPA and the RPA-DNA complexes (1:1 stoichiometry) are noted. In all conditions tested here, one RPA molecule binds to one molecule of ssDNA.

mains (DBDs A, B, C and D), the protein interaction domains (OB-F and wh), and several connecting linkers of non-phosphorylated RPA (Figure 7C and Supplementary Figures S6–S9). Of particular interest are the XLs between OB-F and F-A linker with DBD-A, DBD-B, DBD-C, DBD-D and the wh domains. This finding suggests that all the domains are situated close together in a compacted configuration. (ii) Comparison of RPA in the absence and presence of ssDNA shows crosslinks unique to each condition (denoted by the blue lines in Figure 7), suggesting changes in the configurations/conformations or ssDNA occluded Lys residues. However, the overall contacts between the domains are still observed (Figures 7C and D). The data suggest that ssDNA wraps around the compacted structural architecture of RPA without the need to unravel the domains, as would be expected if the ssDNA were to be linearly stretched. (iii) Surprisingly, introduction of phosphoserine at position 384 (DBD-B; RPA70) produces significantly new contacts within RPA (Figure 7E and Supplementary Figure S6). (iv) Finally, the largest changes in XL patterns are observed upon ssDNA binding to RPA-pSer^{384} suggesting that a single post-translational modification can bring about large-scale configurational changes leading to an altered ssDNA-RPA-pSer^{384} complex (Figure 7F and Supplementary Figure S7).

To understand how ssDNA is shaped when bound to RPA-pSer^{384}, we measured the end-to-end distance using DEER (Figure 5). We observe two distributions for RPA-pSer^{384}: The first overlaps with wild-type RPA and ∼70% of the phosphorylated RPA is in this population (∼7 nm). In addition, there is a 30% increase in the second population where the end-to-

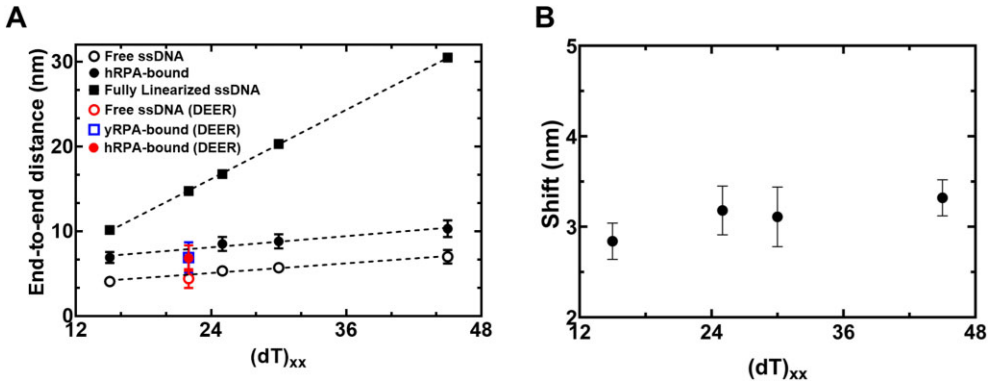

Figure 4. RPA binding produces a modest 3 nm increase in end-to-end distance. (**A**) The estimated end-to-end distance between the 3′ and 5′ ends of ssDNA is plotted as a function of nucleotides which make up the chain. Closed squares represent theoretically calculated end-to-end distances assuming the ssDNA was completely linearized. Open and closed circles represent experimental end-to end distance measurements from smFRET analysis ssDNA -/+ RPA, respectively. The figure also shows that end-to-end distances of yRPA-bound, hRPA-bound, and free $(dT)_{22}$ ssDNA, measured using DEER spectroscopy. The DEER measurements fall on the respective trend lines suggesting good agreement between experimental measurements performed using two independent biophysical approaches. (**B**) A ∼3.1 ± 0.2 nm shift is observed in the end-to-end distances between the free ssDNA and RPA-bound ssDNA. This ssDNA-independent uniform expansion suggests that the average dimensions of the DNA ensemble are increasing due to interactions with RPA.

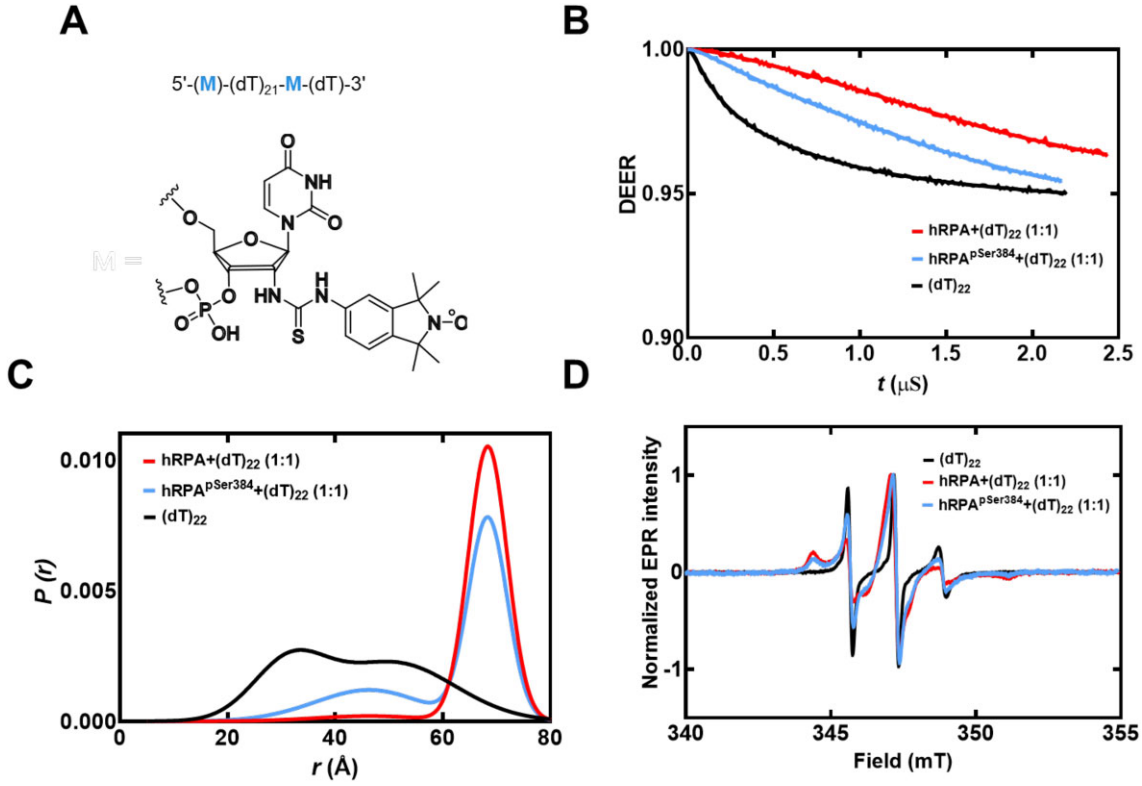

Figure 5. DEER spectroscopy of RPA and RPA-pSer^{384} bound to ssDNA. (**A**) Structure of the isoindoline nitroxide spin label and the position on the (dT) oligonucleotide. (**B**) Raw DEER decays and fits are presented for the experimentally determined distance distributions *P*(*r*) (**C**). (**D**) CW EPR spectra of labeled ssDNA in the absence and presence of RPA and RPA-pSer^{384}.

end distance is much shorter (∼5 nm). Along with the XL-MS data, we interpret these changes as remodeling of the DBDs without large-scale changes to the wrapping pattern of the ssDNA. Thus, from a functional standpoint, phosphorylation remodels RPA such that segments of ssDNA are made accessible to RPA-interacting proteins with minimal alterations to the wrapping of DNA. For RPA-pSer^{384}, these interactions are specific to mitosis.

Coarse-grained MD simulations showcase the binding properties of one versus two RPA-bound ssDNA complexes

The end-to-end distances we have thus far experimentally measured were for free ssDNA or ssDNA bound to a single RPA. Due to limitations in the maximal end-to-end distances that can be measured using FRET or DEER, we were not able to extend these investigations to scenarios where more than

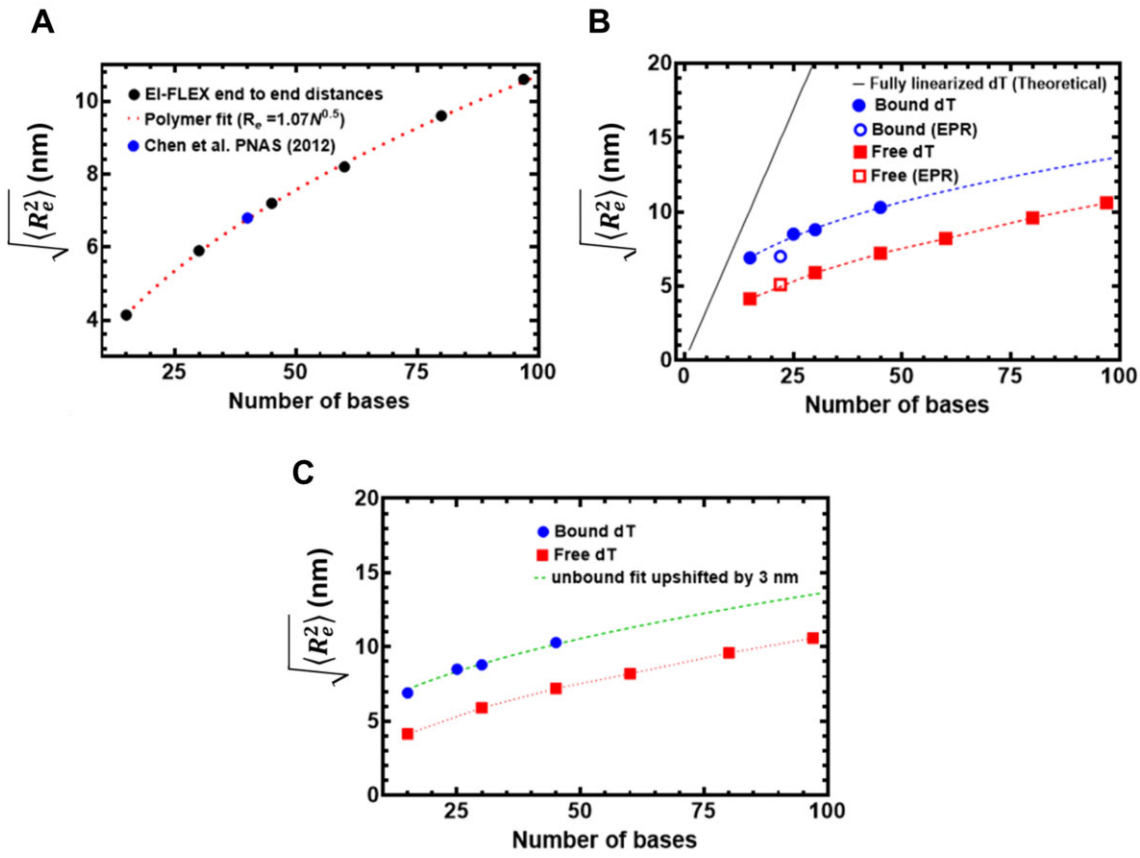

Figure 6. Computational predictions of ssDNA wrapping agree well with experimental measurements. (**A**) Black circles are data, and the red dashed line is a fit to those data using a polymer scaling model. The blue circle is data reporting on the end-to-end distance for $(dT)_{40}$ made by Chen et. al. 2011. (**B**) Blue circles are from RPA-bound (dT) oligonucleotides, red squares are from RPA-free (dT) oligonucleotides. Data include distances measured by both EPR and smFRET experiments. Blue and red dashed lines are polymer model fits to the data, respectively. The black line is the theoretical expected end-to-end distance if the DNA were fully linearized and stretched to its contour length. (**C**) The root mean squared end-to-end distance dependence on the number of bases is essentially identical for the bound and unbound states, as highlighted by the fact that the exact polymer fit upshifted by 3.1 ± 0.2 nm fully describes the bound dT dependency.

one RPA is bound. So, we turned to coarse-grain molecular dynamics (MD) simulations to gain a better understanding of such complexes. First, free ssDNA of varying lengths was simulated and the end-to-end distances across varying lengths of ssDNA ranging from 15 to 80 nucleotides are shown (Figure 8A). The data shown in pink (Figure 8A) attempts to replicate the scenario observed in the original crystal structure PDB: 4GNX (18), where the central 23 nucleotides were constrained to a distance of 55 Å for the ssDNA, without the presence of RPA in the simulation. In contrast, the data in grey (Figure 8A) illustrates the extreme scenario where the 23 nucleotides interacting with RPA are arranged linearly, while the remaining ssDNA is free to move. This simulation was conducted solely with ssDNA in the absence of RPA. Both the grey and pink plots were simulated for DNA lengths ranging from 25 to 100 nucleotides (Figure 8A). Next, we performed simulations with two RPA molecules at different initial configurations, along with varying lengths of ssDNA ranging from 60 to 100 nucleotides. The distribution of end-to-end distances for free ssDNA, ssDNA bound to a single RPA, and ssDNA bound to two RPAs on a $(dT)_{80}$ ssDNA shows a significant overlap of end-to-end distances in the three mentioned cases ((Figure 8B). Additionally, snapshots from the simulations illustrating some instances of end-to-end distances for free ssDNA, ssDNA bound to a single RPA, and ssDNA bound to two RPAs are shown (Figure 8C and Supplementary Movies S1–S3). These movies provide an excellent view of how ssDNA is wrapped along the DNA binding domains of RPA while retaining the intrinsic flexibility and curvature that are experimentally captured in smFRET and DEER analysis.

Discussion

RPA binds ssDNA with high affinity and coats the substrate to form a regulatory protein-interaction hub to orchestrate a variety of DNA metabolic processes (1,3). RPA possesses multiple DNA binding and protein interaction domains that are connected by disordered linkers and spread across its heterotrimeric architecture. An incoming RPA-interacting protein could access the ssDNA buried under RPA by remodeling on one or more domains without the need to displace RPA (57,58). To better understand how such remodeling occurs, knowledge of how ssDNA is bound by RPA is required. Canonically, models for RPA postulate that the DNA binding domains (DBDs) are assembled in a linear array to stretch the DNA leading to multiple binding modes (59). In contrast, structural studies show that the ssDNA is bent around the DBDs (18–20). In solution, an ensemble of states ranging from linear to the bent form can also be envisioned to exist in equilibrium (57,60).

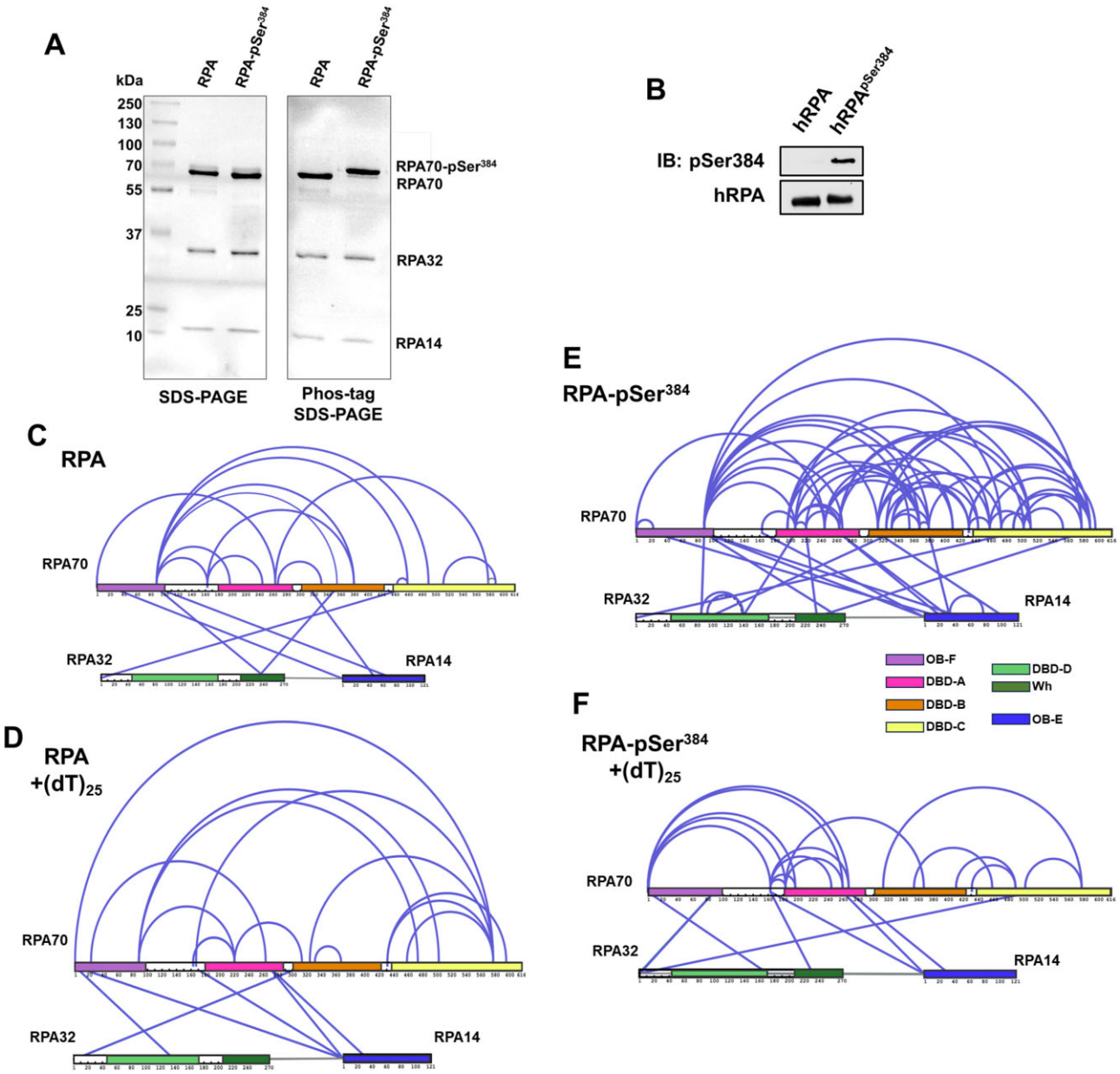

Figure 7. Phosphorylation at a single position in RPA70 alters access to the ssDNA with minimal alternations of end-to-end distance. (**A**) SDS-PAGE and Phos-tag SDS-PAGE analysis of RPA and RPA-pSer^{384} proteins show selective shift of the RPA70 band only in the RPA-pSer^{384} sample confirming 100% incorporation of pSer. (**B**) Western blotting of RPA and RPA-pSer^{384} with an antibody specific to pSer^{384} confirms the site-specific phosphorylation. (**C, D**) Cross-linking mass spectrometry (XL-MS) analysis of RPA in the absence or presence of ssDNA $(dT)_{25}$. A direct comparison of the XLs between RPA and the RPA-$(dT)_{25}$ experiments are presented with XLs unique to each condition denoted in blue. (**F**) A similar comparative XL-MS analysis RPA-pSer^{384} and the RPA-pSer^{384}-$(dT)_{25}$ complex is shown and the XLs unique to each condition is shown in blue. The XL patterns show differences in ssDNA driven changes upon phosphorylation.

From the perspective of the binding properties of the individual domains, recent data from our group and others support the idea of RPA behaving as two functional halves with a dynamic F-A-B half (OB-F, DBD-A and DBD-B) and a less-dynamic Tri-C half (DBD-C, RPA32 and RPA14) (1,19,22,26,27,61). Here Tri-C is modeled to provide ssDNA binding stability to RPA. Support for this model also arises from single-molecule C-trap experiments where the diffusion rate of RPA is dictated by the Tri-C half (46). Here, we show that ssDNA wraps around RPA and end-to-end distance measurements suggest uniform contact throughout the ssDNA–RPA complex. The data argues against linearization of ssDNA and an array-like assembly of the DBDs.

Crosslinking MS data supports a structural model for RPA where both the DBDs and protein-interaction domains (PIDs) are in close proximity. Crosslinks were also detected between the disordered OB-F:DBD-A linker and almost all DBDs and PIDs, suggesting a compacted structure for human RPA (Figure 8 and Supplementary Figure S6). The end-to-end distance measurements, performed as a function of ssDNA length, mirror that of free ssDNA in solution with a ∼3 nm shift. This

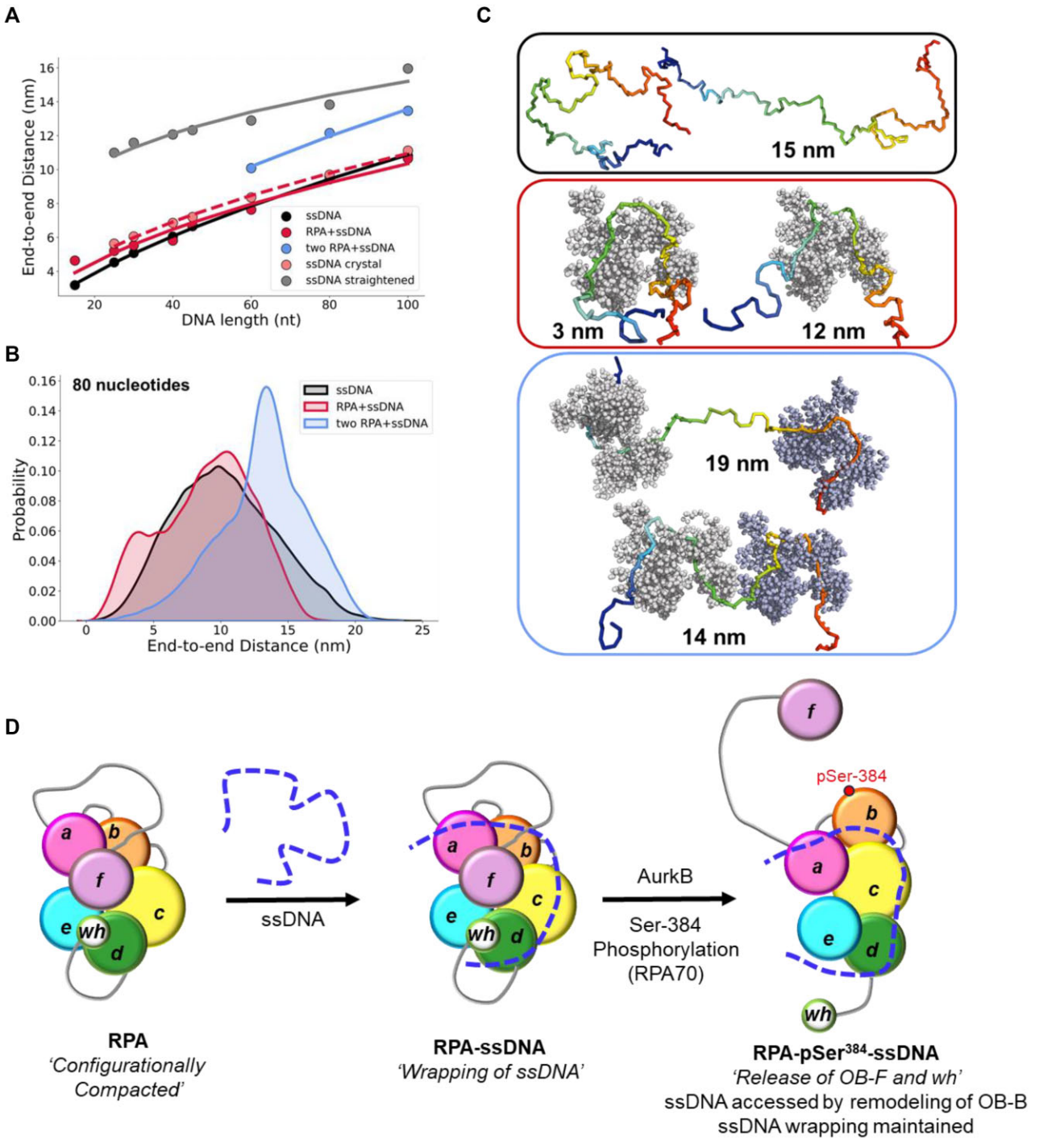

Figure 8. Conformational analysis of ssDNA-RPA complexes from coarse-grained molecular dynamics simulation and a model for ssDNA wrapping by RPA. (**A**) Mean end-to-end distances for ssDNA of varying lengths in different conditions: free ssDNA (black), ssDNA bound to a single RPA (red), and ssDNA bound to two RPAs (blue). Additionally, ssDNA was studied in isolation (i.e. in the absence of explicit RPA) but with a restraint applied on the end-to-end distance of the middle 23 nucleotides, which was set to be 55 Å (mimicking curved binding to RPA) or 138 Å (mimicking stretched conformations of the ssDNA). The coarse-grained simulations were based on *Ustilago maydis* RPA (PDB: 4GNX), but the five OB-domains were considered as non-dynamic for simplicity. (**B**) Distribution of end-to-end distances of ssDNA $(dT)_{80}$ nucleotides in length, modeled as free ssDNA (black), ssDNA bound to a single RPA (red), and ssDNA bound to two RPAs (blue). The distributions are based on multiple long simulations for each system. The distribution of the end-to-end distances for ssDNA interacting with two RPA molecules combines simulations in which the excess ssDNA is placed either as a linker between the two RPAs or as flanking ssDNA at the ends. (**C**) Snapshots from coarse-grained simulations showing varying end-to-end distances for 80-nucleotide ssDNA in different states: free ssDNA, bound to a single RPA, and bound to two RPAs. Please also refer to videos provided in the Supplemental Information. (**D**) The OB-domains of RPA are depicted along with the connecting disordered linkers. The XL-MS data suggest that the domains are compacted together, and ssDNA is wrapped around this architecture. The domains are remodeled upon phosphorylation by Aurora kinase B at position Ser-384 in the RPA70 subunit. This modification releases the OB-F and wh domains and promotes RPA interactions with other proteins. While the wrapping of ssDNA is not altered, remodeling allows access to the ssDNA.

data suggest that ssDNA wraps around the compacted RPA core without much of a change in the intrinsic flexibility of ssDNA, likely owing to the dynamic interactions with RPA. The fact our data fit well to a flexible polymer model in both the bound and unbound states (i.e. end-to-end distance scales with a number of nucleotides proportional to a scaling exponent) suggests that the DNA is not in a fixed structure when bound to RPA (or when unbound, as expected), but is highly flexible, and exists in a collection of different conformations that rapidly interconvert between one another. As such, the uniform expansion suggests that the average dimension of this ensemble increases. In other words, the DNA is not 'stretching' because this implies it is tightly extended, instead, the average dimensions of the DNA ensemble are increasing due to interactions with RPA. This explanation fits perfectly with the wrapped conformation observed in the structural studies where the ssDNA follows along the curvature imposed by the DNA binding domains with the Tri-C providing the central stability to maintaining this architecture. From the context of the individual domains, the more-dynamic versus less-dynamic ssDNA binding attributes assigned to the domains of RPA (23) also explain how the OB-A & OB-B domains can be dynamic with rapid on-off rates while the curvature of the ssDNA is maintained by the less-dynamic Tri-C core (composed of OB-C, OB-D and OB-E).

In such a model, access to internal regions in the ssDNA or the ends can be provided to incoming RPA-interacting proteins by rearranging one or more DBDs (62,63). Such rearrangements could be promoted by post-translational modification (s) of one or more DBDs (Figure 8). As a proof of concept, we here show how phosphorylation of RPA at a single position in DBD-B (Ser-384 in RPA70) drives changes in ssDNA access. Aurora kinase B phosphorylates RPA at Ser-384 during mitosis to suppress homologous recombination and to facilitate chromosome segregation by maintaining Aurora B activity (22). Surprisingly, the end-to-end ssDNA distance does not change in RPA-pSer^{384}, but the patterns of crosslinking between the domains in XL-MS are strikingly altered. Thus, the DBDs and PIDs have been repositioned or remodeled through phosphorylation without altering the overall wrapping path of ssDNA (Figure 8). Such changes would grant access to internal regions of the ssDNA wrapped by RPA upon phosphorylation.

In summary, measurement of end-to-end distances using smFRET and DEER spectroscopy supports a model where ssDNA is wrapped around a compacted structure of RPA with remodeling of the domains enacted through post-translational modifications. Thus, RPA can be differentially modulated to serve varying DNA metabolic needs without major changes to the ssDNA organization within the complex. How these changes transpire within the context of multiple RPA molecules bound to longer ssDNA remains to be established. The MD simulations presented here show how multiple RPA molecules can be engaged on longer ssDNA while retaining the wrapped architecture within the DNA binding domains. At the moment, experimentally capturing how ssDNA wrapping or stretching changes upon binding of multiple RPA molecules is not feasible as the changes in end-to-end distances described here are already at the limits of detection for the smFRET and DEER methodologies. Thus, structural approaches such as CryoEM will be needed to further address such questions.

Data availability

Raw data are available in the associated Supplemental Data File. Plasmids for protein overproduction as available upon request. Code for computational modeling can be accessed through these repositories: https://github.com/holehouse-lab/supportingdata/tree/master/2024/chadda_kaushik_2024 and https://doi.org/10.5281/zenodo.12205956.

Supplementary data

Supplementary Data are available at NAR Online.

Acknowledgements

Authors thank the lab members and Dr Timothy Craggs (Exciting Instruments) for technical advice and critical reading of the manuscript. We thank Dr Greg Sabat, University of Wisconsin-Madison, for phospho-proteomic MS analysis. XL-MS data were obtained at the Mass Spectrometry Technology Access Center (MTAC) at Washington University in St. Louis. We thank Dr Byoung-Kyu Cho at MTAC for collecting the XL-MS spectra.

Author contributions Rahul Chadda: Formal analysis, Methodology, Validation, Writing—original draft. Vikas Kaushik: Protein Purification, pSer incorporation, XL-MS experiments and data analysis, Writing—review & editing. Jaigeeth Deveryshetty, Edwin Antony, & Brian Bothner: Cross-linking mass spectrometry and structural analysis, Writing—review & editing. Alex Holehouse: Formal analysis, Methodology, Validation, Writing—original draft. Iram Munir Ahmad and Snorri Th.d Sigurdsson: Design and synthesis of spin-labeled oligonucleotides, Writing—review & editing. Gargi Biswas and Yaakov Levy: MD simulation of RPA–ssDNA interactions, Writing—review & editing. Richard Cooley and Ryan Mehl: Design of cells and strategies for pSer-incorporation. Writing—review & editing. Reza Dastvan: EPR - Formal analysis, Methodology, Validation, Writing—review & editing. Sofia Origanti: Conceptualization, Formal analysis, Methodology, Validation, Writing—review & editing. Edwin Antony: Conceptualization, Formal analysis, Methodology, Validation, Writing—original draft.

Funding

National Institutes of Health [R35-GM149320 and S10-OD030343 to E.A., R01-GM145783 to R.D., R01-GM143179 to S.O., DP2-CA290639-01 to A.S.H.]; S.Th.S. acknowledges financial support from the Icelandic Research Fund [206708]; Acquisition of the EI-FLEX microscope was supported through a grant from the Department of Energy, Office of Basic Energy Sciences [DE-SC0020965 to E.A.]; Y.L. was supported by grants from the Israeli Science Foundation [2072/22]; Estate of Gerald Alexander; pSer incorporation was supported in part by the GCE4All Biomedical Technology Development and Dissemination Center supported by National Institute of General Medical Science grant [RM1-GM144227 to R.M]; XL-MS data collection supported by the Washington University Institute of Clinical and Translational Sciences which is, in part, supported by the NIH/National Center for Advancing Translational Sciences (NCATS), CTSA [UL1TR002345]. Funding for open access charge: National Institutes of Health [R35-GM149320].

Conflict of interest statement

None declared.

References

1. Caldwell,C.C. and Spies,M. (2020) Dynamic elements of replication protein A at the crossroads of DNA replication, recombination, and repair. *Crit. Rev. Biochem. Mol. Biol.*, **55**, 482–507.
2. Wold,M.S. and Kelly,T. (1988) Purification and characterization of replication protein A, a cellular protein required for in vitro replication of simian virus 40 DNA. *Proc. Natl. Acad. Sci. U.S.A.*, **85**, 2523–2527.
3. Wold,M.S. (1997) Replication protein A: A heterotrimeric, single-stranded DNA-binding protein required for eukaryotic DNA metabolism. *Annu. Rev. Biochem.*, **66**, 61–92.
4. Iftode,C., Daniely,Y. and Borowiec,J.A. (1999) Replication protein A (RPA): the eukaryotic SSB. *Crit. Rev. Biochem. Mol. Biol.*, **34**, 141–180.
5. Kim,C., Paulus,B.F. and Wold,M.S. (1994) Interactions of human replication protein A with oligonucleotides. *Biochemistry*, **33**, 14197–14206.
6. Kumaran,S., Kozlov,A.G. and Lohman,T.M. (2006) Saccharomyces cerevisiae replication protein A binds to single-stranded DNA in multiple salt-dependent modes. *Biochemistry*, **45**, 11958–11973.
7. Treuner,K., Ramsperger,U. and Knippers,R. (1996) Replication protein A induces the unwinding of long double-stranded DNA regions. *J. Mol. Biol.*, **259**, 104–112.
8. Lao,Y., Lee,C.G. and Wold,M.S. (1999) Replication protein A interactions with DNA. 2. Characterization of double-stranded DNA-binding/helix-destabilization activities and the role of the zinc-finger domain in DNA interactions. *Biochemistry*, **38**, 3974–3984.
9. Bartos,J.D., Willmott,L.J., Binz,S.K., Wold,M.S. and Bambara,R.A. (2008) Catalysis of strand annealing by replication protein A derives from its strand melting properties. *J. Biol. Chem.*, **283**, 21758–21768.
10. Salas,T.R., Petruseva,I., Lavrik,O., Bourdoncle,A., Mergny,J.L., Favre,A. and Saintome,C. (2006) Human replication protein A unfolds telomeric G-quadruplexes. *Nucleic Acids Res.*, **34**, 4857–4865.
11. Marechal,A. and Zou,L. (2015) RPA-coated single-stranded DNA as a platform for post-translational modifications in the DNA damage response. *Cell Res.*, **25**, 9–23.
12. Namiki,Y. and Zou,L. (2006) ATRIP associates with replication protein A-coated ssDNA through multiple interactions. *Proc. Natl. Acad. Sci. U.S.A.*, **103**, 580–585.
13. Zou,L. and Elledge,S.J. (2003) Sensing DNA damage through ATRIP recognition of RPA–ssDNA complexes. *Science*, **300**, 1542–1548.
14. Zou,L., Liu,D. and Elledge,S.J. (2003) Replication protein A-mediated recruitment and activation of Rad17 complexes. *Proc. Natl. Acad. Sci. U.S.A.*, **100**, 13827–13832.
15. de Laat,W.L., Appeldoorn,E., Sugasawa,K., Weterings,E., Jaspers,N.G. and Hoeijmakers,J.H. (1998) DNA-binding polarity of human replication protein A positions nucleases in nucleotide excision repair. *Genes Dev.*, **12**, 2598–2609.
16. Acharya,A., Kasaciunaite,K., Gose,M., Kissling,V., Guerois,R., Seidel,R. and Cejka,P. (2021) Distinct RPA domains promote recruitment and the helicase-nuclease activities of Dna2. *Nat. Commun.*, **12**, 6521.
17. Zhou,C., Pourmal,S. and Pavletich,N.P. (2015) Dna2 nuclease-helicase structure, mechanism and regulation by Rpa. *eLife*, **4**, e09832.
18. Fan,J. and Pavletich,N.P. (2012) Structure and conformational change of a replication protein A heterotrimer bound to ssDNA. *Genes Dev.*, **26**, 2337–2347.
19. Yates,L.A., Aramayo,R.J., Pokhrel,N., Caldwell,C.C., Kaplan,J.A., Perera,R.L., Spies,M., Antony,E. and Zhang,X. (2018) A structural and dynamic model for the assembly of replication protein A on single-stranded DNA. *Nat. Commun.*, **9**, 5447.
20. Madru,C., Martinez-Carranza,M., Laurent,S., Alberti,A.C., Chevreuil,M., Raynal,B., Haouz,A., Le Meur,R.A., Delarue,M., Henneke,G., *et al.* (2023) DNA-binding mechanism and evolution of replication protein A. *Nat. Commun.*, **14**, 2326.
21. Bochkareva,E., Korolev,S., Lees-Miller,S.P. and Bochkarev,A. (2002) Structure of the RPA trimerization core and its role in the multistep DNA-binding mechanism of RPA. *EMBO J.*, **21**, 1855–1863.
22. Roshan,P., Kuppa,S., Mattice,J.R., Kaushik,V., Chadda,R., Pokhrel,N., Tumala,B.R., Biswas,A., Bothner,B., Antony,E., *et al.* (2023) An Aurora B-RPA signaling axis secures chromosome segregation fidelity. *Nat. Commun.*, **14**, 3008.
23. Ahmad,F., Patterson,A., Deveryshetty,J., Mattice,J.R., Pokhrel,N., Bothner,B. and Antony,E. (2021) Hydrogen-deuterium exchange reveals a dynamic DNA-binding map of replication protein A. *Nucleic Acids Res.*, **49**, 1455–1469.
24. Chen,J., Le,S., Basu,A., Chazin,W.J. and Yan,J. (2015) Mechanochemical regulations of RPA's binding to ssDNA. *Sci. Rep.*, **5**, 9296.
25. Sugitani,N. and Chazin,W.J. (2015) Characteristics and concepts of dynamic hub proteins in DNA processing machinery from studies of RPA. *Prog. Biophys. Mol. Biol.*, **117**, 206–211.
26. Pokhrel,N., Caldwell,C.C., Corless,E.I., Tillison,E.A., Tibbs,J., Jocic,N., Tabei,S.M.A., Wold,M.S., Spies,M. and Antony,E. (2019) Dynamics and selective remodeling of the DNA-binding domains of RPA. *Nat. Struct. Mol. Biol.*, **26**, 129–136.
27. Pokhrel,N., Origanti,S., Davenport,E.P., Gandhi,D., Kaniecki,K., Mehl,R.A., Greene,E.C., Dockendorff,C. and Antony,E. (2017) Monitoring Replication Protein A (RPA) dynamics in homologous recombination through site-specific incorporation of non-canonical amino acids. *Nucleic Acids Res.*, **45**, 9413–9426.
28. San Filippo,J., Sung,P. and Klein,H. (2008) Mechanism of eukaryotic homologous recombination. *Annu. Rev. Biochem.*, **77**, 229–257.
29. Heyer,W.D., Ehmsen,K.T. and Liu,J. (2010) Regulation of homologous recombination in eukaryotes. *Annu. Rev. Genet.*, **44**, 113–139.
30. Symington,L.S. (2014) End resection at double-strand breaks: mechanism and regulation. *Cold Spring Harb. Perspect. Biol.*, **6**, a016436.
31. Sugawara,N. and Haber,J.E. (1992) Characterization of double-strand break-induced recombination: homology requirements and single-stranded DNA formation. *Mol. Cell. Biol.*, **12**, 563–575.
32. Nguyen,B., Sokoloski,J., Galletto,R., Elson,E.L., Wold,M.S. and Lohman,T.M. (2014) Diffusion of human replication protein A along single-stranded DNA. *J. Mol. Biol.*, **426**, 3246–3261.
33. Schiemann,O., Heubach,C.A., Abdullin,D., Ackermann,K., Azarkh,M., Bagryanskaya,E.G., Drescher,M., Endeward,B., Freed,J.H., Galazzo,L., *et al.* (2021) Benchmark test and guidelines for DEER/PELDOR experiments on nitroxide-labeled biomolecules. *J. Am. Chem. Soc.*, **143**, 17875–17890.
34. Stelzl,L.S., Erlenbach,N., Heinz,M., Prisner,T.F. and Hummer,G. (2017) Resolving the conformational dynamics of DNA with angstrom resolution by pulsed electron-electron double resonance and molecular dynamics. *J. Am. Chem. Soc.*, **139**, 11674–11677.
35. Marko,A., Denysenkov,V., Margraf,D., Cekan,P., Schiemann,O., Sigurdsson,S.T. and Prisner,T.F. (2011) Conformational flexibility of DNA. *J. Am. Chem. Soc.*, **133**, 13375–13379.
36. Prisner,T.F., Marko,A. and Sigurdsson,S.T. (2015) Conformational dynamics of nucleic acid molecules studied by PELDOR spectroscopy with rigid spin labels. *J. Magn. Reson.*, **252**, 187–198.
37. Saha,S., Jagtap,A.P. and Sigurdsson,S.T. (2015) Site-directed spin labeling of 2′-amino groups in RNA with isoindoline nitroxides

that are resistant to reduction. *Chem. Commun.*, **51**, 13142–13145.
38. Binz,S.K., Dickson,A.M., Haring,S.J. and Wold,M.S. (2006) Functional assays for replication protein A (RPA). *Methods Enzymol.*, **409**, 11–38.
39. Zhu,P., Mehl,R.A. and Cooley,R.B. (2022) Site-specific incorporation of phosphoserine into recombinant proteins in *Escherichia coli*. *Bio. Protoc.*, **12**, e4541.
40. Rogerson,D.T., Sachdeva,A., Wang,K., Haq,T., Kazlauskaite,A., Hancock,S.M., Huguenin-Dezot,N., Muqit,M.M., Fry,A.M., Bayliss,R., *et al.* (2015) Efficient genetic encoding of phosphoserine and its nonhydrolyzable analog. *Nat. Chem. Biol.*, **11**, 496–503.
41. Zhu,P., Gafken,P.R., Mehl,R.A. and Cooley,R.B. (2019) A highly versatile expression system for the production of multiply phosphorylated proteins. *ACS Chem. Biol.*, **14**, 1564–1572.
42. Ingargiola,A., Lerner,E., Chung,S., Weiss,S. and Michalet,X. (2016) FRETBursts: an open source toolkit for analysis of freely-diffusing single-molecule FRET. *PLoS One*, **11**, e0160716.
43. Hustedt,E.J., Stein,R.A. and McHaourab,H.S. (2021) Protein functional dynamics from the rigorous global analysis of DEER data: conditions, components, and conformations. *J. Gen. Physiol.*, **153**, e201711954.
44. Graham,M., Combe,C., Kolbowski,L. and Rappsilber,J. (2019) xiView: a common platform for the downstream analysis of Crosslinking Mass Spectrometry data. bioRxiv doi: https://doi.org/10.1101/561829, 26 February 2019, preprint: not peer reviewed..
45. Hoitsma,N.M., Norris,J., Khoang,T.H., Kaushik,V., Chadda,R., Antony,E., Hedglin,M. and Freudenthal,B.D. (2023) Mechanistic insight into AP-endonuclease 1 cleavage of abasic sites at stalled replication fork mimics. *Nucleic Acids Res.*, **51**, 6738–6753.
46. Pangeni,S., Biswas,G., Kaushik,V., Kuppa,S., Yang,O., Lin,C.T., Mishra,G., Levy,Y., Antony,E. and Ha,T. (2024) Rapid long-distance migration of RPA on single stranded DNA occurs through intersegmental transfer utilizing multivalent interactions. *J. Mol. Biol.*, **436**, 168491.
47. Mishra,G., Bigman,L.S. and Levy,Y. (2020) ssDNA diffuses along replication protein A via a reptation mechanism. *Nucleic Acids Res.*, **48**, 1701–1714.
48. Hellenkamp,B., Schmid,S., Doroshenko,O., Opanasyuk,O., Kuhnemuth,R., Rezaei Adariani,S., Ambrose,B., Aznauryan,M., Barth,A., Birkedal,V., *et al.* (2018) Precision and accuracy of single-molecule FRET measurements-a multi-laboratory benchmark study. *Nat. Methods*, **15**, 669–676.
49. Murphy,M.C., Rasnik,I., Cheng,W., Lohman,T.M. and Ha,T. (2004) Probing single-stranded DNA conformational flexibility using fluorescence spectroscopy. *Biophys. J.*, **86**, 2530–2537.
50. Hohlbein,J., Craggs,T.D. and Cordes,T. (2014) Alternating-laser excitation: single-molecule FRET and beyond. *Chem. Soc. Rev.*, **43**, 1156–1171.
51. Ambrose,B., Baxter,J.M., Cully,J., Willmott,M., Steele,E.M., Bateman,B.C., Martin-Fernandez,M.L., Cadby,A., Shewring,J., Aaldering,M., *et al.* (2020) The smfBox is an open-source platform for single-molecule FRET. *Nat. Commun.*, **11**, 5641.
52. Heinz,M., Erlenbach,N., Stelzl,L.S., Thierolf,G., Kamble,N.R., Sigurdsson,S.T., Prisner,T.F. and Hummer,G. (2020) High-resolution EPR distance measurements on RNA and DNA with the non-covalent G spin label. *Nucleic Acids Res.*, **48**, 924–933.
53. Igbaria-Jaber,Y., Hofmann,L., Gevorkyan-Airapetov,L., Shenberger,Y. and Ruthstein,S. (2023) Revealing the DNA Binding Modes of CsoR by EPR Spectroscopy. *ACS Omega*, **8**, 39886–39895.
54. Hofmann,H., Soranno,A., Borgia,A., Gast,K., Nettels,D. and Schuler,B. (2012) Polymer scaling laws of unfolded and intrinsically disordered proteins quantified with single-molecule spectroscopy. *Proc. Natl. Acad. Sci. U.S.A.*, **109**, 16155–16160.
55. Chen,H., Meisburger,S.P., Pabit,S.A., Sutton,J.L., Webb,W.W. and Pollack,L. (2012) Ionic strength-dependent persistence lengths of single-stranded RNA and DNA. *Proc. Natl. Acad. Sci. U.S.A.*, **109**, 799–804.
56. Gong,Z., Ye,S.X. and Tang,C. (2020) Tightening the Crosslinking Distance Restraints for Better Resolution of Protein Structure and Dynamics. *Structure*, **28**, 1160–1167.
57. Wieser,T.A. and Wuttke,D.S. (2022) Replication protein A utilizes differential engagement of its DNA-binding domains to bind biologically relevant ssDNAs in diverse binding modes. *Biochemistry*, **61**, 2592–2606.
58. Fanning,E., Klimovich,V. and Nager,A.R. (2006) A dynamic model for replication protein A (RPA) function in DNA processing pathways. *Nucleic Acids Res.*, **34**, 4126–4137.
59. Chen,R., Subramanyam,S., Elcock,A.H., Spies,M. and Wold,M.S. (2016) Dynamic binding of replication protein a is required for DNA repair. *Nucleic Acids Res.*, **44**, 5758–5772.
60. Wang,Q.M., Yang,Y.T., Wang,Y.R., Gao,B., Xi,X.G. and Hou,X.M. (2019) Human replication protein A induces dynamic changes in single-stranded DNA and RNA structures. *J. Biol. Chem.*, **294**, 13915–13927.
61. Kuppa,S., Deveryshetty,J., Chadda,R., Mattice,J.R., Pokhrel,N., Kaushik,V., Patterson,A., Dhingra,N., Pangeni,S., Sadauskas,M.K., *et al.* (2022) Rtt105 regulates RPA function by configurationally stapling the flexible domains. *Nat. Commun.*, **13**, 5152.
62. Topolska-Wos,A.M., Sugitani,N., Cordoba,J.J., Le Meur,K.V., Le Meur,R.A., Kim,H.S., Yeo,J.E., Rosenberg,D., Hammel,M., Scharer,O.D., *et al.* (2020) A key interaction with RPA orients XPA in NER complexes. *Nucleic Acids Res.*, **48**, 2173–2188.
63. Mer,G., Bochkarev,A., Gupta,R., Bochkareva,E., Frappier,L., Ingles,C.J., Edwards,A.M. and Chazin,W.J. (2000) Structural basis for the recognition of DNA repair proteins UNG2, XPA, and RAD52 by replication factor RPA. *Cell*, **103**, 449–456.

Received: April 1, 2024. **Revised:** May 30, 2024. **Editorial Decision:** June 18, 2024. **Accepted:** June 25, 2024

Supplementary Information

Partial wrapping of single-stranded DNA by Replication Protein A and modulation through phosphorylation

Rahul Chadda[1,#], Vikas Kaushik[1,#], Iram Munir Ahmad[2], Jaigeeth Deveryshetty[1], Alex Holehouse[3], Snorri Th.d Sigurdsson[2], Gargi Biswas[4], Yaakov Levy[4], Brian Bothner[5], Richard B. Cooley[6], Ryan A. Mehl[6], Reza Dastvan[1], Sofia Origanti[7], and Edwin Antony[1,*]

Supplementary Tables 1-5

Supplementary Figures 1-9

Supplemental Videos 1-3

Supplementary Table 1. Oligonucleotides used in this study

Oligonucleotides used for the smFRET experiments

5′ Cy5-(dT)$_{15}$-Cy3 3′	Cy5-TTT TTT TTT TTT TTT-Cy3
5′ Cy5-(dT)$_{30}$-Cy3 3′	Cy5-TTT TTT TTT TTT TTT TTT TTT TTT TTT TTT -Cy3
5′ Cy5-(dT)$_{45}$-Cy3 3′	Cy5-TTT TTT TTT TTT TTT TTT TTT TTT TTT TTT TTT TTT TTT TTT TTT -Cy3
5′ Cy5-(dT)$_{60}$-Cy3 3′	Cy5-TTT TTT TTT TTT TTT TTT TTT TTT TTT TTT TTT TTT TTT TTT TTT TTT TTT TTT TTT -Cy3
5′ Cy5-(dT)$_{80}$-Cy3 3′	Cy5-TTT TTT TTT TTT TTT TTT TTT TTT TTT TTT TTT TTT TTT TTT TTT TTT TTT TTT TTT TTT TTT TTT TTT TTT TTT TT -Cy3
5′ Cy5-(dT)$_{97}$-Cy3 3′	Cy5-TTT TTT TTT TTT TTT TTT TTT TTT TTT TTT TTT TTT TTT TTT TTT TTT TTT TTT TTT TTT TTT TTT TTT TTT TTT TTT TTT TTT TTT TTT TTT TTT TTT TTT T -Cy3

Oligonucleotides used for the DEER experiments

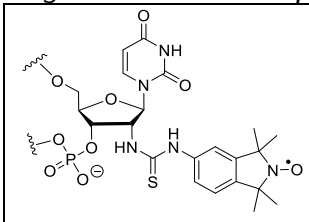 **(M)**	**(dT)$_{22}$** **DEER**	5'-d(**M** TT TTT TTT TTT TTT TTT TTT TT **M** T)-3'

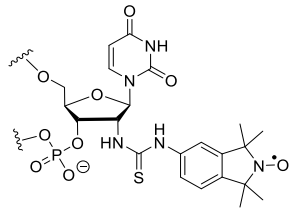 **(M)**	**(dT)$_{50}$** **DEER**	5'-d (TTT **M**TT TTT TTT TTT TTT TTT TTT TTT TTT TTT TTT TTT TTT TTT TTT TTT **M**T) 3'

Supplementary Table 2. Composition of media and reagents used for Phosphoserine incorporation media.

A) ZY-non inducing media (ZY-NIM)

Components	For 50 mL
ZY media	47.25 mL
1 M $MgSO_4$	0.1 mL
25x M-salts	2 mL
40 % (w/v) α-D-glucose	0.625 mL
Trace metals solution (5000x)	0.01 mL

B) ZY-auto inducing media (ZY-AIM)

Components	For 1 L
ZY media	940 mL
1 M $MgSO_4$	2 mL
25x M-salts	40 mL
50x 5052 solution	20 mL
Trace metals solution (5000x)	0.2 mL

C) Composition of 25X M-salts

Components	For 1 L
Sodium phosphate dibasic	88.73 g
Potassium phosphate dibasic	85.05 g
Ammonium chloride	66.86 g
Sodium sulfate anhydrous	17.75 g

D) 50x 5052 solution

Components	For 1 L
α-D-glucose	2.5 g
Lactose	50 g
Glycerol (v/v)	125 mL

Supplementary Table 3. Comparison of FRET efficiencies measured using the EI-FLEX and the Picoquant MT200

	FRET efficiency		**Nbursts**	
	EI-FLEX	**MT200**	**EI-FLEX***	**MT200***
$(dT)_{15}$	0.83 (±0.064)	0.89 (±0.11)	765	10260
$(dT)_{30}$	0.37 (±0.086)	0.426 (±0.097)	268	9056
$(dT)_{45}$	0.15 (±0.060)	0.17 (±0.088)	366	11788
$(dT)_{60}$	0.074 (±0.049)	0.066 (±0.078)	511	18453
$(dT)_{80}$	0.021 (±0.05)	0.022 (±0.075)	426	40425
$(dT)_{97}$	0.027 (±0.37)	0.032 (±0.088)	1257	636

***** Please note that the number of bursts for MT200 appear higher than those in EI-FLEX as EI-FLEX analysis uses ALEX to discard the data for molecules which have either donor or acceptor only.

Supplementary Table 4. FRET efficiencies measurements (smFRET)

$(dT)_{15}$ and hRPA	**FRET efficiency**		
	Free	**Bound**	**N bursts**
$(dT)_{15}$	0.81 (±0.065)	-	527
$(dT)_{15}$ + 0.3 nM hRPA	0.78 (±0.077)	0.22 (±0.10)	443
$(dT)_{15}$ + 1 nM hRPA	0.78 (±0.072)	0.18 (±0.076)	339
$(dT)_{15}$ + 10 nM hRPA	0.80 (±0.074)	0.17 (±0.06)	355

$(dT)_{25}$ and hRPA	**FRET efficiency**			**Mass Photometry**		
	Free	**Bound**	**N bursts**	**Mass (mean; kDa)**	**Mass (±St.dev.)**	**# of spots**
$(dT)_{25}$	0.49 (±0.093)	-	1072			
$(dT)_{25}$ + 0.02 nM hRPA	0.49 (±0.095)	0.07 (±0.032)	1086	115.3	13.28	1098
$(dT)_{25}$ + 0.1 nM hRPA	0.49 (±0.11)	0.075 (±0.047)	852	115.6	14.32	14774
$(dT)_{25}$ + 1 nM hRPA	-	0.07 (±0.2)	912	117.5	15.18	36823

$(dT)_{25}$ and yRPA	**FRET efficiency**		
	Free	**Bound**	**N bursts**
$(dT)_{25}$	0.49 (±0.093)	-	1072
$(dT)_{25}$ + 0.02 nM ScRPA	0.48 (±0.098)	0.09 (±0.031)	773
$(dT)_{25}$ + 0.1 nM ScRPA	0.47 (±0.11)	0.089 (±0.085)	783
$(dT)_{25}$ + 1 nM ScRPA	-	0.091 (±0.12)	1172

Supplementary Table 5. FRET efficiencies measurements (smFRET)

$(dT)_{30}$ and hRPA	**FRET efficiency**		
	Free	**Bound**	**N bursts**
$(dT)_{30}$	0.37 (±0.098)	-	585
$(dT)_{30}$ + 0.03 nM hRPA	0.38 (±0.095)	0.04 (±0.055)	654
$(dT)_{30}$ + 0.1 nM hRPA	0.37 (±0.092)	0.025 (±0.068)	568
$(dT)_{30}$ + 1 nM hRPA	-	0.055 (±0.047)	569

$(dT)_{45}$ and hRPA	**FRET efficiency**		
	Free	**Bound**	**N bursts**
$(dT)_{45}$	0.17 (±0.075)	-	1108
$(dT)_{45}$ + 0.03 nM hRPA	0.17 (±0.081)	0.02 (±0.044)	773
$(dT)_{45}$ + 0.1 nM hRPA	0.17 (±0.059)	0.021 (±0.033)	779
$(dT)_{45}$ + 1 nM hRPA	-	0.02 (±0.035)	677

End-to-end distance measurements						
$(dT)_{xx}$	**Free ssDNA**	**hRPA-bound**	**Fully Linearized ssDNA**	**Free ssDNA (DEER)**	**hRPA-bound (DEER)**	**yRPA-bound (DEER)**
$(dT)_{15}$	4.06 (± 0.44)	6.9 (± 0.64)	10.14			
$(dT)_{22}$			14.74	4.4 (± 1.1)	6.83 (± 1.5)	6.9 (± 1.8)
$(dT)_{25}$	5.32 (± 0.55)	8.5 (± 0.82)	16.75			
$(dT)_{30}$	5.69 (± 0.51)	8.8 (± 0.84)	20.3			
$(dT)_{45}$	6.98 (± 0.79)	10.3 (± 0.99)	30.5			

Supplementary Table 6. DEER measurements

	<*R*> [nm]	σ [nm]	*f* (%)
$(dT)_{22}$	3.1±1.0	0.7±0.6	36
	5.1±2.0	1.1±3.1	64
$(dT)_{22}$+*hRPA*	4.6±0.4	1.0±0.7	5
	6.8±0.8	0.4±1.2	95
$(dT)_{22}$+*hRPA*-^{pSer384}	4.6±0.4	1.0±0.7	30
	6.8±0.8	0.4±1.2	70
$(dT)_{22}$+*yRPA*	6.9±0.3	1.0±0.3	100

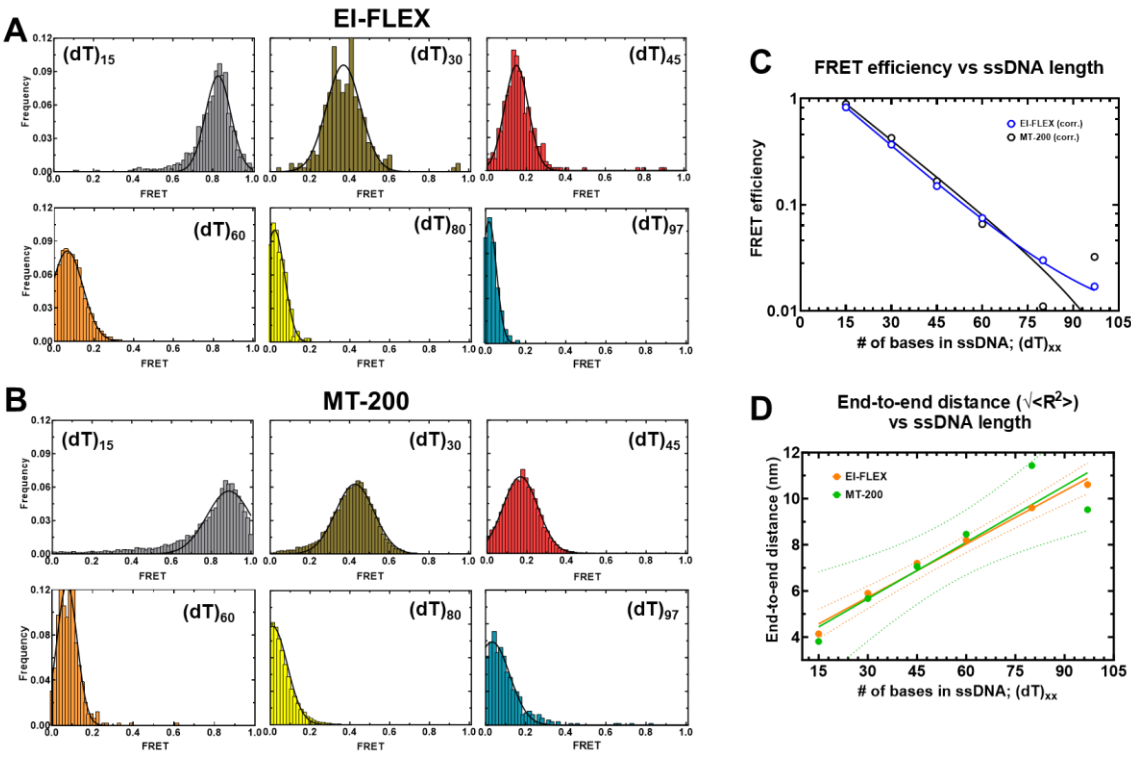

Supplementary Figure 1. Comparison of smFRET data collected using the EI-FLEX and MT-200 microscopes. smFRET data collected for various lengths of ssDNA using the **A)** EI-FLEX and **B)** Picoquant MT-200 microscopes. **C)** Plot of the FRET efficiencies versus ssDNA shows excellent agreement between measurements made using both instruments. **D)** Similarly, end-to-end distance measurements calculated from the smFRET data show excellent agreement for both instruments. The dotted lines represent a 95% confidence interval for the linear fit for the MT-200 (green) and EI-FLEX (orange), respectively.

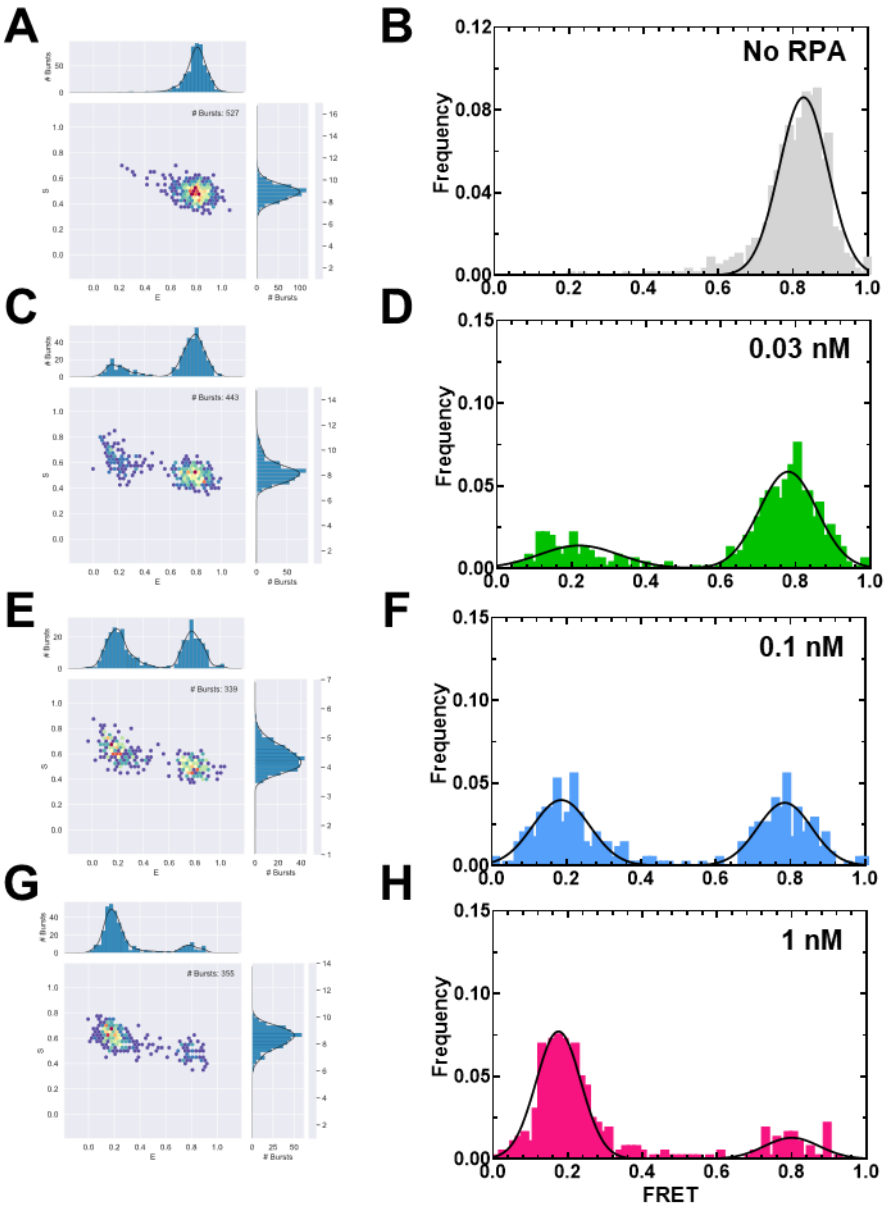

Supplementary Figure 2. smFRET data for RPA-(dT)$_{15}$ complexes. smFRET data collected for the (dT)$_{15}$ substrate in the absence of RPA **(A & B)** and increasing concentrations of RPA **(C-H)**.

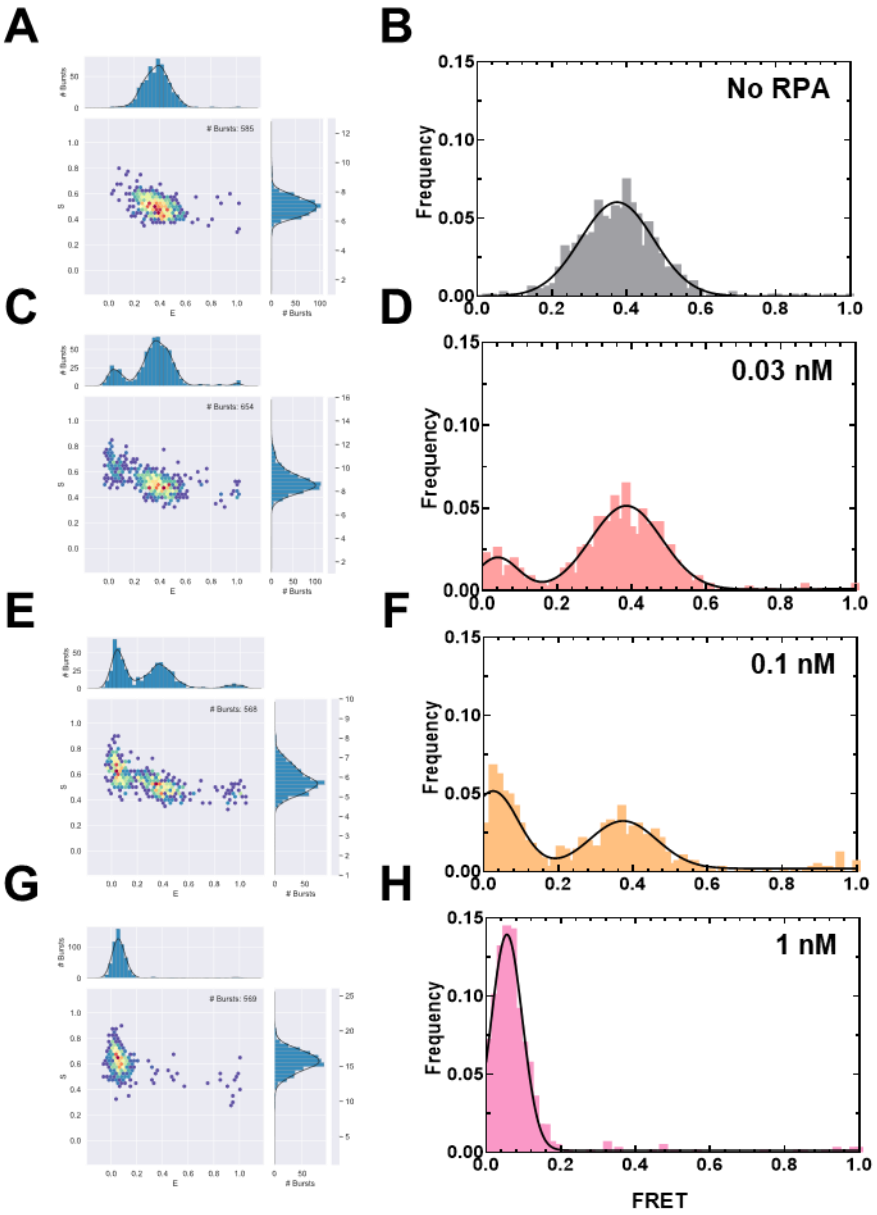

Supplementary Figure 3. smFRET data for RPA-(dT)$_{30}$ complexes. smFRET data collected for the (dT)$_{30}$ substrate in the absence of RPA **(A & B)** and increasing concentrations of RPA **(C-H)**.

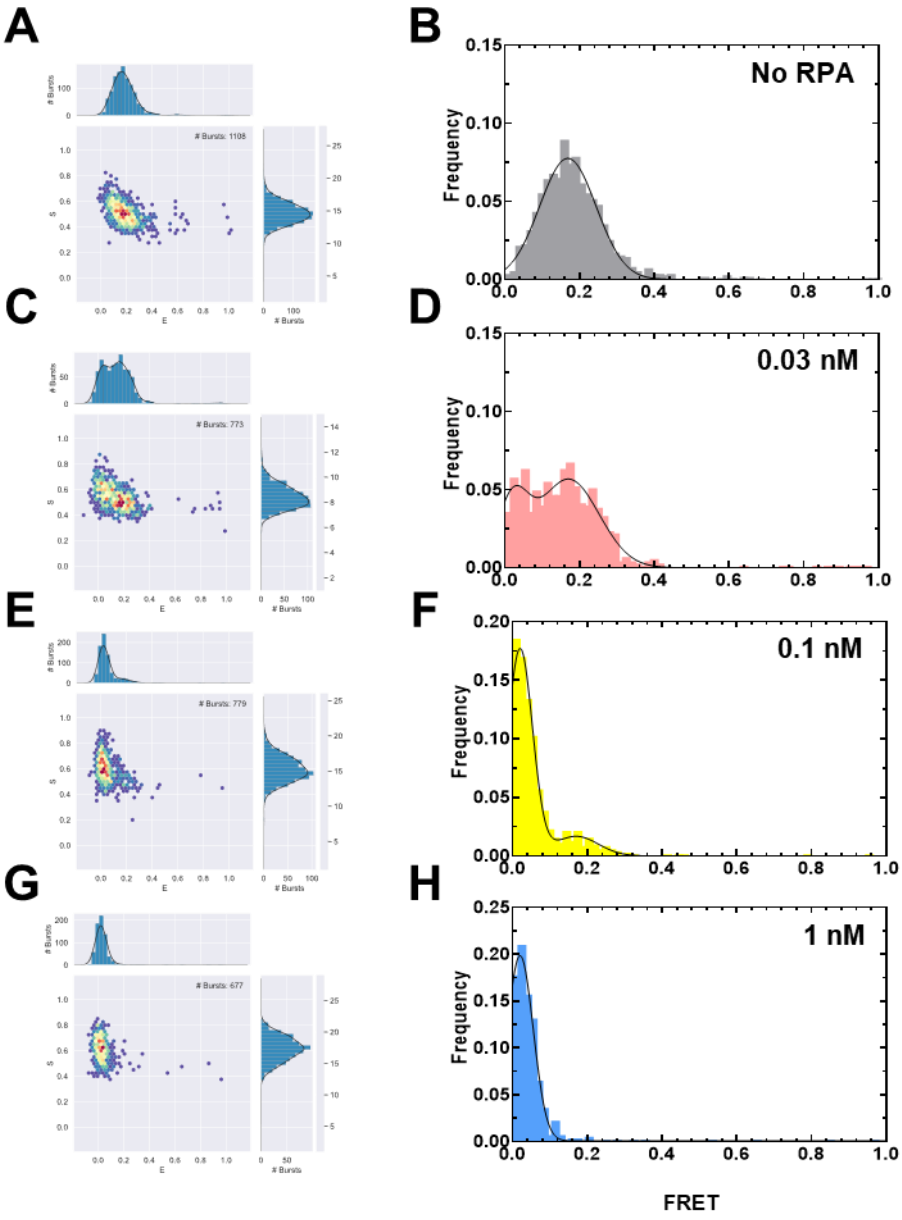

Supplementary Figure 4. smFRET data for RPA-$(dT)_{45}$ complexes. smFRET data collected for the $(dT)_{45}$ substrate in the absence of RPA **(A & B)** and increasing concentrations of RPA **(C-H)**.

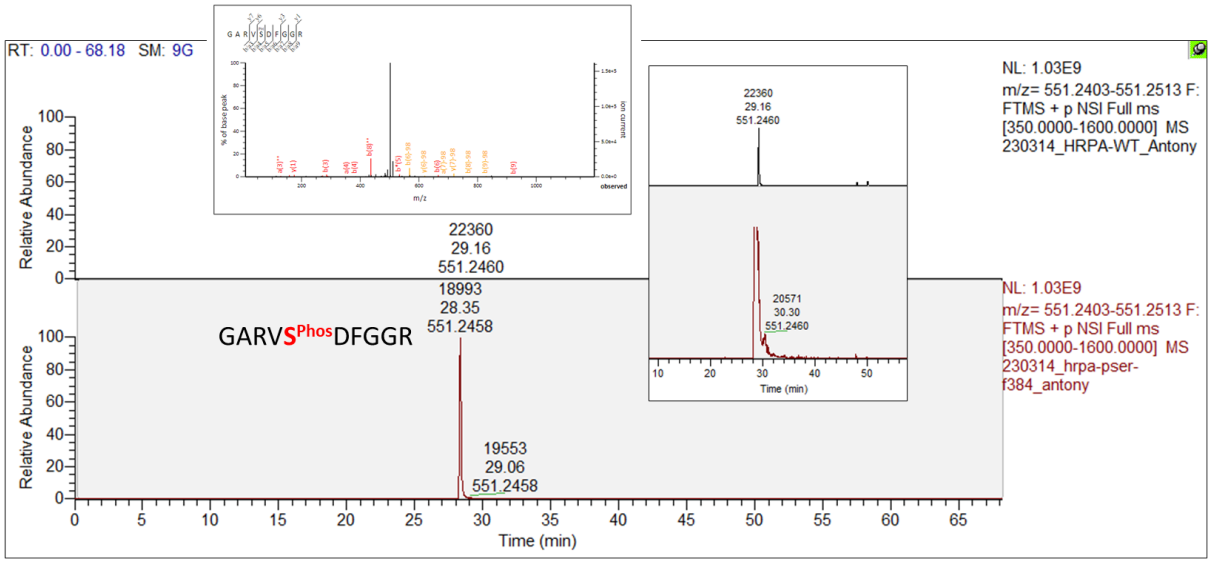

Supplementary Figure 5. Mass spectrometry analysis of pSer incorporation in hRPA. Mass spectrometry analysis of RPA-pSer^{384} shows site-specific phosphoserine incorporation.

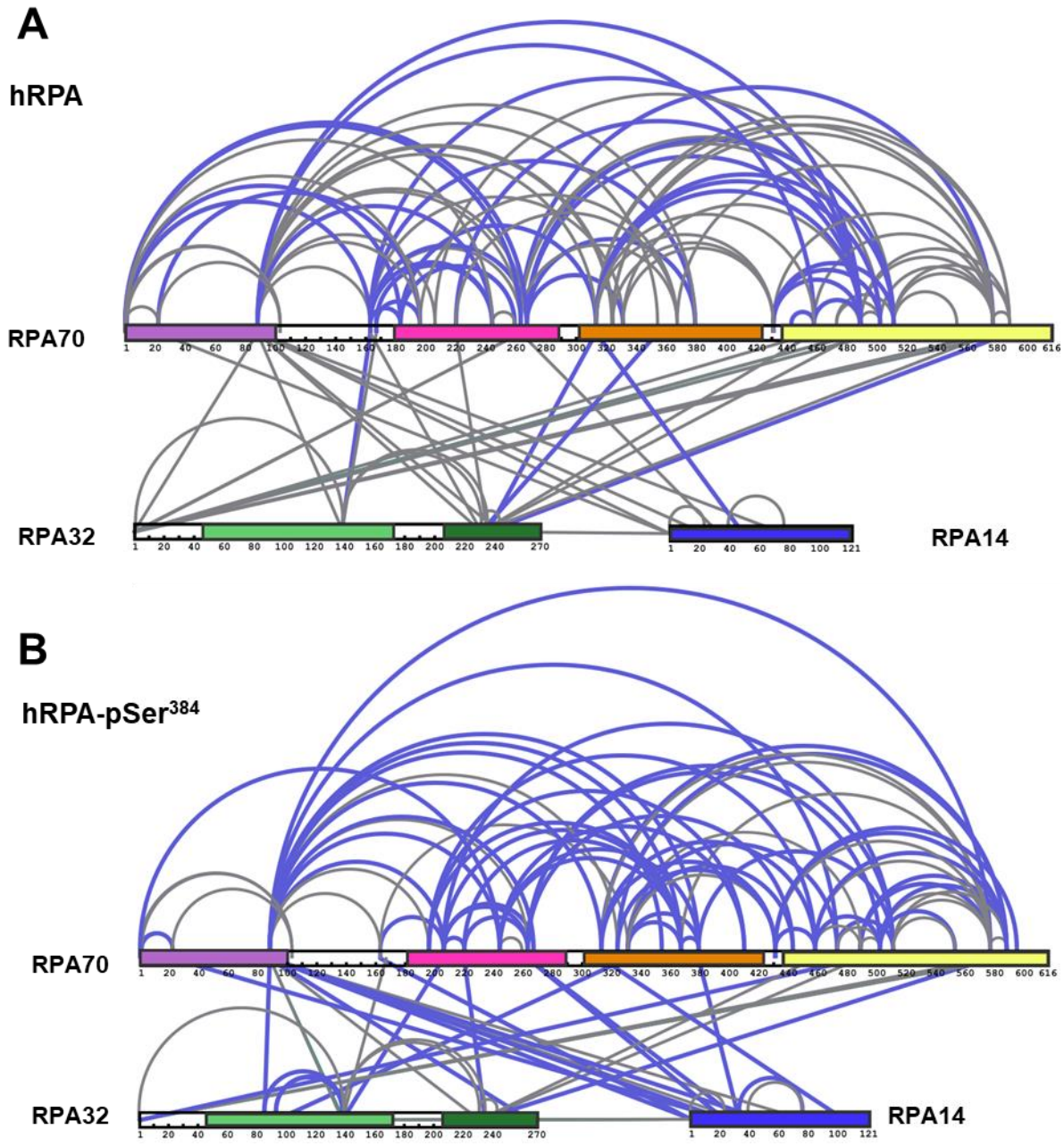

Supplementary Figure 6. Unique XLs in the RPA introduced by phosphorylation at Ser-384 in RPA70. Crosslinking mass spectrometry (XL-MS) analysis of **A)** RPA and **B)** RPA-pSer^{384} are shown. The two datasets are compared relative to each other and the crosslinks unique to each sample are shown in blue. Crosslinks in grey are common to both datasets and depict intra-subunit crosslinks within RPA70-, RPA32 and RPA14.

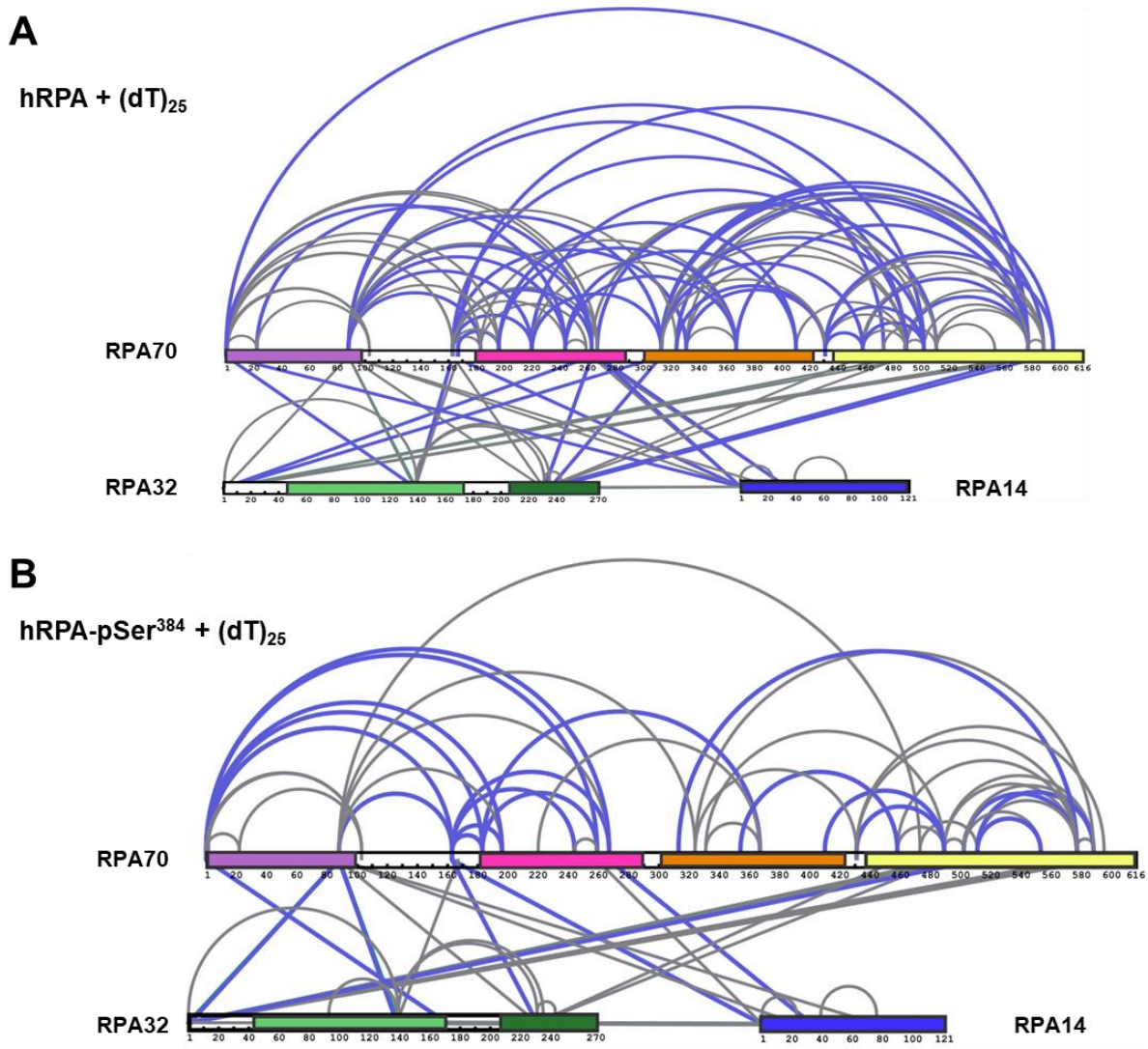

Supplementary Figure 7. Unique XLs in the RPA-ssDNA complex introduced by phosphorylation at Ser-384 in RPA70. Crosslinking mass spectrometry (XL-MS) analysis of **A)** RPA-ssDNA and **B)** RPA-pSer^{384}-ssDNA complexes are shown. The two datasets are compared relative to each other and the crosslinks unique to each sample are shown in blue. Crosslinks in grey are common to both datasets and depict intra-subunit crosslinks within RPA70-, RPA32 and RPA14.

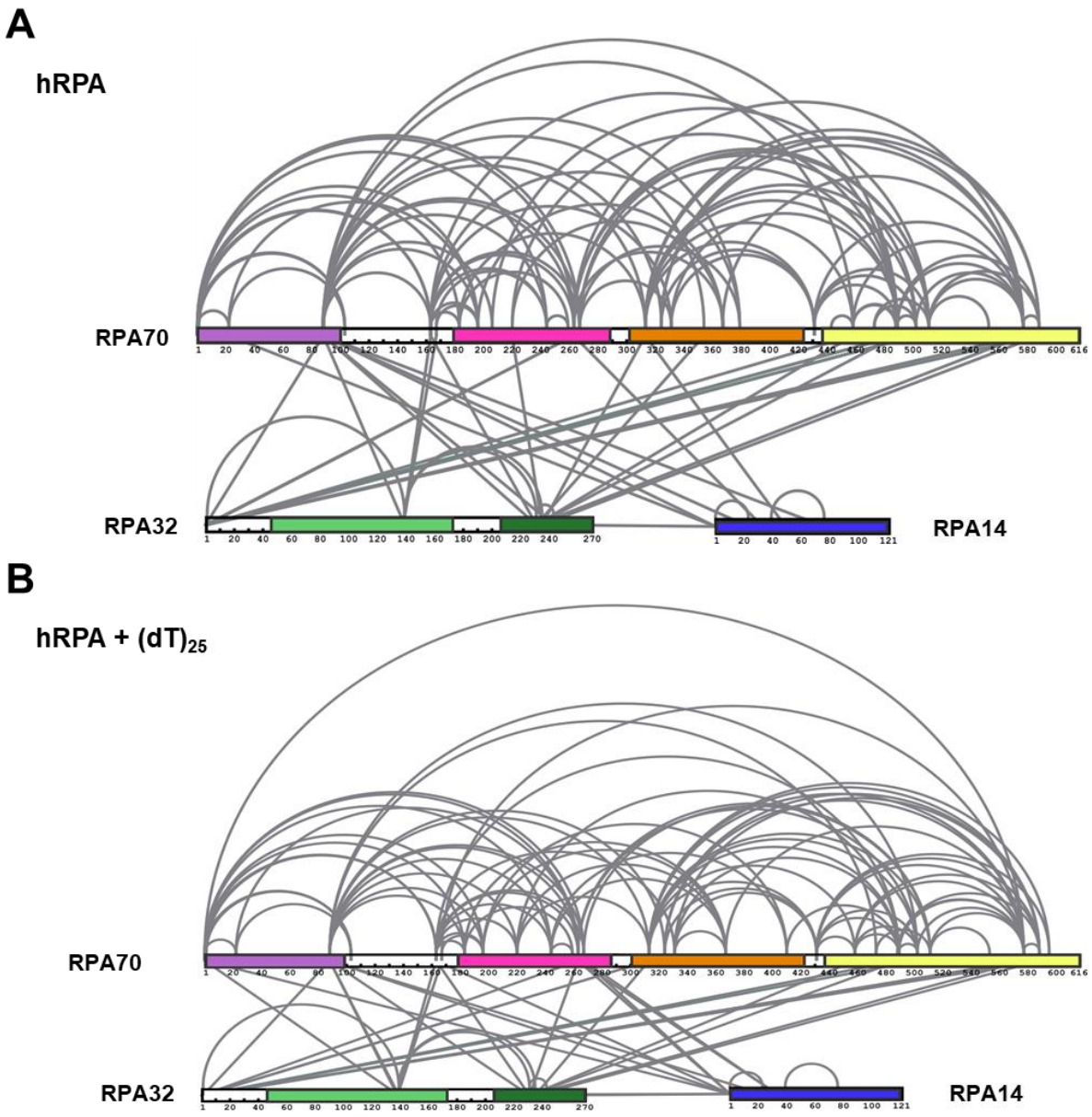

Supplementary Figure 8. Summary of all the XLs in the RPA and RPA-ssDNA complex. All the crosslinks identified by MS for **A)** RPA and **B)** RPA-ssDNA complexes are shown.

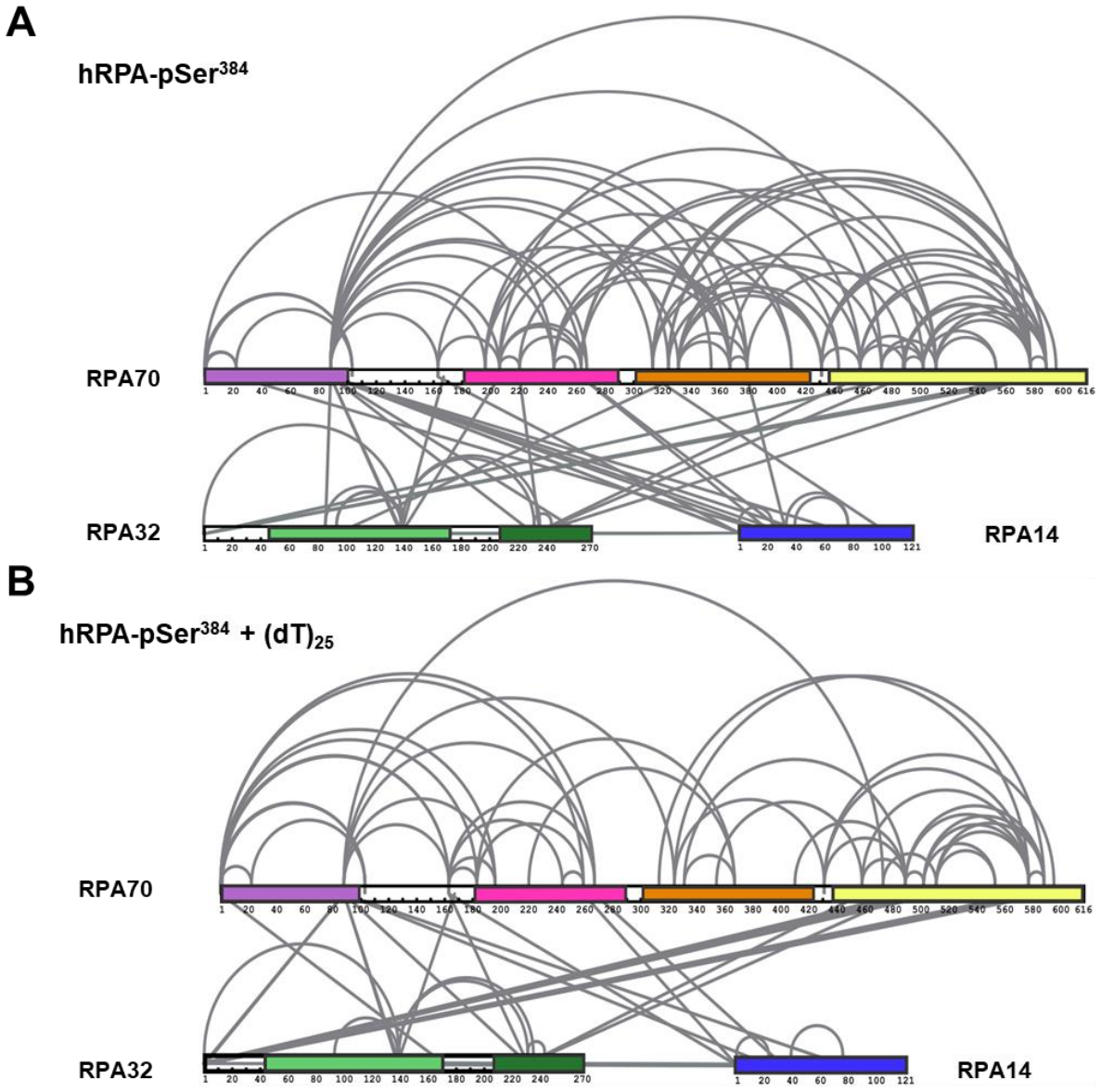

Supplementary Figure 9. Summary of all the XLs in the RPA-pSer^{384} and RPA-pSer^{384} - ssDNA complex. All the crosslinks identified by MS for **A)** RPA-pSer^{384} and **B)** RPA-pSer^{384}-ssDNA complexes are shown.

Paper IV

Paper IV. Förster resonance energy transfer within the neomycin aptamer

Florian H, Halbritter A-LJ, Ahmad IM, Braun M, Sigurdsson ST and Wachtveitl J, *Phys. Chem. Chem. Phys*. **2024**, 26, 7157-65

PCCP

ROYAL SOCIETY OF CHEMISTRY

PAPER

Cite this: *Phys. Chem. Chem. Phys.*, 2024, **26**, 7157

Förster resonance energy transfer within the neomycin aptamer†

Florian Hurter,[a] Anna-Lena J. Halbritter,[bc] Iram M. Ahmad,[b] Markus Braun,[a] Snorri Th. Sigurdsson[b] and Josef Wachtveitl*[a]

Received 24th November 2023,
Accepted 18th January 2024

DOI: 10.1039/d3cp05728c

rsc.li/pccp

Förster resonance energy transfer (FRET) measurements between two dyes is a powerful method to interrogate both structure and dynamics of biopolymers. The intensity of a fluorescence signal in a FRET measurement is dependent on both the distance and the relative orientation of the dyes. The latter can at the same time both complicate the analysis and give more detailed information. Here we present a detailed spectroscopic study of the energy transfer between the rigid FRET labels $\mathbf{C_{7m}^{f}}$ (donor) and $\mathbf{tC_{nitro}}$ (quencher/acceptor) within the neomycin aptamer N1. The energy transfer originates from multiple emitting states of the donor and occurs on a low picosecond to nanosecond time-scale. To fully characterize the energy transfer, ultrafast transient absorption measurements were performed in conjunction with static fluorescence and time-correlated single photon counting (TCSPC) measurements, showing a clear distance dependence of both signal intensity and lifetime. Using a known NMR structure of the ligand-bound neomycin aptamer, the distance between the two labels was used to estimate κ^2 and, therefore, make qualitative statements about the change in orientation after ligand binding with unprecedented temporal and spatial resolution. The advantages and potential applications of absorption-based methods using rigid labels for the characterization of FRET processes are discussed.

Introduction

Ribonucleic acids (RNAs) play a central role in cellular regulation such as transcription, translation and gene expression.[1] This includes functional non-coding RNAs, such as riboswitches that often target the 5′-untranslated regions of bacterial mRNA.[2] A riboswitch contains two interacting domains, an aptamer region that binds with high affinity and specificity to a metabolite and the expression platform.[3–5] These two domains act in concert to activate or repress gene expression through a conformational change that is triggered by ligand binding.[2,6–9]

RNA aptamers can be readily generated by the technique of **s**ystematic **e**volution of **l**igands by **ex**ponential enrichment (SELEX)[10–13] and have found use as diagnostic agents,[14,15] biosensors,[16,17] and therapeutics.[18–20] It is of great interest to create artificial riboswitches for regulation of gene expression using ligands of choice, but only a few RNA aptamers have been utilized for creating non-natural riboswitches.[6,7,21–23] Increased understanding of the structure–function relationships of aptamers and riboswitches is required to be able to purposefully design new functional riboswitches.[24–26]

Of the several methods that have been established for studying the structure and dynamics of RNA, fluorescence spectroscopy is particularly valuable.[27,28] It has the advantages of being highly sensitive, nondestructive for the sample of interest and offers the ability to conduct experiments under native conditions. It is a very useful tool to detect the dynamics of biomolecules through various approaches. In addition to unraveling detailed information about RNA dynamics, fluorescence spectroscopy is a powerful method to study structure, even of single molecules, through Förster resonance energy transfer (FRET). This high-resolution fluorescence technique can obtain information about both distance and relative orientation of FRET pairs.[29–33]

The relative orientation between the donor and the acceptor is described with κ^2, which is not easy to determine. For free moving labels a κ^2 of 2/3 is usually assumed, which is valid in the dynamic isotropic regime.[34] However, this assumption is in many cases insufficient,[30,35–39] especially for rigid FRET pairs, where this assumption is considered invalid.[35,40] On the flip side, rigid FRET labels can provide more structural details through interrogation of the relative orientation of the dyes.

The structural elements of nucleic acids provide a good framework for rigid labels, in particular when the labels are

[a] *Institute of Physical and Theoretical Chemistry, Goethe University Frankfurt, Main, Max-von-Laue-Str. 7, Frankfurt 60438, Germany. E-mail: wveitl@theochem.uni-frankfurt.de*
[b] *Science Institute, University of Iceland, Dunhaga 3, Reykjavik 107, Iceland*
[c] *Department of Chemistry, Ludwig-Maximilians-University (LMU), Munich, Germany*

† Electronic supplementary information (ESI) available: Methods, Fig. S1–S4 and Tables S1–S3. See DOI: https://doi.org/10.1039/d3cp05728c

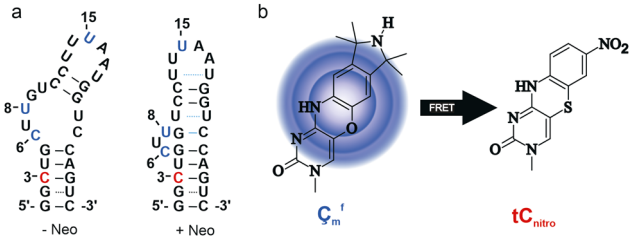

Fig. 1 (a) Secondary structure of the N1-aptamer in its free state (left) and when bound to its ligand (right).[44] (b) Structure of the rigid labels **Çm^f** and **tC$_{nitro}$**.

nucleobase analogues. When embedded in helical regions, they provide accurate distance measurements and the possibility to study relative orientations.[41]

We have previously prepared and evaluated the fluorescent nucleobase analogue **Çm^f** (Fig. 1b), which forms a base pair with guanine, as a fluorescent probe for RNA.[42] It was shown that **Çm^f** does not perturb the structure of RNA duplexes and that it is highly sensitive to its microenvironment. Moreover, it was used to study ligand binding by the neomycin aptamer.

Interestingly, the fluorescent label **Çm^f** has multiple emitting states. This makes **Çm^f** even more interesting as a donor in FRET-studies, since the energy transfer can take place from multiple states.[43]

Here we present a detailed spectroscopic study of the energy transfer between the rigid labels **Çm^f** (donor) and **tC$_{nitro}$** (quencher/acceptor) (Fig. 1b) inside the neomycin aptamer N1 (Fig. 1a). The neomycin aptamer was chosen because both its structure and dynamics have been well studied and because this aptamer is one of the few aptamers that functions as an active riboswitch.[6,26,42,44–46] We found that the energy transfer between **Çm^f** and **tC$_{nitro}$** extends over several orders of magnitude, from nanoseconds to the low picosecond range. This required application of different methods, to adequately describe the energy transfer over this large time-range. In general, static fluorescence measurements can be used to determine whether FRET occurs and on what time scale. Once this is known, it can be decided whether TCSPC or TAS is suitable to obtain temporal information about the energy transfer, depending on how fast the process proceeds.

By combining different spectroscopic and data evaluation methods, we provide new approaches to gain a deeper understanding of the distance and orientation dependence of rigid labels in RNA, specifically to precisely determine structural changes with unprecedented temporal and spatial resolution, even at donor–acceptor distances below 2 nm.

Results & discussion

Preparation of oligonucleotides/labeling strategy

We have previously labeled the N1-aptamer at positions C6, U8 and U15 with **Çm^f** to study the kinetics of ligand binding.[42] Since the label was well accommodated in these positions, we used the same labeling strategy for **Çm^f** in this FRET study and chose the C3 position for **tC$_{nitro}$**. Thus, this labeling strategy yielded three different samples, **N1-tC$_{nitro}$3-Çm^{f}6**, **N1-tC$_{nitro}$3-Çm^{f}8** and **N1-tC$_{nitro}$3-Çm^{f}15** (**N-N3C6**, **N-N3C8** and **N-N3C15**, respectively) (Fig. 2), with increasing distance between donor and acceptor in this order.

To investigate the binding capabilities of the doubly labeled aptamers, we initially performed ITC experiments (ESI,† Fig. S1). The dissociation constants of the doubly labeled aptamers are generally larger than the K_Ds of the unlabeled aptamer (ESI,† Table S1). However, the K_Ds of the doubly- and singly-labeled aptamers are in the same order of magnitude.[42] This demonstrates that the incorporation of **tC$_{nitro}$** as a second label does not significantly affect the binding capabilities to the ligand.

FRET: data collection and analysis. The donor and the acceptor used in this study were covalently linked to the

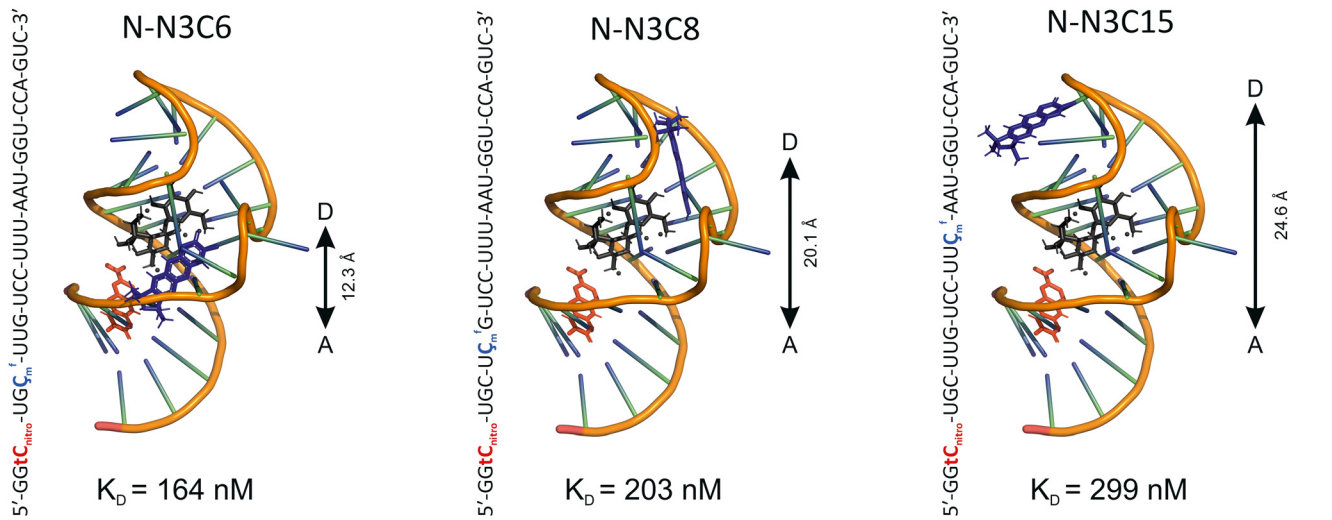

Fig. 2 Positions of the donor (**Çm^f**) and acceptor (**tC$_{nitro}$**) within the N1-aptamer, outlined in PDBID:2KXM(NDB/PDB).[44] **Çm^f** is highlighted in blue and **tC$_{nitro}$** in red. The ligand neomycin is shown in black. Donor acceptor distances (center to center) from the modified NMR structure indicated on the side of the samples and the K_D values are shown below.

backbone of the N1-aptamer and thus, both the distance (r) and the relative orientation of the transition dipole moments determine the efficiency of the FRET process. Since **tC$_{nitro}$** acts as an efficient quencher, the fluorescence signal originates exclusively from the **Ç$_m^f$** chromophore, which greatly simplifies the evaluation of the FRET data. We began by investigating the static fluorescence behavior.

Static FRET characterization

The singly **Ç$_m^f$**-labeled N1-aptamers **N-C6**, **N-C8** and **N-C15**,[42] have previously been shown to have slightly different fluorescence intensity, due to the different flanking bases of **Ç$_m^f$** (Fig. 3a).[42] Upon ligand binding, the microenvironment of the **Ç$_m^f$** changed, leading to an increased fluorescence signal for **N-C6**, **N-C8** and to a decrease for **N-C15**.[42] For the doubly-labeled aptamers (**N-N3C6**, **N-N3C8** and **N-N3C15**), all signal intensities were significantly lower than the singly **Ç$_m^f$**-labeled aptamers (Fig. 3b). Moreover, the fluorescence signals show a clear correlation with the distance between donor and acceptor: It is almost completely quenched for the shortest distance (**N-N3C6**), but the signals get stronger as the chromophores are further apart.

Ligand binding only resulted in a minor change in fluorescence for both **N-N3C6** and **N-N3C15**. In contrast a large relative change was observed for **N-N3C8**, which was even larger than for the singly labeled aptamer **N-C8**.

For a quantitative analysis, the FRET efficiencies can be calculated. The reduction of the FRET efficiency (E) is dominated by the donor–acceptor distance, but also the relative orientation of the transition dipole moments (eqn (1)):

$$E = \frac{k_{\mathrm{FRET}}(r)}{\tau_{\mathrm{D}}^{-1} + k_{\mathrm{FRET}}(r)} = \frac{R_0^6}{R_0^6 + r^6} \tag{1}$$

Here, R_0 (eqn (2)) corresponds to the Förster radius, r to the distance between donor and acceptor, τ_D to the fluorescence lifetime of the donor alone and $k_{FRET}(r)$ (eqn (3)) to the transfer rate.

$$R_0 = 0.211\left(J_{\mathrm{DA}}\kappa^2 n^{-4}\varphi_{\mathrm{D}}\right)^{\frac{1}{6}} \tag{2}$$

$$k_{\mathrm{FRET}}(r) = \frac{1}{\tau_D}\left(\frac{R_0}{r}\right)^6 \tag{3}$$

The relative orientation between the transition dipole moments of the donor and acceptor is described by κ^2 (eqn (4)). Here, J_{DA} is the overlap integral between the emission spectrum of the donor and the absorption spectrum of the acceptor, n corresponds to the refractive index of the solvent and φ_D to the fluorescence quantum yield of the donor.[30]

$$\kappa^2 = (\sin\theta_{\mathrm{D}}\sin\theta_{\mathrm{A}}\cos\phi - 2\cos\theta_{\mathrm{D}}\cos\theta_{\mathrm{A}})^2 \tag{4}$$

The static FRET efficiencies (E_{sta}) can be determined using the integrated donor fluorescence signal of the donor only (I_D) and the doubly labeled (I_{DA}) aptamers (eqn (5), Table 1). The Förster radii $R_{0,sta}$ for the FRET pair labeled aptamers were determined by use of these estimated distances between donor and acceptor (Fig. 2, eqn 1 and Table 1).

$$E_{\mathrm{sta}} = 1 - \frac{I_{\mathrm{DA}}}{I_{\mathrm{D}}} \tag{5}$$

Overall, high static FRET efficiencies (E_{sta}) were obtained for all samples (Table 1). The most drastic change of E_{sta} upon ligand binding can be seen for **N-N3C8** (14%). For **N-N3C6** and **N-N3C15**, the FRET efficiencies change by only 1% and 2%, respectively. The absolute FRET efficiencies, as well as their change due to ligand binding, are strongly dependent on the distance and κ^2 (see below). Since the largest flexibility is expected at position 8, it is reasonable that the actual distance between donor and acceptor for the aptamer without ligand is different from the modelled one. Moreover, the comparatively large Förster radius for **N-N3C8** (– Neo) could also suggest a more favorable orientation between donor and acceptor for the energy transfer (eqn (1) and (2)).

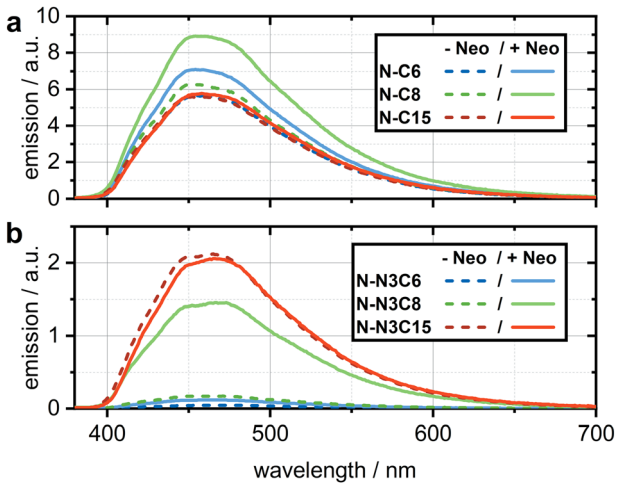

Fig. 3 Time-integrated fluorescence spectra of (a) **Ç$_m^f$** labeled neomycin aptamers published by Gustman *et al.*[42] (b) **Ç$_m^f$** and **tC$_{nitro}$** labeled neomycin aptamers. The fluorescence spectra of the aptamers without neomycin (– Neo) are shown as a segmented line.

Time-resolved FRET characterization

In conjunction with the static experiments, it is essential to characterize the energy transfer by time-resolved fluorescence measurements. Time-resolved FRET efficiencies (E_{trf}) can be

Table 1 Experimentally determined static FRET efficiencies E_{sta} for the doubly labeled N1-aptamers (eqn (5)), donor–acceptor distances from the NMR structure r_{DA} and calculated Förster radii $R_{0,sta}$ (eqn (1)). Values given in percent and Ångström, respectively

	Neo	E_{sta} [%]	r_{DA} [Å]	$R_{0,sta}$ [Å]
N-N3C6	–	99.1	12.3	26.8
	+	98.2		23.8
N-N3C8	–	97.1	20.1	36.1
	+	83.5		26.3
N-N3C15	–	61.9	24.6	26.6
	+	64.0		27.0

Table 2 Amplitude weighted averaged fluorescence lifetimes of the donor alone (τ_D), the measured fluorescence lifetimes of the donor in presence of the acceptor (τ_{DA}), the time-resolved FRET efficiencies E_{trf} (eqn (6)) and the calculated Förster radii $R_{0,trf}$ (eqn (1))

	Neo	τ_D [ns][42]	τ_{DA} [ns][a]	E_{trf} [%]	$R_{0,trf}$ [Å]
N-N3C6	−	4.06	0.02	99.5	29.2
	+	4.97	0.12	97.5	22.6
N-N3C8	−	4.14	0.30	92.8	30.7
	+	3.73	1.09	70.7	23.3
N-N3C15	−	4.35	1.42	67.3	27.7
	+	5.96	1.64	72.6	28.9

[a] Amplitude weighted averaged fluorescence lifetime for the time-resolved fluorescence signals from Fig. 4.

obtained by measuring the respective amplitude weighted averaged fluorescence lifetimes τ_D and τ_{DA} (eqn (6), Table 2).[30]

$$E_{trf} = 1 - \frac{\tau_{DA}}{\tau_D} \quad (6)$$

Time-correlated single photon counting (TCSPC) and E_{trf}

We performed TCSPC measurements to monitor the fluorescence decay of the doubly labeled aptamers and to determine the corresponding fluorescence lifetimes.

Similarly to the static fluorescence measurements, the time-resolved fluorescence data (Fig. 4) show a faster decay of the fluorescent state compared to the singly labeled aptamers.[42]

Fitting the data with two respectively three exponential functions results in the averaged fluorescence lifetimes shown in Table 2 (τ_D, τ_{DA}, for further information see ESI,† Table S2).[42] It should be noted that the fast decays from **N-N3C6** (−/+ Neo) and **N-N3C8** (− Neo) were deconvoluted from the IRF (Instrument response function) of the used spectrometer.

Using the averaged fluorescence lifetimes of the donor in presence of the acceptor (τ_{DA}) and the donor alone (τ_D),[42] the time-resolved FRET efficiencies E_{trf} can be derived mathematically using eqn (6) (Table 2).[30,47] The efficiencies from the static measurements (E_{sta}, Table 1) are in good agreement with those from the time-resolved measurements (E_{trf}), within an error of roughly 10%.

The energy transfer rate $k_{FRET,sta}(r)$ was subsequently calculated from the donor fluorescence lifetime τ_D and the static FRET efficiencies E_{sta}, using eqn (1). The reciprocal of this transfer rate, $\tau_{FRET,sta}$ (in ns), indicates the time scale in which the energy transfer predominantly takes place. Likewise, the FRET efficiencies (E_{trf}), determined by TCSPC, yielded

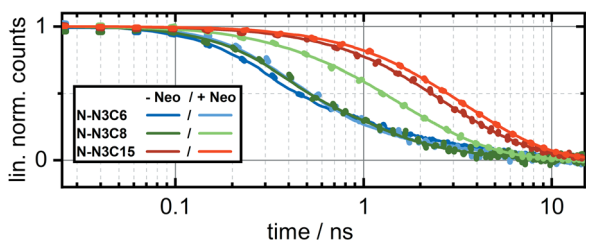

Fig. 4 Time-resolved fluorescence signals for **N-N3C6**, **N-N3C8** and **N-N3C15** (−/+ Neo). Data points are shown as dots, the fits are shown as solid lines.

Table 3 Calculated transfer rates by static and time-resolved fluorescence measurements ($k_{FRET,sta}(r)$ and $k_{FRET,trf}(r)$) and the respective FRET times given in ns ($\tau_{FRET,sta}$ and $\tau_{FRET,trf}$)

	Neo	$k_{FRET,sta}(r)$ [ns^{-1}][a]	$\tau_{FRET,sta}$ [ns][b]	$k_{FRET,trf}(r)$ [ns^{-1}][a]	$\tau_{FRET,trf}$ [ns][b]
N-N3C6	−	27.06	0.04	45.63	0.02
	+	10.94	0.09	7.85	0.13
N-N3C8	−	8.20	0.16	3.11	0.32
	+	1.36	0.74	0.65	1.54
N-N3C15	−	0.37	2.68	0.47	2.11
	+	0.30	3.35	0.44	2.25

[a] Determined transfer rates for the energy transfer using eqn (1) and the FRET efficiencies E_{sta} from Table 1 or E_{trf} from Table 2. [b] Reciprocal of $k_{FRET,sta}(r)$ and $k_{FRET,trf}(r)$ correspond to the FRET time given in ns.

$k_{FRET,trf}(r)$ and $\tau_{FRET,trf}$. The transfer-rates and -times from the static and the time-resolved measurements are in good agreement (Table 3).

For high static FRET efficiencies (E_{sta}), when the fluorescence of $Ç_m^f$ in the doubly labeled samples is strongly quenched, it is possible that the weak signals can be distorted by signals from impurities or detector noise. For high time-resolved FRET efficiencies (E_{trf}, determined by TCSPC), the fluorescence lifetimes were so short that they had to be deconvoluted from the IRF. The fact that FRET takes place in the picosecond time-range (*e.g.* for **N-N3C6**, Table 3), shows that both experimental methods are at their limits, although the derived FRET times are similar with both methods. The dependence of the FRET times on the distance between the FRET pairs is also evident. However, we decided to examine the energy transfer more closely with femtosecond transient absorption experiments in order to resolve the FRET process for the high FRET rates.

Ultrafast FRET dynamics

Ultrafast measurements were performed to characterize energy transfer processes that are at the edge of the time-resolution limit of the TCSPC setup. This is especially important for the **N-N3C6** and **N-N3C8** samples, both of which have high FRET efficiencies and thus ultrafast FRET dynamics. The transient absorption data (Fig. 5) were fitted by global lifetime analysis (GLA) to obtain the lifetimes of the observed states.[48]

The aptamer that was singly labeled with tC_{nitro} (**N-N3**) served as a control. tC_{nitro} shows a ground state absorption in the range of 350 to 550 nm.[41] Therefore, a fraction of the acceptor is always directly excited at the same time as $Ç_m^f$, when irradiating at 388 nm. Upon excitation, tC_{nitro} shows an excited state difference absorption signal ($ESA1_A$) between 450 and 530 nm with a maximum at 505 nm and a second signal ($ESA2_A$) above 600 nm. The directly excited tC_{nitro} (−/+ Neo) decays with a lifetime of 5.1 and 3.8 ps, respectively. Due to the co-excitation, the dynamics of the directly excited acceptor are visible in all the measurements. The $Ç_m^f$ donor shows similar excited state dynamics as the free chromophore, with several emitting states that decay with different lifetimes (Fig. 5).[43]

Next to the transient absorption measurements (Fig. 5) are the corresponding decay associated spectra (DAS), along with

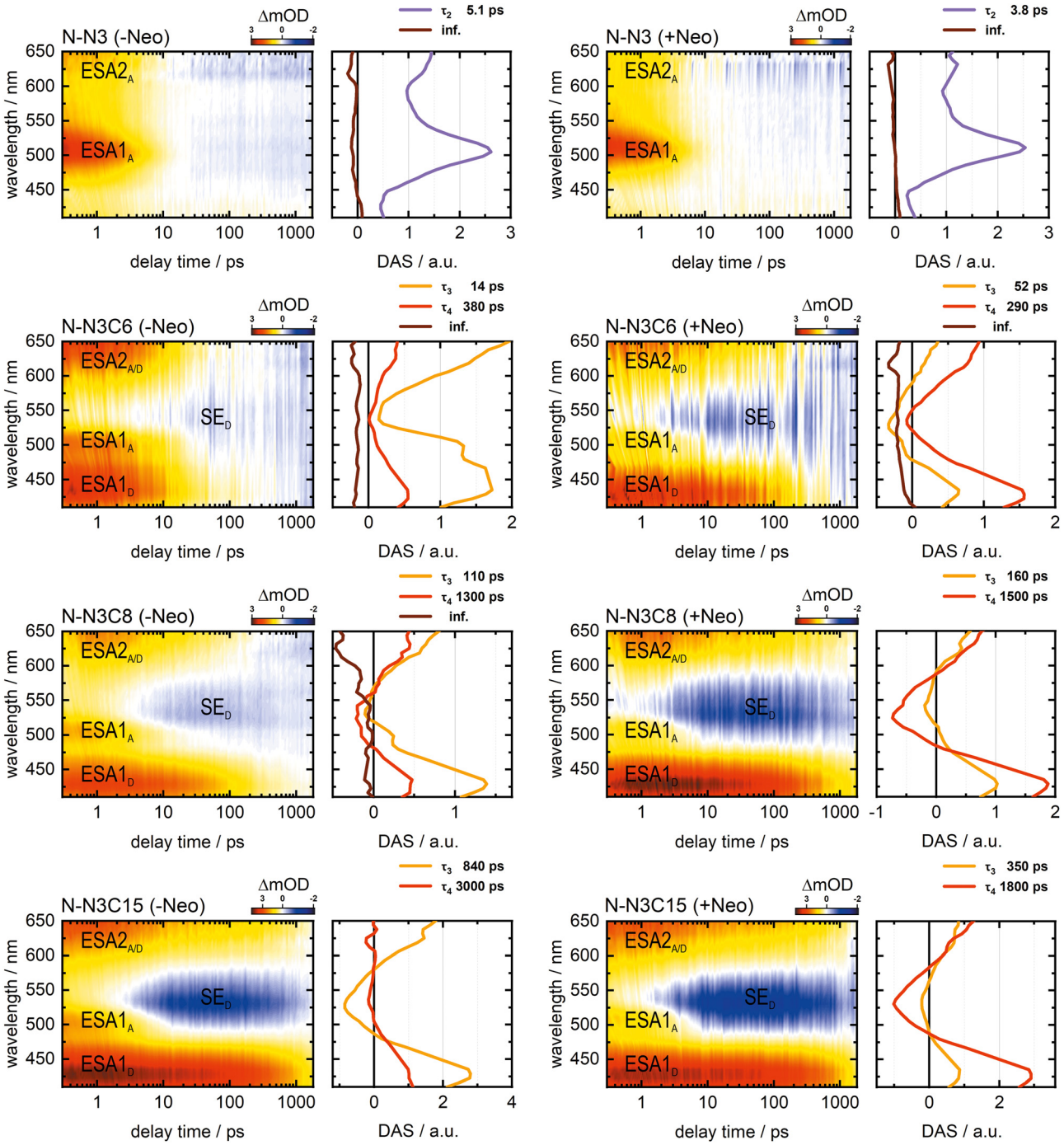

Fig. 5 Transient absorptions maps (left) and decay associated spectra (DAS) (right), top to bottom **N-N3**, **N-N3C6**, **N-N3C8** and **N-N3C15**: left column without neomycin, right column with neomycin. τ_2 for the decay of the directly excited $\mathbf{tC_{nitro}}$ is shown in violet, τ_3 for one emitting state of $\mathbf{Ç_m^f}$ is shown in orange, τ_4 for later emitting states is shown in red. For the samples **N-N3** (−/+ Neo), **N-N3C6** (−/+ Neo), and **N-N3C8** (− Neo) an additional residual lifetime (inf.) is needed to fit the data properly (shown in brown).

the most importantant decay times. A positive signal for $ESA1_D$, between 410 to 490 nm, partially overlaps the signal of the directly excited $\mathbf{tC_{nitro}}$. A second positive signal, between 590 and 650 nm, also overlaps the signal of the directly excited $\mathbf{tC_{nitro}}$ ($ESA2_{A/D}$).

For $\mathbf{Ç_m^f}$, a negative signal is expected between the two ESA bands at 490 to 590 nm, which is assigned to the stimulated emission difference signal (SE_D). Due to the high FRET efficiency for **N-N3C6** (− Neo) and the simultaneous overlap by the dynamics of the directly excited acceptor ($ESA1_A$ & $ESA2_A$), the SE_D signal only contributes with a small amplitude to this measurement. However, for the other measurements, the stimulated emission is clearly identifiable.

The decay of the excited state of $\mathbf{Ç_m^f}$ in the FRET system follows an identical path for each sample; only the corresponding

Table 4 Decay lifetimes derived from transient absorption measurements

	Neo	τ_1 [ps]	τ_2 [ps]	τ_3 [ps]	τ_4 [ps]
N-N3C6	–	0.5	3.1	14	380
	+	0.4	5.6	52	290
N-N3C8	–	0.7	4.7	110	1300
	+	0.3	3.9	160	1500
N-N3C15	–	0.3	5.2	840	3000
	+	0.3	4.3	350	1800

lifetimes are different (Table 4 and ESI,† Fig. S3). The decay occurs in a multi-exponential fashion. The smallest lifetime (τ_1) corresponds to an internal relaxation process after excitation, which leads to the formation of several emitting states.[43] The formation of the emitting states is described with τ_3 and τ_4, while the lifetime τ_2 describes the decay of the directly excited **tC$_{nitro}$**.

Comparing the lifetimes of the emitting states of **Ç$_m^f$** with $k_{FRET,trf}(r)$, and consequently $\tau_{FRET,trf}$ (Table 3), shows that the $\tau_{FRET,trf}$ value is either closer to the lifetime τ_3 or τ_4. It can thus be deduced that, depending on the efficiency, FRET tends to occur predominantly from one of the first or the later emerging emitting states of **Ç$_m^f$**. However, it must be kept in mind that in all cases, energy transfer starts from the first emitting state, but since this state decays rapidly, the transfer progressively shifts towards a second state at lower efficiencies.

In the DAS of τ_3 and τ_4 of the individual transient absorption measurements (Fig. 5), a shoulder at 505 nm (ESA1$_A$) can be observed. When **tC$_{nitro}$** was directly excited, the excited state decayed within approximately 5 ps, indicating that the decay of **tC$_{nitro}$** in the FRET system occurs after the energy transfer. This shoulder is more recognizable in the normalized DAS of the emitting states (ESI,† Fig. S4) further supporting a FRET process from several emitting states.

To further analyze the ultrafast measurements, the transients at 428 nm (ESA1$_D$) and 505 nm (ESA1$_A$) were plotted (Fig. 6). The transients at 428 nm correspond to the decay of the excited state of the **Ç$_m^f$**. It is evident that the excited state of **Ç$_m^f$** is longer-lived at relative greater DA distances and therefore at lower FRET efficiencies.

The transients at 505 nm, associated with the decay of the excited state of **tC$_{nitro}$**, also include the SE$_D$ signal of **Ç$_m^f$**. The transient of the directly excited **tC$_{nitro}$** (– Neo) (black) is almost identical to the transient of **N-N3C8** (– Neo) (yellow). This also applies to the transients of the directly excited **tC$_{nitro}$** (+ Neo) and **N-N3C6** (+ Neo) (blue). For these labeling positions, the FRET occurs after 50 ps, so the transient reflects the decay of the directly excited acceptor up to approximately 10 ps. The transient of **N-N3C6** (– Neo) (blue) decays later than for N-N3 (– Neo), because of the superposition of the signal for both the directly excited **tC$_{nitro}$** and the excited **tC$_{nitro}$** after FRET, due to the high efficiency of the energy transfer. The transients of **N-N3C8** (+ Neo) (yellow) and **N-N3C15** (–/+ Neo) (pink) show a superposition of the positive signal of the directly excited **tC$_{nitro}$** and the negative signal of the stimulated emission of **Ç$_m^f$**. Thus, it appears that the signal of the directly excited acceptor decays faster. Taken together, the transients clearly elucidate the distance dependence of the energy transfer within the aptamer.

Table 5 Averaged lifetimes of the donor in presence of the acceptor achieved by means of TAS experiments ($\tau_{DA(TAS)}$), the FRET efficiencies derived from the TAS experiments (E_{TAS}), the time-resolved FRET efficiencies (E_{trf}), and the static FRET efficiencies (E_{sta})

	Neo	$\tau_{DA(TAS)}$[a] [ps]	E_{TAS} [%]	E_{trf} [%]	E_{sta} [%]
N-N3C6	–	110	97.3	99.5	99.1
	+	224	95.5	97.5	98.2
N-N3C8	–	411	90.1	92.8	97.1
	+	1032	72.3	70.7	83.5
N-N3C15	–	1427	67.2	67.3	61.9
	+	1475	75.3	72.6	64.0

[a] Averaged fluorescence lifetime obtained using the amplitudes in the respective DAS of the two observed emitting states for **Ç$_m^f$** (Fig. 5).

An averaged lifetime $\tau_{DA(TAS)}$ can also be derived from the transient absorption measurements, specifically using the amplitudes of the two DAS spectra (associated with τ_3 and τ_4) for the emitting states of **Ç$_m^f$**. The respective lifetimes were weighted by percentage according to their amplitudes to obtain $\tau_{DA(TAS)}$ (Table 5 and Table S3, ESI†). Despite small deviations, the averaged lifetimes are in good agreement with those obtained by the TCSPC.

With $\tau_{DA(TAS)}$ (Table 5) and τ_D (Table 2) the FRET efficiency can now be derived from the transient absorption measurements

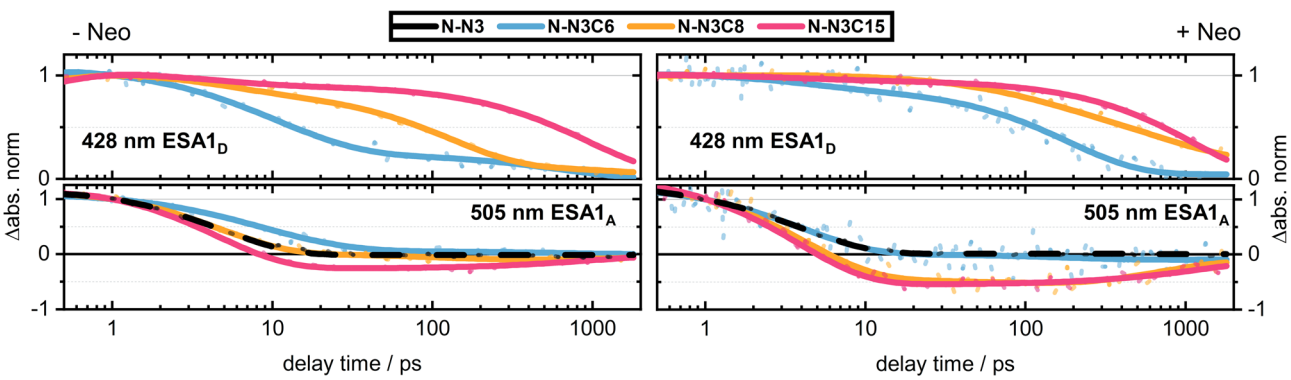

Fig. 6 Transients of the samples **N-N3** (black), **N-N3C6** (blue), **N-N3C8** (yellow) and **N-N3C15** (pink) without (– Neo) and with neomycin (+ Neo). 428 nm corresponds to the wavelength of the excited state of **Ç$_m^f$**. 505 nm corresponds to the wavelength where **tC$_{nitro}$** shows its strongest signal.

(E_{TAS}, Table 5). When comparing the FRET efficiencies derived from the three different methods, it can be seen that similar energy transfer efficiencies are obtained for all three.

Discussion of the label movement and orientation in the aptamer

The FRET efficiency (E) for the labeled aptamers can be experimentally determined, with steady state fluorescence, time-resolved fluorescence (TCSPC) or transient absorption experiments (Table 5). From eqn (1) and (2), it is obvious that E depends on the donor–acceptor distance (r_{DA}) and the relative orientation of the transition dipole moments (κ^2). Therefore, it is not possible to determine this relative orientation, without independent knowledge about the distance r_{DA} and *vice versa*.[38,49]

Nevertheless, the donor–acceptor distance r_{DA} can be extracted with reasonable accuracy (see Table 6) from the NMR structure of the ligand-bound N1-aptamer.[44] Thus the Förster radius R_0 and the orientation factor κ^2 can be calculated from E (Table 6; the time-resolved FRET efficiencies E_{trf} from Table 5 are used for the calculation).

The three-dimensional structure of N1 without the ligand is not available and, therefore, it is not possible to calculate κ^2 from the distance r_{DA} for the FRET pair in this case. However, using eqn (1) and (2) and keeping E_{trf} constant, the distance r_{DA} can be plotted as a function of orientation κ^2 (Fig. 7). These value pairs result in the corresponding FRET efficiency (here E_{trf}, Table 5). For the ligand-bound aptamer the data from Table 6 is marked in Fig. 7 with crosses.

Table 6 Donor–acceptor distances r_{DA} from the NMR structure, calculated Förster radi $R_{0,trf}$ and κ^2 for the different samples. E_{trf} is used for the calculations

	Neo	r_{DA} [Å]	$R_{0,trf}$ [Å]	κ^2
N-N3C6	–	12.3	29.2	0.40
	+		22.6	0.07
N-N3C8	–	20.1	30.7	0.49
	+		23.3	0.06
N-N3C15	–	24.6	27.7	0.29
	+		28.9	0.36

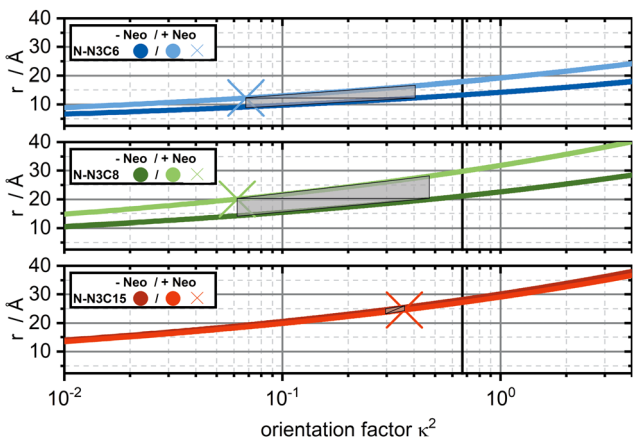

Fig. 7 Dependence of the distance between donor and acceptor (r_{DA}) on the orientation κ^2 for a given FRET efficiency (E_{trf}), areas marked in grey indicate the region of value pairs between r_{DA} and κ^2.

For **N-N3C15**, it is obvious that the resulting curves from the combinations between r_{DA} and κ^2 are almost identical in the absence and presence of the ligand (Fig. 7). This is in agreement with previous a EPR study in which the distance between positions 4 and 15 did not change upon ligand binding.[50] This indicates that the small changes in FRET efficiency could be due to a slight change in the relative orientation between donor and acceptor in the ligand-bound state.

Assuming the same behavior for **N-N3C6** and **N-N3C8**, the corresponding values for κ^2 in the unbound state can be calculated (Table 6). Although the structure in the unbound state is unknown, the value pairs (r_{DA} and κ^2) and the FRET curves (Fig. 7) for both forms of the aptamer can be used to construct areas (gray regions in Fig. 7) that reflect the range of motion of the labels relative to each other. The flexibility of the RNA is accounted for by the construction of the gray areas. This flexibility and the resulting slight differences in κ^2 lead to changes in the FRET efficiency. The gray areas take this into account, with the measured FRET efficiencies corresponding to the average FRET efficiencies in the ensemble.

Based on this analysis, neither distance nor orientation changes significantly for **N-N3C15** upon ligand binding. For **N-N3C6**, a more significant change in both distance and orientation can be observed, which is in agreement with a previous NMR study.[46] The greatest range of changes is seen for **N-N3C8**, which is to be expected, because the $Ç_m^f$ is located at the edge of the binding pocket where ligand binding should result the most pronounced movement. Therefore, our results are consistent with previous studies that have indicated that the N1-aptamer is already prefolded to a significant extent; the binding pocket conformation primarily adapts to the ligand, with little change in the rest of the aptamer.[42]

Conclusions

We have presented a detailed spectroscopic study of the energy transfer process between $Ç_m^f$ and tC_{nitro} using experimental methods that can address a range of time-scales. The FRET efficiency was determined for FRET times from about 20 ps to 3 ns (Table 3). While methods using steady state fluorescence (E_{sta}) and TCSPC (E_{trf}) are commonly used, the third method, transient absorption spectroscopy (E_{TAS}), allowed determination of fast FRET processes (*e.g.* **N-N3C6**) with appropriate time-resolution; even small changes at very high FRET efficiencies (and therefore very small distances) can be determined, for which TCSPC is not sensitive enough.

We were able to evaluate several emitting states for $Ç_m^f$ and showed that the resulting FRET efficiencies, from the three methods that we used, E_{sta}, E_{trf} and E_{TAS} are identical within a range of 10%. It should be noticed that for the transient absorption method it is not necessary for the donor to be a strong-emitting fluorophore with high quantum yield, as for the evaluation, exclusively the absorption data is used. A lower quantum yield results in lower FRET efficiency and also makes TCSPC experiments difficult to perform, because the method

depends on emitted photons. In the case presented here, TAS can be used to study the ultrafast (excited state) dynamics of the donor and the change in dynamics due to energy transfer.This extends the toolbox for the experimentalist.

We have shown that the FRET pair $\mathbf{Ç_m^f}$ and $\mathbf{tC_{nitro}}$ is highly efficient whereby the fluorescence of the donor can be almost completely quenched. However, as with other pairs, it is not possible to determine the exact distance and orientation for this pair from the FRET efficiency $\boldsymbol{E}$ alone. Using a known NMR structure of the ligand-bound N1-aptamer, a distance can be approximated to determine $\boldsymbol{\kappa^2}$ and, therefore, make qualitative statements about the change in orientation after ligand binding.

It is clear that the normal approximation of $\boldsymbol{\kappa^2}$ having the value of 2/3 is insufficient when rigid labels are incorporated. A distinct advantage of rigid labels is the possibility to reveal the dynamic binding behaviour of aptamers.

This study also highlights the importance of the photophysical properties of both the donor and the acceptor in a FRET pair. Ideally, the acceptor should fluoresce spectrally separately from the donor. This would enable measurements of the angle between donor and acceptor using anisotropy measurements.[51] With the procedure described here, in particular using transient absorption experiments, the determination of the angle between donor and acceptor is also possible without fluorescence. This requires a different acceptor than $\mathbf{tC_{nitro}}$, whose excited state lives longer and is spectrally separated from the signal of the excited state of the donor.

Author contributions

Florian Hurter conducted all experiments, data analysis and interpretation and wrote the manuscript. Anna-Lena J. Halbritter and Iram M. Ahmad prepared the labeled RNA aptamers. Markus Braun helped with data interpretation. All experiments were performed under the supervision of Snorri Th. Sigurdsson and Josef Wachtveitl. All authors read and agreed to the final manuscript.

Conflicts of interest

There are no conflicts to declare.

Acknowledgements

We thank Prof. J. Wöhnert for access to his ITC and J. Vögele for the help during the measurements. This work was financially supported by the Deutsche Forschungsgemeinschaft (DFG) through the Collaborative Research Center (CRC) 902; 'Molecular Principles of RNA-based Regulation' sub-project A7.

References

1 R. R. Breaker and G. F. Joyce, *Chem. Biol.*, 2014, **21**, 1059–1065.
2 N. Pavlova, D. Kaloudas and R. Penchovsky, *Gene*, 2019, **708**, 38–48.
3 A. Ruscito and M. C. DeRosa, *Front. Chem.*, 2016, **4**, 1–14.
4 R. J. Trachman, A. Autour, S. C. Y. Jeng, A. Abdolahzadeh, A. Andreoni, R. Cojocaru, R. Garipov, E. V. Dolgosheina, J. R. Knutson, M. Ryckelynck, P. J. Unrau and A. R. Ferré-D'Amaré, *Nat. Chem. Biol.*, 2019, **15**, 472–479.
5 A. D. Keefe, S. Pai and A. Ellington, *Nat. Rev. Drug Discovery*, 2010, **9**, 537–550.
6 M. Etzel and M. Mörl, *Biochemistry*, 2017, **56**, 1181–1198.
7 F. Groher and B. Suess, *Biochim. Biophys. Acta, Gene Regul. Mech.*, 2014, **1839**, 964–973.
8 A.-S. V. Bédard, E. D. M. Hien and D. A. Lafontaine, *Biochim. Biophys. Acta, Gene Regul. Mech.*, 1863, **2020**, 194501.
9 A. V. Sherwood and T. M. Henkin, *Annu. Rev. Microbiol.*, 2016, **70**, 361–374.
10 R. D. Jenison, S. C. Gill, A. Pardi and B. Polisky, *Science*, 1994, **263**, 1425–1429.
11 S. C. B. Gopinath, *Anal. Bioanal. Chem.*, 2006, **387**, 171–182.
12 A. D. Ellington and J. W. Szostak, *Nature*, 1990, **346**, 818–822.
13 C. Tuerk and L. Gold, *Science*, 1990, **249**, 505–510.
14 Y. Zhang, B. S. Lai and M. Juhas, *Molecules*, 2019, **24**, 941.
15 P. Kumar Kulabhusan, B. Hussain and M. Yüce, *Pharmaceutics*, 2020, **12**, 646.
16 A. K. Deisingh, in *RNA Towards Medicine*, ed. V. Erdmann, J. Barciszewski and J. Brosius, Springer, 2006.
17 W. Zhou, P.-J. J. Huang, J. Ding and J. Liu, *Analyst*, 2014, **139**, 2627–2640.
18 S. Ni, Z. Zhuo, Y. Pan, Y. Yu, F. Li, J. Liu, L. Wang, X. Wu, D. Li, Y. Wan, L. Zhang, Z. Yang, B.-T. Zhang, A. Lu and G. Zhang, *ACS Appl. Mater. Interfaces*, 2021, **13**, 9500–9519.
19 H. Kaur, J. G. Bruno, A. Kumar and T. K. Sharma, *Theranostics*, 2018, **8**, 4016–4032.
20 K.-N. Kang and Y.-S. Lee, in *Future Trends in Biotechnology*, ed. J.-J. Zhong, Springer, Berlin, Heidelberg, 2013, pp. 153–169.
21 C. Berens, F. Groher and B. Suess, *Biotechnol. J.*, 2015, **10**, 246–257.
22 A. Wittmann and B. Suess, *FEBS Lett.*, 2012, **586**, 2076–2083.
23 J. E. Weigand, S. R. Schmidtke, T. J. Will, E. Duchardt-Ferner, C. Hammann, J. Wöhnert and B. Suess, *Nucleic Acids Res.*, 2011, **39**, 3363–3372.
24 J. Hoetzel and B. Suess, *J. Mol. Biol.*, 2022, **434**, 167631.
25 C. Berens and B. Suess, *Curr. Opin. Biotechnol*, 2015, **31**, 10–15.
26 J. E. Weigand, M. Sanchez, E.-B. Gunnesch, S. Zeiher, R. Schroeder and B. Suess, *RNA*, 2008, **14**, 89–97.
27 P. St-Pierre, K. McCluskey, E. Shaw, J. C. Penedo and D. A. Lafontaine, *Biochim. Biophys. Acta, Gene Regul. Mech.*, 2014, **1839**, 1005–1019.
28 B. Y. Michel, D. Dziuba, R. Benhida, A. P. Demchenko and A. Burger, *Frontiers in Chemistry*.
29 T. Förster, *Ann. Phys.*, 1948, **437**, 55–75.
30 J. R. Lakowicz, *Principles of fluorescence spectroscopy*, Springer, 2006.
31 P. G. Wu and L. Brand, *Anal. Biochem.*, 1994, **218**, 1–13.
32 A. Y. Kobitski, M. Hengesbach, M. Helm and G. U. Nienhaus, *Angew. Chem., Int. Ed.*, 2008, **47**, 4326–4330.
33 H. Li, S. Cao, S. Zhang, J. Chen, J. Xu and J. R. Knutson, *Phys. Chem. Chem. Phys.*, 2023, **25**, 7239–7250.
34 S. S. Vogel, B. W. Van der Meer and P. S. Blank, *Methods*, 2014, **66**, 131–138.

35 S. Ranjit, K. Gurunathan and M. Levitus, *J. Phys. Chem. B*, 2009, **113**, 7861–7866.
36 L. Loura, *Int. J. Mol. Sci.*, 2012, **13**, 15252–15270.
37 S. S. Vogel, T. A. Nguyen, B. W. van der Meer and P. S. Blank, *PLOS ONE*.
38 C. Steinmetzger, C. Bäuerlein and C. Höbartner, *Angew. Chem., Int. Ed.*, 2020, **59**, 6760–6764.
39 S. C. Y. Jeng, R. J. Trachman, F. Weissenboeck, L. Truong, K. A. Link, M. D. E. Jepsen, J. R. Knutson, E. S. Andersen, A. R. Ferré-D'Amaré and P. J. Unrau, *RNA*, 2021, **27**, 433–444.
40 A. F. Füchtbauer, M. S. Wranne, M. Bood, E. Weis, P. Pfeiffer, J. R. Nilsson, A. Dahlén, M. Grøtli and L. M. Wilhelmsson, *Nucleic Acids Res.*, 2019, **47**, 9990–9997.
41 K. Börjesson, S. Preus, A. H. El-Sagheer, T. Brown, B. Albinsson and L. M. Wilhelmsson, *J. Am. Chem. Soc.*, 2009, **131**, 4288–4293.
42 H. Gustmann, A.-L. J. Segler, D. B. Gophane, A. J. Reuss, C. Grünewald, M. Braun, J. E. Weigand, S. T. Sigurdsson and J. Wachtveitl, *Nucleic Acids Res.*, 2019, **47**, 15–28.
43 H. Gustmann, D. Lefrancois, A. J. Reuss, D. B. Gophane, M. Braun, A. Dreuw, S. T. Sigurdsson and J. Wachtveitl, *Phys. Chem. Chem. Phys.*, 2017, **19**, 26255–26264.
44 E. Duchardt-Ferner, J. E. Weigand, O. Ohlenschläger, S. R. Schmidtke, B. Suess and J. Wöhnert, *Angew. Chem., Int. Ed.*, 2010, **49**, 6216–6219.
45 S. Stampfl, A. Lempradl, G. Koehler and R. Schroeder, *ChemBioChem*, 2007, **8**, 1137–1145.
46 E. Duchardt-Ferner, S. R. Gottstein-Schmidtke, J. E. Weigand, O. Ohlenschläger, J.-P. Wurm, C. Hammann, B. Suess and J. Wöhnert, *Angew. Chem., Int. Ed.*, 2016, **55**, 1527–1530.
47 A. Sillen and Y. Engelborghs, *Photochem. Photobiol.*, 1998, **67**, 475–486.
48 C. Slavov, H. Hartmann and J. Wachtveitl, *Anal. Chem.*, 2015, **87**, 2328–2336.
49 M. Khrenova, I. Topol, J. Collins and A. Nemukhin, *Biophys. J.*, 2015, **108**, 126–132.
50 I. Krstić, O. Frolow, D. Sezer, B. Endeward, J. E. Weigand, B. Suess, J. W. Engels and T. F. Prisner, *J. Am. Chem. Soc.*, 2010, **132**, 1454–1455.
51 D. Laskaratou, G. S. Fernández, Q. Coucke, E. Fron, S. Rocha, J. Hofkens, J. Hendrix and H. Mizuno, *Nat. Commun.*, 2021, **12**, 1–12.

Supporting information: Förster resonance energy transfer within the Neomycin aptamer

Florian Hurter,[a] Anna-Lena J. Halbritter,[b,c] Iram M. Ahmad,[b] Markus Braun,[a] Snorri Th. Sigurdsson[b] and Josef Wachtveitl*[a]

[a.] Institute of Physical and Theoretical Chemistry, Goethe University Frankfurt, Main, Max-von-Laue-Str. 7, 60438 Frankfurt, Germany
[b.] Science Institute, University of Iceland, Dunhaga 3, 107 Reykjavik, Iceland here
[c.] Department of Chemistry, Ludwig-Maximilians-University (LMU), Munich
† Electronic Supplementary Information (ESI) available: [details of any supplementary information available should be included here]. See DOI: 10.1039/x0xx00000x

Material and methods

Oligonucleotide synthesis. The synthesis of the phosphoramidite of **$Ç_m^f$** [1] was prepared as previously described, and the phosphoramidite used for incorporation of **tC_{nitro}** was purchased from Glen Research. Synthesis and purification of the labeled N1-aptamers was performed according to published procedures.[2]

Sample preparation. The neomycin aptamer was dissolved in a solution of 100 mM NaCl and 20 mM sodium cacodylate buffer at pH 7.4. Static as well as time-resolved fluorescence measurements were performed with an aptamer concentration of 1 µM (without neomycin: -Neo). For the experiments that included the ligand, neomycin was added in a 4-fold excess (4 µM: +Neo). The aptamer was prefolded prior to measurements: The aptamer solution was heated and held at 90 °C for 5 min and then cooled to room temperature for 30 min.

Steady state measurements. Static fluorescence measurements were recorded in a 10 x 2 mm UV-degree quartz cuvette using a JASCO FP 8500 fluorescence spectrometer. Offset, absorption, reabsorption, excitation, and detector corrections were performed for the obtained data.

Time-correlated single photon counting (TCSPC). The TCSPC equipment was composed of three parts: the laser diode driver PDL800-D (PicoQuant), the spectrometer FluoTime100 (FT100, PicoQuant) and the counting card TimeHarp260 Pico (TH260 P, PicoQuant). The repetition frequency range was set to 10 MHz. A pulsed LED with a FWHM of 600 ps was used for excitation at a constant wavelength of 360 nm (PLS360). The UVB390 filter was used to block the excitation light from detection.

Isothermal titration calorimetry (ITC). An iTC200 microcalorimeter was used for the ITC experiments. The sample compartment was filled with a solution of the RNA (10 µM RNA, 20 mM sodium cacodylate, 200 mM NaCl, pH 7.4). The injection syringe was filled with a neomycin solution (100 µM neomycin, 20 mM sodium cacodylate, 200 mM NaCl, pH 7.4). Before the experiment, the system was equilibrated at 20 °C for 10 min. The measurement started after an initial delay of 120 s and a 0.2 µL injection. Subsequently, 20 injections of 2 µL each were applied with a time interval of 180 s while the sample chamber was stirred at 750 rpm.

UV/vis pump-probe transient absorption experiments. The time-resolved transient absorption data were recorded with a home-built pump-probe setup, which has been described in detail elsewhere.[3] The ultra-short fundamental pulses of about 150 fs were generated by a Ti:Sa amplifier system (Clark, MXR-CPA-iSeries, repetition rate of 1 kHz, 775 nm). The excitation wavelength of 388 nm was generated by a frequency doubling (SHG) the laser fundamental (110 nJ, 220 fs). The white light pulse for detection (410 to 650 nm) was generated by focusing the laser fundamental into a CaF_2 crystal of 5 mm thickness. The pulse was split into a reference beam and a sample beam. Both white light pulses were then detected in two separate spectrographs (AMKO multimode). All experiments were performed under magic angle conditions (54.7° angle difference of pump and probe pulse polarization) to avoid anisotropy effects. Finally, the sample was measured in a fused silica cuvette with a path length of 1 mm, constantly moving in the plane perpendicular to the direction of beam propagation to prevent photodegradation.

Isothermal titration calometry (ITC)

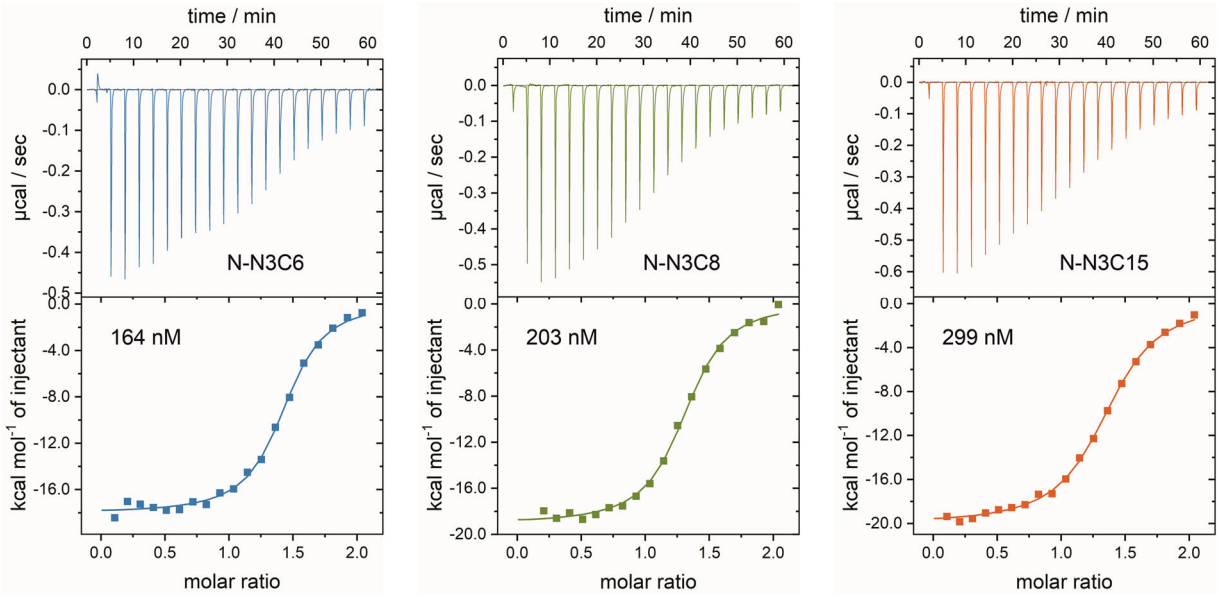

Figure S1 ITC data of **N-N3C6** (blue), **N-N3C8** (green), **N-N3C15** (orange) with the respective K_D values

The determined K_D values (Figure S1) indicate that the binding affinity is comparable to donor only labeled aptamers (Table S1).[4] This comparability further supports the assumption that the data are equivalent to those of the donor only labeled aptamer, regardless of the implementation of the **tC$_{nitro}$**.

Table S1 Dissociation konstants (K_D) values for the unlabeled N1-aptamer as well as for the singly and doubly labeled N1-aptamers.[2]

	K_D [nM]
N1 (unlabeled)	6
N-C6	375
N-C8	318
N-C15	480
N-N3C6	164
N-N3C8	203
N-N3C15	299

Table S2 Lifetimes obtained from the TCSPC experiments. Shown are the lifetimes of the multiexponential decay and their percentage weighting, resulting in the averaged amplitude weighted lifetime τ_{DA}.

	Neo	τ_1 [ns]	τ_2 [ns][a]	τ_3 [ns]	τ_{DA} [ns][a]
N-N3C6	-	0.0147 (99.02%)	0.4731 (0.98%)	/	0.0218
	+	0.0279 (59.08%)	0.2632 (40.92%)	/	0.1242
N-N3C8	-	0.1155 (84.97%)	0.7995 (13.28%)	5.340 (1.75%)	0.2980
	+	0.177 (31.16%)	0.7903 (35.56%)	2.264 (33.29%)	1.0898
N-N3C15	-	0.1236 (28.17%)	1.7673 (64.01%)	3.272 (7.83%)	1.4221
	+	0.3505 (10.88%)	1.1577 (13.46%)	1.905 (75.66%)	1.6353

[a] τ_{DA} corresponds to the averaged amplitude weighted fluorescence lifetime of donor in presence of the acceptor.

The lifetimes (τ_1, τ_2, τ_3) contributing to the multiexponential decay and the averaged lifetime τ_{DA} are given in Table S1. For samples **N-N3C8** and **N-N3C15**, three lifetimes are needed to fit the data correctly. Only two are needed for **N-N3C6**, which is due to the very high FRET efficiency. The lifetimes were obtained by performing a reconvolution fit (equation S1).

$$I(t) = \int_{-\infty}^{t} IRF(t') \sum_{i=1}^{n} A_i e^{-\frac{t-t'}{\tau_i}} \, dt' \qquad \textbf{(S1)}$$

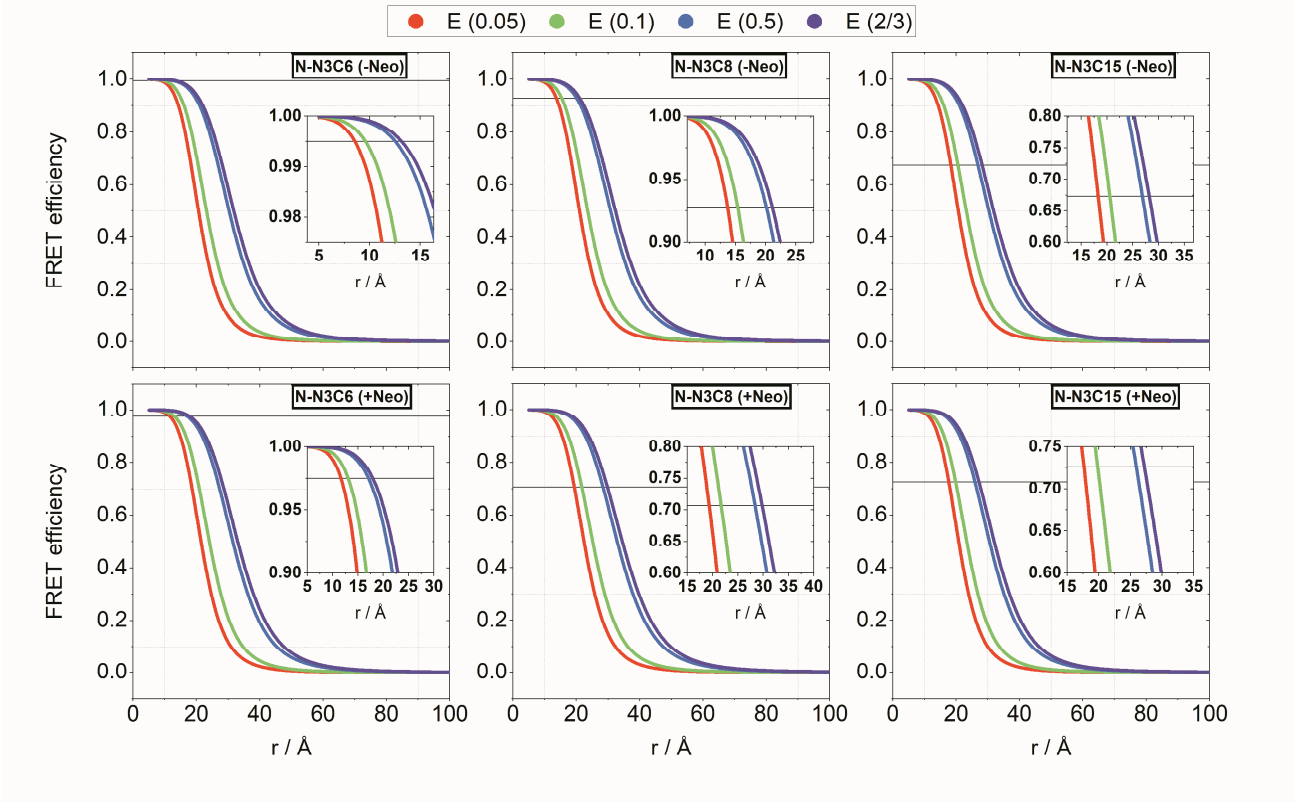

Figure S2 Plot of FRET efficiency E against distance r for samples **N-N3C6**, **N-N3C8**, **N-N3C15** (-/+ Neo). The horizontal gray lines indicate the measured FRET efficiencies E_{trf}. Fluorescence quantum yields of donor alone and κ^2 of 0.05, 0.1, 0.5, and 2/3 were used as input.

The plot of FRET efficiencies as a function of the relative distance between donor and acceptor clearly shows that the change in efficiency is greatest around the Förster radius (Figure S2). Especially for the lower measured efficiencies, this explains the deviations of the measured values from the simulated values for the efficiencies of the energy transfer. Since RNA structures are very flexible and the simulated values are based on the NMR structure of the N1-aptamer, which does not take into account the influence of the incorporation of $\mathbf{tC_{nitro}}$ or $\mathbf{Ç_m^f}$, it is not surprising that these values differ.

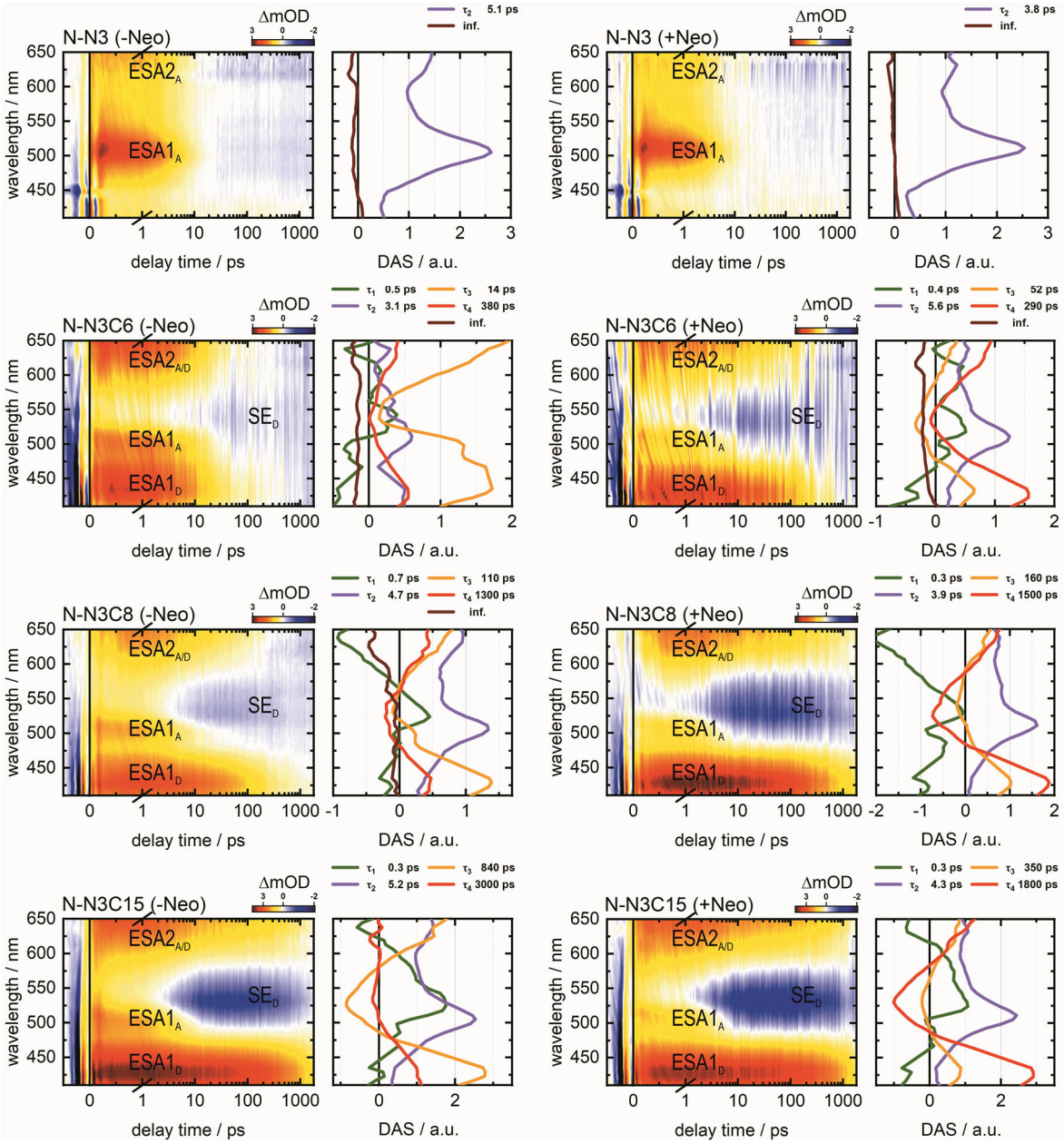

Figure S3 Transient absorptions maps and Decay associated spectra (DAS) of the samples **N-N3**, **N-N3C6**, **N-N3C8** and **N-N3C15**: left column without neomycin, right column with neomycin, top to bottom **N-N3**, **N-N3C6**, **N-N3C8**, **N-N3C15**. τ_1 for the depature of the Franck Condon region is shown in green, τ_2 for the decay of the directly excited tC_{nitro} is shown in violett, τ_3 for the first emitting state of $Ç_{mf}$ is shown in orange, τ_4 for later emitting states is shown in red and the infinity lifetimes shown in brown.

Figure S3 shows all transient absorption measurements including the respective DAS with all determined lifetimes.

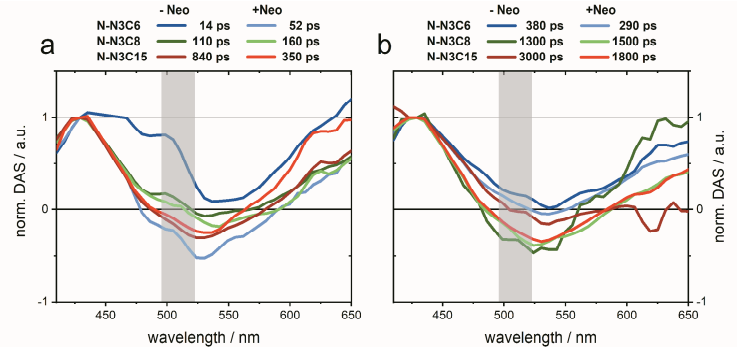

Figure S4 Decay associated spectra (DAS) of the samples **N-N3C6**, **N-N3C8** and **N-N3C15** (-/+Neo). a) DAS spectra for the first emitting state of **Çmf**. b) DAS spectra for the second emitting state of **Çmf**.

Normalized DAS of the first and second emitting state of **Ç$_m$^{f}** (Figure S4) The DAS are comparable for all samples and differ only slightly in their amplitudes. Gray line around 505 nm indicates the wavelength at which the excited state of **tC$_{nitro}$** decays after energy transfer.

Table S3 Lifetimes of the first (τ_3) and second (τ_4) emitting state of **Ç$_m$^{f}**, the percentages of the respective lifetimes and the averaged lifetimes ($\tau_{DA(TAS)}$) based on the percentages of the first and second emitting state.

	Neo	τ_3 [ps]	τ_4 [ps]	τ_3 [%]	τ_4 [%]	$\tau_{DA(TAS)}$ [ps]
N-N3C6	-	14	380	73.79%	26.21%	110
	+	52	290	27.73%	72.27%	224
N-N3C8	-	110	1300	74.70%	25.30%	411
	+	160	1500	34.95%	65.05%	1032
N-N3C15	-	840	3000	72.83%	27.17%	1427
	+	350	1800	22.40%	77.60%	1475

Table S3 shows the lifetimes of the first and second emitting states as well as the percentages of the respective lifetimes and the averaged lifetimes based on the percentages of the first and second emitting state. To determine the percentage of lifetimes, the corresponding DAS of the first and second emitting states were integrated in the range from 416 nm to 435 nm and the integrals were put in relation to each other.

References

1 C. Höbartner, G. Sicoli, F. Wachowius, D. B. Gophane and S. T. Sigurdsson, *The Journal of Organic Chemistry*, 2012, **77**, 7749–7754.

2 H. Gustmann, A.-L. J. Segler, D. B. Gophane, A. J. Reuss, C. Grünewald, M. Braun, J. E. Weigand, S. T. Sigurdsson and J. Wachtveitl, *Nucleic Acids Research*, 2019, **47**, 15–28.

3 C. Slavov, N. Bellakbil, J. Wahl, K. Mayer, K. Rück-Braun, I. Burghardt, J. Wachtveitl and M. Braun, *Physical Chemistry Chemical Physics*, 2015, **17**, 14045–14053.

4 H. Gustmann, A.-L. J. Segler, D. B. Gophane, A. J. Reuss, C. Grünewald, M. Braun, J. E. Weigand, S. T. Sigurdsson and J. Wachtveitl, *Nucleic Acids Research*, 2019, **47**, 15–28.